The Astrophysical Journal Supplement Series, 271:55 (93pp), 2024 April https://doi.org/10.3847/1538-4365/ad24e2

The Initial Mass Function Based on the Full-sky 20 pc Census of ∼3600 Stars and Brown Dwarfs

J. Davy Kirkpatrick[1,2], Federico Marocco[1,2], Christopher R. Gelino[3], Yadukrishna Raghu[2,4], Jacqueline K. Faherty[2,5], Daniella C. Bardalez Gagliuffi[2,5], Steven D. Schurr[1], Kevin Apps[6], Adam C. Schneider[2,7], Aaron M. Meisner[2,8], Marc J. Kuchner[2,9], Dan Caselden[2,5], R. L. Smart[10], S. L. Casewell[11], Roberto Raddi[12], Aurora Kesseli[1], Nikolaj Stevnbak Andersen[2,13], Edoardo Antonini[2], Paul Beaulieu[2], Thomas P. Bickle[2,14], Martin Bilsing[2], Raymond Chieng[2], Guillaume Colin[2], Sam Deen[2], Alexandru Dereveanco[2], Katharina Doll[2], Hugo A. Durantini Luca[2], Anya Frazer[2], Jean Marc Gantier[2], Léopold Gramaize[2], Kristin Grant[2], Leslie K. Hamlet[2], Hiro Higashimura (東村 滉)[15], Michiharu Hyogo[2,16], Peter A. Jałowiczor[2], Alexander Jonkeren[2], Martin Kabatnik[2], Frank Kiwy[2], David W. Martin[2], Marianne N. Michaels[2], William Pendrill[2], Celso Pessanha Machado[2], Benjamin Pumphrey[2], Austin Rothermich[2,17], Rebekah Russwurm[2], Arttu Sainio[2], John Sanchez[2], Fyodor Theo Sapelkin-Tambling[2], Jörg Schümann[2], Karl Selg-Mann[2], Harshdeep Singh[2], Andres Stenner[2], Guoyou Sun (孙国佑)[2,18], Christopher Tanner[2], Melina Thévenot[2], Maurizio Ventura[2], Nikita V. Voloshin[2], Jim Walla[2], Zbigniew Wędracki[2], Jose I. Adorno[5,19], Christian Aganze[20], Katelyn N. Allers[21], Hunter Brooks[2,22], Adam J. Burgasser[23], Emily Calamari[5,24], Thomas Connor[25,26], Edgardo Costa[27], Peter R. Eisenhardt[25], Jonathan Gagné[28], Roman Gerasimov[29], Eileen C. Gonzales[30,31,42], Chih-Chun Hsu[32,33], Rocio Kiman[34], Guodong Li[35,36], Ryan Low[37], Eric Mamajek[25], Blake M. Pantoja[38], Mark Popinchalk[5,24,39], Jon M. Rees[40], Daniel Stern[25], Genaro Suárez[5], Christopher Theissen[23], Chao-Wei Tsai[36], Johanna M. Vos[5,41], and David Zurek[5]
(The Backyard Worlds: Planet 9 Collaboration)

[1] IPAC, Mail Code 100-22, California Institute of Technology, 1200 E. California Boulevard, Pasadena, CA 91125, USA; davy@ipac.caltech.edu
[2] Backyard Worlds: Planet 9
[3] NASA Exoplanet Science Institute, Mail Code 100-22, California Institute of Technology, 770 S. Wilson Avenue, Pasadena, CA 91125, USA
[4] Washington High School, 38442 Fremont Boulevard, Fremont, CA 94536, USA
[5] Department of Astrophysics, American Museum of Natural History, Central Park West at 79th Street, New York, NY 10024, USA
[6] Independent scholar, UK
[7] United States Naval Observatory, Flagstaff Station, 10391 West Naval Observatory Road, Flagstaff, AZ 86005, USA
[8] NSF's National Optical-Infrared Astronomy Research Laboratory, 950 N. Cherry Avenue, Tucson, AZ 85719, USA
[9] NASA Goddard Space Flight Center, Exoplanets and Stellar Astrophysics Laboratory, Code 667, Greenbelt, MD 20771, USA
[10] Istituto Nazionale di Astrofisica, Osservatorio Astrofisico di Torino, Strada Osservatorio 20, I-10025 Pino Torinese, Italy
[11] School of Physics and Astronomy, University Of Leicester, University Road, Leicester LE1 7RH, UK
[12] Universitat Politècnica de Catalunya, Departament de Física, c/ Esteve Terrades 5, 08860 Castelldefels, Spain
[13] Sygehus Lillebalt, Department of Cardiology, Kolding, Denmark
[14] School of Physical Sciences, The Open University, Milton Keynes, MK7 6AA, UK
[15] Earl of March Intermediate School, 4 The Pkwy, Kanata, ON K2K 1Y4, Canada
[16] Meisei University, 2-1-1 Hodokubo, Hino, Tokyo 191-0042, Japan
[17] Physics Department, University of Central Florida, 4000 Central Florida Boulevard, Orlando, FL 32816, USA
[18] Xingming Observatory, Mt. Nanshan, Urumqi, 830011, Xinjiang, People's Republic of China
[19] Department of Physics, University of Miami, Coral Gables, FL 33124, USA
[20] Department of Physics, Stanford University, Stanford, CA 94305, USA
[21] Department of Physics and Astronomy, Bucknell University, Lewisburg, PA 17837, USA
[22] Department of Astronomy and Planetary Science, Northern Arizona University, Flagstaff, AZ 86011, USA
[23] Department of Astronomy & Astrophysics, University of California San Diego, 9500 Gilman Drive, La Jolla, CA 92093, USA
[24] The Graduate Center, City University of New York, New York, NY 10016, USA
[25] Jet Propulsion Laboratory, California Institute of Technology, 4800 Oak Grove Drive, Pasadena, CA 91109, USA
[26] Center for Astrophysics, Harvard & Smithsonian, 60 Garden Street, Cambridge, MA 02138, USA
[27] Universidad de Chile, Casilla 36-D, Santiago, Chile
[28] Institute for Research on Exoplanets, Université de Montréal, Montréal, Canada
[29] Department of Physics & Astronomy, University of Notre Dame, Notre Dame, IN 46556, USA
[30] Department of Physics and Astronomy, San Francisco State University, 1600 Holloway Avenue, San Francisco, CA 94132, USA
[31] Department of Astronomy and Carl Sagan Institute, Cornell University, 122 Sciences Drive, Ithaca, NY 14853, USA
[32] Center for Astrophysics and Space Science, University of California San Diego, La Jolla, CA 92093, USA
[33] Center for Interdisciplinary Exploration and Research in Astrophysics (CIERA), Northwestern University, 1800 Sherman, Evanston, IL 60201, USA
[34] Department of Astronomy, California Institute of Technology, Pasadena, CA 91125, USA
[35] National Astronomical Observatories, Chinese Academy of Sciences, Beijing 100012, People's Republic of China
[36] University of Chinese Academy of Sciences, Beijing 100049, People's Republic of China
[37] Department of Physics and Astronomy, University of Kansas, Lawrence, KS 66046, USA
[38] Departamento de Astronomía, Universidad de Chile, Camino al Observatorio, Cerro Calán, Santiago, Chile
[39] Department of Physics and Astronomy, Hunter College, City University of New York, 695 Park Avenue, New York, NY 10065, USA
[40] Lick Observatory, P.O. Box 85, Mount Hamilton, CA 95140, USA

[41] School of Physics, Trinity College Dublin, The University of Dublin, Dublin 2, Ireland
Received 2023 October 8; revised 2023 November 30; accepted 2023 December 3; published 2024 April 9

Abstract

A complete accounting of nearby objects—from the highest-mass white dwarf progenitors down to low-mass brown dwarfs—is now possible, thanks to an almost complete set of trigonometric parallax determinations from Gaia, ground-based surveys, and Spitzer follow-up. We create a census of objects within a Sun-centered sphere of 20 pc radius and check published literature to decompose each binary or higher-order system into its separate components. The result is a volume-limited census of ∼3600 *individual* star formation products useful in measuring the initial mass function across the stellar ($<8M_{\odot}$) and substellar ($\gtrsim 5M_{\rm Jup}$) regimes. Comparing our resulting initial mass function to previous measurements shows good agreement above $0.8M_{\odot}$ and a divergence at lower masses. Our 20 pc space densities are best fit with a quadripartite power law, $\xi(M) = dN/dM \propto M^{-\alpha}$, with long-established values of $\alpha = 2.3$ at high masses ($0.55 < M < 8.00M_{\odot}$), and $\alpha = 1.3$ at intermediate masses ($0.22 < M < 0.55M_{\odot}$), but at lower masses, we find $\alpha = 0.25$ for $0.05 < M < 0.22M_{\odot}$, and $\alpha = 0.6$ for $0.01 < M < 0.05M_{\odot}$. This implies that the rate of production as a function of decreasing mass diminishes in the low-mass star/high-mass brown dwarf regime before increasing again in the low-mass brown dwarf regime. Correcting for completeness, we find a star to brown dwarf number ratio of, currently, 4:1, and an average mass per object of 0.41 $M_{\odot}$.

Unified Astronomy Thesaurus concepts: Initial mass function (796); Stellar mass functions (1612); Brown dwarfs (185); Trigonometric parallax (1713); Solar neighborhood (1509); Binary stars (154)

Supporting material: machine-readable tables

1. Introduction

The concept of the initial mass function is one of the most fundamental paradigms in astronomy. It embodies the observational evidence for how the universe turns gas into stars and provides an empirical framework on which to test and inform the underlying theory. The initial mass function has far-reaching influence, from providing the cornerstone for galaxy formation scenarios across all cosmic epochs to determining which stellar and substellar populations we see in our own solar neighborhood.

Debate continues on whether the initial mass function is variable with time or dependent on environment, but its description over most of the range of stellar masses in the Milky Way is well determined. Bastian et al. (2010) conclude that the initial mass function is universal for hydrogen-burning stars, at least within the measurement errors of most current observations, and Andersen et al. (2008) specifically conclude that there is no strong evidence for environment-specific effects at masses above $\sim 30M_{\rm Jup}$. However, far less is known about the mass function at the low-mass end. Knowledge in this area tells us the creation ratio between stars and brown dwarfs and enlightens us on whether planetary mass objects formed via star formation are common compared to those formed via protoplanetary disks.

In this paper, we use recent advances in our knowledge of the nearby stellar census to explore in unprecedented detail the field initial mass function. Gaia has helped refine the nearby census down to spectral types of mid-/late-L out to 20 pc (Gaia Collaboration et al. 2021a). For colder spectral types, the Wide-field Infrared Survey Explorer (WISE) mission, together with follow-up parallaxes measured by Spitzer, has filled out this census down to early-Y dwarfs (Kirkpatrick et al. 2019a, 2021a), with the help of many other ground-based endeavors (e.g., Best et al. 2021). Our understanding of the low-mass end is dominated by solivagant L, T, and Y dwarfs, but much less is known about the frequency with which these low-mass objects exist as companions to hotter objects in the census. We rectify that gap in our understanding by building a complete census of all objects within 20 pc of the Sun and splitting those systems into their individual components.

In Section 2, we use previous nearby star lists, additions from Gaia, and published or newly discovered objects lacking Gaia astrometry to construct the census of objects in the 20 pc volume. In Section 3, we discuss the format of the compiled census, which includes data on nomenclature, astrometry, spectral types, photometry, radial velocities, multiplicity, masses, and effective temperatures. In Section 4, we discuss the methods used to directly measure masses. In Section 5, we discuss the fact that some objects in our sample have strong evidence for multiplicity but generally lack sufficient evidence to characterize the mass of the subcomponents, which is a source of uncertainty in our final analysis. In Section 6, we discuss mass estimation for white dwarf progenitors, giants/subgiants, brown dwarfs, young stars, low-metallicity stars (subdwarfs), and normal main-sequence stars and discuss what role objects labeled as exoplanets play in our analysis. In Section 7, we perform analysis of the brown dwarf initial mass function, and then, we mate that to the stellar initial mass function. In Section 8, we discuss the resulting initial mass function over the entire mass range by comparing our fit of the functional form to other estimates in the literature, and in Section 9, we summarize our conclusions. Auxiliary data and analyses are found in the Appendices. In Appendix A, we present photometric, spectroscopic, and astrometric follow-up used to further characterize 20 pc census members and candidates, and in Appendix B, we present a list of the *proximal* systems for each constellation.

2. Creating the 20 pc Census

2.1. Building the List of 20 pc Systems

Our starter list for compiling the census of 20 pc systems was the Preliminary Version of the Third Catalog of Nearby Stars (CNS3; Gliese & Jahreiß 1991), which represents the sum

[42] 51 Pegasi b Fellow.

knowledge, prior to large-area digital surveys, of stars believed to lie within 25 pc of the Sun. We took all objects in CNS3 and cross-identified them with the Gaia Early Data Release 3 (eDR3; Gaia Collaboration et al. 2021b) to provide updated parallaxes. Objects with parallax values <50 mas were removed from further consideration, and those with values ⩾50 mas or lacking a Gaia eDR3 parallax were retained. Two objects listed in the CNS3 as possibly being within 20 pc had no parallax in Gaia DR2, Gaia eDR3, or the literature. These were added to a list, shown in Table 1, of potential 20 pc members to consider further. Other additions to this list are discussed in Section 2.1.1.

As the next step, we searched the SIMBAD Astronomical Database (Wenger et al. 2000) for all objects with reported parallaxes ⩾50 mas that were not already included above. We crossmatched these against Gaia eDR3, again retaining those with values ⩾50 mas or lacking a Gaia eDR3 parallax and removing from further consideration those objects with Gaia parallax values <50 mas.

Next, we created an independent list of 20 pc members by selecting objects with Gaia eDR3 parallax values ⩾50 mas. This list was vetted by a group of Backyard Worlds: Planet 9 (hereafter, Backyard Worlds; Kuchner et al. 2017)[43] citizen scientists to produce a list of bona fide 20 pc members alongside a list of potential 20 pc members that lacked independent verification of proximity, such as displaying unmistakable proper motion in archival imagery. Although most objects in the first Gaia-selected list were already in the master census discussed above, this Gaia selection nonetheless added another ∼60 discoveries to the total, as well as another ∼70 objects needing further scrutiny.

With this revised master census in hand, we checked against several other online sources and published papers to ensure that no objects had inadvertently been dropped. We consulted the lists of 10 pc objects produced by Reylé et al. (2021)[44] and the Research Consortium on Nearby Stars (RECONS),[45] but this did not add any new objects. We also searched the Gaia Catalog of Nearby Stars (GCNS) published by Gaia Collaboration et al. (2021a), but this likewise did not indicate any missing objects. For white dwarfs specifically, we further checked recent lists by Sion et al. (2014), McCook & Sion (2016), Hollands et al. (2018),[46] McCleery et al. (2020), Gentile Fusillo et al. (2021), and O'Brien et al. (2023) and also found no omissions.

With the release of Gaia DR3 (Gaia Collaboration et al. 2023a), we performed final checks of our list. The astrometry in DR3 is identical to that in eDR3 except for binary and higher-order systems in which the astrometric and/or spectroscopic data could be used to establish physical parameters for individual components. Specifically, we found 55 objects within 20 pc that had revised astrometry. For two of these—HD 64606 and NLTT 25223—the revised DR3 parallaxes place them outside the 20 pc volume. These objects were dropped from our list, and we updated the Gaia astrometry for the other 53. We also checked each of the non-single-star lists accompanying the DR3 release to search for systems in which the revised astrometry may have pushed a distance closer than 20 pc. We found one such object—Ross 59—which we added to our list.

Roughly three-quarters of our resulting master census is comprised of objects with parallaxes in Gaia DR3. The other quarter is missing from DR3. Some of these objects, such as Sirius, are too bright for Gaia astrometry, whereas others, such as very faint brown dwarfs, are undetected by Gaia. Most of the rest are missing because they are likely in multiple systems for which the Gaia five-parameter astrometric solution has still not converged to a publishable solution.

Given that even Gaia DR3 has limitations for nearby multiple systems and very faint brown dwarfs, we have consulted additional publications to check for other possible 20 pc members that we may have missed in our checks above. Given that earlier type stars are likely bright enough to have been identified prior to 1991, these missing objects fall into two categories: (1) nearby M dwarfs—which constitute the majority of stars in the solar neighborhood—discovered since the 1991 update of CNS3, and (2) newly discovered L, T, and Y dwarfs. These additional checks are discussed in the subsections below.

2.1.1. Other Published M Dwarfs

To better complete the M dwarf list, we first consulted the all-sky compilation of Finch et al. (2014), who used the US Naval Observatory fourth CCD Astrograph Catalog (UCAC4; Zacharias et al. 2013) in concert with the American Association of Variable Star Observers (AAVSO) Photometric All-Sky Survey (APASS[47]) and Two Micron All Sky Survey (2MASS; Skrutskie et al. 2006) to identify objects within 25 pc of the Sun. The methodology used a suite of color-to-absolute-magnitude relations to provide distance estimates for detections, although this was supplemented with proper-motion detection in order to further distinguish nearby stars from background sources. We took this list (their Tables 5 and 6) and selected those candidates having Finch et al. (2014) estimated distances ⩽20 pc and, if available, other published distance estimates ⩽20 pc from their Table 6. This resulted in 267 objects not already in our master census created above. Of these, 251 had parallaxes in Gaia eDR3 (or Gaia DR2, if parallaxes were lacking in eDR3) placing them outside of 20 pc. Of the remaining 16 objects, seven were found to have other published parallaxes or additional distance estimates placing them beyond 20 pc. The final nine possible additions are listed in Table 1 for further scrutiny.

Second, we cross-checked our master table against a volume-complete subsample of 0.1–0.3 $M_{\odot}$ M dwarfs within 15 pc of the Sun (Winters et al. 2021) whose parallax data were pulled from both Gaia DR2 and the literature. We found that all of the host stars in those systems were already included in our master list.

Third, we combed through The Solar Neighborhood series of papers by RECONS—specifically Papers I (Henry et al. 1994) through XLIX (Vrijmoet et al. 2022)—to identify all objects verified or suspected to fall within 20 pc of the Sun. Our earlier checks had identified all of the confirmed 20 pc objects, but

[43] https://www.zooniverse.org/projects/marckuchner/backyard-worlds-planet-9

[44] See also https://gucds.inaf.it/GCNS/The10pcSample.

[45] This 2020 November 1 list is available at http://recons.org/publishedpi.2020.1101. Note that LHS 225AB, which is noted by RECONS to fall within 20 pc, is confirmed to fall outside 20 pc by Gaia eDR3.

[46] Hollands et al. (2018) suggest that WD 1443+256 is within 20 pc and that the Gaia DR2 parallax of 1.44 ± 0.55 mas is in error, but the Gaia DR3 parallax seems to confirm that the object is truly distant (ϖ_{abs} = 1.43 ± 0.04 mas). Two other objects in Hollands et al. (2018), WD 0454+620 and WD 2140+078, are also shown to be outside of the 20 pc sample by Gaia DR3.

[47] https://www.aavso.org/apass

Table 1
Stars Lacking Trigonometric Parallaxes but Possibly within 20 pc

Name	Approx. J2000 Coords (hhmm ± ddmm)	J2000 R.A. (deg)	J2000 Decl. (deg)	Sp. Ty.	Sp. Ty. References	d_{est} Lit. (pc)	d_{est} Lit. References	d_{est} Adopt.[p] (pc)
(1)	(2)	(3)	(4)	(5)	(6)	(7)	(8)	(9)
EGGR 285 AB	0037−2053[a]	9.352994	−20.895999	DA3+M3.5	(1, 2)	∼16	1	51–63
2MASS J02133021−4654505 AB	0213−4654[b]	33.376130	−46.914003	M3.5+M3.5	(3)	19.0 ± 4.4	2	⩾29
2MASS J03323578+2843554 ABC	0332+2843[c]	53.149418	28.731716	M4+M6γ+L0γ	(4, 5)	15.8 ± 3.1	2	55
TYC 2885-494-1	0401+4254[d]	60.291356	42.908987	⋯	⋯	17.7 ± 3.5	2	⩾20
PM J04248+5339 E	0424+5339[e]	66.220239	53.663644	M4	(6)	19.0 ± 3.2	2	⩾23
LP 780-23 AB	0640−1627[f]	100.036317	−16.456009	M2.5	(7)	∼20.0	3	⩾20
PM J06574+7405	0657+7405[g]	104.357470	74.090588	M4	(8)	17.0 ± 3.2	2	⩾21
2MASS J07543412+0832252	0754+0832[h]	118.641273	8.540408	M2.5	(9)	17.8 ± 3.3	2	⩾24
PM J07591+1719	0759+1719[i]	119.779474	17.329659	M4–5	(10)	19.0 ± 3.7	2	⩾23
LP 617-21 AB	1315−0249[j]	198.827584	−2.831640	M3.5+M4.5	(11)	∼18.7	3	⩾22
GSC 03466-00805 AB	1341+4854[k]	205.365957	48.912086	M3	(12)	19.2 ± 3.6	2	⩾26
LP 386-49 AB	1625+2601[l]	246.383899	26.027218	M3	(8)	∼15	1	⩾21
LTT 8875	2208−0824[m]	332.135825	−8.415613	M2.5	(14)	∼19.3	3	⩾27
L 166-44	2234−6107[n]	338.521173	−61.128008	M4.5	(15)	∼18.9	3	⩾22
LP 822-37 AB	2311−1701[o]	347.991624	−17.032996	M4	(15, 16)	∼18.8	3	⩾18

Notes.
[a] 0037−2053: Farihi et al. (2006) estimate independent distances of 63 pc for the white dwarf and 51 pc for the M dwarf, placing the system well outside of 20 pc.
[b] 0213−4654: There is a single Gaia eDR3 entry for this source with $G = 13.12 \pm 0.01$ mag, and $G_{Bp} - G_{Rp} = 2.83 \pm 0.01$ mag, the latter suggesting an M4 dwarf (Kiman et al. 2019). Kiman et al. (2019) find that $M_G \approx 10.4$ mag for an M3.5 dwarf, or $M_G \approx 10.8$ mag for an M4. If the Gaia source represents joint photometry of the system, then the implied distance is ⩾41 pc; if the Gaia source represents only one component, then the implied distance is ⩾29 pc. In either case, this system appears to be outside of 20 pc.
[c] 0332+2843: this young system, a likely member of the β Pic Moving Group, has a distance estimate of 55 ± 4 pc from Malo et al. (2014b), placing it well outside of 20 pc.
[d] 0401+4254: Gaia eDR3 measures $G = 10.70 \pm 0.01$ mag, and $G_{Bp} - G_{Rp} = 2.19 \pm 0.01$ mag. The color suggests a value of $M_G \approx 9.2$ mag (type ∼M1.5–M2; Kiman et al. 2019), implying a distance of 20 pc if the object is single. Given that the object has no five-parameter astrometric solution in Gaia eDR3, it is likely a multiple system, which would push this distance estimate even larger.
[e] 0424+5339: Gaia eDR3 measures $G = 13.12 \pm 0.01$ mag, and $G_{Bp} - G_{Rp} = 2.86 \pm 0.01$ mag. The color suggests a value of $M_G \approx 11.3$ mag (type ∼M4–M4.5), implying a distance of 23 pc if the object is single.
[f] 0640−1627: Winters et al. (2015) derived the ∼20 pc distance estimate under the assumption that this object was single. Gaia eDR3 splits this into two nearly equal-magnitude components, pushing the distance estimate beyond 20 pc.
[g] 0657+7405: Gaia eDR3 measures $G = 12.37 \pm 0.01$ mag, and $G_{Bp} - G_{Rp} = 2.70 \pm 0.01$ mag. The color suggests a value of $M_G \approx 10.8$ mag (type ∼M4), implying a distance of 21 pc if the object is single. (A previously overlooked measurement of $\varpi_{abs} = 37.8 \pm 4.1$ mas from Finch & Zacharias 2016b places this object at ∼26.5 pc.)
[h] 0754+0832: Gaia eDR3 measures $G = 11.79 \pm 0.01$ mag, and $G_{Bp} - G_{Rp} = 2.46 \pm 0.01$ mag. The color suggests a value of $M_G \approx 10.0$ mag (type ∼M2.5–M3), implying a distance of 24 pc if the object is single.
[i] 0759+1719: Gaia eDR3 measures $G = 12.71 \pm 0.01$ mag, and $G_{Bp} - G_{Rp} = 2.80 \pm 0.01$ mag. The color suggests a value of $M_G \approx 10.9$ mag (type ∼M3.5), implying a distance of 23 pc if the object is single. If the absolute magnitude is even fainter, as the Bowler et al. (2019) spectral type suggests, this moves the single-object estimate within 20 pc.
[j] 1315−0249: There is a single Gaia eDR3 entry for this source with $G = 12.92 \pm 0.01$ mag, and $G_{Bp} - G_{Rp} = 2.83 \pm 0.01$ mag. The color implies $M_G = 11.2$ mag (M4–M4.5). If the Gaia source represents only the primary, then the implied distance is 22 pc. If the Gaia magnitude is a joint magnitude, the implied distance is even larger. In either case, this system appears to be outside of 20 pc.
[k] 1341+4854: There is a single Gaia eDR3 entry for this source with $G = 12.44 \pm 0.01$ mag, and $G_{Bp} - G_{Rp} = 2.64 \pm 0.01$ mag (M3.5–M4). The measured, joint spectral type of the system implies $M_G = 10.0 - 10.4$ mag. (The $\Delta i' = 0.5$ mag of the binary measured by Lamman et al. 2020, would imply M components separated by only a half spectral subclass, so we assume an absolute magnitude range encompassing M3–M3.5.) If the Gaia source represents only the primary, then the implied distance is ⩾26 pc. Other assumptions push this value larger, so this system is assumed to lie beyond 20 pc.
[l] 1625+2601: There is a single Gaia eDR3 entry for this source with $G = 11.59 \pm 0.01$ mag, and $G_{Bp} - G_{Rp} = 2.52 \pm 0.01$ mag (M3). The $\Delta i' = 0.5$ mag of the binary measured by Lamman et al. (2020) would imply M components separated by only a half spectral subclass, so we assume an absolute magnitude range encompassing M2.5–M3, or $M_G = 9.7 - 10.0$ mag. If the Gaia source represents only the primary, then the implied distance is ⩾21 pc. Other assumptions push this value larger, so this system is assumed to lie beyond 20 pc. (A previously overlooked measurement of $\varpi_{abs} = 39.7 \pm 7.2$ mas from Finch & Zacharias 2016b places this object at ∼25.2 pc.)
[m] 2208−0824: Huber et al. (2016) estimate a distance of 31.1 pc using reduced proper motion and colors covering a wide wavelength baseline. Scholz & Meusinger (2005) estimate a distance of 27.5 pc based on the 2MASS J-band magnitude and spectral type.
[n] 2234−6107: Gaia eDR3 measures $G = 13.61 \pm 0.01$ mag, and $G_{Bp} - G_{Rp} = 3.04 \pm 0.01$ mag. The color suggests a value of $M_G \approx 11.9$ mag (type ∼M5), implying a distance of 22 pc if the object is single.
[o] 2311−1701: Reid et al. (2007) estimate a distance of 10.0 pc, and Scholz & Meusinger (2005) estimate 17.4 pc, assuming the object is single in both cases. Gaia eDR3 splits this into two sources with $G = 12.61 \pm 0.01$ mag, and $G = 13.25 \pm 0.01$ mag, having colors of $G_{Bp} - G_{Rp} = 2.85 \pm 0.01$ mag, and $G_{Bp} - G_{Rp} = 2.84 \pm 0.01$ mag, respectively. The colors suggest a value of $M_G \approx 11.3$ mag (type ∼M4.5) for both components, implying a distance of 18–25 pc.
[p] This is the adopted distance estimate. See per-object notes above for details.

References for Sp. Ty.: (1) Koester et al. (2009), (2) Farihi et al. (2006), (3) Bergfors et al. (2016), (4) Malo et al. (2014b), (5) Calissendorff et al. (2020), (6) Terrien et al. (2015), (7) Jeffers et al. (2018), (8) Lépine et al. (2013), (9) Alonso-Floriano et al. (2015), (10) Bowler et al. (2019), (11) Janson et al. (2012), (12) Rajpurohit et al. (2020), (14) Scholz & Meusinger (2005), (15) Rajpurohit et al. (2013), (16) Reid et al. (2007). References for d_{est}: (1) Gliese & Jahreiß (1991), (2) Finch et al. (2014), (3) Winters et al. (2015).

(This table is available in machine-readable form.)

there were, however, a small number of nearby candidates from Winters et al. (2015) that still lack a trigonometric parallax from any source. These were also added to Table 1.

As discussed in the footnotes to Table 1, we have used available photometry and spectroscopy to update the distance estimates for these objects. After additional scrutiny, we find that only one of these—LP 822-37 AB—likely falls within 20 pc, so it has been added to our master census.

2.1.2. M, L, T, and Y Dwarf Discoveries from Backyard Worlds

Since the recent publication of our 20 pc L, T, and Y dwarf census (Kirkpatrick et al. 2021a), new nearby low-mass stars and brown dwarfs have continued to be recognized via discovery and/or additional follow-up. Examples are a new parallax confirming the nearby nature of the extreme T subdwarf WISEA J181006.18−101000.5 (Lodieu et al. 2022), the discovery and confirming parallax of the late-T dwarf VVV J165507.19−421755.5 (Schapera et al. 2022), and the discovery and established physical companionship of the possible Y dwarf companion to Ross 19 (Schneider et al. 2021). Some other 20 pc suspects, such as CWISE J061741.79+194512.8 AB (Humphreys et al. 2023), have also been shown to fall outside the 20 pc volume after additional follow-up. Still other candidates—other isolated field brown dwarfs identified by the Backyard Worlds team—may yet prove to be new members of the 20 pc census.

To assess the status of each of these, we list in Table 2 all newer M, L, T, and Y dwarf discoveries that had initial distance estimates of <25 pc. To obtain more informed distance estimates of these candidates, in addition to providing additional data on other objects previously believed to be in the 20 pc census, we have searched photometric archives for additional data longward of 1 μm (along with Gaia magnitudes in the case of brighter sources) and have performed other photometric,[48] spectroscopic, or astrometric follow-up on selected targets. Our own 1.25 and 1.65 μm follow-up and reductions, along with our reduction of archival data at 3.6 and 4.5 μm, are described in Appendix A.1. Our optical and near-infrared spectroscopic follow-up is discussed in Appendix A.2. Additional parallactic measurements are described in Appendix A.3.

Using this set of compiled data, we have recomputed distance estimates, as listed in Table 2. Column d_J is the distance estimate derived by comparing the measured $J_{\rm MKO}$ magnitude to the predicted $M_{\rm JMKO}$ magnitude derived from the $M_{\rm JMKO}$ versus $J_{\rm MKO}-{\rm W2}$ relation of Kirkpatrick et al. (2021a).[49] This estimate is valid only for objects with $J_{\rm MKO}-{\rm W2}\geqslant 4.0$ mag, as smaller values may lead to non-unique solutions for $M_{\rm JMKO}$ (Figure 20(a) of Kirkpatrick et al. 2021a). Column d_H is the distance estimate derived by comparing the measured H magnitude to the predicted M_H magnitude derived from the M_H versus spectral type relation of Kirkpatrick et al. (2021a).[50] The published relation is restricted to types of L0 and later. Column $d_{\rm ch2}$ is the distance estimate derived by comparing the measured ch2 magnitude to the predicted $M_{\rm ch2}$ magnitude derived from the $M_{\rm ch2}$ versus ch1 −ch2 relation of Kirkpatrick et al. (2021a). This estimate is valid only for objects with $0.3\leqslant {\rm ch1}-{\rm ch2}\leqslant 3.7$ mag, as shown in Figure 18(c) of Kirkpatrick et al. (2021a). Method 1 ($M=1$ in the table) takes the average of these three independent distance measurements—or as many of these as can be derived—as the adopted distance.

Column d_{W2} is the distance estimate derived by comparing the measured W2 magnitude to the predicted M_{W2} magnitude derived from the M_{W2} ($M_{\rm ch2}$) versus W1−W2 relation of Kirkpatrick et al. (2021a). This estimate is valid only for objects with $1.0\leqslant {\rm W1}-{\rm W2}\leqslant 4.5$ mag, as shown in Figure 19 (c) of Kirkpatrick et al. (2021a). Method 2 ($M=2$ in the table) takes this estimate as the adopted distance.

Column d_G is the distance estimate derived by comparing the measured Gaia G magnitude to the predicted M_G magnitude derived from an M_G versus $G-J$ relation derived specifically for this paper. This estimate is valid only for objects with $1.5\leqslant G-J\leqslant 5.0$ mag. Method 3 ($M=3$ in the table) uses this as the adopted distance. Method 4 ($M=4$ in the table) is exactly the same as Method 3 except that its distance estimate, d_{GRP}, uses the Gaia G_{RP} magnitude instead of G and uses an M_{GRP} versus $G_{RP}-J$ relation also derived specifically for this paper. Method 5 ($M=5$ in the table) uses the Gaia DR3 parallax, if available, to establish the distance.

When none of the five estimation methods above apply, we use combinations of colors to solve for degeneracies among possible spectral type or absolute magnitude solutions, as discussed in the notes to the table. For a very small number of objects, the adopted distance is left blank, as no estimate will be possible until additional follow-up is acquired.

Finally, as another arbiter of proximity to the Sun, Table 2 lists the measured CatWISE2020 proper motions (Eisenhardt et al. 2020; Marocco et al. 2021) and how significantly those measurements differ from zero. Also, using the color versus spectral type relations given in Kirkpatrick et al. (2021a), we have estimated spectral type based on the W1−W2 color (SpW), ch1−ch2 color (SpS), and $J-$W2 color (SpJW), where the valid color ranges are $0.4\leqslant {\rm W1}-{\rm W2}\leqslant 4.0$ mag, $0.3\leqslant {\rm ch1}-{\rm ch2}\leqslant 3.0$ mag, and $4.0\leqslant J-{\rm W2}\leqslant 8.5$ mag.

Of the 211 candidate objects in the table, 44 have adopted distance estimates placing them closer than 20 pc (res = in, as listed in the table). Although we have tentatively added these 44 objects to the 20 pc census, obtaining parallaxes of all objects in Table 2 still believed to be within 25 pc would be desirable to more carefully determine which are the true 20 pc members.

2.2. 20 pc Stars with Newly Discovered Companions

While assembling our nearby census, we discovered a small number of objects that fall in close proximity to other, higher-mass stars in the list. These known stars and their possible companions are discussed further below and are illustrated in Figure 1.

HD 13579 (0215+6740), a K2 dwarf (Bidelman 1985) at 18.6 pc (Gaia DR3). The motion object CWISER J021550.96+674017.2 from Table 2 was discovered by D. Caselden during a targeted search for companions to known 20 pc stars using multiepoch imaging data from WISE (Figure 1(a)). Follow-up $J_{\rm MKO}$-band photometry from Keck/MOSFIRE (see Appendix A.1) shows that the current

[48] All photometry in this paper is reported on the Vega system.

[49] Note that, for this distance estimate and others that follow, we consider WISE W2 and Spitzer/IRAC ch2 photometry to be interchangeable, as shown in Figure 15 of Kirkpatrick et al. (2021a), meaning that we can use the $J_{\rm MKO}-$ ch2 color in the published relation as a proxy for the $J_{\rm MKO}-$ W2 color.

[50] Note that the MKO- and 2MASS-based H-band filters are essentially identical, so we use $H_{\rm MKO}$ and $H_{\rm 2MASS}$ magnitudes interchangeably, as further discussed in Section 3.1 of Kirkpatrick et al. (2011).

Table 2
Potentially New M, L, T, and Y Dwarf Members of the 20 pc Census

Column (1)	Description (2)	Example Entry (3)
Name	Object's discovery designation with J2000 coordinates	CWISE J180308.71−361332.1
DiscoveryRef	Discovery reference[a]	Q
SpOp	Optical spectral type[b]	…
SpIR	Near-infrared spectral type[b]	…
SpRf	Reference for the spectral type[c]	–
G	*G*-band magnitude from Gaia DR3 (mag)	…
G_RP	G_{RP}-band magnitude from Gaia DR3 (mag)	…
W1	W1 magnitude from the WISE catalog indicated by the object designation (mag)[d]	19.048
W1err	Uncertainty in W1 (mag)	null
W2	W2 magnitude from the WISE catalog indicated by the object designation (mag)	14.948
W2err	Uncertainty in W2 (mag)	0.029
ch1	Spitzer/IRAC ch1 magnitude (mag)	…
ch1err	Uncertainty in ch1 (mag)	…
ch2	Spitzer/IRAC ch2 magnitude (mag)	…
ch2err	Uncertainty in ch2 (mag)	…
S	Reference for the Spitzer photometry[e]	–
JMKO	*J*-band magnitude on the Maunakea Observatories filter system (mag)[f]	18.44
Jerr	Uncertainty in JMKO (mag)	0.16
H	*H*-band magnitude on either the Maunakea Observatories or 2MASS filter system (mag)	…
Herr	Uncertainty in *H* (mag)	…
Ph	Reference for *J* and *H* photometry[g]	v-
DateObs	UT date of observation for any JMKO or *H* values reported for the first time in this paper	…
pmra	Proper motion in R.A. from CatWISE2020 (arcsec yr^{-1})	0.25550
pmrerr	Uncertainty in pmra (arcsec yr^{-1})	0.0431
pmdec	Proper motion in decl. from CatWISE2020 (arcsec yr^{-1})	0.01887
pmderr	Uncertainty in pmdec (arcsec yr^{-1})	0.0454
pmtot	Total proper motion (mas yr^{-1})	256.2
pmerr	Uncertainty in pmtot (mas yr^{-1})	62.6
pmsg	Significance of the CatWISE2020 proper-motion measurement (pmtot/pmerr)	4.1
d_J	Distance estimate based on the M_J versus $J-$W2 relation (pc)	…
d_H	Distance estimate based on the M_H versus spectral type relation (pc)	…
d_ch2	Distance estimate based on the M_{ch2} versus ch1−ch2 relation (pc)	…
d_W2	Distance estimate based on the M_{W2} versus W1−W2 relation (pc)	<8.93
d_G	Distance estimate based on the M_G versus $G-J$ relation (pc)	…
d_GRP	Distance estimate based on the M_{GRP} versus $G_{RP}-J$ relation (pc)	…
d_adp	Adopted distance (pc)	16.9
M	Method used to determine d_adp[h]	6
Res	Result[i]	in
JW2	$J-$W2 color (mag)	3.49
ch12	ch1−ch2 color (mag)	…
W12	W1−W2 color (mag)	>4.10
GJ	$G-J$ color (mag)	…
GRPJ	$G_{RP}-J$ color (mag)	…
SpW	Spectral type suggested by the W1−W2 color	…
SpS	Spectral type suggested by the ch1−ch2 color	…
SpJW	Spectral type suggested by the $J-$W2 color	…
Note	Additional notes for this object	$J-$W2 suggests ∼T8–8.5 and implies $d \approx 16.9$ pc; motion confirmed in VVV *J*-band images

Notes.
[a] Alphabetic characters refer to discoveries in this paper by Backyard Worlds citizen scientists, and numeric characters refer to published literature references. Both an alphabetic and a numeric code are listed in cases for which a citizen scientist rediscovered a published object that we felt required a fresh look—A = Nikolaj Stevnbak Andersen, B = Paul Beaulieu, C = Guillaume Colin, D = Dan Caselden, E = Andres Stenner, F = Guoyou Sun, G = Sam Goodman, H = Leslie K. Hamlet, I = Nikita V. Voloshin, J = Jörg Schümann, K = Martin Kabatnik, L = Léopold Gramaize, M = David W. Martin, N = Karl Selg-Mann, O = Frank Kiwy, P = William Pendrill, Q = Tom Bickle, R = Austin Rothermich, S = Arttu Sainio, T = Melina Thévenot, U = Alexandru Dereveanco, V = Christopher Tanner, W = Jim Walla, X = Alexander Jonkeren, Y = Benjamin Pumphrey, Z = Zbigniew Wędracki, a = Hiro Higashimura, b = John Sanchez, c = Martin Bilsing, 1 = Meisner et al. (2020a), 2 = Meisner et al. (2020b), 3 = Schneider et al. (2016), 4 = Schneider et al. (2017), 5 = Schneider et al. (2020), 6 = Schneider et al. (2021), 7 = Schneider et al. (2022), 8 = Zhang et al. (2019), 9 = Kellogg et al. (2017), 10 = Best et al. (2020), 11 = Martin et al. (2018), 12 = Kirkpatrick et al. (2021a), 13 = Faherty et al. (2020), 14 = Bardalez Gagliuffi et al. (2020), 15 = Luhman (2014), 16 = Kota et al. (2022), 17 = Schapera et al. (2022), 18 = Humphreys et al. (2023), 19 = Rothermich et al. (2024, submitted), 20 = Skrzypek et al. (2016).
[b] Codes are −5.0 = M5, 0.0 = L0, 5.0 = L5, 10.0 = T0, 15.0 = T5, 20.0 = Y0, etc.
[c] The first character is for the optical type, and second character for the near-infrared type: A = Schneider et al. (2017), E = Martin et al. (2018), F = Faherty et al. (2020), H = Humphreys et al. (2023), I = Kirkpatrick et al. (2021a), J = Kirkpatrick et al. (2016), K = this paper, L = Kellogg et al. (2017), M = Meisner et al. (2020b), R = Rothermich et al. (2024, submitted), S = Schapera et al. (2022), X = Schneider et al. (2020), Y = Schneider et al. (2022), Z = Zhang et al. (2019).
[d] Values lacking uncertainties are 2σ brightness upper limits.
[e] Codes are—a = Meisner et al. (2020a), b = Meisner et al. (2020b), K = this paper.
[f] Values lacking uncertainties are 5σ brightness upper limits.
[g] Two-character code for the reference to JMKO and H, respectively. Note that *H*-band magnitudes are generally included only for sources with measured spectral types: 2 = 2MASS All-Sky Point Source Catalog, G = Gemini/FLAMINGOS-2 (this paper), K = Keck/MOSFIRE (this paper), P = Palomar/WIRC (this paper), S = Schneider et al. (2021), U = UHS, u = ULAS or UGPS, V = VHS, v = VISTA Variables in the Via Lactea survey (VVV), Z = VVV photometry from Schapera et al. (2022).
[h] Codes are: 1 = The average of d_J, d_H, d_ch2 is used, 2 = d_W2 alone is used, 3 = d_G alone is used, 4 = d_GRP alone is used, 5 = The distance is determined from the Gaia DR3 parallax, 6 = see note for details.
[i] Codes are: in = object assumed to be located within 20 pc of the Sun and included in the 20 pc census, out = object assumed to be located beyond 20 pc and not included in the 20 pc census.

(This table is available in its entirety in machine-readable form.)

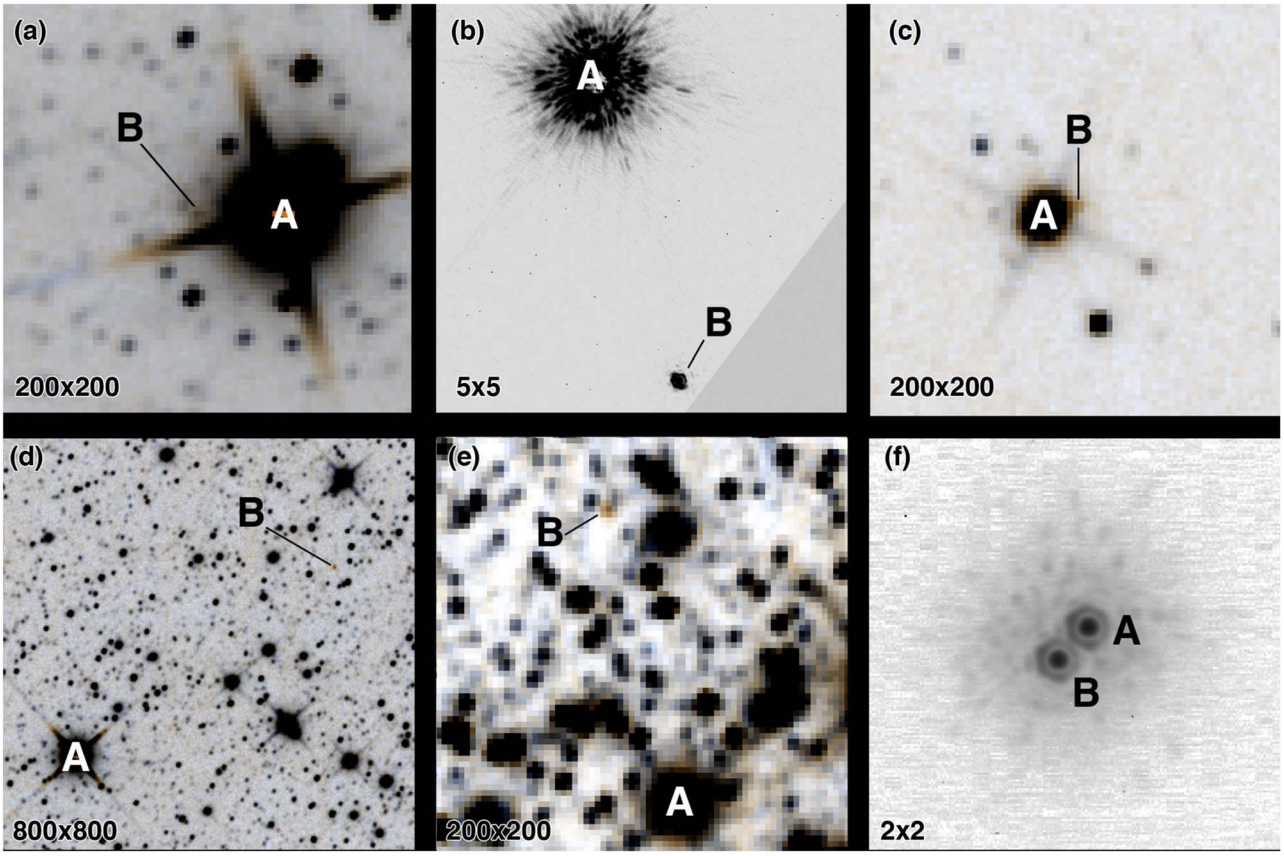

Figure 1. Images illustrating the six new multiple systems discussed in the text. Each image has north up and east to the left, and the size of each (in arcseconds) is noted in the legend. (a) HD 13579 and CWISER J021550.96+674017.2, (b) HD 17230 and Gaia DR3 2548874541191948 8, (c) G 43-23 and WISEU J100241.49 +145914.9, (d) HD 170573 and CWISE J183207.94−540943.3, (e) G 155-42 and CWISE J184803.45−143232.3, and (f) 2MASS J19253089+0938235 A and B. All panels show WISE W1+W2 images from WiseView, except for panel (b), which shows a Keck/NIRC2 K_p-band image, and panel (f), which shows a Keck/NIRC2 K-band image.

location of the companion coincides with a background source, rendering the $J-\mathrm{W2} = 0.78 \pm 0.02$ mag color useless as a gauge of spectral type. The measurement of $\mathrm{W1}-\mathrm{W2} = 0.49 \pm 0.02$ mag from the CatWISE2020 Reject Catalog (Marocco et al. 2021) is also contaminated, as the WISE imaging sequence shown in WiseView[51] (Caselden et al. 2018) indicates that this is a much redder source. The motion measurement from the CatWISE2020 Reject Catalog, 392 ± 11 mas yr^{-1} in R.A. and -102 ± 10 mas yr^{-1} in decl., is also contaminated by background sources but shows a magnitude and direction roughly similar to the values for the 41″ separated K2 star HD 13579 (518.178 ± 0.012 mas yr^{-1} in R.A. and -305.636 ± 0.014 mas yr^{-1} in decl.; Gaia DR3). Using the WISE W2 epochal positions from the unTimely Catalog (Meisner et al. 2023a), a linear least-squares fit results in motions of 698 ± 35 mas yr^{-1} in R.A. and -500 ± 71 mas yr^{-1} in decl., which are discrepant from the primary's motion values by 5.1σ and 2.7σ in R.A. and decl., respectively. Curiously, the CatWISE2020 and unTimely motions bracket the Gaia motion values of the primary despite the fact that both the CatWISE2020 and unTimely measurements are WISE-based and are affected by the same background contaminants. Implanting a fake source into the WiseView image sequence with the same W2 magnitude as CWISER J021550.96 +674017.2 but with the Gaia-measured motions of HD 13579 provides an excellent match to the observed motion of CWISER J021550.96+674017.2 itself, but suggests that the CatWISE2020 value of $\mathrm{W2} = 13.84 \pm 0.01$ mag may be too bright. Given the close separation between the CWISER source and HD 13579 and motions that appear similar, we tentatively denote these as a physical pair with an apparent separation of 760 au. If associated, the distance to HD 13579 implies a spectral type of >T4.5 for CWISER J021550.96+674017.2 based on the CatWISE W2 magnitude's possibly being biased too bright.

HD 17230 (0246+1146), a K6 dwarf (Gray et al. 2003) at 16.2 pc (Gaia DR3). K. Apps (see Section 3.6.3) notes that there is a fainter star, Gaia DR3 2548874541191948 8 ($G = 15.62$ mag, $\Delta G = 7.51$ mag), 3.″6 south of HD 17230 that has no parallax or proper-motion solution in Gaia DR3. A search of the Keck Observatory Archive[52] by C. Gelino reveals two epochs of observations of HD 17230 with Keck/NIRC2 behind the adaptive optics system (Wizinowich et al. 2000). Raw images in the K_p and J filters with HD 17230 under a coronagraph (PI: J. Crepp; program ID: C182N2) clearly show a star located ∼3.″7 from HD 17230 at a position angle of ∼195°. This observation, taken on 2011 August 30 UT, can be compared to another taken on 2014 October 13 UT (PI: J. Crepp; program ID: N100N2) in the narrowband K-continuum. Given the substantial proper motion of HD 17230 of 263.88 ± 0.03 mas yr^{-1} in R.A. and $-211.58 \pm$

[51] http://byw.tools/wiseview

[52] https://koa.ipac.caltech.edu

0.03 mas yr^{-1} in decl. (Table 4), the fainter star should fall at a separation of 3.″4 and position angle of 211° if it were a background source. However, the second epoch shows the secondary at nearly the same separation and position angle as the first epoch, proving that the two stars are a common motion pair. This conclusion is further bolstered by the 2016-epoch Gaia DR3 positions, which place the fainter star at a separation of 3.″64 and position angle of 195.°3 from HD 17230. (Figure 1(b) shows a first-epoch coronagraphic image in which the A component is seen only via its scattered light.) Using the Gaia DR3 parallax for the primary, this implies M_G = 14.58 mag (spectral type ∼M8) for the secondary. However, the true type might be somewhat later than this, as the lack of an astrometric solution in Gaia DR3 may mean that this companion is itself a multiple system. This companion, at an apparent physical separation of 59 au, may be responsible for the radial velocity acceleration seen for HD 17230 over a decades-long timespan by Rosenthal et al. (2021).

G 43-23 (1002+1149), an M4 dwarf (Reid et al. 1995) at 17.9 pc (Gaia DR3). The motion object WISEU J100241.49 +145914.9 from Table 2 was discovered by D. Caselden during a targeted search for companions to known 20 pc stars using multiepoch imaging data from WISE (Figure 1(c)). This object lies only 15.″6 away from G 43-23, which has astrometry from Gaia DR3 of $\varpi_{\rm abs} = 56.01 \pm 0.11$ mas, $\mu_\alpha = 157.02 \pm 0.11$ mas yr^{-1}, and $\mu_\delta = -235.65 \pm 0.10$ mas yr^{-1}. WISEU J100241.49+145914.9 itself is not listed in either the CatWISE2020 Catalog or the CatWISE2020 Reject Table, but a linear least-squares fit to its epochal unTimely positions (Meisner et al. 2023a) in W2 gives motions of 164±56 mas yr^{-1} in R.A. and -233 ± 43 mas yr^{-1} in decl., nearly identical to the Gaia motions for the primary. Implanting a W2 = 14.55 mag source with the motions of G 43-23 into the WISE image sequence of WiseView (Caselden et al. 2018) makes for a convincing doppelgänger to WISEU J100241.49+145914.9 itself. The WISEU source's UHS detection at $J_{\rm MKO} = 18.18 \pm 0.05$ mag results in a color of $J-{\rm W2} = 3.63 \pm 0.11$ mag, suggesting a type of ∼T8.5 and a distance of ∼14.3 pc, which is slightly closer than the 17.9 pc distance measured for G 43-23. Nonetheless, given the proximity of the two objects to each other and their nearly identical motions, we consider this to be a physical pair at an apparent physical separation of 280 au.

HD 170573 (1833−5415), a K4.5 dwarf (Gray et al. 2006) at 19.1 pc (Gaia DR3). The T7 dwarf CWISE J183207.94−540943.3 was discovered by G. Colin and B. Pumphrey and first published in Kirkpatrick et al. (2021a), where Spitzer astrometric monitoring gave $\varpi_{\rm abs} = 57.0 \pm 4.3$ mas, $\mu_\alpha = -129.1 \pm 11.6$ mas yr^{-1}, and $\mu_\delta = -172.1 \pm 9.7$ mas yr^{-1}. In assembling the full 20 pc census for this paper, it was noted that this object lies 10.′3 from the K4.5 dwarf HD 170573 (Figure 1(d)), which has Gaia DR3 astrometric values of $\varpi_{\rm abs} = 52.29 \pm 0.02$ mas, $\mu_\alpha = -121.05 \pm 0.02$ mas yr^{-1}, and $\mu_\delta = -142.04 \pm 0.02$ mas yr^{-1}. Until more accurate astrometry for the T dwarf becomes available, we will consider this pair to be physically associated because these values are only 1.1σ, 0.7σ, and 3.1σ different for $\varpi_{\rm abs}$, μ_α, and μ_δ, respectively. If a true binary, the projected separation is 11,800 au.

G 155-42 (1848−1434), an M3 dwarf (Gaidos et al. 2014) at 17.1 pc (Gaia DR3). The motion object CWISE J184803.45 −143232.3 from Table 2 was discovered by S. Goodman while searching for unpublished motion objects in WISE imaging data. While assembling the 20 pc census for this paper, it was noted that this source falls 2.′45 away from G 155-42 (Figure 1(e)). The CatWISE2020 Catalog (Marocco et al. 2021) lists motions for CWISE J184803.45−143232.3 of $\mu_\alpha = -145 \pm 33$ mas yr^{-1}, and $\mu_\delta = -104 \pm 37$ mas yr^{-1}. A linear least-squares fit to the WISE W2 epochal positions from the unTimely Catalog (Meisner et al. 2023) results in motions of $\mu_\alpha = -181 \pm 22$ mas yr^{-1}, and $\mu_\delta = -158 \pm 31$ mas yr^{-1}. The Gaia DR3 astrometry for G 155-42 is $\varpi_{\rm abs} = 58.60 \pm 0.02$ mas, $\mu_\alpha = -236.45 \pm 0.02$ mas yr^{-1}, and $\mu_\delta = -237.26 \pm 0.02$ mas yr^{-1}. The measured motion values between the two sources differ by 2.8σ and 3.6σ in R.A. and decl., respectively, for the CatWISE2020 motion of the potential secondary and by 2.5σ and 2.6σ for the unTimely motion. The $J-{\rm W2}$ color of CWISE J184803.45−143232.3 from Table 2 suggests a ∼T7.5 dwarf at a distance of ∼15.7 pc, which is sufficiently close to the 17.1 pc distance of G155-42 that we tentatively consider them to be a physical pair with apparent physical separation of 2500 au, pending improved astrometry for the secondary.

2MASS J19253089+0938235, an M8 dwarf (West et al. 2015) at 17.0 pc (Gaia DR3). C. Gelino finds two epochs of Keck/NIRC2 data for this object in the Keck Observatory Archive. The first epoch (2019 May 22 UT; PI: Bond; program ID: H299) shows two objects separated by 194 mas at a position angle of 146° and magnitude difference of $\Delta K = 0.29$ mag. Two objects are still present in the second epoch (2020 June 2 UT; PI: Mawet; program ID: C249) but with a separation of 199 mas and position angle of 137° (Figure 1(f)). We conclude that 2MASS J19253089+0938235 is a closely separated binary showing orbital motion because the pair shows measurably different separations and position angles, but the astrometry of the second object is inconsistent with the motion of a background star, which would have exhibited a relative motion of approximately −80 mas in R.A. and +240 mas in decl. Using a UKIDSS Galactic Plane Survey DR11PLUS star visible in the field and located at J2000 R.A. = 291.3801844 deg, and decl. = +9.6377532 deg, we find $K = 10.53 \pm 0.03$ mag for 2MASS J19253089+0938235A (the northwest component), and $K = 10.82 \pm 0.03$ mag for 2MASS J19253089+0938235B (the southeast component). This object has been flagged as a possible member of the AB Dor Moving Group (Gagné & Faherty 2018).

2.3. Checks against the Fifth Catalog of Nearby Stars

After we had completed our accounting of the 20 pc census, we were presented with an additional opportunity to further check for omissions or subtractions. Golovin et al. (2023) recently published the Fifth Catalog of Nearby Stars (CNS5), a compilation of all stars and brown dwarfs within 25 pc of the Sun. Within the CNS5, there are 3002 objects with parallaxes of 50 mas or greater, whereas our list has 3588 individual objects that meet this criterion.[53] For the purposes of checking the completeness of our own census, we find that only twenty-two of these CNS5 objects were not included in our list. These are given in Table 3. Five of these are Gaia discoveries with relatively large Gaia parallax uncertainties. We show in Appendix A.2 that three of these are background objects based on their spectra, and we assume that the other two, given their

[53] Part of this discrepancy is due to the fact that the CNS5 has some entries whose components are not split into individual sources. Specifically, fifty entries are listed as double stars, seven as triples, and one as a quadruple. Even if these are split out as individual components, that still leaves a difference between the two lists of 519 objects.

Table 3
CNS5 Objects with $\varpi_{abs} \geqslant 50$ mas Not Included in Our 20 pc Census

Object Name	CNS5 R.A. Decl. (J2000) (hhmmss.ss ± ddmmss.s)	CNS5 ϖ_{abs} (mas)	Our ϖ_{abs} (mas)	Our References
(1)	(2)	(3)	(4)	(5)
G 39-9	04 22 34.31+39 00 34.0	50.03 ± 0.03	49.97 ± 0.03	Gaia DR3
2MASS J05160945−0445499	05 16 09.41 −04 45 50.4	54.00 ± 4.00	47.83 ± 2.85	Section 6.2 of Kirkpatrick et al. (2021a)
2MASSI J0639559−741844	06 39 55.99 −74 18 44.6	51.00 ± 8.00	[46.1]	Table 10 of Kirkpatrick et al. (2021a)
WISEA J064313.95+163143.6	06 43 13.99+16 31 44.0	50.05 ± 0.27	49.97 ± 0.25	Gaia DR3
HD 64606 AC	07 54 33.92 −01 24 45.2	50.74 ± 0.58	48.55 ± 0.13	Gaia DR3 non-single-star lists
2MASS J08583467+3256275	08 58 34.32+32 56 26.5	50.30 ± 3.70	40.9 ± 3.6	Best et al. (2020)
NLTT 25223	10 45 14.83+49 41 26.6	53.13 ± 0.42	43.31 ± 0.10	Gaia DR3 non-single-star lists
CD−45 7872	12 35 58.50 −45 56 14.6	52.67 ± 3.05	48.21 ± 0.60	Gaia DR2
SIPS J1256−1257 B	12 56 01.85 −12 57 24.8	52.00 ± 3.00	47.27 ± 0.47	Gaia DR3 (SIPS J1256−1257 A)
Kelu-1 AB	13 05 39.80 −25 41 06.1	53.80 ± 0.70	49.05 ± 0.72	Gaia DR3
LP 220-13	13 56 40.80+43 42 59.8	50.00 ± 0.60	46.30 ± 0.58	Gaia DR3
2MASS J13585269+3747137	13 58 52.73+37 47 12.8	50.00 ± 3.00	49.6 ± 3.1	Best et al. (2020)
Gaia DR3 6305165514134625024	14 59 54.40 −18 32 15.9	174.04 ± 1.83	background object	Table A2
Gaia DR3 6013647666939138688	15 29 22.77 −35 52 20.1	56.76 ± 0.97	background object	Table A2
SDSS J163022.92+081822.0	16 30 22.97+08 18 22.3	55.80 ± 3.40	41.76 ± 2.79	Table A3
Gaia DR3 4118195139455558016	17 38 53.15 −20 53 56.2	53.16 ± 2.33	spurious parallax?	Gaia DR3
Gaia DR3 4062783361232757632	17 59 55.76 −27 38 17.1	59.45 ± 1.18	spurious parallax?	Gaia DR3
Gaia DR3 4479498508613790464	18 39 31.62+09 01 43.1	121.98 ± 0.93	background object	Table A2
Ross 776	21 16 06.06+29 51 51.5	50.79 ± 0.46	49.91 ± 0.02	Gaia DR3 (Ross 826)
2MASSI J2249091+320549	22 49 10.08+32 05 46.3	50.00 ± 3.00	49.7 ± 3.2	Best et al. (2020)
APMPM J2330−4737 B	23 30 15.28 −47 37 00.7	73.67 ± 0.08	⋯	companion does not exist?
2MASS J23312378−4718274	23 31 23.92 −47 18 28.6	56.50 ± 7.50	48.99 ± 4.21	Table A3

(This table is available in machine-readable form.)

even larger parallactic errors, are also background objects. Another 15 have preferred parallaxes that place them beyond 20 pc, and these preferred parallaxes are either revised values in Gaia DR3 or published parallaxes (or new parallaxes discussed in Appendix A.3) with smaller uncertainties than those quoted in CNS5.[54] The remaining two objects in Table 3 deserve special note. The first, 2MASSI J0639559−741844, has a CNS5 parallax with a 16% uncertainty, so we consider our spectrophotometric distance estimate, which places the object beyond 20 pc, to be preferable. (See Kirkpatrick et al. 2021a for a discussion on the credibility of parallaxes when the uncertainties exceed 12.5%.) The second, APMPM J2330 −4737 B, is a bit of a mystery, as we can find no corroborating evidence in the literature that it exists, and this is why it is not included in our census. In conclusion, our comparison to the CNS5 results in no new additions to our list.

3. The 20 pc Census

Our final 20 pc census is presented in Table 4. The content of this table is described in more detail in the subsections that follow.

3.1. Nomenclature

Not all researchers refer to the same star by the same name, so having a list of aliases is needed. As we entered each object into the census, we searched SIMBAD for alternative names. The name listed under the heading "DefaultName" in Table 4 is the one that appeared as the default name in SIMBAD[55] when our initial search was performed. For all of these objects, a deep dive into the literature is required to establish the current knowledge of multiplicity, spectral type, etc., so we also list alternative names to aid the literature search. Table 4 therefore lists common names (e.g., Sirius), Bayer and Flamsteed designations, and designations from the HR, HD, BD, CD, and CPD catalogs.[56] Table 4 also lists designations from proper-motion catalogs (Wolf, Ross, L, LP, Giclas, LHS, LFT, NLTT, LTT, LSPM, SCR, UPM, APMPM, LEHPM, WT, SIPS, PM, and PMJ), white dwarf catalogs (WD, LAWD, EGGR), all-sky photometric catalogs (2MASS, WISE), all-sky astrometric catalogs (Gaia, HIC, HIP, TYC, UCAC4, TIC), along with a few other miscellaneous catalogs that also have high usage (GJ, V*, Karmn, **). The field "VarType" is filled with the type of variability seen, if the object is a known variable star; this information was taken from the General Catalog of Variable Stars.[57] The references from which these designations were drawn are also listed in Table 4 and serve as

[54] We consider SIPS J1256−1257 B to be outside of the 20 pc volume because its primary star, SIPS J1256−1257 A, has a smaller parallax uncertainty and falls outside 20 pc. The same is true of Ross 776, based on the parallactic measurement for Ross 826, with which it shares common proper motion. For 2MASS J13585269+3747137 and 2MASSI J2249091+320549, we suspect that the CNS5 parallax values and uncertainties come from the same source as our values, Best et al. (2020), but have been rounded; however, the CNS5 does not cite individual references for its parallax entries, so we are not able to confirm this.

[55] Note that SIMBAD sometimes conflates system names and individual names. For example, there is a single record combining the system Ross 614 [AB] and the individual component Ross 614 A, although the component Ross 614 B has a separate record. Correcting these associations is beyond the scope of this paper.

[56] The acronyms listed here are defined in Table 4.

[57] Samus' et al. (2017) and https://heasarc.gsfc.nasa.gov/W3Browse/all/gcvs.html

Table 4
The 20 pc Census

Column (1)	Description (2)	Sections (3)	Example Entry (4)
DefaultName	Default name in SIMBAD	3.1	nu Phe
#CompsOnThisRow	Number of known components for this row	3.6.4	1
AdoptedInitialMass	Adopted initial mass of this component ($M_{\odot}$)	7	1.150
AdoptedInitialMassErr	Uncertainty in adopted initial mass ($M_{\odot}$)	7	0.159
AdoptedInitialMassNote	Origin of adopted initial mass	7	TIC
Mass	Directly measured mass ($M_{\odot}$)	4	…
MassErr	Uncertainty in directly measured mass ($M_{\odot}$)	4	…
MassMethod	Method for direct mass measurement	4	…
MassRef	Reference for direct mass measurement	4	…
EstMassLit	Estimated mass from the literature ($M_{\odot}$)	7	…
EstMassLitErr	Uncertainty on estimated mass from the literature ($M_{\odot}$)	7	…
EstMassLitMethod	Method used for this estimated mass determination	7	…
EstMassLitRef	Reference for this estimated mass	7	…
EstMassTIC	Estimated mass from the TESS Input Catalog ($M_{\odot}$)	6.3, 7	1.150
EstMassTICErr	Uncertainty on TESS Input Catalog estimated mass ($M_{\odot}$)	6.3, 7	0.159
EstMassSH	Estimated mass from StarHorse ($M_{\odot}$)	6.3, 7	…
EstMassSHErr	Uncertainty on StarHorse estimated mass ($M_{\odot}$)	6.3, 7	…
EstMassMKs	Estimated mass from M_{Ks} relation ($M_{\odot}$)	6.3, 7	…
EstMassMKsErr	Uncertainty in M_{Ks} relation estimated mass ($M_{\odot}$)	6.3, 7	…
EstMassMG	Estimated mass from M_G relation ($M_{\odot}$)	6.3, 7	…
EstMassMGErr	Uncertainty in M_G relation estimated mass ($M_{\odot}$)	6.3, 7	…
Teff	Effective temperature, for L, T, Y dwarfs only (K)	7.1	…
Teff_unc	Uncertainty in effective temperature (K)	7.1	…
#Planets	No. of known exoplanets in NASA Exoplanet Archive	3.6.4	…
RUWE	Gaia EDR3 renormalized unit weight error	5.2	1.381
LUWE_binary?	Possible binary flagged via local unit weight error	5.2	…
Accelerator?	Accelerator flagged by Brandt (2021) or Khovritchev & Kulikova (2015)	5.1	…
EstMassAt3AU	Kervella et al. (2022) mass estimate of companion if it is at 3 au ($M_{\odot}$)	5.1	…
EstMassAt30AU	Kervella et al. (2022) mass estimate of companion if it is at 30 au ($M_{\odot}$)	5.1	…
SystemHierarchy	System hierarchy value	3.6.4	158
#CompsInThisSystem	No. of components, if this is top level of system	3.6.4	1
SystemCode	System hierarchy value collapsed into an 8-digit integer	3.6.4	01580000
CommonName	Common name	3.1	…
Bayer/Flamsteed	Bayer or Flamsteed designation	3.1	*nu. Phe
HR	Bright Star Catalogue (“Harvard Revised”) designation	3.1	HR 370
HD	Henry Draper Catalogue designation	3.1	HD 7570
BD	Bonner Durchmusterung designation	3.1	…
CD	Cordoba Durchmusterung designation	3.1	CD-46 346
CPD	Cape Photographic Durchmusterung designation	3.1	CPD-46 127
Wolf	Wolf motion survey designation	3.1	…
Ross	Ross motion survey designation	3.1	…
L	Bruce proper-motion designation (“Luyten,” south)	3.1	…
LP	Luyten Palomar designation (north)	3.1	…
Giclas	Giclas motion survey designation	3.1	…
LHS	Luyten Half Second designation	3.1	LHS 1220
LFT	Luyten Five Tenths designation	3.1	LFT 119
NLTT	New Luyten Two Tenths	3.1	NLTT 4186
LTT	Luyten Two Tenths designation	3.1	LTT 696
LSPM	Lepine+Shara proper-motion designation	3.1	…
SCR	SuperCOSMOS+RECONS designation	3.1	…
UPM	UCAC3 proper-motion designation	3.1	…
APMPM	Automated Plate Measurer proper-motion designation	3.1	…
LEHPM	Liverpool–Edinburgh high proper-motion designation	3.1	…
WT	Wroblewski+Torres motion survey designation	3.1	…
SIPS	Southern Infrared Proper Motion Survey designation	3.1	…
PM	Proper-motion (B1950) survey designation	3.1	PM 01129-4548
PMJ	Proper-motion (J2000) survey designation	3.1	…
WD	White dwarf designation	3.1	…
LAWD	Luyten Atlas of White Dwarfs designation	3.1	…
EGGR	Eggen+Greenstein designation	3.1	…

Table 4
(Continued)

Column (1)	Description (2)	Sections (3)	Example Entry (4)
2MASS	Two Micron All Sky Survey designation	3.1	2MASS J01151112-4531540
WISE	Wide-field Infrared Survey Explorer designation	3.1	WISE J011511.83-453152.2
Gaia	Gaia designation	3.1	Gaia EDR3 4934923028038871296
HIC	Hipparcos Input Catalogue designation	3.1	HIC 5862
HIP	Hipparcos Catalogue designation	3.1	HIP 5862
TYC	Tycho-2 Catalog designation	3.1	TYC 8033-1232-1
UCAC4	Fourth USNO CCD Astrograph Catalog designation	3.1	…
TIC	TESS Input Catalog designation	3.1	TIC 229092427
GJ	Gliese+Jahreiß nearby star catalog designation	3.1	GJ 55
V*	Variable star designation	3.1	…
VarType	Type of variability seen, if column V* filled	3.1	…
Karmn	CARMENES designation	3.1	…
**	Multiple system designation	3.1	…
NamesRef	Reference(s) for designations	3.1	SIMBAD
SexagesimalRA	Default J2000 R.A., usually from SIMBAD	3.2	01 15 11.1214282378
SexagesimalDec	Default J2000 decl., usually from SIMBAD	3.2	−45 31 53.992580679
RA	Decimal J2000 R.A., if precision astrometry exists (deg)	3.2	18.80055895
RA_unc	Uncertainty on decimal J2000 R.A. (mas)	3.2	0.0412
Dec	Decimal J2000 decl., if precision astrometry exists (deg)	3.2	−45.53087326
Dec_unc	Uncertainty on decimal J2000 decl. (mas)	3.2	0.0499
Epoch	Epoch to which the decimal R.A. and decl. values above refer (yr)	3.2	2016.0
Parallax	Absolute parallax (mas)	3.2	65.527
Parallax_unc	Uncertainty in the absolute parallax (mas)	3.2	0.0704
PMRA	Proper motion in R.A. (mas yr^{-1})	3.2	665.086
PMRA_unc	Uncertainty in PMRA (mas yr^{-1})	3.2	0.052
PMDec	Proper motion in decl. (mas yr^{-1})	3.2	178.07
PMDec_unc	Uncertainty in PMDec (mas yr^{-1})	3.2	0.064
PlxPMRef	Reference for the parallax and proper-motion values	3.2	Gaia EDR3
Constellation	Constellation in which this object falls	3.2	Phe
SpecTypeOpt	Published spectral type in the optical	3.3	F9 V Fe+0.4
SpTOpt_indx	Machine-readable code for optical spectral type	3.3	19.0
SpTOpt_ref	Reference for the optical spectral type	3.3	Gray2006
SpecTypeNIR	Published spectral type in the near-infrared	3.3	…
SpTNIR_indx	Machine-readable code for the near-infrared type	3.3	…
SpTNIR_ref	Reference for the near-infrared spectral type	3.3	…
Gaia_RV	Radial velocity from Gaia DR3 (km s^{-1})	3.5	11.90
Gaia_RV_unc	Uncertainty in Gaia_RV (km s^{-1})	3.5	0.12
G	*G*-band magnitude from Gaia eDR3 (mag)	3.4	4.828
G_unc	Uncertainty in *G*, as provided by VizieR (mag)	3.4	0.003
G_BP	G_{BP}-band magnitude from Gaia eDR3 (mag)	3.4	5.108
G_BP_unc	Uncertainty in G_{BP}, as provided by VizieR (mag)	3.4	0.003
G_RP	G_{RP}-band magnitude from Gaia eDR3 (mag)	3.4	4.380
G_RP_unc	Uncertainty in G_{RP}, as provided by VizieR (mag)	3.4	0.004
JMKO	*J*-band photometry on the MKO system (mag)	3.4	…
JMKOerr	Uncertainty in JMKO (mag)	3.4	…
J2MASS	*J*-band photometry on the 2MASS system (mag)	3.4	4.094
J2MASSerr	Uncertainty in J2MASS (mag)	3.4	0.346
H	*H*-band photometry on the MKO system (mag)	3.4	3.719
Herr	Uncertainty in H (mag)	3.4	0.268
K	*K*-band photometry (mag)	3.4	…
Kerr	Uncertainty in K (mag)	3.4	…
Ks	K_s-band photometry (mag)	3.4	3.782
Kserr	Uncertainty in Ks (mag)	3.4	0.268
JHK_ref	References for JMKO, J2MASS, H, K, and Ks	3.4	−22-2
2MASS_contam?	Note if the 2MASS photometry is contaminated	3.4	…
W1	W1 photometry from WISE (mag)	3.4	3.714
W1err	Uncertainty in W1 (mag)	3.4	0.117
W2	W2 photometry from WISE (mag)	3.4	3.082
W2err	Uncertainty in W2 (mag)	3.4	0.060
W3	W3 photometry from WISE (mag)	3.4	3.689

Table 4
(Continued)

Column (1)	Description (2)	Sections (3)	Example Entry (4)
W3err	Uncertainty in W3 (mag)	3.4	0.014
W4	W4 photometry from WISE (mag)	3.4	3.609
W4err	Uncertainty in W4 (mag)	3.4	0.023
WISEphot_ref	References for W1, W2, W3, and W4	3.4	WWWW
WISE_contam?	Note if the WISE photometry is contaminated	3.4	…
GeneralNotes	Special notes on this system/component	…	…

Notes. This summary table describes the columns available in the full, online table. This table is also available at the NASA Exoplanet Archive, https://exoplanetarchive.ipac.caltech.edu/docs/20pcCensus.html.
References for mass measurements and estimates, astrometry, spectral types, and general notes: Aberasturi2014 = Aberasturi et al. (2014), Aberasturi2014b = Aberasturi et al. (2014), Abt1965 = Abt (1965), Abt1970 = Abt (1970), Abt1976 = Abt & Levy (1976), Abt1981 = Abt (1981), Abt2006 = Abt & Willmarth (2006), Abt2017 = Abt (2017), Affer2005 = Affer et al. (2005), Agati2015 = Agati et al. (2015), Akeson2021 = Akeson et al. (2021), Albert2011 = Albert et al. (2011), Allen2000 = Allen et al. (2000), Allen2012 = Allen et al. (2012), AllendePrieto1999 = Allende Prieto & Lambert (1999), Allers2013 = Allers & Liu (2013), Alonso-Floriano2015 = Alonso-Floriano et al. (2015), Andrade2019 = Andrade (2019), Artigau2010 = Artigau et al. (2010), Azulay2015 = Azulay et al. (2015), Azulay2017 = Azulay et al. (2017), Bach2009 = Bach et al. (2009), Bagnulo2020 = Bagnulo & Landstreet (2020), Baines2012 = Baines & Armstrong (2012), Baines2018 = Baines et al. (2018), Bakos2006 = Bakos et al. (2006), Balega1984 = Balega et al. (1984), Balega2004 = Balega et al. (2004), Balega2013 = Balega et al. (2013), BardalezGagliuffi2014 = Bardalez Gagliuffi et al. (2014), BardalezGagliuffi2019 = Bardalez Gagliuffi et al. (2019), BardalezGagliuffi2020 = Bardalez Gagliuffi et al. (2020), Baroch2018 = Baroch et al. (2018), Baroch2021 = Baroch et al. (2021), Barry2012 = Barry et al. (2012), Bartlett2017 = Bartlett et al. (2017), Batten1992 = Batten & Fletcher (1992), Bazot2011 = Bazot et al. (2011), Bazot2018 = Bazot et al. (2018), Beamin2013 = Beamín et al. (2013), Beavers1985 = Beavers & Salzer (1985), Beichman2011 = Beichman et al. (2011), Benedict2001 = Benedict et al. (2001), Benedict2016 = Benedict et al. (2016), Berdnikov2008 = Berdnikov & Pastukhova (2008), Bergfors2010 = Bergfors et al. (2010), Bergfors2016 = Bergfors et al. (2016) Bernat2010 = Bernat et al. (2010) Bernkopf2012 = Bernkopf et al. (2012), Berski2016 = Berski & Dybczyński (2016), Best2013 = Best et al. (2013), Best2015 = Best et al. (2015), Best2020 = Best et al. (2020), Best2021 = Best et al. (2021), Beuzit2004 = Beuzit et al. (2004), Bidelman1980 = Bidelman (1980), Bidelman1985 = Bidelman (1985), Bihain2013 = Bihain et al. (2013), Biller2022 = Biller et al. (2022), Bochanski2005 = Bochanski et al. (2005), Bonavita2020 = Bonavita & Desidera (2020), Boden1999 = Boden et al. (1999), Bond2017 = Bond et al. (2017), Bond2018 = Bond et al. (2018), Bond2020 = Bond et al. (2020), Bonfils2005 = Bonfils et al. (2005), Bonfils2013 = Bonfils et al. (2013), Bonnefoy2014 = Bonnefoy et al. (2014), Bonnefoy2018 = Bonnefoy et al. (2018), Borgniet2019 = Borgniet et al. (2019), Bouy2003 = Bouy et al. (2003), Bouy2004 = Bouy et al. (2004), Bouy2005 = Bouy et al. (2005), Bowler2015a = Bowler et al. (2015a), Bowler2015b = Bowler et al. (2015b), Bowler2019 = Bowler et al. (2019), Boyajian2012 = Boyajian et al. (2012), Brandao2011 = Brandão et al. (2011), Brandt2014 = Brandt et al. (2014), Brandt2019 = Brandt et al. (2019), Brandt2020 = Brandt et al. (2020), Brandt2021 = Brandt (2021), BrandtG2021 = Brandt et al. (2021), Breakiron1974 = Breakiron & Gatewood (1974), Brewer2016 = Brewer et al. (2016), Bruntt2010 = Bruntt et al. (2010), Burgasser2003 = Burgasser et al. (2003), Burgasser2004 = Burgasser et al. (2004), Burgasser2006 = Burgasser et al. (2006), Burgasser2007 = Burgasser et al. (2007b), Burgasser2008 = Burgasser et al. (2008b), Burgasser2008b = Burgasser et al. (2008a), Burgasser2010a = Burgasser et al. (2010b), Burgasser2010b = Burgasser et al. (2010a), Burgasser2011 = Burgasser et al. (2011), Burgasser2013 = Burgasser et al. (2013), Burgasser2015a = Burgasser et al. (2015a), Burgasser2015b = Burgasser et al. (2015b), Burningham2010 = Burningham et al. (2010), Burningham2011 = Burningham et al. (2011), Burningham2013 = Burningham et al. (2013), Butler2017 = Butler et al. (2017), Bychkov2013 = Bychkov et al. (2013), Calissendorff2023 = Calissendorff et al. (2023), Cannon1993 = Cannon & Pickering (1993), CardonaGuillen2021 = Cardona Guillén et al. (2021), Carrier2005 = Carrier et al. (2005), Castro2013 = Castro et al. (2013), Catalan2008b = Catalán et al. (2008b), CatWISE2020 = Marocco et al. (2021), Chauvin2007 = Chauvin et al. (2007), Che2011 = Che et al. (2011), Chen2022 = Chen et al. (2022), Chini2014 = Chini et al. (2014), Chiu2006 = Chiu et al. (2006), Chontos2021 = Chontos et al. (2021), Christian2001 = Christian et al. (2001), Christian2003 = Christian et al. (2003), Cifuentes2020 = Cifuentes et al. (2020), Clark2022 = Clark et al. (2022), Climent2019 = Climent et al. (2019), Close2007 = Close et al. (2007), Compton2019 = Compton et al. (2019), Corbally1984 = Corbally (1984), CortesContreras2017 = Cortés-Contreras et al. (2017), Cowley1967 = Cowley et al. (1967), Cowley1976 = Cowley (1976), Creevey2012 = Creevey et al. (2012), Crifo2005 = Crifo et al. (2005), Cruz2002 = Cruz & Reid (2002), Cruz2003 = Cruz et al. (2003), Cruz2007 = Cruz et al. (2007), Cruz2009 = Cruz et al. (2009), Cushing2005 = Cushing et al. (2005), Cushing2011 = Cushing et al. (2011), Cushing2014 = Cushing et al. (2014), Cushing2016 = Cushing et al. (2016), Cvetkovic2010 = Cvetkovic & Ninkovic (2010), Cvetkovic2011 = Cvetković et al. (2011), Dahn1988 = Dahn et al. (1988), Dahn2002 = Dahn et al. (2002), Dahn2017 = Dahn et al. (2017), Dalba2021 = Dalba et al. (2021), Damasso2020 = Damasso et al. (2020), David2015 = David & Hillenbrand (2015), Davison2014 = Davison et al. (2014), Deacon2012a = Deacon et al. (2012a), Deacon2012b = Deacon et al. (2012b), Deacon2017 = Deacon et al. (2017), Deeg2008 = Deeg et al. (2008), Delfosse1999a = Delfosse et al. (1999a), Delfosse1999b = Delfosse et al. (1999b), Delrez2021 = Delrez et al. (2021), Diaz2007 = Díaz et al. (2007), Dieterich2012 = Dieterich et al. (2012), Dieterich2014 = Dieterich et al. (2014), Dieterich2018 = Dieterich et al. (2018), Dieterich2021 = Dieterich et al. (2021), DiFolco2004 = Di Folco et al. (2004), Dittmann2014 = Dittmann et al. (2014), Docobo2006 = Docobo et al. (2006), Docobo2019 = Docobo et al. (2019), DOrazi2017 = D'Orazi et al. (2017), DosSantos2017 = dos Santos et al. (2017), Downes2006 = Downes et al. (2006), Ducati2011 = Ducati et al. (2011), Dupuy2010 = Dupuy et al. (2010), Dupuy2012 = Dupuy & Liu (2012), Dupuy2016 = Dupuy et al. (2016), Dupuy2017 = Dupuy & Liu (2017), Dupuy2019 = Dupuy et al. (2019), Duquennoy1988 = Duquennoy & Mayor (1988), Duquennoy1991 = Duquennoy & Mayor (1991), Durkan2018 = Durkan et al. (2018), Edwards1976 = Edwards (1976), Eggleton2008 = Eggleton & Tokovinin (2008), Endl2006 = Endl et al. (2006), Evans1961 = Evans et al. (1961), Evans1964 = Evans et al. (1964), Fabricius2000 = Fabricius & Makarov (2000), Faherty2012 = Faherty et al. (2012), Faherty2016 = Faherty et al. (2016), Faherty2018 = Faherty et al. (2018), Fan2000 = Fan et al. (2000), Feng2021 = Feng et al. (2021), Finch2016 = Finch & Zacharias (2016a), Finch2018 = Finch et al. (2018), Fischer2014 = Fischer et al. (2014), Forveille1999 = Forveille et al. (1999), Forveille2004 = Forveille et al. (2004), Forveille2005 = Forveille et al. (2005), Fouque2018 = Fouqué et al. (2018), Fuhrmann2008 = Fuhrmann (2008), Fuhrmann2011 = Fuhrmann et al. (2011a), Fuhrmann2012 = Fuhrmann & Chini (2012), Fuhrmann2012b = Fuhrmann et al. (2012), Fuhrmann2016 = Fuhrmann et al. (2016), Fuhrmann2017 = Fuhrmann et al. (2017), Gagne2015 = Gagné et al. (2015), GaiaDR2 = Gaia Collaboration et al. (2016, 2018) GaiaEDR3 = Gaia Collaboration et al. (2016, 2021b), GaiaDR3-NSS = Gaia Collaboration et al. (2023b), Gaidos2014 = Gaidos et al. (2014), Garcia2017 = Garcia et al. (2017), Gardner2021 = Gardner et al. (2021), Gatewood2003 = Gatewood et al. (2003), Geballe2002 = Geballe et al. (2002), GentileFusillo2019 = Gentile Fusillo et al. (2019), Giammichele2012 = Giammichele et al. (2012), Gigoyan2012 = Gigoyan & Mickaelian (2012),

Gizis1997 = Gizis (1997), Gizis1997b = Gizis & Reid (1997), Gizis2000 = Gizis et al. (2000a), Gizis2000b = Gizis et al. (2000b), Gizis2002 = Gizis (2002), Gizis2002b = Gizis et al. (2002), Gizis2011 = Gizis et al. (2011), Gizis2015 = Gizis et al. (2015), Gliese1991 = Gliese & Jahreiß (1991), Gomes2013 = Gomes et al. (2013), Goldin2006 = Goldin & Makarov (2006), Goldin2007 = Goldin & Makarov (2007), Goto2002 = Goto et al. (2002), Grandjean2020 = Grandjean et al. (2020), Gray2001 = Gray et al. (2001), Gray2003 = Gray et al. (2003), Gray2006 = Gray et al. (2006), Greco2019 = Greco et al. (2019), Griffin2004 = Griffin (2004), Griffin2010 = Griffin (2010), Guenther2003 = Guenther & Wuchterl (2003), Guzik2016 = Guzik et al. (2016), Halbwachs2000 = Halbwachs et al. (2000), Halbwachs2012 = Halbwachs et al. (2012), Halbwachs2018 = Halbwachs et al. (2018), Hambaryan2004 = Hambaryan et al. (2004), Hansen2022 = Hansen (2022), Harrington1993 = Harrington et al. (1993), Hartkopf1994 = Hartkopf et al. (1994), Hartkopf2012 = Hartkopf et al. (2012), Hatzes2012 = Hatzes et al. (2012), Hawley1997 = Hawley et al. (1997), Hawley2002 = Hawley et al. (2002), Heintz1986 = Heintz (1986), Heintz1990 = Heintz (1990), Heintz1993 = Heintz (1993), Heintz1994 = Heintz (1994), Helminiak2009 = Hełminiak et al. (2009), Helminiak2012 = Hełminiak et al. (2012), Henry1994 = Henry et al. (1994), Henry1999 = Henry et al. (1999), Henry2002 = Henry et al. (2002), Henry2004 = Henry et al. (2004), Henry2006 = Henry et al. (2006), Henry2018 = Henry et al. (2018), HenryDraperExtension = Cannon & Pickering (1993), Herbig1977 = Herbig (1977), Hinkley2011 = Hinkley et al. (2011), Hipparcos = van Leeuwen (2007), Hollands2018 = Hollands et al. (2018), Horch2011 = Horch et al. (2011), Horch2012 = Horch et al. (2012), Horch2017 = Horch et al. (2017), Holberg2002 = Holberg et al. (2002), Houk1982 = Houk (1982), Houk1988 = Houk & Smith-Moore (1988), Huber2009 = Huber et al. (2009), Hussein2022 = Hussein et al. (2022), Hsu2021 = Hsu et al. (2021), Ireland2008 = Ireland et al. (2008), Jackson1955 = Jackson & Stoy (1955), Jahreiss2001 = Jahreiß et al. (2001), Jahreiss2008 = Jahreiß et al. (2008), Janson2012 = Janson et al. (2012), Janson2014a = Janson et al. (2014a), Janson2014b = Janson et al. (2014b), Jao2003 = Jao et al. (2003), Jao2008 = Jao et al. (2008), Jao2011 = Jao et al. (2011), Jao2014 = Jao et al. (2014), Jeffers2018 = Jeffers et al. (2018), Jeffers2020 = Jeffers et al. (2020), Jeffries1993 = Jeffries & Bromage (1993), Jodar2013 = Jódar et al. (2013), Kallinger2010 = Kallinger et al. (2010), Kallinger2019 = Kallinger et al. (2019), Karovicova2022 = Karovicova et al. (2022), Kasper2007 = Kasper et al. (2007), Katoh2013 = Katoh et al. (2013), Katoh2021 = Katoh et al. (2021), Keenan1989 = Keenan & McNeil (1989), Kellogg2015 = Kellogg et al. (2015), Kendall2004 = Kendall et al. (2004), Kendall2007 = Kendall et al. (2007), Kennedy2012 = Kennedy et al. (2012), Kervella2016 = Kervella et al. (2016b), Kervella2016b = Kervella et al. (2016a), Kervella2019 = Kervella et al. (2019), Kervella2022 = Kervella et al. (2022), Kesseli2019 = Kesseli et al. (2019), Khovritchev2015 = Khovritchev & Kulikova (2015), Kilic2020 = Kilic et al. (2020), King2010 = King et al. (2010), Kirkpatrick1991 = Kirkpatrick et al. (1991), Kirkpatrick1994 = Kirkpatrick & McCarthy (1994), Kirkpatrick1995 = Kirkpatrick et al. (1995), Kirkpatrick1997 = Kirkpatrick et al. (1997), Kirkpatrick1999 = Kirkpatrick et al. (1999), Kirkpatrick2000 = Kirkpatrick et al. (2000), Kirkpatrick2001 = Kirkpatrick et al. (2001), Kirkpatrick2008 = Kirkpatrick et al. (2008), Kirkpatrick2010 = Kirkpatrick et al. (2010), Kirkpatrick2011 = Kirkpatrick et al. (2011), Kirkpatrick2012 = Kirkpatrick et al. (2012), Kirkpatrick2013 = Kirkpatrick et al. (2013), Kirkpatrick2014 = Kirkpatrick et al. (2014), Kirkpatrick2016 = Kirkpatrick et al. (2016), Kirkpatrick2019 = Kirkpatrick et al. (2019a), Kirkpatrick2021a = Kirkpatrick et al. (2021a), Kirkpatrick2021b = Kirkpatrick et al. (2021b), Kirkpatrick2024 = this paper, Kiyaeva2001 = Kiyaeva et al. (2001), Kluter2018 = Klüter et al. (2018), Kniazev2013 = Kniazev et al. (2013), Kochukhov2009 = Kochukhov et al. (2009), Kochukhov2019 = Kochukhov & Shulyak (2019), Koen2017 = Koen et al. (2017), Koizumi2021 = Koizumi et al. (2021), Konopacky2010 = Konopacky et al. (2010), Kraus2011 = Kraus et al. (2011), Kuerster2008 = Kürster et al. (2008), Kuzuhara2013 = Kuzuhara et al. (2013), Lacour2021 = Lacour et al. (2021), Lamman2020 = Lamman et al. (2020), Laugier2019 = Laugier et al. (2019), Law2006 = Law et al. (2006), Lazorenko2018 = Lazorenko & Sahlmann (2018), Lee1984 = Lee (1984), Leggett2012 = Leggett et al. (2012), Leinert2000 = Leinert et al. (2000), Lepine2002 = Lépine et al. (2002), Lepine2003 = Lépine et al. (2003), Lepine2009 = Lépine et al. (2009), Lepine2013 = Lépine et al. (2013), Li2012 = Li et al. (2012), Li2019 = Li et al. (2019), Liebert2003 = Liebert et al. (2003), Liebert2006 = Liebert & Gizis (2006), Liebert2013 = Liebert et al. (2013), Limoges2015 = Limoges et al. (2015), Lindegren1997 = Lindegren et al. (1997), Lindegren2018 = Lindegren et al. (2018), Lindegren2021 = Lindegren & Dravins (2021), Liu2002 = Liu et al. (2002), Liu2005 = Liu & Leggett (2005), Liu2010 = Liu et al. (2010), Liu2012 = Liu et al. (2012), Liu2016 = Liu et al. (2016), Lloyd1994 = Lloyd & Wonnacott (1994), Lodieu2005 = Lodieu et al. (2005), Lodieu2007 = Lodieu et al. (2007), Lodieu2012 = Lodieu et al. (2012), Lodieu2022 = Lodieu et al. (2022), Looper2007 = Looper et al. (2007), Looper2008 = Looper et al. (2008), LopezMorales2007 = López-Morales (2007), Loth1998 = Loth & Bidelman (1998), Loutrel2011 = Loutrel et al. (2011), Low2021 = Low et al. (2021), Lowrance2002 = Lowrance et al. (2002), Luck2017 = Luck (2017), Luhman2012 = Luhman et al. (2012), Luhman2013 = Luhman (2013), Luhman2014 = Luhman (2014), Luhman2014b = Luhman & Sheppard (2014), Lurie2014 = Lurie et al. (2014), Mace2013a = Mace et al. (2013a), Mace2013b = Mace et al. (2013b), Mace2018 = Mace et al. (2018), Makarov2007 = Makarov et al. (2007), Malkov2012 = Malkov et al. (2012), Malkov2006 = Malkov et al. (2006), Malo2014b = Malo et al. (2014a), Malogolovets2007 = Malogolovets et al. (2007), Mamajek2012 = Mamajek (2012), Mamajek2018 = Mamajek et al. (2018), Manjavacas2013 = Manjavacas et al. (2013), Mann2019 = Mann et al. (2019), Mariotti1990 = Mariotti et al. (1990), Marocco2010 = Marocco et al. (2010), Marocco2013 = Marocco et al. (2013), Martin1995 = Martin & Brandner (1995), Martin1998 = Martin & Mignard (1998), Martin1998b = Martin et al. (1998), Martin2018 = Martin et al. (2018), Martinache2007 = Martinache et al. (2007), Martinache2009 = Martinache et al. (2009), Mason2009 = Mason et al. (2009), Mason2017 = Mason et al. (2017), Mason2018 = Mason et al. (2018), Mason2018b = Mason et al. (2018), McCleery2020 = McCleery et al. (2020), McCook2016 = McCook & Sion (2016), Meisner2020a = Meisner et al. (2020a), Meisner2020b = Meisner et al. (2020b), Mendez2021 = Mendez et al. (2021), Merc2021 = Merc et al. (2021), Metcalfe2021 = Metcalfe et al. (2021), Mitrofanova2020 = Mitrofanova et al. (2020), Mitrofanova2021 = Mitrofanova et al. (2021), Monnier2007 = Monnier et al. (2007), Monnier2012 = Monnier et al. (2012), Montagnier2006 = Montagnier et al. (2006), Montes2006 = Montes et al. (2006), Montes2007 = Montes et al. (2007), Morales2009 = Morales et al. (2009), Morbey1987 = Morbey & Griffin (1987), Morgan1973 = Morgan & Keenan (1973), Mosser2008 = Mosser et al. (2008), Mugrauer2022 = Mugrauer et al. (2022), Murray1986 = Murray et al. (1986), Murray2011 = Murray et al. (2011), Muzic2012 = Mužić et al. (2012), Newton2014 = Newton et al. (2014), Neuhauser2007 = Neuhäuser et al. (2007), Nidever2002 = Nidever et al. (2002), Nielsen2019 = Nielsen et al. (2019), Nilsson2017 = Nilsson et al. (2017), Nordstrom2004 = Nordström et al. (2004), OBrien2023 = O'Brien et al. (2023), Pan1990 = Pan et al. (1990), Pepe2011 = Pepe et al. (2011), Peretti2019 = Peretti et al. (2019), Pettersen2006 = Pettersen (2006), Phan-Bao2006 = Phan-Bao & Bessell (2006), Phan-Bao2008 = Phan-Bao et al. (2008), Phan-Bao2017 = Phan-Bao et al. (2017), Piccotti2020 = Piccotti et al. (2020), Pinamonti2022 = Pinamonti et al. (2022), Pineda2016 = Pineda et al. (2016), Pinfield2008 = Pinfield et al. (2008), Pinfield2012 = Pinfield et al. (2012), Pinfield2014a = Pinfield et al. (2014a), Pinfield2014b = Pinfield et al. (2014b), Pourbaix2000 = Pourbaix (2000), Pourbaix2004 = Pourbaix et al. (2004), Poveda2009 = Poveda et al. (2009), Pravdo2006 = Pravdo et al. (2006), Raghavan2010 = Raghavan et al. (2010), Rajpurohit2013 = Rajpurohit et al. (2013), Ramm2005 = Ramm et al. (2005), Ramm2016 = Ramm et al. (2016), Ramm2021 = Ramm et al. (2021), Rebassa-Mansergas2017 = Rebassa-Mansergas et al. (2017), Reffert2011 = Reffert & Quirrenbach (2011), Reid1990 = Reid & Mould (1990), Reid1995 = Reid et al. (1995), Reid2000 = Reid et al. (2000), Reid2001 = Reid et al. (2001), Reid2003 = Reid et al. (2003), Reid2004 = Reid et al. (2004), Reid2005 = Reid & Gizis (2005), Reid2006 = Reid et al. (2006), Reid2007 = Reid et al. (2007), Reid2008a = Reid et al. (2008b), Reid2008b = Reid et al. (2008a), Reiners2012 = Reiners et al. (2012), Ren2013 = Ren & Fu (2013), Reuyl1943 = Reuyl (1943), Reyle2006 = Reylé et al. (2006), Reyle2018 = Reylé (2018), Riaz2006 = Riaz et al. (2006), Ribas2003 = Ribas (2003), Rice1998 = Rice & Strassmeier (1998), Riedel2010 = Riedel et al. (2010), Riedel2014 = Riedel et al. (2014), Riedel2017 = Riedel et al. (2017), Riedel2018 = Riedel et al. (2018), Robert2016 = Robert et al. (2016), Roberts2011 = Roberts et al. (2011), Rodet2018 = Rodet et al. (2018), Rodigas2011 = Rodigas et al. (2011), Rodler2012 = Rodler et al. (2012), Rodriguez2015 = Rodriguez et al. (2015), Rosenthal2021 = Rosenthal et al. (2021), Sahlmann2015 = Sahlmann et al. (2015), Sahlmann2021 = Sahlmann et al. (2021), Sahu2017 = Sahu et al. (2017), Salama2021 = Salama et al. (2021), Salama2022 = Salama et al. (2022),

Salim2003 = Salim et al. (2003), Samus2003 = Samus' et al. (2003), Samus2017 = Samus' et al. (2017), Santos2003 = Santos et al. (2003), SBC9 = Pourbaix et al. (2004), SBC7 = Batten et al. (1978), Schapera2022 = Schapera et al. (2022), Schlieder2014 = Schlieder et al. (2014), Schmidt2007 = Schmidt et al. (2007), Schmidt2010 = Schmidt et al. (2010), Schneider2014 = Schneider et al. (2014), Schneider2015 = Schneider et al. (2015), Schneider2017 = Schneider et al. (2017), Schneider2019 = Schneider et al. (2019), Schneider2020 = Schneider et al. (2020), Schneider2021 = Schneider et al. (2021), Scholz2002 = Scholz & Meusinger (2002), Scholz2002b = Scholz et al. (2002), Scholz2003 = Scholz et al. (2003), Scholz2004 = Scholz et al. (2004), Scholz2005 = Scholz & Meusinger (2005), Scholz2014 = Scholz et al. (2014), Schuster1979 = Schuster (1979), Schweitzer2019 = Schweitzer et al. (2019), Segransan2000 = Ségransan et al. (2000), Seifahrt2008 = Seifahrt et al. (2008), Shan2017 = Shan et al. (2017), Shkolnik2009 = Shkolnik et al. (2009), Shkolnik2010 = Shkolnik et al. (2010), Shkolnik2012 = Shkolnik et al. (2012), Silverstein2022 = Silverstein et al. (2022), Sion2014 = Sion et al. (2014), Skemer2016 = Skemer et al. (2016), Skiff2013 = Skiff (2013), Skrutskie2006 = Skrutskie et al. (2006), Skuljan2004 = Skuljan et al. (2004), Smart-priv-comm = R. L. Smart (priv. comm.), Smart2013 = Smart et al. (2013), Smart2018 = Smart et al. (2018), Smith2014 = Smith et al. (2014), Soderhjelm1999 = Söderhjelm (1999), Soriano2010 = Soriano & Vauclair (2010), Sperauskas2019 = Sperauskas et al. (2019), Stassun2016 = Stassun & Torres (2016), Stassun2019 = Stassun et al. (2019), Stauffer2010 = Stauffer et al. (2010), Stelzer2003 = Stelzer & Burwitz (2003), Stepanov2020 = Stepanov (2020), Stephenson1967 = Stephneson & Terrill (1967), Stephenson1975 = Stephenson & Sanduleak (1975), Strassmeier1990 = Strassmeier & Fekel (1990), Struve1954 = Struve & Ratcliffe (1954), Struve1955 = Struve & Franklin (1955), Subasavage2017 = Subasavage et al. (2017), Takeda2007 = Takeda et al. (2007), Tamazian2006 = Tamazian et al. (2006), Teixeira2009 = Teixeira et al. (2009), Terrien2015 = Terrien et al. (2015), Thevenin2005 = Thévenin et al. (2005), Thompson2013 = Thompson et al. (2013), Thorstensen2003 = Thorstensen & Kirkpatrick (2003), Tinney2003 = Tinney et al. (2003), Tinney2014 = Tinney et al. (2014), Tinney2018 = Tinney et al. (2018), Tokovinin1997 = Tokovinin (1997), Tokovinin2005 = Tokovinin et al. (2005), Tokovinin2006 = Tokovinin et al. (2006), Tokovinin2008 = Tokovinin (2008), Tokovinin2012 = Tokovinin et al. (2012), Tokovinin2014a = Tokovinin et al. (2014), Tokovinin2014b = Tokovinin (2014), Tokovinin2016 = Tokovinin & Horch (2016), Tokovinin2017 = Tokovinin (2017), Tokovinin2019 = Tokovinin et al. (2019), Tokovinin2020 = Tokovinin et al. (2020), Tokovinin2021 = Tokovinin et al. (2021), Tokovinin2021b = Tokovinin (2021b), Toonen2017 = Toonen et al. (2017), Torres2002 = Torres & Ribas (2002), Torres2006 = Torres et al. (2006), Torres2015 = Torres et al. (2015), Torres2022 = Torres (2022), Tremblay2020 = Tremblay et al. (2020), Trifonov2020 = Trifonov et al. (2020), Upgren1972 = Upgren et al. (1972), Valenti2005 = Valenti & Fischer (2005), vanAltena1995 = van Altena et al. (1995), vanBelle2007 = van Belle et al. (2007), vanBiesbroeck1974 = van Biesbroeck (1974), vandeKamp1971 = van de Kamp & Worth (1971), vonBraun2011 = von Braun et al. (2011), Volk2003 = Volk et al. (2003), Vrba2004 = Vrba et al. (2004), Vrijmoet2020 = Vrijmoet et al. (2020), Vrijmoet2022 = Vrijmoet et al. (2022), WandDuong2015 = Ward-Duong et al. (2015), WDS = http://www.astro.gsu.edu/wds/, West2008 = West et al. (2008), West2011 = West et al. (2011), West2015 = West et al. (2015), Willmarth2016 = Willmarth et al. (2016), Wilson1950 = Wilson & Joy (1950), Wilson2003 = Wilson et al. (2003b), Wilson2017 = Wilson et al. (2017), Winters2011 = Winters et al. (2011), Winters2017 = Winters et al. (2017), Winters2018 = Winters et al. (2018), Winters2019 = Winters et al. (2019b), Winters2019b = Winters et al. (2019a), Winters2020 = Winters et al. (2020), Winters2021 = Winters et al. (2021), Wittenmeyer2006 = Wittenmyer et al. (2006), Wittenmeyer2011 = Wittenmyer et al. (2011), Wittrock2017 = Wittrock et al. (2017), Woitas2000 = Woitas & Leinert (2000), Wright2013 = Wright et al. (2013), Wright2018 = Wright et al. (2018), Wyatt2007 = Wyatt et al. (2007), Xia2019 = Xia et al. (2019), Zasche2009 = Zasche et al. (2009), Zeng2022 = Zeng et al. (2022), Zhang2020 = Zhang et al. (2020), Zhuchkov2012 = Zhuchkov et al. (2012), Zurlo2018 = Zurlo et al. (2018).

Designation references (italic formatting identifies the acronyms): *Bayer* = Bayer (1603); *Flamsteed* = Stellarum Inerrantium Catalogus Britannicus (Flamsteed 1725) http://pbarbier.com/flamsteed/flamsteed.html, http://www.ianridpath.com/startales/flamsteed.html, de Lalande (1783); Hoffleit & Jaschek (1991); *HR* = Schlesinger (1930); Schlesinger & Jenkins (1940); Hoffleit (1964); Hoffleit & Jaschek (1982); Hoffleit et al. (1983); Hoffleit & Jaschek (1991); *HD* = Cannon & Pickering (1918a, 1918b, 1919a, 1919b, 1920, 1921, 1922, 1923, 1924); Cannon (1925a, 1925b, 1927, 1928, 1931, 1936); Cannon & Mayall (1949); *BD* = Schönfeld (1886); Argelander (1903); *CD* = Thome (1890, 1892, 1894, 1900, 1914); Perrine (1932); *CPD* = Gill & Kapteyn (1896, 1897, 1900); Innes (1903); *Wolf* = Wolf (1919a, 1919b, 1919c, 1919d, 1919e, 1920a, 1920b, 1920c, 1920d, 1920e, 1920f, 1921b, 1921b,1921c, 1921d, 1921e, 1922, 1923a, 1923b, 1926a, 1924a, 1924b, 1924c, 1923c, 1924d, 1924e, 1924f); Wolf & Reinmuth (1925); Wolf (1925a, 1925b, 1925c, 1925d, 1925e, 1926b, 1926c, 1927a, 1927b, 1929, 1931); *Ross* = Ross (1925, 1926a, 1926b, 1926c, 1927, 1928, 1929, 1930, 1931, 1937, 1939a, 1939b); *L* = Luyten (1963; for which the "L" numbers were obtained from the NLTT Catalogue); *LP* = Luyten (1970a; specifically, volumes 1–9, 11–17, and 23–24), Luyten (1970b, 1970c); Luyten & La Bonte (1971); Luyten (1972a, 1972b); Luyten & La Bonte (1972); Luyten (1972c, 1973a, 1973b, 1974a, 1974b, 1975a, 1975b); Luyten & Kowal (1975); Luyten (1976a, 1976b, 1976c, 1980a); Luyten & Hughes (1980); Luyten et al. (1981); Luyten & Hughes (1982, 1983); Luyten et al. (1985a, 1985b); Luyten & Hughes (1985, 1987a, 1987b); *G* = Giclas et al. (1971, 1978); *LHS* = Luyten (1979a); *LFT* = Luyten (1955); *NLTT* = Luyten (1979b, 1980b, 1980c); *LTT* = Luyten (1957, 1961, 1962); *LSPM* = Lépine & Shara (2005); *SCR* = Hambly et al. (2004); Henry et al. (2004); Subasavage et al. (2005a, 2005b); Finch et al. (2007); Winters et al. (2011); Boyd et al. (2011); *UPM* = Finch et al. (2010, 2012); *APMPM* = Gizis et al. (1997); Scholz et al. (1999); Schweitzer et al. (1999); Scholz et al. (2000); Reylé et al. (2002); *LEHPM* = Pokorny et al. (2003, 2004); *WT* = Wroblewski & Torres (1989, 1991, 1994, 1996, 1997); Wroblewski & Costa (1999, 2001); *SIPS* = Deacon et al. (2005); Deacon & Hambly (2007); *PM* = Eggen (1979, 1980); *PMJ* = Lépine (2005b, 2008); Schlieder et al. (2010); Lépine & Gaidos (2011); Schlieder et al. (2012); Lépine et al. (2013); *WD* = McCook & Sion (1999); *LAWD* = Luyten (1949); *EGGR* = Eggen & Greenstein (1965a, 1965b, 1967); Greenstein (1969, 1970, 1974, 1975, 1976); Greenstein et al. (1977); Greenstein (1979, 1980, 1984); *2MASS* = Cutri et al. (2003); WISE = Cutri et al. (2012, 2013); Eisenhardt et al. (2020); Marocco et al. (2021); Gaia = Gaia Collaboration et al. (2018, 2021b); *HIC* = Turon et al. (1993); *HIP* = ESA (1997); van Leeuwen (2007); *TYC* = Høget al. (2000); *UCAC4* = Zacharias et al. (2013); *TIC* = Stassun et al. (2019); *GJ* = Gliese (1969); Woolley et al. (1970); Gliese & Jahreiß (1979); *V** = Samus & Durlevich (2004); *Karmn* = Alonso-Floriano et al. (2015); Cortés-Contreras et al. (2017); ** = this designation is unique to SIMBAD (Wenger et al. 2000).

Reference for photometry is a five-character code referring to the source of the J_{MKO}, J_{2MASS}, H, K_{MKO}, and Ks_{2MASS} magnitudes, respectively, with these characters as the individual codes: 2 = 2MASS (Skrutskie et al. 2006), a = Meisner et al. (2020a), A = Meisner et al. (2020b), b = Bardalez Gagliuffi et al. (2020) for which the Hubble Space Telescope F125W magnitude limit for WISE 0830+2837 is used as its value for J_{MKO}, B = Bigelow/2MASS from Kirkpatrick et al. (2021a), c = Boccaletti et al. (2003), D = Database of Ultracool Parallaxes as of 2020 April: Dupuy & Liu (2012) and Dupuy & Kraus (2013) and Liu et al. (2016), e = Martin et al. (2018), E = McElwain & Burgasser (2006), f = Faherty et al. (2012), F = Freed et al. (2003), g = Mamajek et al. (2018), G = Gemini-South/FLAMINGOS2 from Kirkpatrick et al. (2021a), h = Pinfield et al. (2014b), H = Pinfield et al. (2014a), i = Ireland et al. (2008), I = Dupuy et al. (2019), j = Janson et al. (2011), J = Faherty et al. (2014), k = Kirkpatrick et al. (2019a), K = Kirkpatrick et al. (2011), m = Mace et al. (2013a), M = Magellan/PANIC from Kirkpatrick et al. (2021a), p = PAIRITEL from Kirkpatrick et al. (2021a), P = Palomar/WIRC from Kirkpatrick et al. (2021a), Q = Deacon et al. (2017), r = Deacon et al. (2012b), s = Schneider et al. (2015), S = SOAR/OSIRIS from Kirkpatrick et al. (2021a), t = Tinney et al. (2014), T = Thompson et al. (2013), u = ULAS or UGPS or UGCS (Lawrence et al. 2007), U = UHS (Dye et al. 2018), v = VVV (Minniti et al. 2010), V = VHS (McMahon et al. 2013), w = Wright et al. (2013), W = Best et al. (2020), x = see Table 2 in this paper, z = Meisner et al. (2023b), Z = Schapera et al. (2022).

(This table is available in its entirety in machine-readable form.)

an homage to the many researchers who have helped advance our knowledge of the nearby census.

A few common names ("CommonName"), not listed in SIMBAD, have been added from the list of star names[58] approved by the International Astronomical Union (IAU) and from Allen (1899), along with certain double star names from the Washington Double Star (WDS) Catalog.[59] The origin of these names is given under the heading "NamesRef," which is populated at the upper level for each system (i.e., on rows having integral values of "SystemHierarchy"). For 2MASS names, we supplemented the SIMBAD listings with the list of Gliese-2MASS crossmatches provided by Stauffer et al. (2010). For objects having no 2MASS-associated name in either of these lists, we searched the 2MASS Point Source Catalog (Cutri et al. 2003) directly. In a few cases, SIMBAD listed more than one name with the "2MASS J" prefix, and for these, we also checked the 2MASS Point Source Catalog directly to remove the incorrect association.

3.2. Astrometry

For each object in the 20 pc census, we list approximate sexagesimal R.A. and decl. coordinates at equinox J2000, given under "SexagesimalRA" and "SexagesimalDec" in Table 4. For close multiple systems, the positions of the two objects may be identical, as these coordinates are meant to provide only a crude position for matching the system across catalogs. For more precise coordinates, we also provide R.A. and decl. in decimal degrees ("RA" and "Dec") at the yearly epoch provided in the "Epoch" column, along with the coordinate uncertainties ("RA_unc" and "Dec_unc"). Also, listed are the absolute parallax ("Parallax") and its uncertainty ("Parallax_unc") and the (usually) absolute proper motions and their uncertainties in R.A. and decl. ("PMRA," "PMDec," "PMRA_unc," and "PMDEC_unc"). The reference for these decimal coordinates, parallax, and motion measurements is also given ("PlxPMRef"). Note that, for some multiple systems, this more precise astrometry may exist only for the composite system or primary and not for each individual component. (An asterisk in the "PlxPMRef" column indicates that the parallax and motion values for another object in the system are used in lieu of actual measurements for this component.) Furthermore, for some recent brown dwarf discoveries, only positions and proper motions are given, as parallaxes have not yet been measured.

As a final note on positions, we provide the constellation in which each object is located ("Constellation"), based on the VizieR tool[60] that uses the constellation boundaries provided by Roman (1987). This column can be used to determine the nearest object in each constellation, as further explored in Appendix B.

3.3. Spectral Types

For higher-mass stars—typically those with types earlier than mid-M—our primary sources for spectral types were the NStars papers by Gray et al. (2003, 2006). This was done to assure that as many of our referenced types as possible were classified against a homogeneous system of standards, in this case, the Morgan–Keenan–Kellman System of Morgan et al. (1943). This system was subsequently updated to the Morgan–Keenan system of Johnson & Morgan (1953), which itself was expanded and updated by Morgan & Keenan (1973; the revised MK system), Keenan & McNeil (1976), and Morgan et al. (1978). (See Hearnshaw 2014 for a more detailed history.)

Classification for objects of later type has followed the precepts of the MK System, thereby pushing this homogeneity into the late-M (Boeshaar 1976; Boeshaar & Tyson 1985; Kirkpatrick et al. 1991, 2010), L (Kirkpatrick et al. 1999, 2010), T (Burgasser et al. 2006; Kirkpatrick et al. 2010), and Y (Cushing et al. 2011; Kirkpatrick et al. 2012) dwarf sequences. Classification is dependent upon the wavelength range over which the typing is done, so Table 4 specifies whether the spectral type was obtained in the visible to photographic near-infrared region (<1 μm; "SpecTypeOpt") or the classical near-infrared region (1–2.5 μm; "SpecTypeNIR"). References for the spectral types can be found under "SpTOpt_ref" and "SpTNIR_ref." For ease of plotting, the spectral types have been converted into a numerical code, with the luminosity type (if listed) ignored. The scale[61] is set so that 0 = A0, 10 = F0, 20 = G0, 30 = K0, 40 = M0, 50 = L0, 60 = T0, and 70 = Y0; a type of L8.5 would thus be encoded as 58.5. These codes can be found under "SpTOpt_indx" and "SpTNIR_indx." Note that the original MK classification system's standards jump from K5 to K7 to M0 in the late-K sequence, although K6 standards were eventually added in the late 1980s (Keenan & Yorka 1988; Keenan & McNeil 1989). As a result, there are very few objects with codes of ∼36 or ∼38–39.

For white dwarfs, Table 4 uses types primarily taken from the compilations of Sion et al. (2014) and McCook & Sion (2016), with post-2016 discoveries taken from more recent literature or from Appendix A.2. The use of these references assures that all white dwarfs are on the spectroscopic classification system proposed by Liebert & Sion (1994). All white dwarf classifications have been assigned based on optical spectra, and the corresponding optical spectral index, "SpTOpt_indx," is coded to be the Liebert & Sion (1994) temperature index + 100. That is, our index is set so that DA2 = 102, DAZ5.8 = 105.8, DA9.2 = 109.2, DZ12.6 = 112.6, etc. For any white dwarf lacking a temperature index, our spectral index has been arbitrarily assigned a code of 100, as a temperature index of 0.0 cannot exist (and no white dwarf in Table 4 has a temperature index lower than 2.0).

3.4. Photometry

Table 4 provides photometry in several systems that have hemispheric or all-sky coverage. As discussed in Section 5.3, objects in the 20 pc census span a vast dynamic range in absolute luminosity, amounting to over 29 mag (a difference of 5×10^{11} in brightness) in J band alone. Thus, special care must be taken when choosing photometry for Table 4.

For the traditional *visible* wavelength regime, Gaia eDR3 magnitudes and uncertainties at G, G_{BP}, and G_{RP} are listed ("G," "G_BP," "G_RP," "G_unc," "G_BP_unc," and "G_RP_unc"). The brightest reported G-band magnitude is ∼2 mag (Gaia Collaboration et al. 2021b), and objects with $G < 8$ mag, $G_{BP} \lesssim 4$ mag, and $G_{RP} \lesssim 4$ mag have residual saturation effects, as detailed in Gaia Collaboration et al. (2021b) and Riello et al. (2021). At the faint end, Gaia is

[58] https://www.iau.org/public/themes/naming_stars/

[59] http://www.astro.gsu.edu/wds/ and https://vizier.cds.unistra.fr/viz-bin/VizieR?-source=B/wds.

[60] http://vizier.cfa.harvard.edu/viz-bin/VizieR?-source=VI/42

[61] There are no O- or B-type stars within the 20 pc volume. The closest O star is ζ Oph (O9.5 V, $d = 112$ pc; Howarth et al. 2014; van Leeuwen 2007), and the closest B star is α Leo (B8 IVn, $d = 24.3$ pc; Fuhrmann et al. 2011b; van Belle & von Braun 2009; van Leeuwen 2007).

complete to $G \approx 20$ mag (depending upon source crowding and galactic latitude; Gaia Collaboration et al. 2021b), which means that the more distant late-L dwarfs in the 20 pc census, along with most of the T dwarfs and all of the Y dwarfs, are too faint for Gaia photometric measurements (Figure 26 of Gaia Collaboration et al. 2021a; see also Figure 2 of Theissen 2018).

For the traditional near-infrared wavelength regime, *J*, *H*, and *K* magnitudes are provided, with the caveat that there are two main filter systems in use: the 2MASS filter system[62] and the MKO filter system (Tokunaga et al. 2002). The *H*-band filter is almost identical between the two, but the *J* and *K* filters are quite different. As a result, we provide five separate entries to cover the possibilities—J_{MKO}, J_{2MASS}, *H*, *K*, and K_s—along with their uncertainties ("JMKO," "J2MASS," "H," "K," "Ks," "JMKOerr," "J2MASSerr," "Herr," "Kerr," and "Kserr"). The references for this photometry are given in the "JHK_ref" column. The J_{2MASS} entries mostly come from 2MASS, whereas the J_{MKO} entries come mostly from surveys based at the UKIRT (e.g., the UKIRT Hemisphere Survey, UHS—McMahon et al. 2013) and the Visible and Infrared Survey Telescope for Astronomy (VISTA; e.g., the VISTA Hemisphere Survey, VHS—Dye et al. 2018). The K_{MKO} entries come primarily from UKIRT-based surveys, whereas the K_s entries come from both 2MASS and VISTA-based surveys. The *H* entries are pulled from all three sets of surveys. 2MASS provides the only reliable photometry at the bright end of our sample, albeit with large uncertainties, and extends to a signal-to-noise ratio (S/N) = 10 limit, of $J = 15.8$ mag, $H = 15.1$ mag, and $K_s = 14.3$ mag at its faint end.[63] UKIRT and VISTA provide reliable photometry between their bright limit ($J \approx 12$ mag for UHS and ~11.5–12.5 mag in *J*, *H*, and K_s for VHS; Dye et al. 2018; González-Fernández et al. 2018) and their detection limit ($J \approx 19$ mag for UHS and $J \approx 20$ mag, $H \approx 19$ mag, and $K_s \approx 18$ mag for VHS; Dye et al. 2018; González-Fernández et al. 2018) and provide higher angular resolution than that of 2MASS. We have therefore favored 2MASS photometry for near-infrared magnitudes brighter than ~12 mag and UKIRT/VISTA for fainter magnitudes. For objects even fainter than the UKIRT/VISTA limits, or for objects in areas not yet covered by the public UKIRT and VISTA releases, we have pulled objects from the literature or from Appendix A.1.

At longer near-infrared wavelengths and extending into the near mid-infrared, we also provide WISE-based W1 (3.4 μm), W2 (4.6 μm), W3 (12 μm), and W4 (22 μm) magnitudes and their uncertainties ("W1," "W2," "W3," "W4," "W1err," "W2err," "W3err," and "W4err"). The reference for the WISE photometry is given in the "WISEphot_ref" column. For W1 and W2, magnitudes brighter than W1 ≈ 8 mag and W2 ≈ 7 mag were pulled from the WISE All-sky Source Catalog, and fainter magnitudes were pulled from the AllWISE Source Catalog, in accordance with the suggestion made in the AllWISE Explanatory Supplement.[64] Photometry at W3 and W4 was pulled from the WISE All-sky Release. The only exceptions to the above are objects that were not detected in either of these releases and are instead found only in the CatWISE2020 Catalog. For these sources, only W1 and W2 photometry is presented, as CatWISE2020 has no W3 or W4 photometry.

In the case of 2MASS and WISE photometry, we further provide columns "2MASS_contam?" and "WISE_contam?." A "yes" in these columns indicates that the associated photometry is likely compromised by another nearby object or artifact, as judged via our by-eye assessments of the multiepoch WiseView image blinks (Caselden et al. 2018), as the poorer image scales of 2MASS (pixel scale of 1″) and WISE (pixel size of 1.″375) translate to a higher likelihood of source blending.

3.5. Radial Velocities

Gaia DR3 provides all-sky radial velocities for stars with $G_{RVS} \lesssim 14$ mag (Katz et al. 2023) and effective temperatures as high as 14,500 K (Blomme et al. 2023). These radial velocities and their uncertainties are also listed in Table 4 ("GaiaRV" and "GaiaRV_unc").

3.6. Multiplicity

Even after all systems within the 20 pc volume have been noted, one difficult step remains: correctly determining, based on current knowledge, the multiplicity of each system so that each individual component can be correctly accounted for in the mass distribution. We took a multipronged approach at tackling this problem, as described below.

3.6.1. The Stellar Ambassadors Program

The first approach was to crowdsource the initial reconnaissance of the literature. With the help of the citizen scientist super users of the Backyard Worlds: Planet 9 project, we set up a program whereby volunteers could sign up to investigate the multiplicity of randomly selected 20 pc systems. To make this more enjoyable, the following mission statement was provided:

> *"Our science-fictional Earth Coalition is currently laying the groundwork to explore all of the 'worlds' within 20 parsecs (65 light years) of the Sun. Scientists on the Earth Coalition's Board of Advisors have a list of host 'suns' within this volume of space, but the details in that list are a bit spotty. The Coalition is seeking to flesh out these details using our Stellar Ambassadors program. If you choose to become a Stellar Ambassador, your role will be to represent planet Earth to a small number of stellar systems within 20 parsecs. As we reach out for the first time to each of these stellar neighbors, you will be Earth's representative to them. But you need to be knowledgeable of the systems for which you are responsible, and that will involve your gaining knowledge of each system you are assigned. (By 'system' we are referring to a host star and any of its companions—other stars, brown dwarfs, or exoplanets—in orbit around it.)"*

Each volunteer was tasked with determining (a) the number of stars, brown dwarfs, and exoplanets in each system, (b) the spectral types of the (sub)stellar components, and (c) the masses of each component, if the masses have been measured. Each Stellar Ambassador was initially assigned a set of ~12

[62] https://irsa.ipac.caltech.edu/data/2MASS/docs/releases/allsky/doc/sec6_4b.html
[63] https://irsa.ipac.caltech.edu/data/2MASS/docs/releases/allsky/doc/sec2_2.html
[64] https://wise2.ipac.caltech.edu/docs/release/allwise/expsup/sec2_1.html

systems, and additional sets would be assigned if the Ambassador wished to analyze more. Importantly, participants were asked to track the reference material that they used for their data collection, regardless of whether they started with SIMBAD, VizieR, Wikipedia, or some other encyclopedic compendium. In total, 21 super users participated in the program, which allowed us to cover 56% of the systems with primaries earlier than L0. (All 20 pc objects with primaries later than this had already been scrutinized in Kirkpatrick et al. 2021a.) These efforts were coordinated in weekly and biweekly calls with the volunteers.

The product of this exercise was, as expected, an inhomogeneous set of results, as individual Ambassadors concentrated on different portions of the exercise or used entirely different methodologies in their workflows. Nonetheless, it was these varied approaches that enabled us to determine the references on which it would be the most lucrative to focus our early attention. For example, despite the varied approaches, many of the same references kept appearing again and again in the Ambassadors' reports. These repeating references underscored the vast groundwork laid by exoplanet-finding searches in characterizing potential host stars, as well as the breadth of methods used to measure the masses of stars within the solar neighborhood, a topic explored more fully in Section 4. The references that arose from the Stellar Ambassador program were the first resources we used to populate Table 4 with information on multiplicity, mass measurements, and mass estimates.

3.6.2. In-depth Literature Checks

After this first reconnaissance of the oft-referenced literature, our second approach was the inevitable deep-dive into the literature for each individual object. For this, we used the extensive per-object references compiled by SIMBAD. We concentrated on literature with high-resolution imaging and radial velocity monitoring, in order to judge the multiplicity of each system. We also looked for paper titles that referenced mass measurements and variability (such as eclipsing binaries, RS CVn variables, etc.). Because of time constraints, we were not able to review each reference in detail, but a paper well stocked with results would often allow us to populate Table 4 with information for many systems at once, which sped up the process for objects farther down the list. We also relied heavily on the Washington Double Star Catalog[65] and the Ninth Catalog of Spectroscopic Binaries (Pourbaix et al. 2009), although the former reference lists both confirmed and possible companions that themselves must be studied individually to gauge true companionship.

3.6.3. The Apps Catalog

After our in-depth literature checks were completed, we became aware of an unpublished list of objects within 30 pc of the Sun that (now coauthor) K. Apps has been carefully curating since 2009. A comparison of the Apps catalog to our list revealed 28 objects, mainly companions, that have been disproved via published literature but that our list still included. These have now been removed from Table 4. The comparison to the Apps list also revealed another 23 objects, almost all of which are the second components in spectroscopic binaries or companions revealed by high-resolution imaging, whose discovery literature we had missed. These objects have now been added to Table 4.

3.6.4. Multiplicity Parameters and Exoplanets

To encapsulate knowledge from the multiplicity checks above, we include several additional columns in Table 4 and split the components of each system into separate rows. An example for one system is illustrated in the mobile diagram (see Evans 1968) of Figure 2. In the column "DefaultName," the entry for the system as a whole appears as "`xi UMa AB & WISE 111838.70+312537.9`." The names of the first subdivision in the mobile diagram of this multiple are denoted by a double hyphen at the beginning of the name, which in this case are "`--xi UMa AB`" and "`--WISE 111838.70 +321537.9`." Further hierarchical branches are denoted by four hyphens (e.g., "`----xi UMa A`"), six hyphens (e.g., "`------xi UMa Aa`"), etc. The column "#CompsOnThisRow" refers to the number of known components on that row of the table. To select only individual objects in the census, for example, one can downselect only those rows for which "#CompsOnThisRow" equals 1. There is also a "SystemHierarchy" column, giving a code for each division within the system. This is comprised of a four-digit integer (e.g., "`1290`") that uniquely identifies the system, followed by decimal subdivisions (e.g., "`1290.1`" and "`1290.2`") to identify subcomponents. For subcomponents that are themselves binaries, further decimal subdivisions (e.g., "`1290.1.1`" and "`1290.1.2`") are assigned, etc. Table 4 also lists a column called "#CompsInThisSystem" that gives the total number of components in the system. This field is populated only for the top level of each system (those rows having no decimal subdivisions in the "SystemHierarchy" column) and can be summed to find the total number of individual components in the table. Additionally, Table 4 includes a column called "SystemCode" that collapses the "SystemHierarchy" format into an eight-digit integer comprised of the four-digit system identifier followed by four additional digits representing any other subdivisions of the "SystemHierarchy" code, but with the decimals removed (e.g., "`12901210`"). Note that, when lower subdivisions are lacking, those digits are filled with zeros. This "SystemCode" column is useful if the user prefers to sort the systems in Table 4 into their mobile diagrams rather than keeping the table's default ordering, which sorts by R.A.

Note that our accounting of components above includes only those stellar and brown dwarf members of the system, but not any of the known exoplanets. For the latter, we also include a column in Table 4 named "#Planets" that reports the number of exoplanets listed in the NASA Exoplanet Archive[66] as of 2022 September 1. To match objects from Table 4 to objects in this archive, we used the Transiting Exoplanet Survey Satellite (TESS; Ricker et al. 2015) Input Catalog (TIC; Stassun et al. 2019) designations. It should be noted that, whereas we use a formation-based definition for brown dwarfs in this paper, the NASA Exoplanet Archive uses a mass-based definition for exoplanet versus brown dwarf and sets the dividing line, somewhat arbitrarily, at 30 $M_{\rm Jup}$.[67] As a result, there will be some double counting of objects, as these may appear in both

[65] https://vizier.cds.unistra.fr/viz-bin/VizieR?-source=B/wds

[66] https://exoplanetarchive.ipac.caltech.edu/

[67] https://exoplanetarchive.ipac.caltech.edu/docs/exoplanet_criteria.html

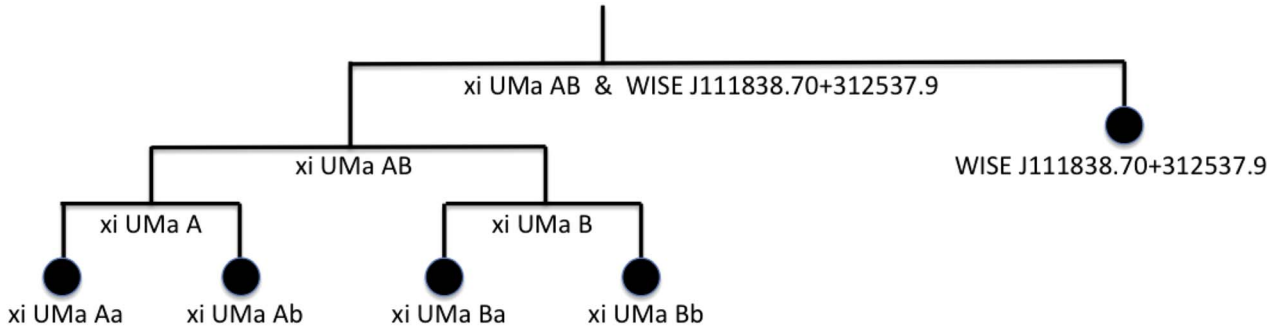

DefaultName	#CompsOnThis Row	System Hierarchy	#CompsIn ThisSystem	System Code
xi UMa AB & WISE J111838.70+312537.9	5	1290	5	12900000
--xi UMa AB	4	1290.1		12901000
----xi UMa A	2	1290.1.1		12901100
------xi UMa Aa	1	1290.1.1.1		12901110
------xi UMa Ab	1	1290.1.1.2		12901120
----xi UMa B	2	1290.1.2		12901200
------xi UMa Ba	1	1290.1.2.1		12901210
------xi UMa Bb	1	1290.1.2.2		12901220
--WISE J111838.70+321537.9	1	1290.2		12902000

Figure 2. Mobile diagram for the ξ UMa system along with sample columns from Table 4. The mobile diagram at top shows a stylized representation of this quintuple system, illustrating the pair of close doubles (ξ UMa A and ξ UMa B) and their distant common proper-motion companion (WISE J111838.70+312537.9). The table at bottom shows the nine rows for this system, representing the nine vertices (with labels) in the mobile diagram. Table 4 entries for DefaultName, #CompsOnThisRow, SystemHierarchy, #CompsInThisSystem, and SystemCode are shown for illustration.

the substellar and exoplanet lists. We will return to this point in Section 6.2.3.

3.7. Mass Parameters and Effective Temperature

The final parameters in Table 4 relate to our need to assign masses to all individual objects within the 20 pc census. In Section 4, we discuss the various methods for which masses can be directly measured. For objects whose masses must, instead, be estimated, Section 6 provides additional discussion. Stars with measured accelerations (see Section 4.1.4) are further discussed in Section 5.1, and objects whose Gaia astrometry suggests hidden companions are discussed in Section 5.2.

Mass estimation techniques work well for hydrogen-burning stars because there is a direct mapping from color, temperature, and spectral type to mass on the main sequence. These same techniques fail for brown dwarfs because color, temperature, and spectral type vary with age, and the age of a brown dwarf is generally an unmeasurable quantity. Estimating the masses for brown dwarfs, therefore, requires a different tack, one that we approach statistically through their distribution of effective temperatures, as further discussed in Section 6.1.3.

4. Masses from Direct Measurement

There are many ways of measuring stellar masses. Some methods (1) measure mass directly using only observational data, (2) lean lightly on theoretical assumptions when a full suite of needed observational data is not available, (3) derive masses by comparing available data to an empirical data grid for stars with directly measured masses, and (4) compare observables to theoretical models. Examples of these third and fourth groups are methodologies such as The Cannon (Ness et al. 2016) and StarHorse (Queiroz et al. 2018). However, the aim of this section is to establish nearby fiducial objects for which masses have been (semi)directly measured, in order to establish our own empirical grid (Method 3) to estimate masses for the remainder of the 20 pc census. Toward this goal, we use the next two subsections to discuss Methods 1 and 2 as they have been applied to nearby objects. Table 4 includes directly measured masses for objects that have such values ("Mass" and "Mass err") along with the technique

used for the measurement ("Mass method") and its citation ("Mass reference").

4.1. Multiple Systems

Mass measurements can be made for objects in binary or multiple systems, once sufficient information has been collected to define the orbits. For compact objects, mass can also be deduced from the gravitational redshift; observationally, this can only be done in multiple systems, as it requires at least one additional, noncompact, comoving object with which to disentangle the part of the redshift due to radial velocity. More specifics are given below.

4.1.1. Visual Binaries

For a visual binary whose orbit can be observed, the ratio of the masses is just

$$\frac{M_1}{M_2} = \frac{a_2}{a_1}, \tag{1}$$

where M_1 and M_2 are the masses of the two objects, and a_1 and a_2 are the (physical, not apparent) semimajor axes of their respective orbits. The total mass of the system, $M_1 + M_2$, can be derived from the equation

$$M_1 + M_2 = \frac{4\pi^2(a_1 + a_2)^3}{GP^2 \cos^3 i}, \tag{2}$$

where G is the gravitational constant, P is the orbital period, and i is the inclination of the orbit on the plane of the sky. The distance to the system must also be measured so that a_1 and a_2 are in physical, not angular, units, and the inclination can be deduced from the difference between the offset of the center of mass and the focus of the projected ellipse (Carroll & Ostlie 1996). Individual masses can be measured by combining Equations (1) and (2). A list of visual (and other) multiple systems can be found in the Washington Double Star Catalog.[68]

4.1.2. Spectroscopic Binaries with Eclipses

For spectroscopic binaries in which the radial velocities of both stars can be measured (SB2s), the ratio of the masses is just

$$\frac{M_1}{M_2} = \frac{v_2}{v_1}, \tag{3}$$

where v_1 and v_2 are the maximum velocity amplitudes with respect to the mean radial velocity curves of the system. The sum of the masses can be obtained via the equation

$$M_1 + M_2 = \frac{P(v_1 + v_2)^3}{2\pi G \sin^3 i}. \tag{4}$$

The inclination cannot be determined unless the SB2 is also an eclipsing system, in which case the nearly edge-on orientation means that $i \approx 90°$, allowing for a mass determination for both components.

There is a class of eclipsing single-lined spectroscopic binary (SB1) systems for which masses can also be derived (Stassun et al. 2017; Stevens et al. 2018). These are systems with a single stellar host and a transiting exoplanet. Because the combined light of the system is almost entirely that of the host star, available all-sky data sets can provide photometry across a wide swath of the electromagnetic spectrum—from the ultraviolet to the near mid-infrared—so that the star's apparent bolometric luminosity can be measured. Accurate parallaxes from Gaia provide the distances needed to convert this to absolute bolometric luminosity. These photometric points span either side of the flux peak in these objects, so they also provide a semiempirical measurement of effective temperature, as well. The radius of the host star, R, can then be derived from the Stefan–Boltzmann law

$$R = \sqrt{\frac{L_{\rm bol}}{4\pi\sigma T_{\rm eff}^4}}, \tag{5}$$

where $L_{\rm bol}$ is its bolometric luminosity, $T_{\rm eff}$ is its effective temperature, and σ is the Stefan–Boltzmann constant. In the limit where the mass and radius of the exoplanet are far smaller than those of the host star, the density of the host star, ρ, can be calculated directly from observable quantities using the equation

$$\rho = \frac{3\pi}{GP^2} {a_{\rm n}}^3, \tag{6}$$

where $a_{\rm n}$ is the "normalized" semimajor axis (see Sandford & Kipping 2017 for details), and P is the orbital period, both of which can be measured from the transit light curve. (This simplified form assumes a circular orbit. More generalized forms of this equation can be found in Seager & Mallén-Ornelas 2003.) The stellar mass, M, then follows from

$$M = \frac{4}{3}\pi R^3 \rho. \tag{7}$$

A list of SB1 and SB2 systems (see Pourbaix et al. 2009) can be found at the Centre de Données astronomiques de Strasbourg.[69] A list of 158 detached eclipsing binaries with well measured stellar properties is given in Stassun & Torres (2016).

4.1.3. Astrometric Binaries

Astrometric binaries are those systems in which the presence of an unseen companion can be inferred from the nonlinear motion of the primary, once its parallactic motion is accounted for. A careful mapping of the astrometric orbit results in the following measurement

$$\frac{M_2}{(M_1 + M_2)^{2/3}} = \frac{r_{\rm ap}}{(1 + e)} \left(\frac{2\pi}{P\sqrt{G}} \right)^{2/3} \tag{8}$$

where M_1 is the mass of the luminous component, M_2 is the mass of the invisible component, $r_{\rm ap}$ is the orbital separation of the luminous component at apastron, e is the eccentricity of the orbit, P is the orbital period, and G is the gravitational constant (Andrews et al. 2019).

It is possible to measure individual masses in astrometric binaries if the right conditions are met. We consider here an astrometric binary in which the secondary contributes little or no light to the system, as would be the case in a system comprised of a main-sequence star and a black hole, neutron

[68] https://vizier.cds.unistra.fr/viz-bin/VizieR?-source=B/wds

[69] http://cdsarc.u-strasbg.fr/ftp/cats/B/sb9

star, cold brown dwarf, or exoplanet companion. In this case, the light of the system comes almost entirely from the primary star, so an analysis of its broad-wavelength spectrum or spectral energy distribution built from broad-wavelength photometry can be used to deduce, with the help of empirical relations, its mass, M_1. Then, the mass of the companion, M_2, can be measured using Equation (8). Gaia will produce orbits of hundreds of thousands of such astrometric binaries over its anticipated lifetime (Halbwachs et al. 2023).

4.1.4. Binaries with Acceleration (Aka Proper-motion Anomaly)

Proper-motion measurements at two different epochs have the capability of identifying hidden companions if those two motion values differ significantly from one another. (This would be labeled as an astrometric binary— see Section 4.1.3 — once additional astrometric epochs are obtained.) The reason is that the proper motion of the system's photocenter will deviate from a straight line unless both components contribute equally to the light output. This methodology was first used by Bessel (1844) to deduce hidden companions to Sirius and Procyon. An illustration of the effect, which is known both as *proper-motion anomaly* and as *acceleration*, is shown in Figure 3. This procedure has seen a recent revival now that high-quality Hipparcos motions from the early 1990s and high-quality Gaia DR2 motions from the mid-2010s can be compared.

The lack of agreement between the motion measurements is sufficient to identify a hidden companion, and only a few other measurements are needed to derive the companion's mass. This can be computed from the following equation from Brandt et al. (2019)

$$M = \frac{s^2\left(a_{\rm PM}{}^2 + a_{\rm RV}{}^2\right)^{\frac{3}{2}}}{G\left(\varpi a_{\rm PM}\right)^2}, \tag{9}$$

where s is the projected separation between the companion and host star, $a_{\rm PM}$ is the host star's acceleration on the plane of the sky, $a_{\rm RV}$ is the host star's acceleration along the line of sight, and ϖ is the parallax of the system. (See Equation (17) for a different treatment.) This equation holds only if all measurements can be approximated to refer to the same orbital epoch. Otherwise, as detailed in Brandt et al. (2019), a more complex orbital fitting is required.

4.1.5. Compact Objects with Gravitational Redshifts

Finally, gravitational redshift can be used to measure the mass if the surface gravity can also be determined. Within the 20 pc sample, this is realistically measurable only in relatively massive compact objects like white dwarfs.[70] The observed velocity shift, $v_{\rm gr}$, due to gravitational redshift is given by

$$v_{\rm gr} = \frac{GM}{Rc}, \tag{10}$$

where c is the speed of light (e.g., Chandra et al. 2020). Because the star's mass is related to its surface gravity, g, via

[70] Brown dwarfs, like white dwarfs, are electron degenerate but are less compact and less massive, so their gravitational redshifts are only ~0.5 km s^{-1} for the most massive examples. Although this is comparable to the effect seen for the Sun, ~0.6 km s^{-1}, it is 100 times smaller than the effect seen for a 0.8 $M_\odot$ white dwarf (~50 km s^{-1}).

Figure 3. Schematic diagram demonstrating the concept of proper-motion anomaly. A binary star system, comprised of an A component (solid black orbit and black points) and a lower-mass B component (dotted pink orbit and pink points) is shown at four separate times corresponding to approximate start and end dates of Hipparcos (left pair) and Gaia DR2 (right pair). The center of mass (gray squares) moves from left to right over time, and the true proper motion of the system over the Hipparcos and Gaia timeframes is represented by the two gray arrows. Assuming that the A component dominates the light of the system, neither Hipparcos nor Gaia will measure this true motion because the center of light will move with component A as the stars orbit their barycenter. The black arrow at left thus shows the proper motion that would be measured by Hipparcos, and the black arrow at right shows the motion measured by Gaia DR2. The disagreement between these two independent measurements is termed *proper-motion anomaly* and provides evidence that the system has an unseen component. (For simplicity, we have removed parallactic motion by showing only those points at the same parallax factor, as depicted by the time stamps at the bottom of the figure.)

the equation

$$g = \frac{GM}{R^2}, \tag{11}$$

the mass can be computed from

$$M = \frac{c^2 v_{\rm gr}{}^2}{Gg}. \tag{12}$$

The surface gravity can be measured from the white dwarf's spectrum by comparing to model atmospheres. In practice, though, this method cannot be applied to single white dwarfs because the gravitational redshift is not separable from the radial velocity. If the star is part of a comoving multiple system or is a member of a young cluster or association, however, then the degeneracy between the radial velocity component and gravitational redshift component can be broken.

4.2. Single Objects

Researchers have employed several methods that are capable of measuring the masses of *individual* objects. These techniques—gravitational lensing, asteroseismology, and surface convection monitoring (aka *flickering*)—are described below.

4.2.1. Gravitational Lensing

Gravitational lensing occurs when a mass moves very close to the line of sight between an observer and a background object. The mass of the intervening object acts as a lens that alters the apparent position of the background source as seen by the observer (Gaudi 2012) and is potentially measurable for any object. The two temporarily generated images of the background source have a morphology that is azimuthally asymmetric, and this manifests itself observationally as a shift in the centroid. The astrometric shift of the photocenter is given by

$$\boldsymbol{\delta}(t) = \boldsymbol{u}(t)\frac{\theta_E}{u(t)^2 + 2} \tag{13}$$

where θ_E is the angular Einstein radius, which can be expressed as

$$\theta_E{}^2 = \frac{4GM_l}{c^2}(D_l{}^{-1} - D_s{}^{-1}) \quad (14)$$

(Walker 1995; Lu et al. 2016). Here, u and $\boldsymbol{u}$ represent the scalar and vector time-dependent lens-source separation in the plane of the sky normalized to θ_E, M_l is the mass of the lens, and D_l and D_s are the distances to the lens and source, respectively. When the distances to the lens and source are known, the monitoring of the astrometric shift as a function of time enables a measurement of the mass of the lens. These equations show that closer lenses produce larger astrometric signals, which makes this a valuable technique for measuring the masses of nearby objects, the main limitation being that such encounters of a lens and a background source happen only rarely, and very accurate astrometry is needed to predict such encounters a priori. This technique has so far been successfully applied to only two objects in the 20 pc sample (Sahu et al. 2017; Zurlo et al. 2018) but promises to become more valuable as more accurate Gaia parallaxes and proper motions become available for stars all across the Milky Way.

4.2.2. Asteroseismology

Asteroseismology is the study of oscillations in stellar atmospheres, and the characteristics of these oscillations can be used to deduce a star's physical parameters. Any star having a mechanism that can drive oscillations—such as surface convection, pulsations, tidal effects in a close binary, or opacity effects (the κ-mechanism)—can potentially have its mass measured. Equation (52) in Aerts (2021) can be rewritten to show that the stellar mass, M, can be determined from these oscillations using the relation

$$M \sim \frac{{\nu_{\max}}^3 {T_{\rm eff}}^{\frac{3}{2}}}{\Delta\nu^4}. \quad (15)$$

(In the absence of a definitive theoretical model for convection, the scaling of this relation is based on observations of the Sun, as described in Kjeldsen & Bedding 1995.) Here, $\Delta\nu$ is the large frequency separation, $\nu_{\max}$ is the frequency of maximum power, and $T_{\rm eff}$ is the effective temperature. The quantity ν can also be thought of as the inverse of twice the sound travel time between the stellar center and the stellar surface (Equation (39) of Aerts 2021). Figures 4 and 10 of Aerts (2021) graphically demonstrate how ν and $\nu_{\max}$ are measured in practice. The effective temperature, $T_{\rm eff}$, is obtained by comparing broad-wavelength spectroscopy of the star to model atmospheres.

4.2.3. Surface Convection Monitoring (Flickering)

The full asteroseismology treatment above requires high-quality data over a sufficient time baseline with which to resolve the individual oscillation modes. However, variations in surface convection alone require less exquisite data and can be used to measure the mass, if certain ancillary quantities have also been well measured (Stassun et al. 2018a). The needed quantity is $\nu_{\max}$ from above, which has been shown to depend on the star's gravity, g, and effective temperature, $T_{\rm eff}$, through the relation

$$g = \frac{\nu_{\max}\sqrt{T_{\rm eff}}}{C} \quad (16)$$

(Brown et al. 1991), where C is a normalization constant obtained by calibrating to stars with gravity measurements independently determined via asteroseismology (Kallinger et al. 2016). The effective temperature is, as above, obtained by comparing broad-wavelength spectroscopy to model atmospheres. The mass can then be measured via Equation (11), where the star's radius can be measured directly via interferometry or through the Stefan–Boltzmann law in Equation (5). The bolometric luminosity can be measured from the aforementioned broad-wavelength spectrum along with an accurate trigonometric parallax.

5. Multiples Lacking Sufficient Data for Mass Determination

There are some systems for which acceleration has been measured or whose astrometry indicates the presence of multiple components but for which insufficient data exist to compute the masses of the individual objects. Such systems are important to note because their mass accounting is still incomplete. This serves as an additional source of uncertainty in our mass function analysis.

5.1. Multiples Known Only through Limited Acceleration Data

Currently, there are many accelerating objects within the 20 pc census that lack the additional data needed for companion mass computations via Equation (9). We nonetheless still note these as binaries in Table 4, and we split out those cases here for individual discussion.

Khovritchev & Kulikova (2015) have identified likely accelerators by comparing the proper motion measured between the first and second Palomar Observatory Sky Surveys (POSS-I and POSS-II; Minkowski & Abell 1963; Reid et al. 1991; Lasker & STSCI Sky-Survey Team 1998) to a motion derived using first-epoch data from other sky surveys (2MASS, SDSS, WISE) and their own second-epoch follow-up astrometry. With these two independent measurements, they can compare a long-baseline motion over 50 yr to one derived more instantaneously, over only ∼10 yr. Brandt (2021) have similarly intercompared the near-instantaneous Hipparcos-measured proper motion from the early 1990s, the near-instantaneous Gaia-measured motion from the mid- to late-2010s, and a long-baseline motion constructed from the Hipparcos-to-Gaia baseline. Both sets of authors have identified objects with significant motion discrepancies and labeled these as likely binaries. These objects are noted in Table 4 using the column labeled "Accelerator?."

5.1.1. Accelerators from POSS versus Recent Motion Comparison

The Khovritchev & Kulikova (2015) list of ∼2400 objects covers only a portion of the northern sky ($30° < \text{decl.} < 70°$) for bright ($V < 17$ mag), high motion ($\mu > 300$ mas yr^{-1}) stars. Within 20 pc of the Sun, nine such accelerators are identified, only two of which—BD+66 34 and G 96-29 (Capella HL)—were already identified as known multiples in Table 4. The other seven are listed in Table 5.

Table 5
New 20 pc Accelerators from the Khovritchev & Kulikova (2015) Sample

J2000 R.A. and Decl. (1)	Name (2)	Sp. Type (3)
00 38 59.04+30 36 58.4	Wolf 1056	M2.5
00 57 02.69+45 05 09.8	G 172-30	M3
01 03 19.84+62 21 55.8	Wolf 47	M5 V
01 38 21.62+57 13 57.0	Ross 10	M2.5
06 01 11.05+59 35 49.9	G 192-13	M3.5 V
19 08 29.93+32 16 51.6	G 207-19	M3.5
23 07 29.92+68 40 05.2	G 241-45	M3

(This table is available in machine-readable form.)

We note that none of these seven objects is identified as a high-significance accelerator in the Brandt (2021) reference discussed in the following subsection. This is because the Brandt (2021) Hipparcos-to-Gaia accelerations could not be computed for these seven stars, as none are in the Hipparcos Catalog.[71] To further explore the underlying data for these Khovritchev & Kulikova (2015) accelerators, we have produced finder charts that show all seven in the POSS-I, POSS-II, 2MASS, and WISE images. A few of these appear to be blended with a background object at one of the POSS epochs. The most notably affected are G 172-30, which is blended at POSS-I with an object fainter by $\Delta G = 5.8$ mag; Wolf 47,[72] which is blended at POSS-I with an object fainter by $\Delta G = 6.4$ mag; and G 192-13, which is blended at POSS-II with an object fainter by $\Delta G = 6.2$ mag. (Ross 10 moves past a star of near-equal magnitude in all of the images, the possible blending being the worst at the POSS-II and 2MASS epochs.) This having been noted, whether or not objects with these magnitude differences could perturb the POSS measurements enough to affect the 50 yr proper-motion measurements is not clear. Future releases from a longer baseline Gaia data set should determine whether the accelerations seen for these seven objects are real.

5.1.2. Accelerators from Hipparcos versus Gaia Comparisons

The Brandt (2021) list of ∼115,000 objects covers the entire sky for objects in common to Hipparcos and Gaia eDR3 ($G \lesssim 11$ mag). This list also gives the computed χ^2 value between the two proper motions measured with the best precision, which is usually the Gaia-specific and Hipparcos-to-Gaia measurements. We conservatively set a false alarm rate of $Q = e^{-\chi^2/2} < 0.1\%$, corresponding to $\chi^2 > 13.8$, to select high-confidence accelerators for analysis here. Using this criterion produces ∼33,750 objects, of which 194 fall within the 20 pc census. These 194 are denoted in Table 4 with a "yes" in the "Accelerator?" column.

Kervella et al. (2022) have also produced a catalog of possible accelerators based on a comparison of the short-baseline Gaia-specific motions and the long-baseline Hipparcos-to-Gaia motions. As this list is based on the same underlying data as the list produced by Brandt (2021), many of the same accelerators are flagged by both teams. Under the assumption that the companion mass is much less than that of the primary and that the (circular) orbit is perpendicular to the line of sight, Kervella et al. (2022) have further used the proper-motion measures to estimate the mass of the hidden companion using the equation

$$m = \left(4740.470\frac{\Delta\mu}{\varpi}\right)\sqrt{\frac{rM}{G}}, \quad (17)$$

where m is the companion mass, M is the primary mass, G is the gravitational constant, r is the orbital radius, $\Delta\mu$ (the difference in motion measurements) is in units of milliarcseconds per year, and ϖ is in units of milliarcseconds. The constant of 4740.470 is used to convert $\Delta\mu/\varpi$ into units of meters per second (Kervella et al. 2019). Companion masses are estimated using estimated primary masses generally from isochrone fitting for the brightest stars or from an absolute K-band relation for the fainter stars, as described further in Kervella et al. (2022). Companion masses are dependent upon the unknown value of the separation between components, so Kervella et al. (2022) constructed estimates for assumed separations of 3, 5, 10, and 30 au. In Table 4, we include the extrema of these mass estimates in columns labeled "EstMassAt3AU" and "EstMassAt30AU" for all objects tagged as accelerators. (In a small number of cases, a Brandt 2021 accelerator was not deemed to be an accelerator by Kervella et al. 2022, so these estimates are not given.)

We divide the resulting list of 20 pc accelerators into three subgroups. The first, listed in Table 6, comprises eighty-three objects in known close binary and multiple systems. For all of these, the host star is known to have a close-in companion that Gaia eDR3 fails to detect or provide a full astrometric solution for, and these companions range in mass from the substellar regime into the planetary regime. For a host star at a distance of 10 pc, its Hipparcos-to-Gaia acceleration can be detected if the companion has a separation below a few ×100 au (Figure 12 from Kervella et al. 2022). Companions at this separation range can also be detected with high-resolution imaging techniques or via radial velocity monitoring, and some have independently measured masses. As one example, the companion in the 19.5 yr spectroscopic binary HD 10307 AB has a measured dynamical mass from Torres (2022) of $0.254 \pm 0.019\,M_\odot$, and that system has $a = 7.7$ au, $i = 100°$, and $e = 0.44$. The Kervella et al. (2022) companion mass estimates of $0.20\,M_\odot$ at 3 au and $0.63\,M_\odot$ at 30 au bracket the dynamically measured values well, as the assumptions used were reasonable for this system. As another example, the companion to the 1.35 yr spectroscopic binary HD 184467 AB has a measured dynamical mass of $0.868 \pm 0.025\,M_\odot$ (Piccotti et al. 2020), and the system has $a = 0.7$ au, $i = 145°$, and $e = 0.34$ (Arenou et al. 2000). The Kervella et al. (2022) companion mass estimate of $0.03\,M_\odot$ at 3 au compares unfavorably to the measured value possibly because of the Kervella et al. (2022) assumption that the secondary mass is much less than that of the primary. This demonstrates that, although the Kervella et al. (2022) companion mass estimates listed in Table 6 provide a guide as to whether the companion causing the acceleration is already known or is a still hidden member, additional astrometric data are needed before the masses can be reliably measured. As can be seen from the full entries in Table 4, many objects in Table 6 are triples, so it is also unclear *how many* objects are contributing to the measured acceleration.

[71] Ross 10 has a Hipparcos designation in SIMBAD (HIP 7635) but does not appear in van Leeuwen (2007).
[72] The primary in this system, BD+61 195, is 295″ away from Wolf 47 itself and would not be responsible for any acceleration.

Table 6
20 pc Accelerators in Known Close Binary/Multiple Systems

J2000 R.A. and Decl.	Name	Sp. Type	χ^2	M_{est} @ 3 au ($M_\odot$)	M_{est} @ 30 au ($M_\odot$)	Note
(1)	(2)	(3)	(4)	(5)	(6)	(7)
00 49 26.76−23 12 44.9	HD 4747 AB	G9 V	12980	0.0338	0.1532	⋯
00 50 33.25+24 49 00.2	FT Psc AB	M3 V kee[a]	768.3	null	null	⋯
00 58 27.94−27 51 25.4	CD−28 302 AB	M3 V	24.25	0.0078	0.0772	⋯
01 41 47.13+42 36 48.2	HD 10307 AB	G1 V	2540	0.1971	0.6338	⋯
01 55 57.46−51 36 32.0	χ Eri AB	G9 IV	569.3	0.0970	0.1717	⋯
02 05 04.88−17 36 52.7	BD−18 359 AB	M3	6920	0.0925	0.6897	⋯
02 10 25.92−50 49 25.5	HD 13445 AB	K1 V	78930	0.0957	0.4335	1 known exoplanet
02 19 10.08−36 46 41.2	L 440-30 AB	M2.5+V	90.10	0.0034	0.0273	⋯
02 36 04.90+06 53 12.4	HD 16160 AB	K3 V	6078	0.0942	0.4769	⋯
02 45 06.20−18 34 21.4	τ^1 Eri AB	F6 V	4366	0.1935	0.5594	⋯
02 46 17.28+11 46 30.9	HD 17230 AB	K6 V	60.88	0.0022	0.0125	⋯
03 01 51.39−16 35 36.0	BD−17 588 ABC	M2.5 V	215.2	0.0147	0.1728	2 known exoplanets
03 48 01.70+68 40 38.8	G 221-24 AB	K6 V + M2 V	1011	0.1764	1.2275	⋯
05 08 35.04−18 10 19.4	L 737-9 AB	M3.5 V	41.46	0.0024	0.0169	⋯
05 19 12.66−03 04 25.7	HD 34673 AB	K3 V	2500	0.0128	0.0739	⋯
05 22 37.48+02 36 11.6	HD 35112 AB	K2.5 V	192800	0.0806	1.0007	⋯
05 28 44.87−65 26 55.2	AB Dor ACaCb	K2 V k	1173	0.1355	0.6137	⋯
05 32 14.66+09 49 14.9	Ross 42 AB	M4	17.34	0.0010	0.0079	⋯
05 54 22.96+20 16 34.5	χ^1 Ori AB	G0 V CH-0.3	430.1	0.0578	0.2097	⋯
06 10 34.61−21 51 52.7	Gl 229 AB	M1 V	13040	0.0078	0.0544	2 known exoplanets
06 17 16.13+05 05 59.9	HD 43587 AaAb	G0 V	22570	0.2482	0.7983	⋯
06 26 10.25+18 45 24.8	HD 45088 AaAb	K3 V k	19680	0.0712	0.3606	⋯
06 36 18.29−40 00 23.6	CD−39 2700 AB	K8 V k	14140	0.2114	1.4834	⋯
07 16 19.77+27 08 33.1	G 109-55 AB	M2.5 V	243.4	0.0240	0.1787	⋯
07 19 31.27+32 49 48.3	BD+33 1505 AB	M0 V	1301	0.0174	0.1160	⋯
07 20 07.37+21 58 56.3	δ Gem AaAb	F2 V kF0mF0	36.94	0.0322	0.0612	⋯
07 28 51.36−30 14 49.3	CD−29 4446 AB	M2	1377	0.1433	0.8673	⋯
07 36 07.07−03 06 38.7	BD−02 2198 AB	M1 V	18520	0.1057	0.7205	⋯
08 31 37.57+19 23 39.4	CU Cnc AaAbAc	M4	2767	0.0466	0.3328	⋯
08 36 25.47+67 17 41.8	BD+67 552 AB	M0.5	9935	0.1336	0.8255	⋯
08 39 07.90−22 39 42.8	HD 73752 AaAbB	G5 IV	2804	0.2452	0.8217	⋯
08 42 44.53+09 33 24.1	BD+10 1857 AaAb	M0	186.0	0.3145	1.9750	⋯
08 57 04.68+11 38 48.8	BD+12 1944 AB	M1.5	25170	0.0973	0.6882	⋯
09 14 53.65+04 26 34.2	HD 79555 AB	K3+V	22350	0.1772	1.0191	also in Table 9
09 29 08.93−02 46 08.2	τ^1 Hya AaAb	F5.5 IV-V	2351	0.3076	0.7993	⋯
09 32 51.43+51 40 38.3	θ UMa AB	F5.5 IV-V	518.5	0.0727	0.1540	⋯
09 35 39.50+35 48 36.5	11 LMi AaAb	G8+V	496.1	0.0091	0.0364	⋯
09 45 40.07−39 02 26.5	L 462-119 AB	M2.5 V	1697	0.1046	0.8348	⋯
09 53 11.78−03 41 24.4	BD−02 3000 AB	M2	80.34	0.0052	0.0351	⋯
11 11 33.15−14 59 28.9	HD 97233 AB	K5 V (k)	471.7	0.1108	0.7535	⋯
11 21 26.67−20 27 14.0	HD 98712 A	K6 V ke	6618	0.1439	0.8376	⋯
12 00 44.46−10 26 46.1	HD 104304 AB	G8 IV	57500	0.2325	0.8631	⋯
12 23 33.20+67 11 18.5	G 237-64 AB	M2.5	1767	null	null	⋯
12 28 57.59+08 25 31.1	Wolf 414 AB	M3.5 V + M5 V	2059	0.1223	1.0562	⋯
12 44 14.55+51 45 33.4	HD 110833 AaAbB	K3	95.44	0.0307	0.1438	⋯
13 00 46.56+12 22 32.7	BD+13 2618 AB	M1.5	3393	0.0530	0.3667	1 known exoplanet
13 19 33.59+35 06 36.6	BD+35 2436 AaAb	M1	79.89	0.0151	0.0948	⋯
13 47 15.74+17 27 24.8	τ Boo AB	F7 IV-V	7745	0.1133	0.2944	1 known exoplanet
13 52 35.85−50 55 18.1	HD 120780 AaAb	K2 V	479.5	0.0332	0.1594	⋯
14 03 32.34+10 47 12.3	HD 122742 AB	G6 V	640.6	0.0597	0.2446	⋯
14 54 29.24+16 06 03.8	BD+16 2708 ABaBb	M3 V	2764	0.0089	0.0654	⋯
15 41 16.57+75 59 34.0	Ross 1057 AB	M3.5	1780	0.0576	0.6208	⋯
15 44 01.82+02 30 54.6	ψ Ser ABaBb	G5 V	4965	null	null	⋯
16 05 40.48−20 27 00.1	HD 144253 AB	K3 V	189.3	0.0439	0.2222	⋯
16 28 28.14−70 05 03.8	ζ TrA AaAb	F9 V	47.58	0.0110	0.0369	⋯
17 09 31.54+43 40 52.8	G 203-47 AB	M3.5 V + wd	51.01	0.0072	0.0830	⋯
17 19 03.84−46 38 10.4	41 Ara A	G9 V	832.7	0.0160	0.0689	⋯
17 30 11.20−51 38 13.1	CD−51 10924 AB	M0 V	270.2	0.0044	0.0274	4 known exoplanets
17 34 59.62+61 52 28.2	26 Dra AB	G0 IV-V	11960	0.3382	1.1333	⋯
17 46 14.42−32 06 08.4	CD−32 13298 AaAb	M3 V	27.02	0.0080	0.0597	⋯
17 46 27.55+27 43 14.6	μ^1 Her AaAb	G5 IV	12600	0.1266	0.4130	⋯
18 07 01.59+30 33 43.6	b Her AB	F9 V	66470	0.0973	1.0649	⋯

Table 6
(Continued)

J2000 R.A. and Decl.	Name	Sp. Type	χ^2	M_{est} @ 3 au ($M_\odot$)	M_{est} @ 30 au ($M_\odot$)	Note
(1)	(2)	(3)	(4)	(5)	(6)	(7)
18 10 26.15−62 00 08.0	ι Pav AB	G0 V	192.8	0.0356	0.1192	⋯
18 57 01.64+32 54 04.7	HD 176051 AB	F9 V	38160	null	null	⋯
19 23 34.01+33 13 19.1	HD 182488 AB	G9+V	1700	0.0085	0.0349	⋯
19 31 07.97+58 35 09.6	HD 184467 AB	K2 V	27.50	0.0314	0.1422	⋯
19 54 17.74−23 56 27.9	HD 188088 AaAb	K2 IV (k)	15.46	0.0011	0.0050	⋯
20 04 06.22+17 04 12.7	15 Sge AB	G0 V	31560	0.0890	0.3162	⋯
20 05 09.78+38 28 42.6	HD 190771 AB	G2 V	12760	0.0639	0.2319	⋯
20 10 19.57−20 29 36.4	HD 191391 AB	K6 V k	38130	0.0819	0.4895	⋯
20 44 21.95+19 44 58.7	HD 352860 AB	M0.5 V	1583	0.1875	1.2533	⋯
20 56 48.54−04 50 49.1	Ross 193 AaAb	M3	72.54	0.0050	0.0395	⋯
21 00 05.39+40 04 12.7	BD+40 883 AaAbB	M2	46070	0.1350	0.8783	⋯
21 19 45.63−26 21 10.4	HD 202940 AaAbB	G7 V	600.4	0.0172	0.1989	⋯
21 49 05.76−72 06 09.1	CD−72 1700 AB	M1	19020	null	null	⋯
22 07 00.67+25 20 42.4	ι Peg AaAb	F5 V	66.25	0.0205	0.0533	⋯
22 18 15.61−53 37 37.5	HD 211415 AB	G0 V	612.3	0.0132	0.0478	⋯
22 36 09.69−00 50 29.8	HD 214100 AB	M1 V	27200	0.0672	0.4472	⋯
22 38 45.57−20 37 16.1	FK Aqr AaAb	M2	47.50	0.0014	0.0091	⋯
23 01 51.54−03 50 55.4	HD 217580 AB	K2.5 V	232.6	0.0591	0.2966	⋯
23 39 20.91+77 37 56.5	γ Cep AB	K1 III	4771	0.2376	0.4206	1 known exoplanet
23 52 25.41+75 32 40.4	HD 223778 AaAbB	K3 V	124300	0.1261	0.5909	⋯
23 55 39.78−06 08 33.4	BD−06 6318 AB	M2.5 V k	2137	0.0497	0.3530	⋯

Note.
[a] Some optical spectral types for late-K and M dwarfs include information about chromospheric activity. An "e" generally indicates that Hα emission is present. Other values include "(k)" for slight emission reversals or infilling of the Ca II H and K lines, "k" for emission reversals in Ca II H and K that do not rise to the level of the local continuum, "ke" for such emission that rises above the local continuum level, and "kee" for strong emission in Ca II H and K along with Hβ and possibly Hγ and Hδ (Gray et al. 2003). Because chromospheric activity is variable, these emission-line classification suffixes pertain only to the epoch of spectroscopic observation.

(This table is available in machine-readable form.)

The second list, shown in Table 7, gives fourteen objects known to host exoplanets but lacking any *close* stellar or substellar companions. Here, we define *close* to mean within ∼50 au. Six of these objects, as listed in the final column of the table, have more widely separated stellar companions at apparent separations of $\gtrsim$70 au. The Kervella et al. (2022) mass estimates for all fourteen of these objects are quite low and, for assumed separations of a few astronomical units, correspond to masses traditionally thought of as being in the planetary range. Thus, the accelerations for these objects are likely caused by the known exoplanet(s) in the system. Kervella et al. (2022) provides an additional analysis on the stars ϵ Eri, Kapteyn's Star, ϵ Ind A, and π Men, while noting that Kapteyn's Star has no significant proper-motion anomaly as measured by them.

The final list, shown in Table 8, has 97 objects whose closest known companions are resolved by Gaia eDR3 or have no known companions at all. For many of these, the nearest known companion falls close enough to the accelerator star ($\lesssim$100 au; Figure 12 of Kervella et al. 2022) that it may be the object causing the acceleration. Examples are CD−44 3045 A, VV Lyn Aa, CD−36 6589 A, Ross 52 A, BD+45 2247 A, and Wolf 1225 A. Objects for which the nearest known companion lies beyond this separation or for which no companions are currently known are the hosts most likely to harbor new additions to the 20 pc census. Examples of stars with likely hidden companions are G 32-7, CD−22 526, HD 13579, LP 837-53, HD 43162 A, HD 52698, G 250-34, BD −17 3088, μ Vir, β TrA, and θ Cyg.

Tables 6–8 highlight that the accounting of all components within the 20 pc census is still incomplete, as there is overwhelming evidence of additional, tightly separated companions. As only <200 of the ∼3000 Gaia-detected primaries show such evidence, it is tempting to conclude that our tally of higher-mass (nonexoplanet) companions is nearing completion. We caution, however, that our criteria for selecting accelerators was set very conservatively and that many real accelerators likely exist with a measured significance below our cutoff value. As the time baseline of Gaia observations is extended, accelerations will be increasingly sensitive to longer-period companions that, for higher (nonexoplanet) masses, are potentially verifiable with direct imaging techniques. Furthermore, Gaia observations over this same extended time baseline will remove the need to compare to the shallower Hipparcos data, enabling acceleration data for lower-mass primaries between the Hipparcos and Gaia limits ($11 \lesssim G \lesssim 21$ mag). Finally, less than a third of all systems in the 20 pc census of Table 4 have both a Hipparcos entry and a Gaia DR3 astrometric solution, so many objects within our sample volume are unavailable for similar acceleration analysis.

5.2. Multiples with Large RUWE Values

The Gaia renormalized unit weight error (RUWE) is a measure of the goodness of fit of the single-star astrometric model to the observed astrometry and is expected to be ∼1.0 if the fit is a good representation (Lindegren et al. 2021). This parameter is pulled from Gaia DR3 and is listed in the "RUWE" column of Table 4. Values significantly higher than

Table 7
20 pc Accelerators Whose Only Close Companions Are Known Exoplanets

J2000 R.A. and Decl.	Name	Sp. Type	χ^2	M_{est} @ 3 au ($M_\odot$)	M_{est} @ 30 au ($M_\odot$)	No. of Known Exoplanets	Distance to Stellar Companion (au)
(1)	(2)	(3)	(4)	(5)	(6)	(7)	(8)
00 16 12.68−79 51 04.2	HD 1237 A	G8.5 V (k)	26.86	0.0019	0.0080	1	70
00 18 22.88+44 01 22.6	GX And	M1.5 V	2456	0.0013	0.0114	2	122
03 32 55.84−09 27 29.7	ϵ Eri	K2 V (k)	33.89	0.0013	0.0062	1	…
04 52 05.73+06 28 35.6	Wolf 1539	M3.5	35.10	0.0014	0.0137	1	…
05 11 40.59−45 01 06.4	Kapteyn's Star	sdM1 p	29.58	0.0001	0.0007	1	…
05 37 09.89−80 28 08.8	π Men	G0 V	60.98	0.0073	0.0244	3	…
07 54 10.88−25 18 11.4	CD−24 6144	M0	18.89	0.0007	0.0043	2	7110
09 14 24.68+52 41 10.9	HD 79211	K7 V	27.48	0.0059	0.0401	1	108
10 08 43.14+34 14 32.1	HD 87883	K2.5 V	713.6	0.0087	0.0408	1	…
16 10 24.32+43 49 03.5	14 Her	K0 IV-V	1009	0.0126	0.0502	2	…
16 12 41.78−18 52 31.8	LP 804-27	M3 V	331.0	0.0076	0.0562	1	…
20 03 37.41+29 53 48.5	HD 190360	G7 IV-V	14.83	0.0016	0.0054	2	2847
21 33 33.98−49 00 32.4	HD 204961	M2	278.3	0.0008	0.0062	2	…
22 03 21.65−56 47 09.5	ϵ Ind A	K4 V (k)	287.5	0.0030	0.0157	1	1464

(This table is available in machine-readable form.)

Table 8
20 pc Accelerators with More Distant (or No Known) Companions

J2000 R.A. and Decl.	Name	Sp. Type	χ^2	M_{est} @ 3 au ($M_\odot$)	M_{est} @ 30 au ($M_\odot$)	No. of Components in System	Dist. to Next Nearest Known Member (au)	Note
(1)	(2)	(3)	(4)	(5)	(6)	(7)	(8)	(9)
00 05 41.02+45 48 43.6	HD 38 A	K6 V	6209	0.0219	0.1406	2	70	…
00 16 14.63+19 51 37.5	G 32-7	M4	14.42	0.0082	0.0677	3	387	…
00 45 48.29−41 54 33.1	HD 4378 A	K5	64.43	0.0021	0.0120	2	75	…
00 49 06.29+57 48 54.6	η Cas A	F9 V	659.4	0.0220	0.0780	2	79	…
00 49 09.90+05 23 19.0	Wolf 28	DZ7.4	1621	0.0007	0.0044	1	…	…
01 03 14.15+20 05 52.3	G 33-35 A	M1.5	28.44	0.0040	0.0300	2	40	…
01 32 26.20−21 54 18.4	CD−22 526	M1.5 V (k)	151.0	0.0039	0.0284	1	…	…
01 39 47.56−56 11 47.2	p Eri B	K2 V	1077	0.0184	0.0864	2	94	…
02 15 42.55+67 40 20.3	HD 13579	K2	58.54	0.0041	0.0184	2	736	…
02 37 52.79−58 45 11.1	L 174-28	M3 V	14.88	0.0010	0.0111	1	…	…
03 12 04.53−28 59 15.4	α For A	F6 V	2451	0.0692	0.1861	3	75	…
03 16 13.83+58 10 02.5	Ross 370 A	M2	130.2	0.0058	0.0441	2	69	…
03 23 35.26−40 04 35.0	HD 21175 A	K1 V	69,960	0.0950	0.4497	2	46	…
03 48 01.03+68 40 22.4	HD 23189	K2 V	41.23	0.0036	0.0222	3	303	…
03 57 28.70−01 09 34.1	HD 24916 A	K4 V	62.16	null	null	3	168	…
04 31 11.51+58 58 37.5	G 175-34	M4.5 V	208.4	0.0018	0.0203	2	57	…
04 53 31.20−55 51 37.1	CD−56 1032 A	M3 V	117.4	0.0032	0.0265	2	83	…
05 03 23.90+53 07 42.5	BD+52 911 A	M0.5	82.34	0.0023	0.0167	2	78	…
05 45 48.28+62 14 12.4	BD+62 780	M0	94.82	0.0013	0.0078	1	…	…
05 55 43.21−26 51 23.4	LP 837-53	M2.5 V	21.48	0.0010	0.0070	1	…	…
06 13 45.30−23 51 43.0	HD 43162 A	G6.5 V	16.04	0.0013	0.0053	4	408	…
06 33 43.28−75 37 48.0	L 32-9	M3	25.61	0.0013	0.0106	2	192	…
06 37 11.23−50 02 17.7	CD−49 2340 A	K8 V (k)	7109	0.0262	0.1645	2	35	…
06 57 46.63−44 17 28.2	CD−44 3045 B	M3	21,590	0.0283	0.2796	2	19	…
07 01 13.73−25 56 55.5	HD 52698	K1 V (k)	734.1	0.0491	0.2224	1	…	Also in Table 9
07 07 50.42+67 12 04.9	G 250-34[a]	M1.5	16,320	0.1070	0.7770	1	…	…
07 31 57.71+36 13 10.1	VV Lyn Aa	M3	48,470	0.0862	0.6179	3	19	…
07 57 57.78−00 48 51.9	HD 65277 A	K3+V	645.3	0.0081	0.0409	2	95	…
08 08 13.19+21 06 18.2	BD+21 1764 A	K7 V	140.8	0.0058	0.0359	4	190	…
08 50 42.30+07 51 52.5	BD+08 2131 A	K5 V	206.6	null	null	2	21	…
09 01 17.48+15 15 56.8	HD 77175 A	K5	210.8	0.0062	0.0361	2	93	…
09 06 45.35−08 48 24.6	BD−08 2582	M0	143.1	0.0007	0.0042	2	123	…
09 14 22.77+52 41 11.8	HD 79210	M0 V	178.2	0.0053	0.0344	2	108	…
09 43 55.61+26 58 08.4	Ross 93	M3.5	23.32	0.0023	0.0211	1	…	…
10 12 08.15−18 37 04.1	BD−17 3088	M0	267.3	0.0561	0.3563	2	7225	…
10 31 24.22+45 31 33.8	BD+46 1635 A	K7 V	111.8	0.0026	0.0151	2	74	…
10 41 09.30−36 53 43.7	CD−36 6589 A	M0.5 V	101,600	0.1453	0.9567	2	13	…
10 41 51.83−36 38 00.1	CD−35 6662	M0 V (k)	31.36	0.0045	0.0306	2	305	…
11 05 28.58+43 31 36.3	BD+44 2051 A	M1 V	25.09	0.0004	0.0040	2	156	…
11 11 19.48+43 25 02.4	G 122-2 A	M2.5 V	140.0	0.0178	0.1259	2	60	…
11 15 11.90+73 28 30.7	HD 97584 A	K3	47.01	0.0014	0.0072	2	94	…
11 34 29.49−32 49 52.8	20 Crt A	K0- V	257.4	0.0039	0.0175	2	146	…
11 45 34.44−20 21 12.4	LP 793-33	M2.5 V	618.2	0.0245	0.1946	2	295	…
11 45 42.92−64 50 29.5	LAWD 37	DQ6.4	37.90	0.0006	0.0040	1	…	…
12 08 24.82−24 43 44.0	α Crv A	F1 V	34.53	0.0166	0.0431	2	47	…

Table 8
(Continued)

J2000 R.A. and Decl.	Name	Sp. Type	χ^2	M_{est} @ 3 au ($M_\odot$)	M_{est} @ 30 au ($M_\odot$)	No. of Components in System	Dist. to Next Nearest Known Member (au)	Note
(1)	(2)	(3)	(4)	(5)	(6)	(7)	(8)	(9)
12 23 00.16+64 01 51.0	Ross 690	M3	125.9	0.0039	0.0288	1	…	…
12 41 06.49+15 22 36.0	HD 110315 A	K4.5 V	21830	0.0394	0.2098	2	32	…
12 41 39.63−01 26 57.9	γ Vir A	F2 V	551.7	0.1854	0.4774	2	28	…
13 02 20.69−26 47 13.6	HD 113194	K5 V (k)	82.76	0.0092	0.0528	1	…	Also in Table 9
13 06 15.40+20 43 45.3	BD+21 2486 A	K7	4329	0.0282	0.1623	3	31	…
13 14 15.14−59 06 11.7	HD 114837 A	F6 V Fe-0.4	76.39	0.0117	0.0327	2	84	…
13 16 51.05+17 01 01.8	HD 115404 A	K2.5 V (k)	2205	0.0089	0.0588	2	85	…
13 20 58.05+34 16 44.2	BD+35 2439	M1.5	199.1	0.0042	0.0301	1	…	…
13 23 32.78+29 14 15.0	HD 116495 A	M0 V	213.5	0.0072	0.0414	2	30	…
13 28 21.08−02 21 37.1	Ross 486 A	M3 V	20.64	0.0015	0.0118	2	112	…
13 32 44.60+16 48 39.1	G 63-36 A	M2.5 V	51.28	0.0258	0.1893	2	45	…
13 47 42.16−32 25 48.1	HD 120036 A	K6.5 V (k)	173.5	0.0071	0.0431	2	135	…
13 49 04.00+26 58 47.8	HD 120476 A	K3.5 V	63,800	0.0441	0.3214	2	39	…
13 55 02.56−29 05 25.9	HD 121271 A	M0 V k	172,300	0.0536	0.3033	2	38	…
14 19 00.90−25 48 55.5	HD 125276 A	F9 V Fe-1.5 CH-0.7	904.8	0.0170	0.0616	2	64	…
14 42 21.58+66 03 20.8	G 239-25 A	M2	62.92	0.0056	0.0497	2	25	…
14 43 03.62−05 39 29.5	μ Vir	F2 V	23.50	0.0384	0.0746	2	793	…
14 51 23.39+19 06 01.6	ξ Boo A	G7 V	11,500	0.0689	0.2820	2	38	…
14 53 51.40+23 33 21.0	Ross 52 A	M3 V	6509	0.1125	0.9852	2	10	…
14 57 28.00−21 24 55.7	HD 131977	K4 V	354.6	0.0046	0.0239	4	145	…
15 00 55.57+45 25 34.6	BD+45 2247 A	M0.5	80,070	0.0951	0.6269	2	23	…
15 47 29.10−37 54 58.7	HD 140901 A	G7 IV-V	18.43	0.0023	0.0085	2	220	…
15 55 08.56−63 25 50.6	β TrA	F1 V	31.48	0.0163	0.0295	1	…	…
16 16 45.31+67 15 22.5	EW Dra	M3	15.22	0.0007	0.0052	2	695	…
16 20 03.51−37 31 44.4	CD−37 10765 A	M2 V	2809	0.0074	0.0656	2	36	…
16 28 52.66+18 24 50.6	HD 148653 A	K2 V	2069	0.0163	0.0827	2	46	…
16 55 25.22−08 19 21.3	Wolf 629	M3.5 V	15.84	0.0005	0.0059	5	469	…
16 55 38.01−32 04 03.7	HD 152606	K8 V k	1687	0.0142	0.0874	1	…	…
16 56 48.57−39 05 38.2	CD−38 11343 A	M3	550.3	0.0184	0.1312	3	49	…
16 57 53.18+47 22 00.1	HD 153557 A	K3 V	875.6	0.0102	0.0514	3	91	…
17 15 20.98−26 36 10.2	36 Oph B	K0 V	29.24	0.0017	0.0078	3	30	…
17 21 00.37−21 06 46.6	ξ Oph A	F2 V	82.92	0.0248	0.0646	2	71	…
17 35 13.62−48 40 51.1	CD−48 11837 A	M1.5 V	8601	0.0174	0.1332	2	45	…
17 46 34.23−57 19 08.6	L 205-128	M4	37.12	0.0001	0.0012	1	…	…
17 57 48.50+04 41 36.1	Barnard's Star	M4 V	74.89	0.0000	0.0005	1	…	…
18 42 46.70+59 37 49.4	HD 173739	M3 V	723.0	0.0020	0.0209	2	41	…
18 42 46.89+59 37 36.7	HD 173740	M3.5 V	91.38	0.0026	0.0309	2	41	…
18 57 30.59−55 59 30.8	HD 175224 A	M1	412.4	0.0066	0.0378	2	33	…
19 36 26.53+50 13 16.0	θ Cyg	F3+V	103.1	0.0277	0.0648	2	2150	Other component in Table 9
19 45 49.75+32 23 13.7	G 125-30	M1.5	25.44	0.0044	0.0353	1	…	…
19 46 23.93+32 01 01.4	HD 331161 A	M0.5 V	420.0	0.0068	0.0472	2	79	…
20 02 34.16+15 35 31.5	HD 190067 A	K0 V Fe-0.9	679.7	0.0071	0.0322	2	62	…
20 41 51.13−32 26 06.7	AT Mic A	M4.5 V	20,360	0.0891	0.5735	3	21	…

Table 8
(Continued)

J2000 R.A. and Decl.	Name	Sp. Type	χ^2	$M_{\rm est}$ @ 3 au ($M_\odot$)	$M_{\rm est}$ @ 30 au ($M_\odot$)	No. of Components in System	Dist. to Next Nearest Known Member (au)	Note
(1)	(2)	(3)	(4)	(5)	(6)	(7)	(8)	(9)
21 02 40.75+45 53 05.2	HD 200560 A	K2.5 V	6003	0.0230	0.1106	2	52	…
21 06 53.94+38 44 57.9	61 Cyg A	K5 V	317.4	0.0068	0.0386	2	111	…
21 06 55.26+38 44 31.4	61 Cyg B	K7 V	16,640	0.0070	0.0431	2	111	…
21 07 10.38−13 55 22.5	HD 200968 A	G9.5 V (k)	4553	0.0180	0.0816	2	64	…
21 38 00.39+27 43 25.4	BD+27 4120 A	M0.5+V	359.2	0.0266	0.1860	2	44	…
22 14 31.41+27 51 18.7	G 188-49 A	K7.5	20.55	0.0023	0.0157	2	59	…
22 23 29.13+32 27 33.9	Wolf 1225 A	M3.5	5174	0.1158	0.7867	2	19	…
23 31 52.17+19 56 14.1	BD+19 5116 A	M3.5 V	17,570	0.0172	0.1549	2	34	…
23 39 37.39−72 43 19.8	HD 222237	K3+V	700.6	0.0046	0.0231	1	…	…

Note.
[a] A single epoch of Keck/NIRC2 data is available in the Keck Observatory Archive for this object. The K_s- and H-band observations taken on 2021 January 22 (UT; PI: Crepp; program ID: D313) show an object $0\farcs22$ from G 250-34 at a position angle of 328° and $\Delta K_s = 2.9$ mag. No other high-resolution observations were found in other archives to help confirm or refute this possible companion.

(This table is available in machine-readable form.)

unity can indicate either that the object is an unresolved, physical multiple (Penoyre et al. 2020) or that some other effect is causing the photocenter to deviate from expectations. Two examples of the latter are a chance alignment with a marginally resolved background star or single-star variability that confounds the RUWE renormalization itself (Belokurov et al. 2020). The typically quoted value for selecting likely binaries using this statistic is RUWE $>$ 1.4 (e.g., Fabricius et al. 2021), although Stassun & Torres (2021) have shown that values of 1.0 $<$ RUWE $<$ 1.4 are also highly predictive of unresolved multiplicity. While the RUWE normalization works well across the full population of Gaia-measured stars, Penoyre et al. (2022b) note that it does a somewhat less adequate job when a selection of nearby (d $<$ 100 pc; the GCNS of Gaia Collaboration et al. 2021a) stars alone is analyzed. For that reason, they define a new statistic, which they term the local unit weighted error (LUWE), that improves upon RUWE for these nearer objects.

Values of RUWE and LUWE change with each subsequent release of Gaia data, and there is valuable information contained within the differences. Later Gaia releases have data (and astrometric solutions) covering a longer timespan, so for unresolved multiple systems with periods roughly equal to or longer than the timespans of the data release, the RUWE (or LUWE) values may continue to run high or even become larger between Gaia DR2 and Gaia eDR3 simply because the photocentric displacement caused by orbital motion in an unresolved binary makes the single-object astrometric solution fit less well with an extended data set. (See Penoyre et al. 2022a for additional discussion.) Conversely, unresolved binaries with shorter periods should improve and eventually get full astrometric solutions in the Gaia non-single-star lists.

With these observations in mind, Penoyre et al. (2022b) devised a two-part criterion to select the most likely hidden multiples in the 100 pc sample: (1) $\mathrm{LUWE_{eDR3}} > 2$ and (2) $\Delta\mathrm{LUWE} \equiv \mathrm{LUWE_{eDR3}} - \mathrm{LUWE_{DR2}} > -\mathrm{LUWE_{eDR3}}/3$. Within our 20 pc census, 104 objects meet these criteria, and these are the ones labeled with a "yes" in the Table 4 column named "LUWE_binary?." Of these, 73 are known from previous literature to be binary and were already labeled as such in our census. The other 31, listed in Table 9, are newly identified multiples. Nine of these are part of higher-order multiples, as indicated by the notes in the table. For eight of these systems, Gaia has detections of both the new high-LUWE object and the other component (sometimes a double itself) with which it has physical companionship. The ninth system, however, is a new triple system for which Gaia detects only the new high-LUWE binary G 43-23 but not the common-proper-motion T dwarf companion, WISEU J100241.49+145914.9, discussed in Section 2.2. Note that the LUWE criteria from Penoyre et al. (2022b) are meant to be conservative, so other hidden binaries will exist with LUWE or ΔLUWE values outside of the bounds noted above.

5.3. Multiplicity (and Oddities) Identified through Color–Magnitude Diagrams

In Figures 4–9, we show several color-type, color–color, and color–magnitude diagrams as a final method for identifying unresolved binaries. These diagrams also illustrate the rich diversity of colors and absolute magnitudes that objects within the 20 pc census possess.

Each plot shows photometry only for those objects believed to be single components ("#CompsOnThisRow" = 1 in Table 4) and whose photometry is uncontaminated ("2MASS_contam?" and/or "WISE_contam?" not equal to "yes" in Table 4). Each object is color coded by its spectral type, as shown by the color bar in each figure.[73] Preference is given to the near-infrared spectral type if listed; otherwise, the optical spectral type is used. (It should be noted that, for stars of type A through M, near-infrared classifications are given in Table 4 only when no optical type is available, so this criterion is only relevant for the L, T, and Y dwarfs.) Each object is plotted as a solid black dot, the center of which is colored if the spectral type is known; that is, objects lacking a spectral type appear only as black dots. Furthermore, for plots that involve J or K bands, preference is given to MKO magnitudes; otherwise, 2MASS magnitudes are used.

In Figure 4, only those objects with absolute magnitude uncertainties below 1.0 mag are shown, to keep the plots more legible. In Figure 5, objects are shown only if their uncertainties in M_G are below 1.0 mag and their color uncertainties are below 0.5 mag. In Figure 6 (or 7), objects are shown only if their absolute magnitude uncertainties are below 1.0 mag and their $J-\mathrm{W2}$ (or $H-\mathrm{W2}$) uncertainties are also below 1.0 mag. In Figure 8, objects are shown only if the color uncertainty is less than 0.5 mag for Gaia-based color plots or less than 1.0 mag for all other colors. In Figure 9, points are shown only if their color uncertainties are generally less than 0.10–0.20 mag.

We have examined each of these diagrams in detail and have identified objects that fall significantly far from the common loci of main-sequence stars or white dwarfs to warrant special attention. There are several classes of objects, however, that we do not discuss in this section but address elsewhere: (1) Stars with bright magnitudes may be problematic and have quoted uncertainties insufficiently small to capture these problems. Given that these bright stars are generally well characterized already, we concentrate only on those not believed to be main-sequence stars (category (4) below). (2) L, T, and Y dwarfs have already been examined in detail via color-type, color–magnitude, and color–color diagrams in Kirkpatrick et al. (2021a). (3) Subgiant, giant, and bright giant stars are discussed in Section 6.1.2. (4) Low-metallicity (subdwarf) stars are discussed in Section 6.2.2. (5) Young objects are discussed in Section 6.2.1.

We begin with objects whose placement on these diagrams could potentially highlight a problem with their measured parallaxes. These are all objects that the Gaia survey is placing within the 20 pc volume for the first time. With the exception of the object at $11^{\mathrm{h}}59^{\mathrm{m}} - 36°34'$, all of these objects have higher than normal Gaia parallax uncertainties as compared to objects of similar G magnitude. We discuss each of these individually below:

1. *Gaia EDR3 4966072879648455296 (0229−3606).* This object, whose spectral type has yet to be determined but whose Gaia eDR3/DR3 parallax is 50.66 ± 0.61 mas, falls near or just above the main sequence on most color–magnitude diagrams. Its apparent magnitudes are similar to 20 pc objects of the same color, so there is no reason to question its inclusion in our census. Its location on color–

[73] This color palette was chosen so that each color could also be differentiated by readers with deuteranopia, protanopia, tritanopia, or achromatopsia.

Table 9
New 20 pc Multiple Systems Identified through LUWE

J2000 R.A. (1)	J2000 Decl. (2)	Name (3)	Note (4)	Sp. Type[a] (5)
01 46 29.35	−53 39 32.6	2MASS J01462935−5339325	1	M4.5e
04 34 45.33	−00 26 46.5	G 82-33		M4 V
07 01 13.73	−25 56 55.5	HD 52698[b]		K1 V (k)
07 08 07.01	−22 48 47.3	LP 840-16		M2
07 49 42.14	−03 20 34.0	UCAC4 434-042012	2	M3.5 V
08 25 52.82	+69 02 01.1	LP 35-347		M5.5 V
10 02 42.45	+14 59 13.0	G 43-23	3	M4 V
10 14 53.12	+21 23 46.0	G 54-19		M4.5 V
10 39 45.41	−44 30 37.0	TYC 7722-1583-1		M3
11 45 34.44	−20 21 12.4	LP 793-33	4	M2.5 V
13 02 20.69	−26 47 13.6	HD 113194[b]		K5 V (k)
13 30 40.95	−20 39 03.7	UCAC4 347-066233		M4
13 40 08.79	+43 46 38.0	Ross 1026		M3.5
13 58 52.21	+27 52 14.2	UPM J1358+2752		…
14 17 22.10	+45 25 46.0	FBS 1415+456	5	M5/6
14 23 43.74	+14 26 51.4	LP 440-17		M7 (NIR)
14 24 18.70	−35 14 32.7	2MASSI J1424187−351432		M6.5 V
14 28 17.58	+05 18 45.8	G 65-53	6	M3.5
15 10 16.82	−02 41 08.1	TVLM 868-110639		M9 V
15 18 31.46	+20 36 28.2	UCAC4 554-051865		M4.5 V
15 52 06.55	−33 59 19.0	UCAC3 113-186615		…
17 33 53.18	+16 55 13.1	LSPM J1733+1655		M5.5
18 30 39.45	−03 56 18.9	UCAC4 431-076686		M4.5 V
18 43 12.51	−33 22 46.1	CD−33 13497	7	M1
18 53 25.37	+02 50 48.7	G 141-46		M2.5
19 36 14.39	+50 13 10.1	UCAC3 281-150921	8	M2/3
20 12 59.94	+01 12 58.3	2MASS J20125995+0112584		M6
20 33 36.67	−21 20 10.1	2MASS J20333668−2120096		M2
22 10 13.19	−71 46 06.2	PM J22102−7146		…
22 17 18.97	−08 48 12.3	Wolf 1561 A	9	M4 V
22 24 24.65	−58 26 13.6	UCAC3 64-480761		…

Notes. (1) 0146−5339: this is the 35.′9 distant companion to the F9 dwarf q01 Eri. (2) 0749−0320: this is the 3.′9 distant companion to the M3.5 binary PM J07498−0317 AB. (3) 1002+1459: this object also has a 15.″6 distant companion, WISEU J100241.49+145914.9, announced in this paper (Section 2.2). (4) 1145−2021: this is a physical system with the M5e star LP 793-34, 15.″2 distant. (5) 1417+4525: this is the 59.″2 distant companion of the M0 star BD+46 1951. (6) 1428+0518: this is a physical system with the M4 star G 65-54, 1.′0 distant. (7) 1843−3322: this is a physical system with the M6 star CE 507, 15.″0 distant. (8) 1936+5013: this is the 1.′9 distant companion to the F3+ dwarf θ Cyg, which is listed among the accelerators in Table 8. (9) 2217−0848: this is a physical system with the M5 dwarf binary Wolf 1561 BaBb, 7.″9 distant.

[a] Spectral types are taken from Table 4. All are optical types except for LP 440-17, which is a near-infrared type.

[b] This object is also in the accelerator list of Table 8.

(This table is available in machine-readable form.)

magnitude diagrams along with its high DR3 RUWE value of 5.438 indicates possible unresolved binarity.

2. *Gaia EDR3 3330473222213987072 (0623+1018).* This M3 dwarf (see Appendix A.2) has a Gaia eDR3/DR3 parallax of 50.80 ± 1.55 mas. The derived M_G value is ∼8 mag fainter than that expected for an average M3 dwarf, and the M_{W2} value is ∼9 mag fainter. The Gaia parallax value for this object is clearly in error, so it has been removed from the 20 pc census.
3. *Gaia EDR3 3460907947316392704 (1159−3634).* This is an M9.5 dwarf with a Gaia eDR3/DR3 parallax of 50.10 ± 0.18 mas. Its apparent magnitudes fall within the range of other M9.5 dwarfs within the 20 pc census. In absolute magnitude, it falls above the main sequence by as much as a magnitude for objects of a similar color, and its Gaia RUWE value is 1.482. This position on color–magnitude diagrams cannot be explained by binarity alone, but a slightly larger parallax in tandem would solve the discrepancy. In any event, there is no reason to exclude this object from Table 4.
4. *Gaia EDR3 6025146733201615616 (1624−3212).* This object, of an unknown type, has a Gaia eDR3/DR3 parallax of 59.01 ± 0.12 mas. Its apparent magnitude falls in the range expected for objects of a similar color within 20 pc. On plots of absolute magnitude versus color, however, it appears anomalous. On the M_G versus $G_{BP} - G_{RP}$ plot, it falls 0.4 mag more luminous than objects of a similar color; on the M_G versus $G - J$ plot, it is also more luminous, but by 2.4 mag. Whether these issues indicate a problem with the measured photometry, the measured astrometry, or both—or whether the object has an unusual spectrum—is currently unknown. This object is retained in Table 4.
5. *Gaia DR2 4062191480304598656 (AB) (1736−2515).* This object, also of an unknown type, has a Gaia DR2 parallax of 60.24 ± 0.83 mas and is a known double (Vrijmoet et al. 2022). Gaia DR3 lists two sources near this position, but neither have a parallax or proper-motion

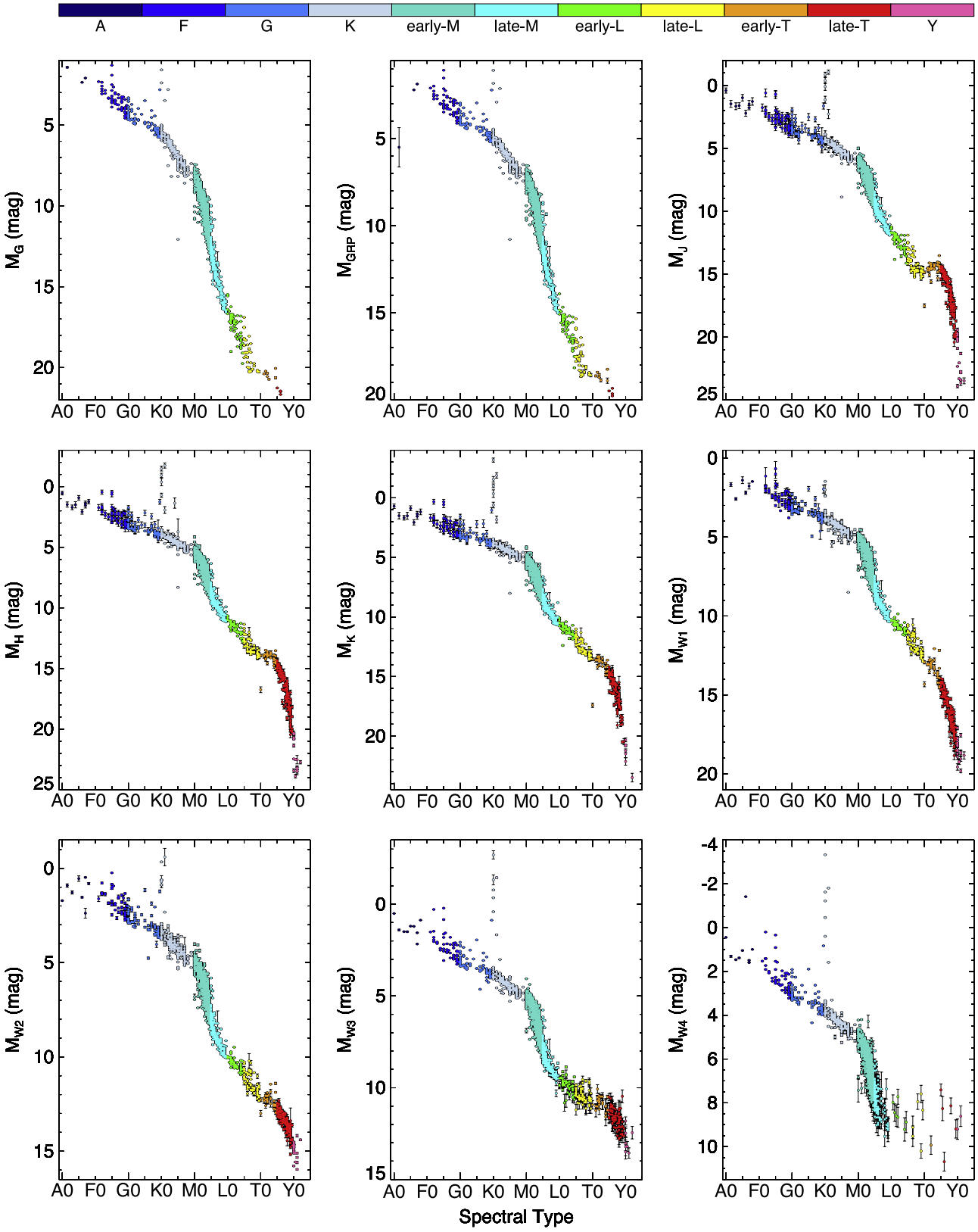

Figure 4. Various absolute magnitudes plotted against spectral type for the 20 pc census. See text for details.

measurement. The apparent magnitude of the DR2 source is at odds with the range expected for objects of a similar color within 20 pc for many combinations of apparent magnitude versus color, such as G versus $G-\mathrm{W2}$, J versus $J-\mathrm{W2}$, and H versus $J-K_s$. The object also has a very small Gaia-measured proper motion of 25.2 ± 1.1 mas yr^{-1} and lies near the Galactic Center at $l,\ b=(2\overset{\circ}{.}1,\ +3\overset{\circ}{.}1)$. This object is most likely a background object with a faulty parallax, so we have removed it from the 20 pc census.

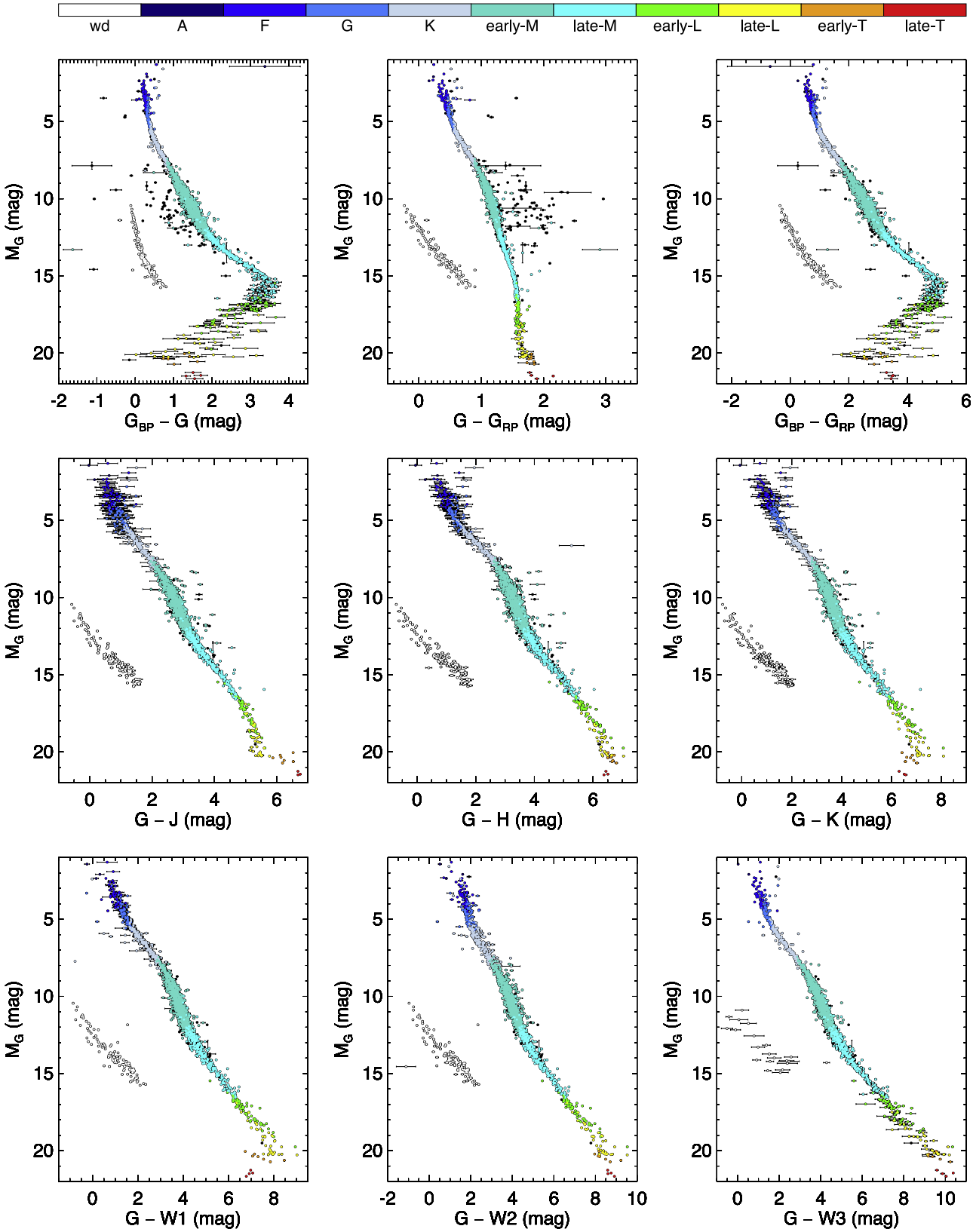

Figure 5. Absolute G-band magnitude plotted against various colors for the 20 pc census. See text for details. The spray of mostly black points (i.e., objects with no measured spectral types) to the left of the main sequence in the $G_{BP} - G$ vs. M_G diagram and to the right of the main sequence in the $G - G_{RP}$ vs. M_G diagram represents components in close binaries near the Gaia resolution limit. The G_{BP} and G_{RP} magnitudes are calculated from the fluxes in a 3.5×2.1 arcsec^2 field, whereas the G magnitudes are calculated from a profile fit to a much higher-resolution image (Section 8 of Evans et al. 2018). For binaries just above the Gaia resolution limit, this means that per-component BP and RP fluxes will often include light from the other object, whereas the G flux will not (Halbwachs et al. 2023). This effect pushes such objects blueward in $G_{BP} - G$ color and redward in $G - G_{RP}$ color, as these diagrams show.

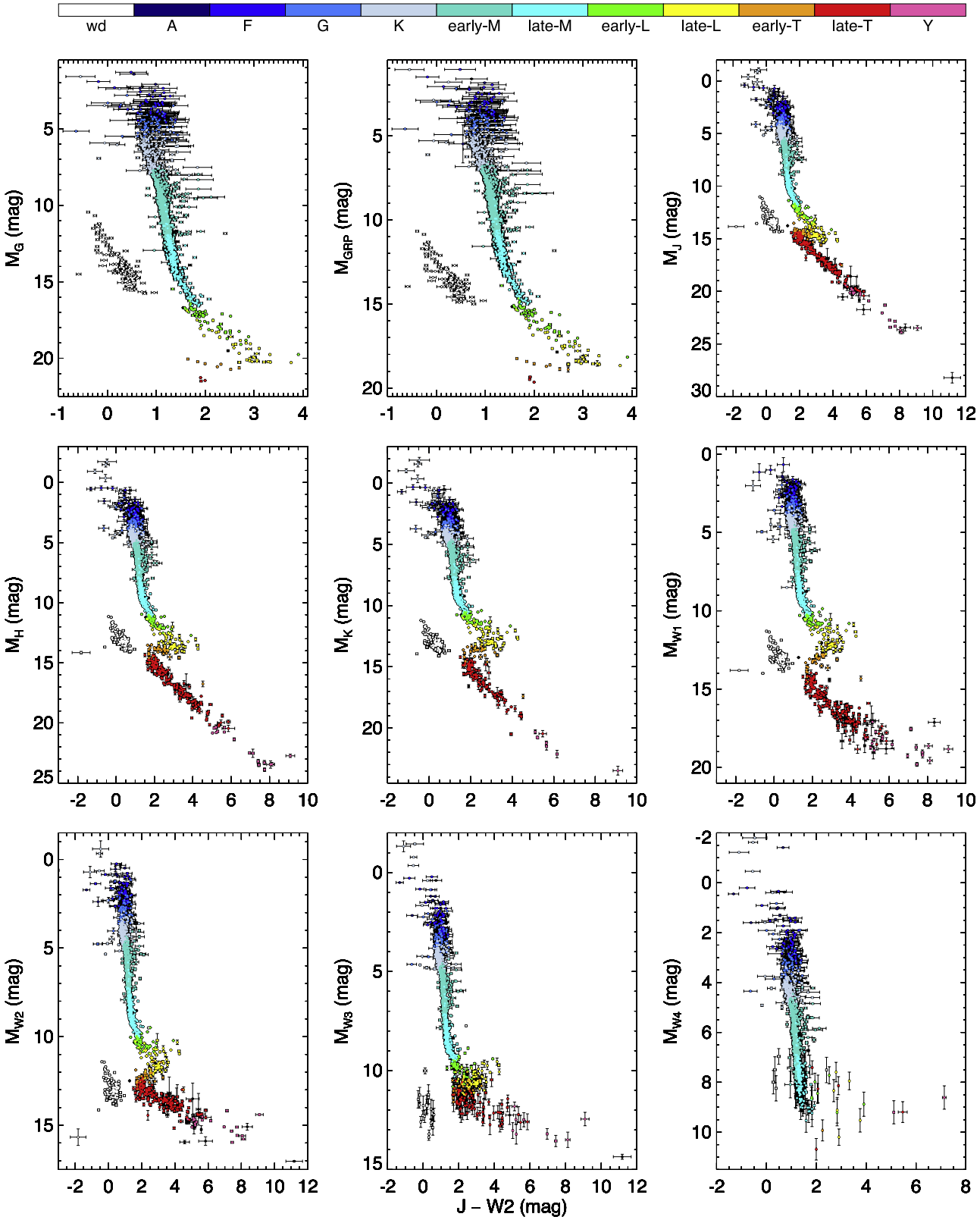

Figure 6. Various absolute magnitudes plotted against $J - \mathrm{W2}$ color for the 20 pc census. See text for details.

6. *Gaia DR2 1795813379365971072 (2151+2328).* No spectrum has been acquired of this object, and it appears to be a very close double in both Gaia DR2 and eDR3/DR3. However, only one of these components has a parallax measurement in DR2, and neither one does in DR3. This object lies well below and blueward of the main sequence on many apparent magnitude versus color plots such as J versus $G - J$, W2 versus $G_{BP} - GRP$, and

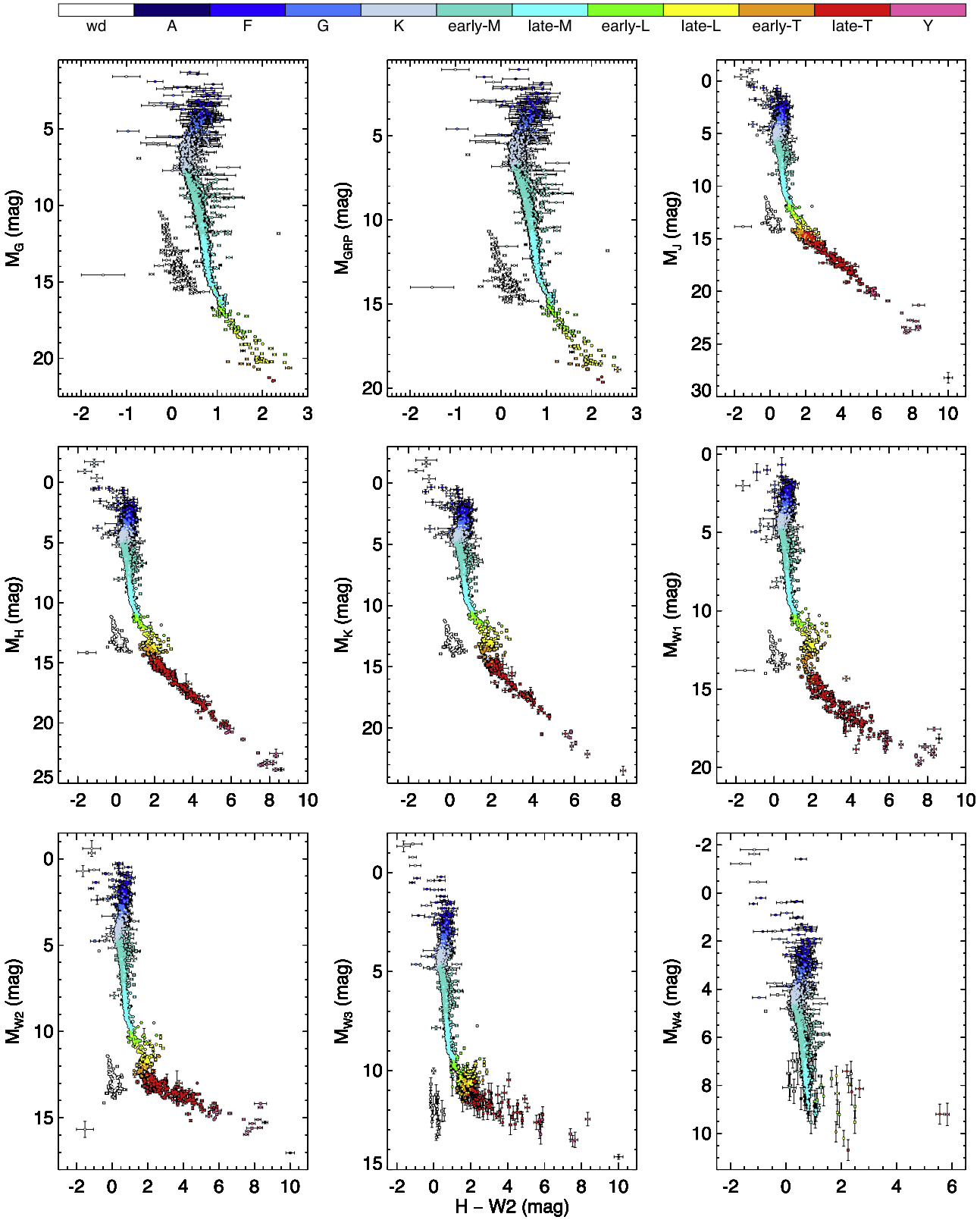

Figure 7. Various absolute magnitudes plotted against $H - \mathrm{W2}$ color for the 20 pc census. See text for details.

H versus $J - \mathrm{W2}$. The object also has a small Gaia DR2 motion of only 45.7 ± 0.7 mas yr^{-1}. This is likely a background source with a bogus parallax, so we have removed it from the 20 pc census.

The rest of our analysis deals with objects that are outliers for various other reasons. As discussed below, these reasons include possible unresolved binarity, unusual atmospheric composition, variability corrupting pan-epoch

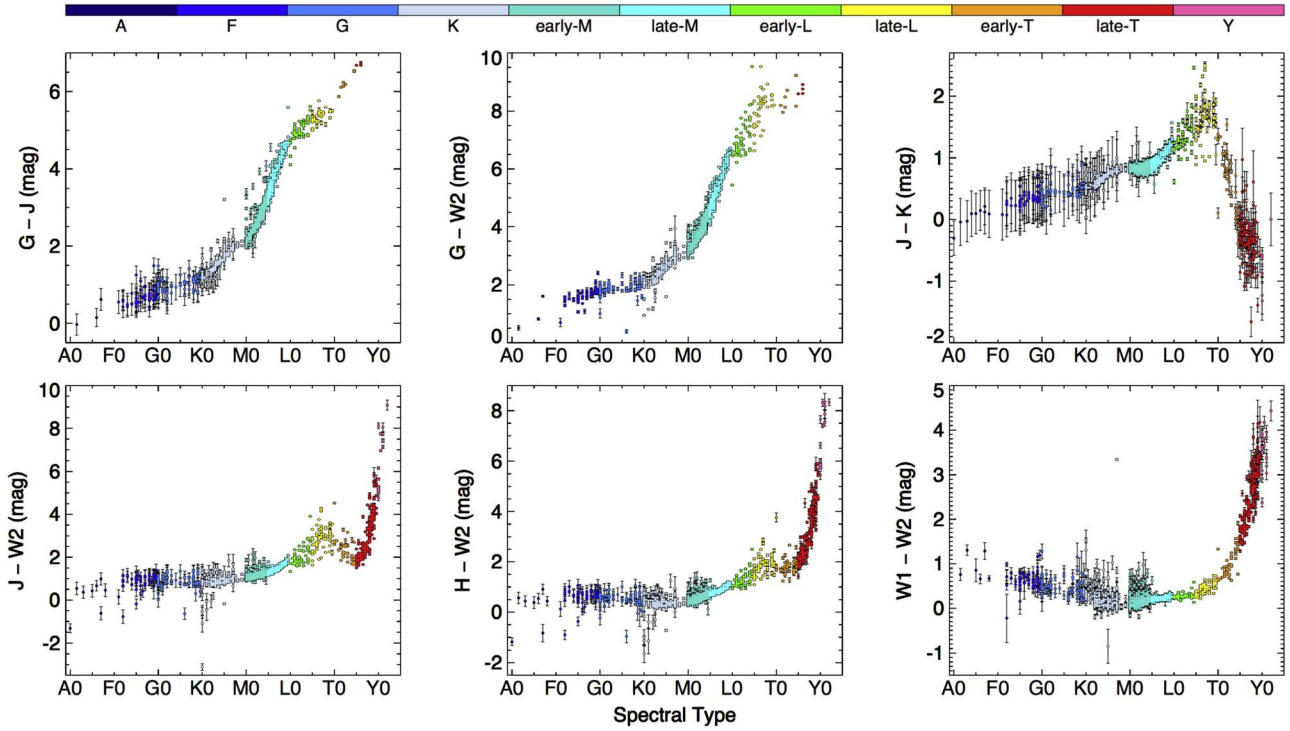

Figure 8. Various colors plotted against spectral type for the 20 pc census. See text for details.

colors, and suspected typographical errors in published literature values.

1. *HD 1237 B (0016−7951).* For its spectral type of M4, this object has $G_{BP} - G$ and $G_{BP} - G_{RP}$ colors much bluer than expected, while its $G - G_{RP}$ color is much redder than expected. No other separate photometry of the B component is given in Table 4. Given that the A component is 8 mag brighter in G than the B component and lies only 4.″0 away, we suspect a problem with the measured photometry of B that is not adequately reflected in its quoted uncertainties.
2. *EGGR 246 (0041−2221).* This is an oddly blue white dwarf in colors that use W1 or W2 magnitudes. The object is also blue relative to other white dwarfs in $J - H$ color, although normal in $G - J$. This carbon-bearing object has a peculiar spectral type, DQpec9.3, and is believed to have a mixed hydrogen–helium atmosphere. The known infrared flux deficit is thought to be caused by absorption by H_2 via collisions with neutral He (Bergeron et al. 1994, 2022; Giammichele et al. 2012).
3. *LP 941-19 (0213−3345).* Although this DA4.5 white dwarf has contaminated WISE photometry, it falls in an odd position on plots based only on Gaia photometry. Specifically, at its value of M_G, it falls ∼0.5 mag blueward of the white dwarf locus in $G_{BP} - G$ and ∼0.3 mag redward in $G - G_{RP}$. There is very little literature on this source, and our spectrum of it (Appendix A.2) is the first published. It is not yet clear if this spectrum differs markedly enough from other DA white dwarfs to account for the color discrepancies or whether the Gaia magnitudes themselves are at fault.
4. *HD 21209 A (0323−4959).* The only oddity with this K dwarf is its anomalously blue W1−W2 color. The value in Table 4, which is from the WISE All-Sky Source Catalog, is W1−W2 = −0.17 ± 0.06 mag. Although this is the preferred WISE catalog for sources of this brightness (W1 = 5.56 mag), the AllWISE Source Catalog gives a very similar color of W1−W2 = −0.15 ± 0.13 mag. This color may be due to the slightly subsolar metallicity of the object ([Fe/H] = −0.44 ± 0.19, Soto & Jenkins 2018; −0.41 ± 0.04, Sousa et al. 2008; −0.39 ± 0.02, Tsantaki et al. 2013).
5. *HD 23189 (0348+6840).* This early K dwarf is underluminous for its type at M_G, M_J, M_H, M_{Ks}, and M_{W2}. When colors formed from Gaia-based magnitudes are compared to the mean colors of objects of the same type, it appears normal, whereas the W1−W2 color is slightly bluer than normal. We suspect that the Gray et al. (2003) type of K2 V is a typographical error, as independent assessments of the type from spectra, colors, and luminosity considerations (Adams et al. 1935; Bidelman 1985; Mermilliod 1987; Stassun et al. 2019) suggest a spectral type closer to K7.
6. *2MASS J05053461+4648017 (0505+4648).* This is an M8 dwarf (see Appendix A.2) with a Gaia DR3 parallax value of 56.84 ± 0.60 mas. The absolute values calculated with this parallax are similar to those of other known M8 dwarfs in the census, and a previous parallax of 69.5 ± 4.7 mas (Dittmann et al. 2014) also places it within 20 pc. Its location on color–magnitude diagrams such as M_G versus $G - W2$ along with its high DR3 RUWE value of 4.823 indicate possible unresolved binarity.
7. *DENIS J071807.3−350220 (0718−3502).* On the $G_{BP} - G_{RP}$ and $G - J$ versus various absolute magnitude diagrams, this object appears to be ∼0.7 mag above the locus of other objects of the same color. This is, therefore, likely a near-equal-magnitude double. This object is also flagged as a possible binary in the Apps Catalog, again based on its position in color–magnitude diagrams.

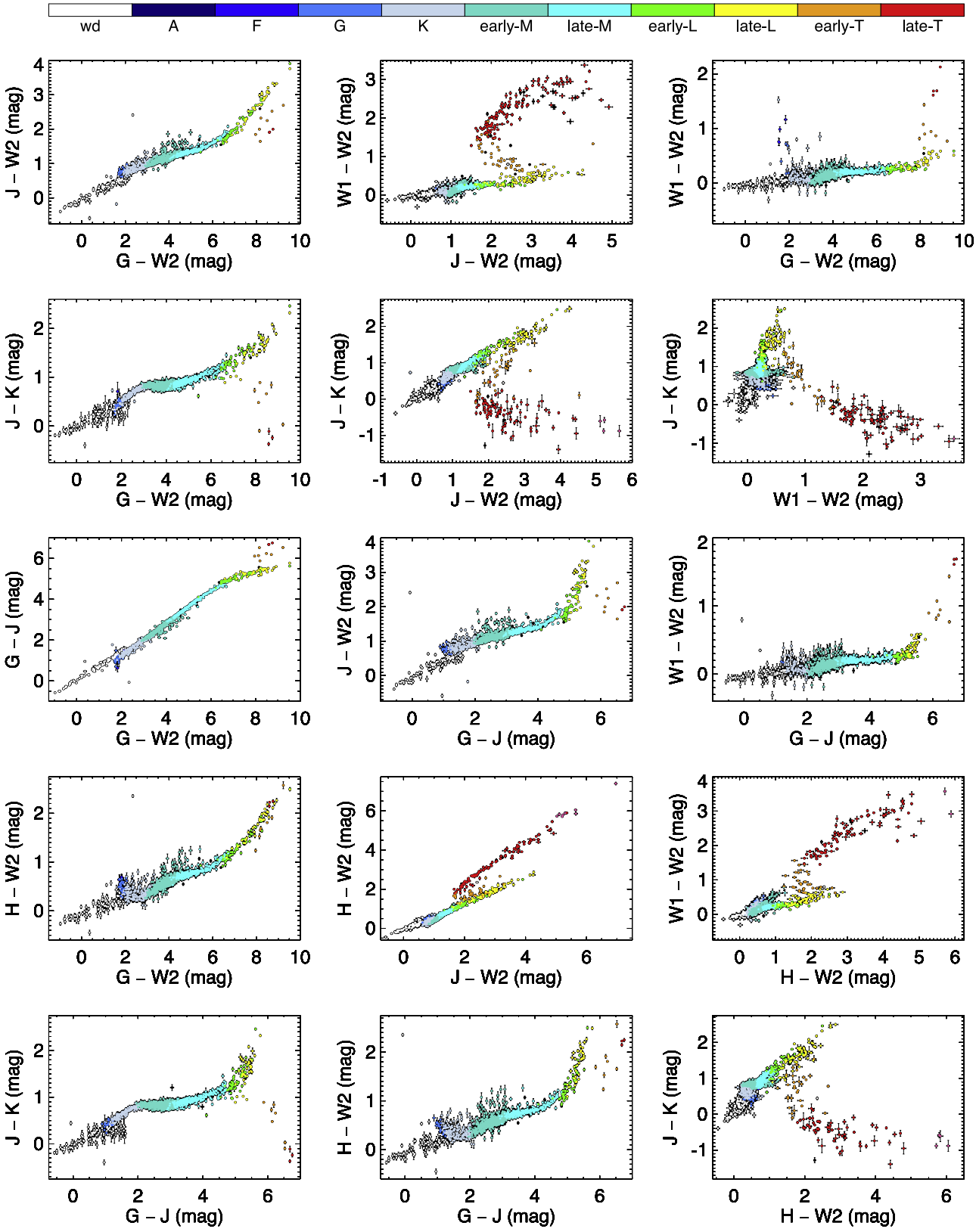

Figure 9. Various color–color diagrams for the 20 pc census. See text for details.

8. *SCR J0818−3110 (0818−3110).* This DZ white dwarf is an outlier on the $G-J$ versus W1−W2 diagram and, in fact, any diagram involving W1−W2 color. This issue has been hinted at previously in Figure 4 of Kawka et al. (2021), which shows that the best model fit to existing spectra and photometry fails to match the observed W1−W2 color. Although the effect is known, its reason has apparently not yet been established and may be caused by variability or missing opacity sources in the models.

9. *UPM J0901−6526 (0901−6526).* This K5 dwarf is an outlier on all plots showing spectral type but appears normal on color–color and color–magnitude plots. We suggest that the published type of K5 (Riaz et al. 2006) results from a transcription error in the data for this star and that the actual spectral type is closer to M5.
10. *APMPM J1251−2121 (1250−2121).* This M6/6.5 dwarf has a Gaia DR3 parallax of 56.79 ± 0.19 mas. Its apparent magnitudes fall within the range expected for an M6 dwarf within the 20 pc volume, and a previous parallax measurement of 57.7 ± 1.7 mas (Winters et al. 2015) is in agreement with the Gaia one. On the M_G versus $G_{BP} - G_{RP}$ diagram, it falls ∼0.5 mag above the main sequence, and on the M_G versus $G - \mathrm{W2}$ diagram, it falls ∼0.7 mag above. This and the Gaia DR3 RUWE value of 2.888 suggest unresolved binarity.
11. *HD 113194 (1302−2647).* Although this K5 dwarf has a Gaia DR3 parallax with a relatively large uncertainty (56.94 ± 0.19 mas), the earlier Hipparcos parallax (56.87 ± 1.11 mas) is in agreement. This object also has a high Gaia DR3 RUWE value, is listed as a high-LUWE object (see Section 5.2), and shows acceleration (see Section 4.1.4), in addition to falling ∼0.5 mag above the main sequence on the G versus $G_{BP} - G_{RP}$ diagram. This object is almost certainly an unresolved binary. It is also considered to be binary in the Apps Catalog, based on its position on color–magnitude diagrams. The Gaia DR3 main catalog reports a radial velocity of -17.56 ± 7.24 km s^{-1} using seventeen observations over 920 days, along with an amplitude of radial velocity variations of 60.25 km s^{-1}, further supporting the hypothesis of binarity. The P-value for radial velocity constancy (`rv_chisq_pvalue`) is also 0.0.
12. *2MASSW J1421314+182740 (1421+1827).* This M9.5 dwarf has WISE photometry contaminated by a background source, but it appears unusual in non-WISE colors as well. Specifically, it has oddly blue $G_{BP} - G$ and $G_{BP} - G_{RP}$ colors compared to other objects of similar M_G. However, it appears normal for its M_G in $G - G_{RP}$, $G - J$, $G - H$, and $J - K_s$. This may simply indicate an issue with the G_{BP} magnitude that the formal uncertainty fails to adequately capture.
13. *LP 222-65 (1516+3910).* This mid-M dwarf lies consistently ∼0.6 mag above the main sequence relative to objects of the same color and spectral type on color–magnitude diagrams. This is an isolated object with no obvious problems with its photometry, so we believe this is an unresolved near-equal-magnitude binary.
14. *UCAC4 554-051865 (1518+2036).* This mid-M dwarf is ∼0.6 mag more luminous than objects of a similar color on the M_G versus $G_{BP} - G_{RP}$ and M_G versus $G_{BP} - G$ diagrams and has a large RUWE and LUWE value (see Section 5.2). It is likely an unresolved binary.
15. *L 339-19 (1640−4559).* This M3 dwarf shows anomalously red $G - \mathrm{W3}$ and $J - \mathrm{W3}$ colors for its absolute magnitude, and even more anomalously red $G - \mathrm{W4}$ and $J - \mathrm{W4}$ colors. A more careful look at the WISE images shows that the W3 detection is likely real, but the W4 detection likely is not. The W3 photometry from AllWISE (reported in Table 4) is 7.10 ± 0.05 mag and that from WISE All-Sky is 6.57 ± 0.04 mag. In $G - \mathrm{W3}$ and using the AllWISE value, the object lies 1.0 mag redward of objects of the same absolute G magnitude; using the WISE All-Sky value shows the object lies 0.5 mag redward. Archival Spitzer/IRAC and Spitzer/MIPS photometry of this object exists in the GLIMPSE I Spring '07 Catalog (Benjamin et al. 2003) and MIPSGAL Archive (Carey et al. 2009) at IRSA: ch1 = 7.830 ± 0.038, ch2 = 7.781 ± 0.045, ch3 = 7.724 ± 0.037 (5.8 μm), ch4 = 7.705 ± 0.026 (8.0 μm), and [24 μm] = 7.14 ± 0.24 mag. Running these new data points and the tabulated Table 4 photometry through the Virtual Observatory Spectral energy distribution Analyzer (VOSA;[74] Bayo & Rodrigo 2008) suggests not only that the W4 magnitude is in error but that the W3 magnitude is spuriously bright relative to the bracketing IRAC and MIPS data points. The spectral energy distribution is otherwise typical of that of an M3 dwarf. We therefore conclude that there is no infrared excess in this object.
16. *UCAC4 317-104829 (1706−2643).* This DAH white dwarf is normal in Gaia-only colors, colors formed using Gaia minus near-infrared magnitudes, and colors formed from J, H, and K_s magnitudes. It is, however, oddly blue in W1−W2. We assume that this anomalous color may be intrinsic to the star and a result of its strong magnetic field, although it should be cautioned that this white dwarf is located against a busy region of the Galactic plane and may suffer from contamination in its WISE photometry.
17. *DENIS-P J1733423−165449 (1733−1654).* This L1 dwarf has WISE photometry that is contaminated by background sources, but it also shows unusual colors in Gaia-only measurements. Gaia DR3 lists two other point sources within 2.″1 of this object, so its Gaia photometry may be adversely affected in a way that the formal uncertainties fail to capture.
18. *LSPM J1733+1655 (1733+1655).* The Gaia DR3 parallax of 60.91 ± 0.48 mas has a relatively large uncertainly for its magnitude and is in disagreement with an earlier published value of 85.40 ± 3.30 mas by Dittmann et al. (2014). This mid-M dwarf is more luminous than objects of a similar color by ∼1.6 mag on the G versus $G_{BP} - G$, $G_{BP} - G_{RP}$, $G - G_{RP}$, $G - J$, and $G - \mathrm{W2}$ diagrams, if the Gaia DR3 parallax is used. This overluminosity decreases to ∼0.9 mag if the Dittmann et al. (2014) parallax is used instead. This is a high-RUWE/LUWE object as well (Section 5.2), and so is likely an unresolved multiple system with problematic Gaia astrometry. Clark et al. (2022) identify a candidate companion at separation 0.″14 and position angle 101° at epoch 2017.3 and again at separation 0.″36 and position angle 63° at epoch 2019.7. C. Gelino also finds a single epoch of Keck/NIRC2 data in the Keck Observatory Archive for LSPM J1733+1655. These are Brγ and J-continuum observations taken on 2015 July 10 UT (PI: Hansen; program ID: U050N2), from which we measure a separation of 0.″11 at position angle 248°. If we assume all three of these measurements refer to the same star and it is a stationary background object, we derive motions of LSPM J1733+1655 of $-0.''100\,\mathrm{yr}^{-1}$ in R.A. and $-0.''051\,\mathrm{yr}^{-1}$ in decl., which can be compared to the measured Gaia DR3 values of $-0.''135\,\mathrm{yr}^{-1}$ in R.A. and $-0.''130\,\mathrm{yr}^{-1}$ in decl. The derived magnitude and

[74] http://svo2.cab.inta-csic.es/theory/vosa/

direction of motion lead us to conclude that the background star hypothesis is sound.

19. *LP 388-55 A (1735+2634).* This late-M dwarf is anomalously red, by 0.25 mag, in $G - G_{RP}$ color but looks normal in the $G_{BP} - G$ color compared to objects of similar M_G magnitude. Curiously, all Gaia-based absolute magnitudes (M_G, M_{GBP}, and M_{GRP}) are consistent with the reported spectral type. The B component is an early-L that is not directly imaged by Gaia but may nonetheless be subtly affecting the Gaia magnitudes of the A component.
20. *LP 44-334 A (1840+7240).* This primary in a M6.5 dwarf system has a Gaia DR3 parallax (52.78 ± 0.09 mas) with a relatively large uncertainty for its magnitude, but this value compares favorably to the earlier published value of 59.3 ± 2.2 mas by Lépine et al. (2009). The $G_{BP} - G$ color is too blue for its M_G value, the $G_{BP} - G_{RP}$ color is normal, and the $G - G_{RP}$ color is too red. These issues are likely caused by the nearness of the B component, only $0\farcs8$ away, which is likely corrupting the photometry of the A component.
21. *LP 867-15 (1842−2328).* The colors for this M0 dwarf are more consistent with an M4 dwarf than with an M0. Pending spectroscopic verification, we assume that this object has been misclassified.
22. *SCR J2012−5956 (2012−5956).* This object, a DC9.9 white dwarf, falls below the white dwarf locus for most colors. It is very blue relative to other white dwarfs in $J - K_s$, $J - H$, and $H - K_s$ but looks like other white dwarfs in colors made with Gaia-only magnitudes. It is somewhat blue in $G - J$, $G - H$, and $G - K_s$ colors. As with EGGR 246 above, the infrared flux deficit is believed to be caused by H_2–He collision-induced absorption (Giammichele et al. 2012).
23. *LEHPM 2-783 (2019−5816).* This M6.5 dwarf is overluminous in all Gaia-based colors. (Many other colors are nearly degenerate with absolute magnitude or type in this spectral type range.) On both the $G_{BP} - G_{RP}$ versus M_H and the $G - W2$ versus M_{W2} plots, the overluminosity is ∼0.7 mag. Ujjwal et al. (2020) mark this as a possible member of the β Pic Moving Group, and Riaz et al. (2006) note that it is a strong X-ray emitter with strong Hα emission.
24. *LP 12-90 (2322+7847).* This mid-M dwarf lies above the main sequence by ∼0.75 mag on the M_G versus $G_{BP} - G$ plot. On many other plots of absolute magnitude versus color, it lies similarly above (and redward of) the main sequence. This could be another unresolved binary—if confirmed, this would make its system with HD 220140 AB a quadruple—but the primary in this system is a young, naked T Tauri star (Makarov et al. 2007), meaning that its position may be solely due to its youth.
25. *ZZ Psc (2328+0514).* This white dwarf is anomalously red in colors involving WISE magnitudes—so much so that it falls far from the white dwarf sequence itself. On a plot of M_G versus W1−W2, for example, it lies substantially redward of both the white dwarf locus and the main sequence. This object, also known as G 29-38, is known to have a debris disk around it, the first evidence of which was uncovered by Zuckerman & Becklin (1987). For an update on this object, see Cunningham et al. (2022).

6. Masses from Estimation

Only a small fraction of objects within the 20 pc census has masses measurable by Methods 1 or 2 described in the introduction of Section 4. For the rest, we must rely on Methods 3 and 4 of that section, which depend on a comparison to empirical trends or to theoretical models.

In the first subsection below, we discuss mass measurements for objects not on the main sequence—namely, white dwarfs, giants/subgiants, and brown dwarfs. In the second subsection, we summarize mass estimation for main-sequence stars. In the third subsection, we discuss other complications—youth, subsolar metallicity, and formation scenario—that may need to be considered when assigning accurate mass estimates for special objects.

6.1. Individual Objects not on the Main Sequence

6.1.1. White Dwarfs

Masses have been measured via one of the methods described in Section 4 for a handful of white dwarfs in the 20 pc census, but these represent the end-state masses of the stellar remnants and are not suitable for analysis of the *initial* mass function. Rather, what is needed are the initial masses *before* evolution off the main sequence. Techniques have been established that use the final mass of the remnant to estimate the initial mass of the progenitor.

For white dwarfs lacking a direct mass measurement, one can estimate the final mass of the white dwarf using one of the following two semiempirical methods. The first is to use spectroscopic observations of the depth and width of the hydrogen Balmer, He I, or He II lines to establish, after comparison to atmospheric models, the $\log(g)$ and $T_{\rm eff}$ for each object. Further comparison of these two parameters to cooling models provides the remnant mass (e.g., Bergeron et al. 1992; Finley et al. 1997; Tremblay et al. 2011; Genest-Beaulieu & Bergeron 2019). Whereas this first method is applicable only to DA (hydrogen atmosphere) or DB (helium atmosphere) white dwarfs, an alternate method can be used both for objects lacking hydrogen lines as well as for objects lacking spectroscopic observations. In this second method, masses can still be estimated if an accurate parallax has been measured. Here, absolute fluxes across as wide a swath of wavelength space as possible are compared to model atmospheres to provide $\log(g)$ and R, from which the mass can be derived from Equation (11) (e.g., Koester et al. 1979; Bergeron et al. 2001, 2019; Giammichele et al. 2012; Tremblay et al. 2019).

The next step is to convert this final mass into an initial mass using an initial-to-final mass relation (e.g., Weidemann 2000). The empirical form of this relationship has been established using white dwarfs that are members of open clusters of known age. As described above, spectroscopic observations of the Balmer lines in these stars can be compared to atmospheric models to derive $\log(g)$ and $T_{\rm eff}$ for each object. A comparison of these parameters to cooling models provides both the remnant mass as well as the cooling time since the object left the tip of the asymptotic giant branch. The known cluster age minus this cooling time gives the main-sequence lifetime of the object, which can then be related back to an initial mass using theoretical evolutionary isochrones. This same technique can also be applied to white dwarfs in globular clusters. Due to their much older ages, these clusters can provide white dwarfs

of lower final mass than those available in young open clusters. Because these globular clusters are much more distant, their white dwarfs are faint and more difficult to study, so old low-mass white dwarfs are still not well represented by cluster methods.

This lack of low-mass examples can be partly mitigated by the use of old, wide binaries for which the second component can be age dated, and the separation between components is large enough that no mass transfer has occurred during the system's evolution. Examples are wide subgiant + white dwarf binaries in which the system can be dated from its more recently evolved member (Barrientos & Chanamé 2021), wide F/G/K dwarf + white dwarf binaries in which the age of the main-sequence star can be estimated from activity diagnostics (Catalán et al. 2008a; Zhao et al. 2012), and white dwarf pairs in which comparison of the higher-mass white dwarf to known cluster white dwarfs can provide an age for the binary, and the difference in the cooling times for the white dwarf pair gives the main-sequence lifetime of the lower-mass white dwarf (Andrews et al. 2015). Using the results of these methods, the trend of final mass with initial mass can be fit. As can be seen from Figure 9 of Barrientos & Chanamé (2021), the relation shows considerable scatter at lower masses, as the age dating methods for individual systems are generally less robust than those from clusters. The relations we adopt here are the cluster-based tripartite parameterization found in Equations (4)–(6) of Cummings et al. (2018) and the quadripartite parameterization found in Table 1 of El-Badry et al. (2018). The former relation is applicable to white dwarfs with $0.56 < M_{\rm final} < 1.24 M_{\odot}$ ($0.83 < M_{\rm initial} < 7.20 M_{\odot}$), and the latter relation, which is based on nearby white dwarfs with accurate Gaia parallaxes, is applicable to white dwarfs with $0.50 < M_{\rm final} < 1.37 M_{\odot}$ ($0.95 < M_{\rm initial} < 8.00 M_{\odot}$). We further note that neither the cluster nor field methods have yet extended the initial-to-final mass relation below final masses of $0.50 M_{\odot}$. (As discussed further below, white dwarfs with final masses below $0.45 M_{\odot}$ require binary interactions, as a single progenitor would imply an age older than that of the Universe; Marsh et al. 1995.)

Specifically, we apply the following methodology to assign *final* masses to white dwarfs in the 20 pc census. First, we use directly measured masses, whenever such measurements are available. For others, we use final mass estimates that are based on accurate parallaxes, high S/N spectra, and/or broad-wavelength data spanning the white dwarf's spectral energy distribution. For all other objects, we resort to the Gaia-centric estimates of Gentile Fusillo et al. (2019, 2021). These estimates use only a small fraction of the white dwarf's spectral energy distribution—spanning the Gaia optical bandpasses—and thus lead to separate solutions for hydrogen- versus helium-atmosphere objects. When our own follow-up has determined the spectral type of the object, we use this information to break the degeneracy; otherwise, a hydrogen-atmosphere object is assumed, as noted in Table 10.

There are a number of caveats that must be addressed before proceeding with the *initial* mass determinations, however: (1) The parameterization of the initial-to-final mass relation is heavily reliant on white dwarfs with hydrogen lines in their spectra, but roughly half of the white dwarfs in the 20 pc census have no hydrogen lines and are classified as DB (helium lines), DC (no lines), DQ (carbon bands), or DZ (metal lines). Are such objects expected to follow the same initial-to-final mass relation as the DA white dwarfs? (2) Several 20 pc white dwarfs have masses lower than the $0.50 M_{\odot}$ lower bound of current initial-to-final mass relations. How do we address this complication? (3) Given the age of the Milky Way, a white dwarf with mass below $\sim 0.45 M_{\odot}$ should not yet exist (Fontaine et al. 2001; Sun & Arras 2018), as there has been insufficient time for its single-star progenitor to have evolved off the main sequence. Nonetheless, a few 20 pc white dwarfs have final masses so low that they imply cooling ages longer than a Hubble time. How do we interpret this seeming contradiction? We address these issues below.

For issue (1), consider that, within the 20 pc census, the most massive white dwarfs[75] are akin to Sirius B and have initial mass estimates of $\sim 5\ M_{\odot}$. With this in mind, it is helpful to summarize some relevant facts about white dwarfs, as stated in the excellent review by Fontaine et al. (2001). The alpha process (carbon burning) occurs only in stars more massive than $\sim 8\ M_{\odot}$,[76] so all white dwarfs within 20 pc of the Sun will have stopped their thermonuclear burning at the triple-alpha process (helium burning). These white dwarfs will have a core made primarily of carbon and oxygen and will be compositionally stratified, with a helium-rich envelope and a separate hydrogen-rich envelope. These two layers are very thin, but their opacity regulates the core's energy output. As such, these thin layers play a critical role in determining white dwarf cooling times.

Current observational evidence shows that white dwarfs evolve spectroscopically as they cool, sometimes appearing as hydrogen-atmosphere stars (DA) and sometimes as helium-atmosphere stars (DB and other classes[77]), meaning that some unknown process—convection, diffusion, and/or mixing—reorders the two outer envelopes over time. Specifically, the ratio of helium-atmosphere to hydrogen-atmosphere white dwarfs changes as a function of effective temperature, with relatively few helium-atmosphere stars being identified in the range $30{,}000 < T_{\rm eff} < 45{,}000$ K (Shibahashi 2007) and relatively few helium-atmosphere stars again being found in the cooler range $5000 < T_{\rm eff} < 6000$ K (Bergeron et al. 1997). This implies that most nearby white dwarfs evolve as hydrogen-atmosphere stars, an assertion that Fontaine et al. (2001) say is further bolstered by the fact that the observational data and theoretical predictions—particularly with regards to the white dwarf luminosity function—are in excellent agreement. We are therefore confident in using the initial-to-final mass relations (IFMRs) to estimate the initial masses of 20 pc objects having final masses $>0.50 M_{\odot}$. These initial mass estimates are listed in Table 10 and are noted with "IFMR" in the final column.

For issue (2), we note that of the 161 white dwarfs in Table 10, only twelve have $0.45 \leqslant M < 0.50 M_{\odot}$. An object at the upper end of this range would have a predicted initial mass of $<0.9 M_{\odot}$ according to the initial-to-final mass relation of Cummings et al. (2018; their Equation (4)) or $\sim 1.0 \pm 0.1 M_{\odot}$ according to the relation of El-Badry et al. (2018; their Table 1 and their Figure 3). Additionally, the lowest-mass object to have evolved off the main sequence during the lifetime of the

[75] One possible exception to this is Wolf 1130 B, which is believed to have a progenitor mass near $8 M_{\odot}$ and an oxygen–neon core (Mace et al. 2018).

[76] This is close to the lower-mass boundary of neutron star formation, which is believed to be ~ 8–$11 M_{\odot}$ (Woosley et al. 2002).

[77] The other non-DA spectral classes of white dwarfs are also thought to be helium-atmosphere stars but with different temperatures and/or trace pollutants than normal DB stars, with DO stars (ionized helium present) at the hot end of the evolutionary sequence and DC, DQ, and DZ stars at the cool end (Figure 4 of Fontaine et al. 2013).

Table 10
Mass Measurements and Estimates for White Dwarfs in the 20 pc Census

Name	Abbrev. Coords (J2000)	WD Name[a]	Final Mass ($M_\odot$)	Final Mass Method	References	Initial Mass (Cummings)[b] ($M_\odot$)	Initial Mass (El-Badry)[c] ($M_\odot$)	Initial Mass (Adopted)[d] ($M_\odot$)	Initial Mass Method
(1)	(2)	(3)	(4)	(5)	(6)	(7)	(8)	(9)	(10)
LAWD 96	0002−4309	WD 2359−434	0.78 ± 0.03	Spec	(1)	3.2 ± 1.5	3.4 ± 0.2	3.3 ± 1.5	IFMR
LAWD 1	0002−3413	WD 0000−345	0.88 ± 0.10	Phot	(1)	3.8 ± 1.3	4.7 ± 0.3	4.3 ± 1.3	IFMR
LP 464-57	0007+1230	WD 0004+122	0.57 ± 0.15	Phot	(2)	1.0 ± 1.9	1.7 ± 0.1	1.4 ± 1.9	IFMR
EGGR 381	0012+5025	WD 0009+501	0.73 ± 0.04	Phot	(1)	2.9 ± 1.4	3.1 ± 0.2	3.0 ± 1.5	IFMR
L 50-73	0013−7149	WD 0011−721	0.59 ± 0.00	Phot	(1)	1.3 ± 0.5	1.9 ± 0.1	1.6 ± 0.5	IFMR
G 158-45	0014−1311	WD 0011−134	0.72 ± 0.07	Phot	(1)	2.9 ± 1.5	3.0 ± 0.2	3.0 ± 1.5	IFMR
EGGR 246	0041−2221	WD 0038−226	0.53 ± 0.01	Phot	(1)	…	1.3 ± 0.1	1.3 ± 0.1	IFMR
Wolf 28	0049+0523	(WD 0046+051)	0.68 ± 0.02	Phot	(1)	2.4 ± 0.7	2.8 ± 0.2	2.6 ± 0.7	IFMR
Wolf 1516	0118+1610	WD 0115+159	0.69 ± 0.04	Phot	(1)	2.5 ± 0.8	2.9 ± 0.2	2.7 ± 0.8	IFMR
LP 991-16 A	0124−4240	WD 0121−429	0.41 ± 0.01[e]	Phot	(1)	…	…	1.9 ± 0.9	Ultra-low
LP 991-16 B	0124−4240	…	…	…	(1)	…	…	1.9 ± 0.9	Ultra-low
EGGR 307	0125−2600	WD 0123−262	0.58 ± 0.00	Phot	(1)	1.1 ± 0.4	1.8 ± 0.1	1.5 ± 0.4	IFMR
LAWD 10 A	0137−0459	WD 0135−052.1	0.47	**Orbit**	(4)	…	…	1.0 ± 0.1	Low
LAWD 10 B	0137−0459	WD 0135−052.2	0.52	**Orbit**	(4)	…	1.2 ± 0.1	1.2 ± 0.1	IFMR
L 88-59	0143−6718	WD 0141−675	0.48 ± 0.06	Spec	(1)	…	…	1.0 ± 0.1	Low
EGGR 268	0151+6425	WD 0148+641	0.81 ± 0.01	**GravRed**	(5)	3.3 ± 1.5	3.5 ± 0.2	3.4 ± 1.5	IFMR
GD 279	0152+4700	WD 0148+467	0.63 ± 0.03	Spec	(1)	1.8 ± 0.6	2.3 ± 0.2	2.1 ± 0.7	IFMR
χ Eri B	0155−5136	…	…	…	…	…	…	1.9 ± 0.9	Conjecture
HD 13445 B	0210−5049	WD 0208−510	0.597 ± 0.010	**Accel**	(6)	1.4 ± 0.5	2.0 ± 0.1	1.7 ± 0.5	IFMR
EGGR 168	0211+3955	WD 0208+396	0.48 ± 0.10	Spec	(7)	…	…	1.0 ± 0.1	Low
LP 649-66	0212−0804	…	0.53 ± 0.02	Gaia H-atm*	(8)	…	1.3 ± 0.1	1.3 ± 0.1	IFMR
LP 941-19	0213−3345	…	0.37 ± 0.05	Gaia H-atm*	(8)	…	…	1.9 ± 0.9	Ultra-low
EGGR 471	0232−1411	WD 0230−144	0.66 ± 0.06	Phot	(1)	2.1 ± 0.9	2.7 ± 0.2	2.4 ± 1.0	IFMR
LP 830-14	0235−2400	WD 0233−242	0.58 ± 0.00	Phot	(1)	1.1 ± 0.4	1.8 ± 0.1	1.5 ± 0.4	IFMR
EGGR 473	0248+5423	WD 0245+541	0.73 ± 0.03	Phot	(1)	2.9 ± 1.4	3.1 ± 0.2	3.0 ± 1.5	IFMR
CPD−69 177	0310−6836	WD 0310−688	0.67 ± 0.03	Spec	(1)	2.3 ± 0.7	2.8 ± 0.2	2.5 ± 0.7	IFMR
α For Bb	0312−2859	…	…	…	…	…	…	1.9 ± 0.9	Conjecture
EGGR 566	0325−0149	WD 0322−019	0.63 ± 0.05	Phot	(1)	1.8 ± 0.8	2.3 ± 0.2	2.1 ± 0.8	IFMR
Wolf 219	0344+1826	WD 0341+182	0.57 ± 0.06	Phot	(1)	1.0 ± 0.9	1.7 ± 0.1	1.4 ± 0.9	IFMR
G 7-16	0400+0814	WD 0357+081	0.61 ± 0.06	Phot	(1)	1.5 ± 0.9	2.1 ± 0.2	1.8 ± 0.9	IFMR
o^2 Eri B	0415−0739	(WD 0413−077)	0.573 ± 0.018	**Orbit**	(9)	1.1 ± 0.5	1.7 ± 0.1	1.4 ± 0.5	IFMR
ϵ Ret B	0416−5917	WD 0415−594	0.60 ± 0.12	Spec	(7)	1.4 ± 1.6	2.0 ± 0.2	1.7 ± 1.6	IFMR
EGGR 169	0425+1211	WD 0423+120	0.65 ± 0.04	Phot	(1)	2.0 ± 0.7	2.6 ± 0.2	2.3 ± 0.8	IFMR
EGGR 180	0431+5858	WD 0426+588	0.675 ± 0.051	**Lensing**	(10)	2.3 ± 0.9	2.8 ± 0.2	2.6 ± 0.9	IFMR
HD 283750 B	0436+2709	WD 0433+270	1.12 ± 0.01	**GravRed**	(5)	6.1 ± 1.2	6.5 ± 0.4	6.3 ± 1.2	IFMR
EGGR 41	0437−0849	WD 0435−088	0.53 ± 0.02	Phot	(1)	…	1.3 ± 0.1	1.3 ± 0.1	IFMR
LP 777-1	0505−1722	WD 0503−174	0.53 ± 0.01	Spec	(23)	…	1.3 ± 0.1	1.3 ± 0.1	IFMR
V371 Ori B	0533+0156	…	0.63 ± 0.17	Dyn+mod	(18)	1.8 ± 2.2	2.3 ± 0.2	2.1 ± 2.2	IFMR
EGGR 248	0551−0010	WD 0548−001	0.69 ± 0.03	Phot	(1)	2.5 ± 0.7	2.9 ± 0.2	2.7 ± 0.8	IFMR
UCAC4 398-010797	0554−1035	…	0.68 ± 0.01	Gaia He-atm	(8)	2.4 ± 0.6	2.8 ± 0.2	2.6 ± 0.7	IFMR
EGGR 45	0555−0410	WD 0552−041	0.82 ± 0.01	Phot	(1)	3.4 ± 1.5	3.7 ± 0.2	3.6 ± 1.6	IFMR
EGGR 290	0556+0521	WD 0553+053	0.72 ± 0.03	Phot	(1)	2.9 ± 1.4	3.0 ± 0.2	3.0 ± 1.4	IFMR
G 249-36 B	0605+6049	…	1.03 ± 0.08	Dyn+mod	(21)	5.2 ± 1.3	5.9 ± 0.4	5.6 ± 1.4	IFMR
α CMa B	0645−1643	WD 0642−166	1.017 ± 0.025	**GravRed**	(11)	5.1 ± 1.1	5.9 ± 0.4	5.5 ± 1.1	IFMR
EGGR 484	0647+0231	WD 0644+025	0.85 ± 0.15	Spec	(7)	3.6 ± 1.8	4.2 ± 0.3	3.9 ± 1.8	IFMR
LAWD 23	0647+3730	WD 0644+375	0.69 ± 0.03	Spec	(1)	2.5 ± 0.7	2.9 ± 0.2	2.7 ± 0.8	IFMR
L 454-9	0657−3909	WD 0655−390	0.59 ± 0.00	Phot	(1)	1.3 ± 0.5	1.9 ± 0.1	1.6 ± 0.5	IFMR
EGGR 485	0700+3157	WD 0657+320	0.60 ± 0.02	Phot	(1)	1.4 ± 0.5	2.0 ± 0.2	1.7 ± 0.6	IFMR
SCR J0708−6706	0708−6706	WD 0708−670	0.57 ± 0.00	Phot	(1)	1.0 ± 0.4	1.7 ± 0.1	1.4 ± 0.4	IFMR
EGGR 52 A	0730+4810	WD 0727+482A	0.51 ± 0.01	Phot	(1)	…	1.1 ± 0.1	1.1 ± 0.1	IFMR
EGGR 52 B	0730+4810	WD 0727+482B	0.65 ± 0.01	Phot	(1)	2.0 ± 0.6	2.6 ± 0.2	2.3 ± 0.6	IFMR
EGGR 321	0733+6409	WD 0728+642	0.58 ± 0.00	Phot	(1)	1.1 ± 0.4	1.8 ± 0.1	1.5 ± 0.4	IFMR
α CMi B	0739+0513	WD 0736+053	0.553 ± 0.022	**Orbit**	(13)	…	1.5 ± 0.1	1.5 ± 0.1	IFMR

Table 10
(Continued)

Name	Abbrev. Coords (J2000)	WD Name[a]	Final Mass ($M_\odot$)	Final Mass Method	References	Initial Mass (Cummings)[b] ($M_\odot$)	Initial Mass (El-Badry)[c] ($M_\odot$)	Initial Mass (Adopted)[d] ($M_\odot$)	Initial Mass Method
(1)	(2)	(3)	(4)	(5)	(6)	(7)	(8)	(9)	(10)
LAWD 25	0740−1724	WD 0738−172	1.11 ± 0.05	**GravRed**	(5)	6.0 ± 1.2	6.4 ± 0.4	6.2 ± 1.3	IFMR
VB 3	0745−3355	(WD 0743−336)	0.55 ± 0.01	Phot	(1)	⋯	1.5 ± 0.1	1.5 ± 0.1	IFMR
EGGR 426	0750+0711	WD 0747+073.1	0.48 ± 0.01	Phot	(1)	⋯	⋯	1.0 ± 0.1	Low
EGGR 427	0750+0711	WD 0747+073.2	0.56 ± 0.01	Phot	(1)	0.9 ± 0.4	1.6 ± 0.1	1.2 ± 0.4	IFMR
LAWD 26	0753−6747	WD 0752−676	0.73 ± 0.06	Phot	(1)	2.9 ± 1.5	3.1 ± 0.2	3.0 ± 1.5	IFMR
SCR J0753-2524	0753−2524	WD 0751−252	0.52 ± 0.01	Gaia-H	(8)	⋯	1.2 ± 0.1	1.2 ± 0.1	IFMR
L 97-3 A	0806−6618	WD 0806−661	0.58 ± 0.03	Phot	(1)	1.1 ± 0.6	1.8 ± 0.1	1.5 ± 0.6	IFMR
UPM J0812−3529	0812−3529	(WD 0810−353)	0.70 ± 0.01	Gaia H-atm*	(8)	2.6 ± 0.7	2.9 ± 0.2	2.8 ± 0.7	IFMR
G 111-64	0814+4845	WD 0810+489	0.57 ± 0.00	Phot	(1)	1.0 ± 0.4	1.7 ± 0.1	1.4 ± 0.4	IFMR
SCR J0818−3110	0818−3110	WD 0816−310	0.57 ± 0.00	Phot	(1)	1.0 ± 0.4	1.7 ± 0.1	1.4 ± 0.4	IFMR
SCR J0821−6703	0821−6703	WD 0821−669	0.66 ± 0.01	Phot	(1)	2.1 ± 0.6	2.7 ± 0.2	2.4 ± 0.6	IFMR
CD−32 5613	0841−3256	WD 0839−327	0.45 ± 0.05	Spec	(7)	⋯	⋯	1.0 ± 0.1	Low
LP 726-1	0842−1347	WD 0840−136	0.57 ± 0.00	Phot	(1)	1.0 ± 0.4	1.7 ± 0.1	1.4 ± 0.4	IFMR
ι UMa Ab	0859+4802	⋯	1.00 ± 0.30	Dyn+mag	(19)	4.9 ± 3.0	5.8 ± 0.4	5.3 ± 3.0	IFMR
LP 606-32	0859−0058	WD 0856−007	0.52 ± 0.01	Gaia He-atm	(8)	⋯	1.2 ± 0.1	1.2 ± 0.1	IFMR
EGGR 250	0915+5325	WD 0912+536	0.75 ± 0.02	Phot	(1)	3.0 ± 1.5	3.2 ± 0.2	3.1 ± 1.5	IFMR
EGGR 252	1001+1441	WD 0959+149	0.70 ± 0.01	Gaia He-atm	(8)	2.6 ± 0.7	2.9 ± 0.2	2.8 ± 0.7	IFMR
LP 315-42	1011+2845	WD 1008+290	0.68 ± 0.01	Phot	(1)	2.4 ± 0.6	2.8 ± 0.2	2.6 ± 0.7	IFMR
WT 1759	1012−1843	WD 1009−184	0.59 ± 0.02	Phot	(1)	1.3 ± 0.5	1.9 ± 0.1	1.6 ± 0.5	IFMR
EGGR 350	1023+6327	WD 1019+637	0.57 ± 0.05	Phot	(1)	1.0 ± 0.8	1.7 ± 0.1	1.4 ± 0.8	IFMR
LP 37-186	1037+7110	WD 1033+714	0.58 ± 0.00	Phot	(1)	1.1 ± 0.4	1.8 ± 0.1	1.5 ± 0.4	IFMR
EGGR 535	1038−2040	WD 1036−204	0.60 ± 0.01	Phot	(1)	1.4 ± 0.5	2.0 ± 0.2	1.7 ± 0.5	IFMR
BD−18 3019 B	1045−1906	WD 1043−188	0.53 ± 0.11	Phot	(1)	⋯	1.3 ± 0.1	1.3 ± 0.1	IFMR
LAWD 34	1057−0731	WD 1055−072	0.85 ± 0.04	Phot	(1)	3.6 ± 1.6	4.2 ± 0.3	3.9 ± 1.6	IFMR
ξ UMa Bb	1118+3131	⋯	⋯	⋯	⋯	⋯	⋯	1.9 ± 0.9	Conjecture
SCR J1118−4721	1118−4721	WD 1116−470	0.57 ± 0.00	Phot	(1)	1.0 ± 0.4	1.7 ± 0.1	1.4 ± 0.4	IFMR
Ross 627	1124+2121	WD 1121+216	0.61 ± 0.11	Spec	(7)	1.5 ± 1.5	2.1 ± 0.2	1.8 ± 1.5	IFMR
20 Crt B	1134−3250	WD 1132−325	0.60 ± 0.01	Gaia He-atm	(8)	1.4 ± 0.5	2.0 ± 0.2	1.7 ± 0.5	IFMR
GD 140	1137+2947	WD 1134+300	0.97 ± 0.03	Spec	(1)	4.7 ± 1.0	5.6 ± 0.4	5.1 ± 1.1	IFMR
LAWD 37	1145−6450	(WD 1142−645)	0.61 ± 0.01	Phot	(1)	1.5 ± 0.5	2.1 ± 0.2	1.8 ± 0.5	IFMR
SSSPM J1148−7458	1147−7457	⋯	0.488 ± 0.003	Gaia He-atm	(8)	⋯	⋯	1.0 ± 0.1	Low
SDSS J115052.32+683116.1	1150+6831	WD 1148+687	0.69 ± 0.04	Spec	(2)	2.5 ± 0.8	2.9 ± 0.2	2.7 ± 0.8	IFMR
LP 852-7	1205−2333	WD 1202−232	0.59 ± 0.03	Spec	(1)	1.3 ± 0.6	1.9 ± 0.1	1.6 ± 0.6	IFMR
G 197-47	1211+5724	WD 1208+576	0.56 ± 0.09	Phot	(1)	0.9 ± 1.2	1.6 ± 0.1	1.2 ± 1.2	IFMR
WG 21	1226−6612	WD 1223−659	0.45 ± 0.02	Spec	(1)	⋯	⋯	1.0 ± 0.1	Low
WG 22	1238−4948	WD 1236−495	1.13 ± 0.14	Spec	(7)	6.2 ± 1.8	6.5 ± 0.4	6.3 ± 1.8	IFMR
Wolf 457	1300+0328	WD 1257+037	0.70 ± 0.06	Phot	(1)	2.6 ± 1.0	2.9 ± 0.2	2.8 ± 1.0	IFMR
EGGR 436	1308+8502	WD 1309+853	0.71 ± 0.02	Phot	(1)	2.8 ± 0.7	3.0 ± 0.2	2.9 ± 0.7	IFMR
ER 8	1312−4728	WD 1310−472	0.63 ± 0.04	Phot	(1)	1.8 ± 0.7	2.3 ± 0.2	2.1 ± 0.7	IFMR
LP 854-50	1319−2147	WD 1316−215	0.99 ± 0.01	Gaia H-atm	(8)	4.9 ± 1.0	5.7 ± 0.4	5.3 ± 1.1	IFMR
LAWD 45	1319−7823	WD 1315−781	0.69 ± 0.02	Phot	(1)	2.5 ± 0.7	2.9 ± 0.2	2.7 ± 0.7	IFMR
BD-07 3632	1330−0834	WD 1327−083	0.50 ± 0.06	**GravRed**	(5)	⋯	1.0 ± 0.1	1.0 ± 0.1	IFMR
Wolf 489	1336+0340	(WD 1334+039)	0.54 ± 0.03	Phot	(1)	⋯	1.4 ± 0.1	1.4 ± 0.1	IFMR
LSPM J1341+0500	1341+0500	(WD 1338+052)	0.58 ± 0.15	Phot	(2)	1.1 ± 1.9	1.8 ± 0.1	1.5 ± 1.9	IFMR
EGGR 438	1348+2334	WD 1345+238	0.45 ± 0.02	Phot	(1)	⋯	⋯	1.0 ± 0.1	Low
PG 1350−090	1353−0916	WD 1350−090	0.68 ± 0.03	Spec	(1)	2.4 ± 0.7	2.8 ± 0.2	2.6 ± 0.7	IFMR
VVV J141159.32−592045.7	1411−5920	⋯	0.66 ± 0.01	Gaia H-atm*	(8)	2.1 ± 0.6	2.7 ± 0.2	2.4 ± 0.6	IFMR
LP 801-9	1447−1742	WD 1444−174	0.82 ± 0.05	Phot	(1)	3.4 ± 1.6	3.7 ± 0.2	3.6 ± 1.6	IFMR
G 137-24	1535+1247	WD 1532+129	0.57 ± 0.15	Phot	(2)	1.0 ± 1.9	1.7 ± 0.1	1.4 ± 1.9	IFMR
HD 140901 B	1547−3755	WD 1544−377	0.58 ± 0.01	**GravRed**	(5)	1.1 ± 0.5	1.8 ± 0.1	1.5 ± 0.5	IFMR
CD−38 10980	1623−3913	WD 1620−391	0.65 ± 0.01	**GravRed**	(5)	2.0 ± 0.6	2.6 ± 0.2	2.3 ± 0.6	IFMR
Ross 640	1628+3646	WD 1626+368	0.58 ± 0.03	Phot	(1)	1.1 ± 0.6	1.8 ± 0.1	1.5 ± 0.6	IFMR
G 138-38	1632+0851	WD 1630+089	0.59 ± 0.15	Spec	(2)	1.3 ± 1.9	1.9 ± 0.1	1.6 ± 1.9	IFMR

Table 10
(Continued)

Name	Abbrev. Coords (J2000)	WD Name[a]	Final Mass ($M_\odot$)	Final Mass Method	References	Initial Mass (Cummings)[b] ($M_\odot$)	Initial Mass (El-Badry)[c] ($M_\odot$)	Initial Mass (Adopted)[d] ($M_\odot$)	Initial Mass Method
(1)	(2)	(3)	(4)	(5)	(6)	(7)	(8)	(9)	(10)
EGGR 258	1634+5710	WD 1633+572	0.57 ± 0.04	Phot	(1)	1.0 ± 0.7	1.7 ± 0.1	1.4 ± 0.7	IFMR
PG 1633+434	1635+4317	WD 1633+433	0.68 ± 0.04	Phot	(1)	2.4 ± 0.8	2.8 ± 0.2	2.6 ± 0.8	IFMR
DN Dra	1648+5903	WD 1647+591	0.77 ± 0.03	**Astero**	(14)	3.1 ± 1.5	3.3 ± 0.2	3.2 ± 1.5	IFMR
UCAC4 317-104829	1706−2643	(WD 1703−267)	0.808 ± 0.009	Gaia H-atm	(8)	3.3 ± 1.5	3.5 ± 0.2	3.4 ± 1.5	IFMR
EGGR 494	1708+0257	WD 1705+030	0.68 ± 0.09	Phot	(1)	2.4 ± 1.3	2.8 ± 0.2	2.6 ± 1.3	IFMR
G 203-47 B	1709+4340	WD 1708+437	>0.50	Dyn+mod	(22)	>1.4	>2.0	>1.4	IFMR
PM J17476−5436	1747−5436	⋯	0.48 ± 0.01	Gaia He-atm	(8)	⋯	⋯	1.0 ± 0.1	Low
EGGR 372	1748+7052	WD 1748+708	0.79 ± 0.01	Phot	(1)	3.2 ± 1.5	3.4 ± 0.2	3.3 ± 1.5	IFMR
EGGR 199	1749+8246	WD 1756+827	0.55 ± 0.13	Spec	(7)	⋯	1.5 ± 0.1	1.5 ± 0.1	IFMR
LSR J1817+1328	1817+1328	WD 1814+134	0.68 ± 0.02	Phot	(1)	2.4 ± 0.7	2.8 ± 0.2	2.6 ± 0.7	IFMR
G 227-28	1821+6101	WD 1820+609	0.56 ± 0.05	Phot	(1)	0.9 ± 0.8	1.6 ± 0.1	1.2 ± 0.8	IFMR
EGGR 176	1824−1308	WD 1821−131	1.06 ± 0.07	Spec	(3)	5.5 ± 1.3	6.1 ± 0.4	5.8 ± 1.3	IFMR
UCAC4 508-079937	1825+1135	⋯	0.51 ± 0.01	Gaia H-atm	(8)	⋯	1.1 ± 0.1	1.1 ± 0.1	IFMR
EGGR 374	1830+5447	WD 1829+547	0.90 ± 0.07	Phot	(1)	4.0 ± 1.1	5.0 ± 0.3	4.5 ± 1.2	IFMR
LAWD 73	1900+7039	WD 1900+705	0.93 ± 0.02	Phot	(1)	4.3 ± 1.0	5.3 ± 0.3	4.8 ± 1.0	IFMR
EGGR 375	1918+3843	WD 1917+386	0.75 ± 0.04	Phot	(1)	3.0 ± 1.5	3.2 ± 0.2	3.1 ± 1.5	IFMR
LAWD 74	1920−0740	WD 1917−077	0.62 ± 0.02	Phot	(1)	1.6 ± 0.6	2.2 ± 0.2	1.9 ± 0.6	IFMR
UCAC4 482-095741	1921+0613	⋯	0.68 ± 0.01	Gaia H-atm	(8)	2.4 ± 0.6	2.8 ± 0.2	2.6 ± 0.7	IFMR
GD 219	1921+1440	WD 1919+145	0.74 ± 0.03	Spec	(1)	3.0 ± 1.4	3.1 ± 0.2	3.1 ± 1.5	IFMR
PY Vul	1937+2743	WD 1935+276	0.66 ± 0.02	**Astero**	(15)	2.1 ± 0.6	2.7 ± 0.2	2.4 ± 0.7	IFMR
LAWD 79	1956-0102	WD 1953−011	0.79 ± 0.13	Spec	(7)	3.2 ± 1.7	3.4 ± 0.2	3.3 ± 1.7	IFMR
Wolf 1130 B	2005+5426	WD 2003+542	1.24 ± 0.17	**Orbit**	(16)	7.2 ± 2.0	7.2 ± 0.4	7.2 ± 2.1	IFMR
EGGR 498	2005−1056	WD 2002−110	0.72 ± 0.01	Phot	(1)	2.9 ± 1.4	3.0 ± 0.2	3.0 ± 1.4	IFMR
CD−30 17706	2010−3013	WD 2007−303	0.60 ± 0.02	Spec	(1)	1.4 ± 0.5	2.0 ± 0.2	1.7 ± 0.6	IFMR
SCR J2012−5956	2012−5956	WD 2008−600	0.44 ± 0.01	Phot	(1)	⋯	⋯	1.9 ± 0.9	Ultra-low
EC 20173−3036	2020−3027	⋯	0.75 ± 0.01	Gaia H-atm*	(8)	3.0 ± 1.5	3.2 ± 0.2	3.1 ± 1.5	IFMR
HD 340611	2034+2503	WD 2032+248	0.64 ± 0.03	Spec	(1)	1.9 ± 0.7	2.4 ± 0.2	2.2 ± 0.7	IFMR
EGGR 140	2044−6805	WD 2039−682	0.98 ± 0.03	Spec	(1)	4.8 ± 1.0	5.6 ± 0.4	5.2 ± 1.1	IFMR
EGGR 261	2049+3728	WD 2047+372	0.81 ± 0.03	Spec	(1)	3.3 ± 1.5	3.5 ± 0.2	3.4 ± 1.5	IFMR
G 187-8 A	2050+2630	WD 2048+263	0.24 ± 0.04[e]	Phot	(1)	⋯	⋯	1.9 ± 0.9	Ultra-low
G 187-8 B	2050+2630	⋯	⋯	⋯	(1)	⋯	⋯	1.9 ± 0.9	Ultra-low
UCAC4 325-215293	2052−2504	(WD 2049−253)	0.47 ± 0.01	Gaia He-atm	(8)	⋯	⋯	1.0 ± 0.1	Low
Ross 193 B	2056−0450	WD 2054−050	0.49 ± 0.01	Spec	(23)	⋯	⋯	1.0 ± 0.1	Low
WT 765	2101−4906	⋯	0.53 ± 0.01	Gaia H-atm	(8)	⋯	1.3 ± 0.1	1.3 ± 0.1	IFMR
LAWD 83	2113−8149	WD 2105−820	0.78 ± 0.10	Spec	(7)	3.2 ± 1.6	3.4 ± 0.2	3.3 ± 1.6	IFMR
EGGR 378	2118+5412	WD 2117+539	0.56 ± 0.03	Spec	(1)	0.9 ± 0.6	1.6 ± 0.1	1.2 ± 0.6	IFMR
ν Oct B	2141−7723	⋯	0.55 ± 0.05	Dyn+mod	(20)	⋯	1.5 ± 0.1	1.5 ± 0.1	IFMR
L 570-26	2141−3300	WD 2138−332	0.70 ± 0.02	Phot	(1)	2.6 ± 0.7	2.9 ± 0.2	2.8 ± 0.7	IFMR
EGGR 148	2142+2059	WD 2140+207	0.48 ± 0.04	Phot	(1)	⋯	⋯	1.0 ± 0.1	Low
PHL 1716	2143−0659	⋯	0.87 ± 0.01	Gaia H-atm	(8)	3.7 ± 0.9	4.5 ± 0.3	4.1 ± 1.0	IFMR
UCAC4 747-070768	2151+5917	(WD 2150+591)	0.57 ± 0.01	Gaia H-atm	(8)	1.0 ± 0.4	1.7 ± 0.1	1.4 ± 0.5	IFMR
WG 39	2157−5100	WD 2154−512	0.60 ± 0.04	Phot	(1)	1.4 ± 0.7	2.0 ± 0.2	1.7 ± 0.7	IFMR
CD Oct	2204−7513	WD 2159−754	0.92 ± 0.04	Spec	(1)	4.2 ± 1.0	5.3 ± 0.3	4.7 ± 1.1	IFMR
WD 2211−392	2214−3859	WD 2211−392	0.80 ± 0.04	Phot	(1)	3.3 ± 1.5	3.5 ± 0.2	3.4 ± 1.5	IFMR
SCR J2230−7515	2230−7515	WD 2226−755	0.58 ± 0.00	Phot	(1)	1.1 ± 0.4	1.8 ± 0.1	1.5 ± 0.4	IFMR
SCR J2230−7513	2230−7513	WD 2226−754	0.58 ± 0.00	Phot	(1)	1.1 ± 0.4	1.8 ± 0.1	1.5 ± 0.4	IFMR
EGGR 155	2249+2236	WD 2246+223	1.11 ± 0.21	Spec	(7)	6.0 ± 2.3	6.4 ± 0.4	6.2 ± 2.3	IFMR
EGGR 283 A	2251+2939	WD 2248+293	0.35 ± 0.07[e]	Phot	(1)	⋯	⋯	1.9 ± 0.9	Ultra-low
EGGR 283 B	2251+2939	⋯	⋯	⋯	(1)	⋯	⋯	1.9 ± 0.9	Ultra-low
EGGR 453	2253−0646	(WD 2251−070)	0.58 ± 0.03	Phot	(1)	1.1 ± 0.6	1.8 ± 0.1	1.5 ± 0.6	IFMR
LSPM J2309+5506E	2309+5506	WD 2307+548	0.59 ± 0.15	Spec	(2)	1.3 ± 1.9	1.9 ± 0.1	1.6 ± 1.9	IFMR

Table 10
(Continued)

Name	Abbrev. Coords (J2000)	WD Name[a]	Final Mass ($M_\odot$)	Final Mass Method	References	Initial Mass (Cummings)[b] ($M_\odot$)	Initial Mass (El-Badry)[c] ($M_\odot$)	Initial Mass (Adopted)[d] ($M_\odot$)	Initial Mass Method
(1)	(2)	(3)	(4)	(5)	(6)	(7)	(8)	(9)	(10)
ZZ Psc	2328+0514	WD 2326+049	0.593 ± 0.012	**Astero**	(15)	1.3 ± 0.5	1.9 ± 0.1	1.6 ± 0.5	IFMR
GD 1212	2338−0741	WD 2336−079	0.62 ± 0.03	**Astero**	(17)	1.6 ± 0.6	2.2 ± 0.2	1.9 ± 0.7	IFMR
LAWD 93	2343+3232	WD 2341+322	0.65 ± 0.11	**GravRed**	(5)	2.0 ± 1.5	2.6 ± 0.2	2.3 ± 1.5	IFMR

Notes. Codes for mass methods: Direct measurements of final mass (in boldface)—**Accel** = dynamical acceleration, **Astero** = asteroseismology, **GravRed** = gravitational redshift, **Lensing** = gravitational lensing, **Orbit** = dynamical orbital analysis. Estimates of final mass (in normal font)—*Dyn+mag* = partial dynamical orbital analysis and absolute magnitude, *Dyn+mod* = partial dynamical orbital analysis used along with modeling, Gaia H-atm = Gaia-centric hydrogen-atmosphere solution, Gaia H-atm* = assumes a Gaia-centric hydrogen-atmosphere solution even though no spectrum is available, Gaia He-atm = Gaia-centric helium-atmosphere solution, *Phot* = uses fit to the spectral energy distribution, *Spec* = uses fit to the spectrum. Method for estimating the initial mass—IFMR = initial-to-final-mass relation, Low = arbitrary assignment for low final masses $0.45 \leqslant M < 0.56 M_\odot$, Ultra-low = special assignment for ultra-low final masses $M < 0.45 M_\odot$ (see text for details), Conjecture = case-by-case handling (see text for details). References for final mass measurements and estimates: (1) Giammichele et al. (2012), (2) Limoges et al. (2015), (3) Gianninas et al. (2011), (4) Maxted et al. (2002), (5) Silvestri et al. (2001), (6) Brandt et al. (2019), (7) Bédard et al. (2017), (8) Gentile Fusillo et al. (2021), (9) Mason et al. (2017), (10) Sahu et al. (2017), (11) Joyce et al. (2018), (12) Gentile Fusillo et al. (2019), (13) Liebert et al. (2013), (14) Romero et al. (2013), (15) Romero et al. (2012), (16) Mace et al. (2018), (17) Hermes et al. (2014), (18) Baroch et al. (2021), (19) Zhuchkov et al. (2012), (20) Ramm et al. (2021), (21) Winters et al. (2020), (22) Delfosse et al. (1999a), (23) Blouin et al. (2019).

[a] White dwarf designations from McCook & Sion (2016). Those in parentheses are "WD" designations found in SIMBAD but not in McCook & Sion (2016).

[b] The initial mass derived using the initial-to-final mass relation of Cummings et al. (2018). Uncertainties are derived by propagating the listed uncertainty for the final mass and the uncertainties listed for the coefficients of the initial-to-final mass relations in Equations (4)–(6) of Cummings et al. (2018).

[c] The initial mass derived using the initial-to-final mass relation of El-Badry et al. (2018). 1σ uncertainties are chosen to match the initial mass 95.4% (2σ) envelope shown in Figure 3 of El-Badry et al. (2018).

[d] This is our adopted initial mass. When both a Cummings et al. (2018) estimate and an El-Badry et al. (2018) estimate are available, this adopted mass is the unweighted average of those two.

[e] Quoted mass estimate assumes the system is a single white dwarf.

(This table is available in machine-readable form.)

Universe (13.8 Gyr; Planck Collaboration et al. 2020) is predicted[78] to have an initial mass of $10^{-\log(1.38)/2.5} = 0.9M_{\odot}$ (Equation (1.88) of Hansen & Kawaler 1994). Thus, we can consider all twelve of these objects to have initial masses of $\sim 1.0 \pm 0.1M_{\odot}$, and these low-mass estimates are noted by "Low" in the final column of Table 10. Non-evolved late-F and early G dwarfs in this same mass range significantly outnumber (by $\sim 5\times$) the lowest-mass white dwarf progenitors, so this part of the white dwarf population makes only a small contribution to this mass slice of the initial mass function anyway.

For issue (3), a small number of white dwarfs in the census have quoted masses below $\sim 0.45M_{\odot}$. There are two scenarios that can explain the existence of such objects. The first is that unresolved white dwarf doubles will be misinterpreted as being overluminous because, at a fixed value of $T_{\rm eff}$, the Stefan–Boltzmann law will imply a falsely large radius, which results in an erroneously small mass. Of the ultra-low-mass systems within 20 pc, three (LP 991-16, G 187-8, and EGGR 283) were suspected to be double degenerate systems by Giammichele et al. (2012), and those predictions appear to have been verified by Gaia DR3: LP 991-16 and G 187-8 both fall significantly above the white dwarf sequence on the Gaia-based color–magnitude diagram, and EGGR 283 is shown to be an astrometric double with an orbital period of 278.0 days. The masses quoted for these objects in Table 10 are therefore biased low, and these white dwarfs likely have masses $>0.45M_{\odot}$. A fourth system, LP 941-19, has a Gaia DR3 RUWE value of 1.817 and may yet prove to be a double star in its own right and thus also have a biased mass estimate.

The second scenario is that common-envelope mergers or episodic mass loss can produce remnants with pure helium cores (Serenelli et al. 2001), and for these, the cooling times are much longer than those of white dwarfs with carbon–oxygen cores, particularly if the hydrogen envelope is massive enough for its own sustained burning (Alberts et al. 1996; Sarna et al. 1999). This scenario likely explains the low-mass estimate for SCR J2012−5956, which has a Gaia DR3 RUWE value of 0.98 and is likely to be a single star.

As Giammichele et al. (2012) explain, without knowing more about the companion objects in the double degenerate systems, determining new mass estimates for the individual objects is not straightforward. Whether or not the other ultra-low-mass systems are the products of a double-object merger or mass loss from a single star is also guesswork. For these seven white dwarf systems, we have estimated the initial masses as follows. We know only that their initial masses likely fall between ~ 0.9 and ~ 8.0 $M_{\odot}$. Because the median initial mass of 20 pc white dwarfs with solid mass estimates is $1.9M_{\odot}$, we arbitrarily assign each a mass of $1.9 \pm 0.9M_{\odot}$ that, at 1σ, encompasses the initial mass range spanned by 72% of the 20 pc white dwarf sample. These estimates are marked with "Ultra-low" in the last column of Table 10.

Finally, we note three objects in Table 10 whose white dwarf natures are more speculative. Each of these objects is discussed individually below:

1. *χEri B.* Both Fuhrmann & Chini (2012), Fuhrmann et al. (2016) posit that the appreciable X-ray luminosity coming from this system emanates not from the G9 subgiant primary (Gray et al. 2006), χ Eri A, but from the secondary, χ Eri B. Although this companion is 7 mag fainter at V band, they stipulate that it could account for the anomalous X-ray flux if it were a white dwarf.
2. *α For Bb.* The primary in this system, α For A, is an F6 dwarf (Gray et al. 2006), and the secondary, α For B, is a G7 dwarf (Corbally 1984). This B component was found to be a 3.75 day radial velocity binary by Fuhrmann et al. (2016). No spectral lines are visible from the tertiary component, meaning that its mass would have to be below $0.35M_{\odot}$ if it were an M dwarf. However, Fuhrmann et al. (2016) find that the spectrum of α For Ba is enhanced in barium content relative to other dwarfs of a similar spectral type and relative to its primary star, α For A. As barium is an abundant product of nucleosynthesis on the red giant branch, the authors speculate that α For Ba was polluted during the post-main-sequence evolution of α For Bb, now a white dwarf.
3. *ξ UMa Bb.* This is part of a quintuple system. The primary, ξ UMa A, is an F8.5: dwarf (Keenan & McNeil 1989), and the secondary, ξ UMa B, is a G2 dwarf (Keenan & McNeil 1989). Both components are spectroscopic binaries. The A component is an RS CVn double (Samus' et al. 2003), and the B component is a well known double with a period of $\sim$4 days, as summarized in Fuhrmann (2008). A distant, comoving fifth member of this system, the T8.5 dwarf WISE J111838.70+312537.9, has also been identified (Wright et al. 2013). As with α For Ba discussed above, ξ UMa Ba has an enhanced barium abundance, leading Fuhrmann et al. (2016) to speculate that ξ UMa Bb is a white dwarf and the donor responsible for the extra barium content.

For these three white dwarfs, we also arbitrarily assign each an initial mass of $1.9 \pm 0.9M_{\odot}$, as done for the objects with ultra-low-mass estimates. Estimates for these three white dwarfs are marked with "Conjecture" in the last column of Table 10.

6.1.2. Giants and Subgiants

There are a number of objects in the 20 pc census that have evolved off the main sequence but have not yet become white dwarfs. Table 11 includes all objects in Table 4 that have a luminosity class more luminous than V and/or fall in a locus on the absolute magnitude versus color diagrams that identifies them as post-main-sequence stars.

Several of these have direct mass measurements from either orbital dynamics or asteroseismology. The rest have had their masses estimated from other methods, primarily via comparison of their placement on the H-R diagram in relation to modeled evolutionary tracks or via fits of their spectra to atmospheric models. For some objects with IV-V or IV luminosity classes, other published spectral types indicate a V luminosity class, or their placement on the H-R diagram suggests a main-sequence star. This is reflected in the mass estimates given in Table 11.

One curious observation from the absolute magnitude versus spectral type diagrams of Figure 4 is the vertical locus of evolved stars lying well above the main sequence but concentrated almost exclusively at a spectral class K0. On the M_{W4} versus spectral type plot, for example, we find fifteen objects (not counting the young,

[78] Below masses of $\sim 5M_{\odot}$, objects of subsolar metallicity are predicted to evolve more rapidly than those of solar metallicity (Figure 5 of Mowlavi et al. 1998; see also Figure 11 of Mowlavi et al. 2012). However, very few stars in the solar neighborhood have metallicities significantly below solar. See Section 6.2.2.

Table 11
Giants and Subgiants in the 20 pc Census

Name	Abbrev. Coords (J2000)	Sp. Type[a]	Mass[b] ($M_\odot$)	Mass References	Method
(1)	(2)	(3)	(4)	(5)	(6)
β Cas	0009+5908	F2 III	1.91 ± 0.02	(9)	Interferometry + rapid-rotation models
α Tri A	0153+2934	F6 IV	1.70	(15)	Spectral fit to atmospheric models
χ Eri A	0155−5136	G9 IV	1.58	(13)	Placement on evolutionary tracks
10 Tau	0336+0024	F9 IV-V	1.139 ± 0.016	(23)	Interferometry + model isochrones
δ Eri	0343−0945	K1 III-IV	1.33 ± 0.07	(8)	**Asteroseismology**
τ^6 Eri	0346−2314	F5 IV-V	1.44 ± 0.13	(13)	Placement on evolutionary tracks
ϵ Ret A	0416−5918	K2 III	1.48	(25)	Spectral fit to atmospheric models
HD 283750 Aa	0436+2707	K3 IV ke	0.84 ± 0.19	(15)	Placement on evolutionary tracks
π^3 Ori	0449+0657	F6 IV-V	1.283 ± 0.006	(23)	Interferometry + model isochrones
α Aur Aa	0516+4559	G1 III	2.569 ± 0.007	(27)	**Orbital dynamics**
α Aur Ab	0516+4559	K0 III	2.483 ± 0.007	(27)	**Orbital dynamics**
ξ Gem	0645+1253	F5 IV-V	1.706 ± 0.012	(23)	Interferometry + model isochrones
HD 53143	0659−6120	K0 IV-V (k)	1.0	(22)	Placement on color–magnitude diagram
α Gem Aa	0734+3153	A1.5 IV+	2.98	(26)	Estimated from spectral type/color
β Gem	0745+2801	K0 III	1.91 ± 0.09	(16)	**Asteroseismology**
ρ Pup[c]	0807−2418	F5II kF2II mF5II	1.9 ± 0.1	(1)	Placement of general ρ Pup class on evolutionary tracks
HD 73752 Aa	0839−2239	G5 IV	1.21	(14)	Spectral fit to atmospheric models
ρ^1 Cnc A	0852+2819	K0 IV-V	0.91 ± 0.02	(28)	Placement on evolutionary tracks
10 UMa A	0900+4146	F5 IV-V	1.396 ± 0.002	(4)	**Orbital dynamics**
HD 78366[d]	0908+3352	G0 IV-V	1.08	(15)	Spectral fit to atmospheric models
τ^1 Hya Aa	0929−0246	F5.5 IV-V	1.20	(11)	Placement on evolutionary tracks
θ UMa A	0932+5140	F5.5 IV-V	1.506 ± 0.095	(23)	Interferometry + model isochrones
15 LMi	0948+4601	G0 IV-V	1.11 ± 0.15	(7)	Spectral fit to atmospheric models
δ Leo	1114+2031	A5 IV(n)	2.061 ± 0.006	(23)	Interferometry + model isochrones
β Vir	1150+0145	F8.5 IV-V	1.42 ± 0.08	(8)	**Asteroseismology**
HD 104304 A	1200−1026	G8 IV	0.98	(25)	Spectral fit to atmospheric models
e Vir Aa	1316+0925	G0 IV	1.22	(12)	Placement on evolutionary tracks
70 Vir	1328+1346	G5 V[f]	1.14 ± 0.08	(31)	$L_{\rm bol}$ + $T_{\rm eff}$ + spectrum-based $\log(g)$
τ Boo A	1347+1727	F7 IV-V	1.34	(25)	Spectral fit to atmospheric models
η Boo Aa	1354+1823	G0 IV	1.77 ± 0.11	(8)	**Asteroseismology**
θ Cen	1406−3622	K0 III	1.27	(13)	Placement on evolutionary tracks
α Boo	1415+1910	K0 III	0.80 ± 0.20[g]	(19)	**Asteroseismology**
HD 125072	1419−5922	K3 IV	0.88	(25)	Spectral fit to atmospheric models
α Cen B	1439−6050	K2 IV C2+1**	0.909 ± 0.003	(30)	**Orbital dynamics**
HD 130948 A	1450+2354	F9 IV-V	1.18 ± 0.16	(7)	Spectral fit to atmospheric models
λ Ser	1546+0721	G0 IV-V	1.15 ± 0.15	(7)	Spectral fit to atmospheric models
HD 140901 A	1547−3754	G7 IV-V	0.99	(25)	Spectral fit to atmospheric models
14 Her	1610+4349	K0 IV-V	0.73 ± 0.10	(7)	Spectral fit to atmospheric models
ζ Her A	1641+3136	G2 IV	1.04 ± 0.03	(20)	**Orbital dynamics**
ϵ Sco A	1650−3417	K1 III	1.4 ± 0.1	(18)	**Asteroseismology**
HD 154088	1704−2834	K0 IV-V	0.92	(25)	Spectral fit to atmospheric models
HD 158614 A	1730−0103	G9- IV-V Hdel1	0.963 ± 0.005	(4)	**Orbital dynamics**
α Oph A	1734+1233	A5 IV nn	2.20 ± 0.06	(17)	**Orbital dynamics**
26 Dra A	1734+6152	G0 IV-V	1.06	10	Orbital dynamics + astrophysical assumptions
μ Ara	1744−5150	G3 IV-V	1.21 ± 0.13	(8)	**Asteroseismology**
μ^1 Her A	1746+2743	G5 IV	$1.10^{+0.11}_{-0.06}$	(21)	**Asteroseismology**
η Ser	1821−0253	K0 III-IV	1.45 ± 0.21	(8)	**Asteroseismology**
110 Her	1845+2032	F5.5 IV-V	1.422 ± 0.009	(23)	Interferometry + model isochrones
b Aql	1924+1156	G7 IV Hdel1	1.186 ± 0.015	(23)	Interferometry + model isochrones
δ Aql Aa	1925+0306	F1 IV-V(n)	1.45	(11)	Placement on evolutionary tracks
HD 188088 Aa	1954−2356	K2 IV (k)	0.85	(29)	Orbital dynamics + other assumptions[e]
β Aql A	1955+0624	G9.5 IV	1.26 ± 0.18	(8)	**Asteroseismology**
HD 190360	2003+2953	G7 IV-V	0.92 ± 0.12	(7)	Spectral fit to atmospheric models
δ Pav	2008−6610	G8 IV	1.07 ± 0.13	(8)	**Asteroseismology**
η Cep	2045+6150	K0 IV	1.6	(2)	Placement on evolutionary tracks
ν Oct A	2141−7723	K1 III	1.6 ± 0.1	(24)	Placement on evolutionary tracks

Table 11
(Continued)

Name	Abbrev. Coords (J2000)	Sp. Type[a]	Mass[b] ($M_\odot$)	Mass References	Method
(1)	(2)	(3)	(4)	(5)	(6)
δ Cap Aa	2147−1607	kA5hF0mF2 III	2.0	(6)	**Orbital dynamics**
γ Cep A	2339+7737	K1 III	1.294 ± 0.081	(5)	**Orbital dynamics**

Notes. References for the mass measurements and estimates: (1) Abt (2017), (2) Affer et al. (2005), (3) Allende Prieto & Lambert (1999), (4) Andrade (2019), (5) Mugrauer et al. (2022), (6) Batten & Fletcher (1992), (7) Brewer et al. (2016), (8) Bruntt et al. (2010). (9) Che et al. (2011), (10) Cvetkovic & Ninkovic (2010), (11) David & Hillenbrand (2015), (12) D'Orazi et al. (2017), (13) Fuhrmann & Chini (2012), (14) Fuhrmann et al. (2011a), (15) Fuhrmann (2008), (16) Hatzes et al. (2012), (17) Gardner et al. (2021), (18) Kallinger et al. (2019), (19) Kallinger et al. (2010), (20) Katoh et al. (2013), (21) Li et al. (2019), (22) Nielsen et al. (2019), (23) Boyajian et al. (2012), (24) Ramm et al. (2021), (25) Takeda et al. (2007), (26) Tokovinin (2008), (27) Torres et al. (2015), (28) von Braun et al. (2011), (29) Fekel et al. (2017), (30) Akeson et al. (2021), (31) Stassun et al. (2017).

[a] References for Sp. Type can be found in Table 4.

[b] Methods in bold involve direct mass measurements.

[c] Luminosity class II suggests a more evolved state for this star than its placement on the H-R diagram—subgiant or giant—attests. The cause for this "anomalous luminosity effect" is unknown but is a feature of the ρ Puppis class of pulsators (Gray & Corbally 2009).

[d] Fuhrmann (2008) believes this object is young, not evolved.

[e] Fekel et al. (2017) calculates minimum masses ($M \sin^3 i$) from orbital dynamics of $0.8463 \pm 0.0014\ M_\odot$ for HD 188088 A and $0.8316 \pm 0.014\ M_\odot$ for HD 188088 B. These authors believe that both components are normal K dwarfs, the subgiant classification likely resulting from the slight metal richness of these stars. Given that these minimum masses are close to the mass expected for this dwarf class, the inclination is suspected of being near 90° despite the lack of eclipses in the system.

[f] Some references classify this object as G4 V-IV (e.g., Strassmeier et al. 2018), and its placement just above the main sequence indicates that it may just be moving into a later stage of evolution.

[g] Evolutionary models suggest a mass of $1.08 \pm 0.06 M_\odot$, toward the upper end of the range deduced from asteroseismology, and a relatively old age of $7.1^{+1.5}_{-1.2}$ Gyr (Ramírez & Allende Prieto 2011). (An object with a mass of $\sim$0.90 $M_\odot$ has a main-sequence lifetime exceeding a Hubble time and will not yet have evolved to a giant state; see Section 1.7 of Hansen & Kawaler 1994.)

(This table is available in machine-readable form.)

main-sequence star β Pic, whose unusual position is caused by its debris disk) that lie more than 1 mag above the main sequence for their spectral classes. These can be divided into a group of five objects (β Cas, ρ Pup, α Tri, η Boo, and ζ Her) with classes between F2 and G2 and a group of ten objects (δ Eri, β Aql A, η Cep, γ Cep A, ν Oct A, η Ser, β Gem, θ Cen, ϵ Sco A, and α Boo) with a very narrow range of types from G9.5 to K1. As we can see from Table 11, this first group of five objects has a mass range of 1.0–1.9 $M_\odot$ and falls in a locus in Figure 4 indicating evolution off the main sequence and onto the evolutionary subgiant branch.[79] The other group, of ten objects, is comprised of stars with an identical mass range (1.0–1.9 $M_\odot$) that are now ascending the red giant branch. Evolution along the subgiant branch is more rapid than the climb up the red giant branch, explaining the overabundance of red giants (Tables 3–4 of Iben 1967). The fact that these latter stars are concentrated so narrowly in spectral type is a consequence of the fact that, at typical disk ages for masses in this same range, the red giant branch is confined narrowly to a temperature of $\sim$5000 K (Figure 13 of Iben 1967; Figure 8 of Bressan et al. 2012), which is the temperature that corresponds to early K giant spectral classes (Figure 2 of Dyck et al. 1996; Figure 4 of Richichi et al. 1999; Table 10 of Heiter et al. 2015). Objects above this mass range ($>1.9 M_\odot$) are few in number in the 20 pc census (<3% of the total; see Table 4) and evolve through their giant phases in no more than a few tens of Myr (Table 3 of Iben 1967); as a consequence of their rarity and rapid evolution, no such giants of earlier type are seen.

[79] Note that the assigning of an object's subgiant or giant *luminosity class* via spectroscopic gravity diagnostics does not necessarily equate to its presumed *evolutionary* status as a subgiant or red giant branch star via its placement in color–magnitude diagrams.

6.1.3. Brown Dwarfs

Brown dwarfs follow no mass–luminosity relation because they constantly cool over time. If the age of the brown dwarf is known, this can be used to estimate the mass from evolutionary models, but age is a difficult parameter to measure for nonyouthful disk objects. We therefore must resort to simulations to tease out information regarding the mass function. In Kirkpatrick et al. (2019a, 2021a), we took the empirical distribution of brown dwarf *effective temperatures* and compared that to various predicted temperature distributions modeled by taking the shape of the brown dwarf mass function, the value of its low-mass cutoff, and the underlying evolutionary model suite as free parameters. For the analysis of this paper, we will employ those same methods, using an updated suite of predictions by Raghu et al. (2024).

Here, we compare the Kirkpatrick et al. (2021a) accounting of all 525 known 20 pc L, T, and Y dwarfs to that given in Table 4. Additions and subtractions to this tally are listed in Table 12. We find that eight objects have fallen out of the 20 pc sample, all because of new parallax measurements or revised distance estimates that place them outside of 20 pc. On the other hand, 65 objects are newly added. These additions include 38 new discoveries (37 by the Backyard Worlds citizen science group, four of which are new companions), nine new companions recently announced in the literature, one new companion announced here but found in Gaia, three new published parallaxes with $d < 20$ pc, 12 previously overlooked companions, and two previously overlooked objects (DENIS J065219.7-253450, presumably due to a transcription error, and SSSPM J1444-2019, whose subdwarf type had earlier been updated from late-M to early-L). To facilitate the analysis on the revised $T_{\rm eff}$ distribution, we have listed in Table 12 the

Table 12
Additions to and Subtractions from the 20 pc L, T, and Y Census of Kirkpatrick et al. (2021a)

Object	Reason for Change	References	$T_{\rm eff}$[a] (K)
(1)	(2)	(3)	(4)
	Additions		
WISE J003110.04+574936.3 B	New companion	Best et al. (2021)	1275 ± 200[b]
CWISE J003507.81−153233.5	New discovery	This paper (Table 2)	686 ± 79
2MASSW J0036159+182110 B	Overlooked companion	Bernat et al. (2010)	1125 ± 79
CWISE J013343.58+803153.1	New discovery	This paper (Table 2)	1181 ± 79
CWISE J014433.03−545545.5	New discovery	This paper (Table 2)	751 ± 79
CWISER J021550.96+674017.2	New companion to HD 13579	This paper (Table 2 and Section 2.2)	1125 ± 79
CWISER J021612.11+423015.9	New discovery	This paper (Table 2)	460 ± 79
L 440-30 B (0219−3646)	Overlooked companion	Kürster et al. (2008)	1613 ± 134
Ross 19 B (0219+3518)	New companion	Schneider et al. (2021)	460 ± 79
CWISE J032600.46+421058.5	New discovery	This paper (Table 2)	624 ± 79
WISE J033605.05−014350.4 B	New companion	Calissendorff et al. (2023)	325 ± 79[c]
Wolf 227B (0352+1701)	Overlooked companion	Winters et al. (2018)	2000 ± 81[h]
CWISE J035856.18+480244.9	New discovery	This paper (Table 2)	511 ± 79
L 375-2 B (0432−3947)	New discovery	Silverstein et al. (2022)	1200 ± 333[i]
LP 775-31 B (0435−1606)	Overlooked companion	Cortés-Contreras et al. (2017)	1600 ± 81[j]
Wolf 230 C (0507+1758)	Overlooked companion	Winters et al. (2020)	1200 ± 333[k]
CWISE J053046.20+440849.2	New discovery	This paper (Table 2)	1125 ± 79
CWISE J060938.91+062513.2	New discovery	This paper (Table 2)	1420 ± 134
DENIS J063001.4−184014 B	New companion	Sahlmann et al. (2021)	1420 ± 134
DENIS J063001.4−184014 (C)	New companion	Sahlmann et al. (2021)	1420 ± 134
WISEA J064750.85−154616.4 B	New companion	Best et al. (2021)	1275 ± 200[b]
DENIS J065219.7−253450	Overlooked object	Gaia DR3	2196 ± 88
PSO J103.0927+41.4601 B (0652+4127)	New companion	Best et al. (2021)	1190 ± 100[d]
CWISE J075227.38+053802.6	New discovery	This paper (Table 2)	1273 ± 79
CWISE J075853.12−232645.8	New discovery	This paper (Table 2)	1209 ± 79
L186-67 Ab (0822−5726)	Overlooked companion	Bergfors et al. (2010)	2091 ± 88[l]
CWISE J083130.98+154018.4	New discovery	This paper (Table 2)	566 ± 79
CWISE J092710.37−474155.5	New discovery	This paper (Table 2)	624 ± 79
LP 788-1 B (0931−1717)	Overlooked companion	Winters et al. (2017), Vrijmoet et al. (2020)	1200 ± 333[m]
WISEU J100241.49+145914.9	New companion to G 43-23	This paper (Table 2 and Section 2.2)	624 ± 79
CWISE J100521.10−691226.8	New discovery	This paper (Table 2)	1190 ± 79
CWISE J100628.98+105408.5	New discovery	This paper (Table 2)	566 ± 79
CWISE J105349.12−460239.1	New discovery	This paper (Table 2)	686 ± 79
1RXS J121408.0-234516 B	New companion	Gaia + this paper (Table 4)	1250 ± 150[n]
e Vir Ab (1316+0925)	Overlooked companion	Kuzuhara et al. (2013), Bonnefoy et al. (2018)	624 ± 79
2MASSW J1326201−272937 B	New companion	Best et al. (2021)	1400 ± 200[e]
WT 460 B (1411−4132)	Overlooked companion	Montagnier et al. (2006)	2096 ± 134
SSSPM J1444−2019	Revised spectral type	Kirkpatrick et al. (2016)	2207 ± 88
DENIS-P J1454078−660447 B	Overlooked companion	Vrijmoet et al. (2020)	1100 ± 250[f]
WISEA J153429.75−104303.3	New parallax	Kirkpatrick et al. (2021b)	686 ± 79
2MASS J15345325+1219495	New parallax	Gaia DR3	1532 ± 88
SCR J1546−5534 B	New companion	Vrijmoet et al. (2022)	2085 ± 88[p]
CWISE J161546.07+671227.4	New discovery	This paper (Table 2)	1254 ± 79
CWISE J163336.14−325305.3	New discovery	This paper (Table 2)	819 ± 79
VVV J165507.19−421755.5	New discovery	Schapera et al. (2022) and this paper (Table 2)	1125 ± 79
DENIS-P J170548.38−051645.7 B	Overlooked companion	Dieterich et al. (2014)	1838 ± 134
CWISE J171221.50+495318.2	New discovery	This paper (Table 2)	624 ± 79
CWISE J171338.81−183322.7	New discovery	This paper (Table 2)	1227 ± 79
CWISE J173830.94−773024.3	New discovery	This paper (Table 2)	624 ± 79
2MASS J17502484−0016151 B	Overlooked companion	Henry et al. (2018)	1100 ± 250[f]
CWISE J180308.71−361332.1	New discovery	This paper (Table 2)	686 ± 79
CWISE J181005.77−101001.2	New parallax	Lodieu et al. (2022)	800 ± 100[g]
CWISE J181125.34+665806.4	New discovery + parallax	This paper (Table 2 and Appendix A.3.2)	412 ± 79
CWISE J184803.45−143232.3	New companion to G 155-42	This paper (Table 2 and Section 2.2)	686 ± 79
CWISE J203438.09−462543.1	New discovery	This paper (Table 2)	624 ± 79
CWISE J210057.80−624555.4	New discovery	This paper (Table 2)	1296 ± 134
CWISE J215841.48+732842.8	New discovery	This paper (Table 2)	624 ± 79
2MASSW J2224438−015852 B	New companion	Best et al. (2021)	1400 ± 200[e]
CWISE J222701.50+260450.0	New discovery	This paper (Table 2)	460 ± 79
CWISE J223002.32+424655.3	New discovery	This paper (Table 2)	751 ± 79

Table 12
(Continued)

Object	Reason for Change	References	$T_{\rm eff}$[a] (K)
(1)	(2)	(3)	(4)
CWISE J224547.21−433341.5	New discovery	This paper (Table 2)	686 ± 79
CWISE J230930.81+145630.6	New discovery	This paper (Table 2)	686 ± 79
CWISE J233817.04−732930.3	New discovery	This paper (Table 2)	624 ± 79
CWISE J233819.49−385421.2	New discovery	This paper (Table 2)	1254 ± 79
CWISE J235120.60−700026.2	New discovery	This paper (Table 2)	460 ± 79
	Subtractions		
CWISE J061741.79+194512.8 A	Revised distance estimate	Humphreys et al. (2023)	1465 ± 134
CWISE J061741.79+194512.8 B	Revised distance estimate	Humphreys et al. (2023)	686 ± 79
Kelu-1 A (1305−2541)	New parallax	Gaia DR3	1931 ± 134
Kelu-1 B (1305−2541)	New parallax	Gaia DR3	1750 ± 134
2MASSI J1526140+204341	New parallax	Gaia DR3	1518 ± 157
SDSS J163022.92+081822.0	New parallax	This paper (Appendix A.3.1)	970 ± 88
2MASS J23174712−4838501	New parallax	Gaia DR3	1537 ± 197
2MASS J23312378−4718274	New parallax	This paper (Appendix A.3.1)	1125 ± 79

Notes.
[a] For the new additions, temperature values with uncertainties of ±88 K were determined via the M_H vs. $T_{\rm eff}$ relation in Table 13 of Kirkpatrick et al. (2021a), and those with uncertainties of ±134 K or ±79 K were determined with the (assumed) spectral type vs. $T_{\rm eff}$ relations in the same table, unless otherwise noted. For subtractions, the temperature values are taken from Table 11 of Kirkpatrick et al. (2021a).
[b] No information is yet available on this companion, so the temperature estimate is set to cover the spectral type range from late-L to mid-T.
[c] Temperature estimate is taken from Calissendorff et al. (2023), although the uncertainty has been inflated to match the typical uncertainties in Kirkpatrick et al. (2021a).
[d] No information is yet available on this companion, so the temperature estimate is set to cover the spectral type range from early-T to mid-T.
[e] No information is yet available on this companion, so the temperature estimate is set to cover the spectral type range from mid-L to early-T.
[f] Little information is available on this companion, so the temperature estimate is set to cover the spectral type range from mid-L to mid-T.
[g] Temperature estimate is taken from Lodieu et al. (2022).
[h] Winters et al. (2018) conclude this is likely an early-L dwarf, so we set the temperature to cover the typical range for L0 to L4 dwarfs.
[i] We assume a huge temperature range to encompass the full substellar regime, as Silverstein et al. (2022) is able to provide only limited constraints on this companion.
[j] The ΔI magnitude from Cortés-Contreras et al. (2017) suggests a mid-L dwarf, so we estimate a temperature corresponding to this range.
[k] We assume a huge temperature range to encompass the full substellar regime, as Winters et al. (2020) is able to provide only a minimum mass of $\sim 44 M_{\rm Jup}$ for this companion.
[l] We use the $\Delta i'$ magnitude listed in Bergfors et al. (2010) to estimate a type of L1, which we use for the temperature estimation.
[m] We assume a huge temperature range to encompass the full substellar regime, as this object is only known as a likely brown dwarf (Vrijmoet et al. 2022).
[n] The M_G value derived from Gaia DR3 data suggests an early-T dwarf, and we assign a temperature appropriate for late-L through mid-T given that no spectrum yet exists.
[p] We base our temperature estimate on the estimated L1 type we derive in Table 4.

(This table is available in machine-readable form.)

estimated temperatures of each of the additions and subtractions. Further analysis can be found in Section 7.

6.2. Other Complications

6.2.1. Youth

Will the estimation of masses for young objects be biased if those estimates use a relation based on much older stars? Evolutionary models suggest that, below a mass of $\sim 0.4 M_\odot$, the contraction of a star down to the main sequence follows a Hayashi track along which the star's effective temperature remains approximately fixed (Section 16.2.5 of Stahler & Palla 2004). If a temperature-based metric is used for estimating the masses of such stars, then such estimates will be accurate. At higher masses, however, the descent along the Hayashi track will be interrupted when a radiative zone develops. The star then moves via a Henyey track along which the temperature slowly increases until the star reaches the main sequence. For stars with masses above $\sim 0.4 M_\odot$, this evolution to the main sequence occurs within the first 100 Myr.

This means that objects in the 20 pc census that have masses above $\sim 0.4 M_\odot$ and ages less than 100 Myr should have their mass estimates more carefully considered. The Montreal Open Clusters and Associations database (J. Gagné et al. 2024, in preparation; Gagné et al. 2018)[80] is a compilation of known stellar associations, stellar streams, moving groups, and open clusters within 500 pc of the Sun. A search of this database on 2023 May 18 for objects within 20 pc of the Sun and likely belonging to one of these young groups yielded 217 systems. The only objects in this list with ages below 100 Myr are those believed to be members[81] of the β Pic Moving Group (∼26 Myr), the Columba Association (∼42 Myr), the Argus Association (∼45 Myr), the Carina Assocation (∼45 Myr),

[80] https://mocadb.ca/
[81] Several 20 pc objects are tentatively associated with Greater Scorpius–Centaurus (age ≈15 Myr) according to Kerr et al. (2021), but closer investigation of kinematics, color–magnitude diagrams, lithium abundances, rotation periods, and nondetections at X-ray wavelengths suggests that these are much older objects.

Table 13
20 pc Members of Young Associations and Moving Groups with Ages < 100 Myr

Objects in System	Coords. (J2000)	Spectral Type[a]	Membership	Likelihood[b]
(1)	(2)	(3)	(4)	(5)
2MASSW J0045214+163445	0045+1634	L2 β	Argus	high
Ross 15	0159+5831	M4	Carina	possible
[BHR2005] 832-2	0311+0106	M5.5	β Pic	possible
LP 944-20	0339−3525	M9	Argus	possible
BD−21 1074 ABC	0506−2135	M1.5 V e, [M1], [M2.5]	β Pic	confirmed
PSO J076.7092+52.6087	0506+5236	T4.5	Argus	possible
V2689 Ori, PM J05366+1117	0536+1119	M0.5 V ek, M4	β Pic	possible
β Pic	0547−5103	A6 V	β Pic	confirmed
AP Col	0604−3433	M4.5 V e	Argus	confirmed
2MASS J06244595−4521548	0624−4521	L5	Argus	high
LSPM J0714+3702	0714+3702	M8	Argus	possible
WISEPA J081958.05−033529.0	0819−0335	T4	β Pic	high
G 161-71[c]	0944−1220	M4.5 V	Argus	high
TWA 22 AB	1017−5354	M5:, M5.5:	β Pic	confirmed
WISE J104915.57−531906.1 AB	1049−5319	L7.5, T0.5:	Argus[d]	high
SDSS J121951.45+312849.4	1219+3128	L9.5	Argus	confirmed
G 164-47	1309+2859	M4 V	Carina	possible
α Cir AB	1442−6458	A7 Vp SrCrEu, K5 V	β Pic	possible[e]
2MASS J17534518−6559559	1753−6559	L4	Argus	possible
WISE J180001.15−155927.2	1800−1559	L4.5	β Pic	possible
UCAC3 152-281185, UCAC3 152-281176	1845−1409	M5 V e, M5 V e	Argus	possible
HD 182488 AB	1923+3313	G9+V, T7:	Argus	confirmed
LEHPM 2-1265 AB	2033−4903	[M5 composite]	β Pic	possible
AU Mic, AT Mic AB	2041−3226	M1, M4.5 V, M4 V	β Pic	confirmed
PSO J319.3102−29.6682	2117−2940	T0:	β Pic	high
WISEPC J225540.74−311841.8	2255−3118	T8	β Pic	high
HD 220140 AB, LP 12-90	2319+7900	K2 V k, M4, M5: V	Columba	possible
G 190-28, G 190-27	2329+4128	M3.5, M4.5	Columba	possible
LP 704-15, LP 704-14	2357−1258	M3 V, M4 V	Argus	possible

Notes.
[a] References for spectral type are listed in Table 4 along with information on whether the types are based on optical or near-infrared data. Spectral types in brackets are estimates based on the absolute G-band magnitude.
[b] Our notes translate to the following codes in the `moca_mtid` column in table `moca_membership_types` of the MOCA database: confirmed = BF (bona fide member), high = HM (high-likelihood candidate member), and possible = CM (candidate member). Objects with MOCA codes of LM (low-likelihood candidate member), AM (ambiguous candidate member), and R (rejected candidate member) were ignored.
[c] On the $G_{BP} - G_{RP}$ vs. M_G and $G - J$ vs. M_G diagrams of Figure 5, this M4.5 dwarf appears to be ∼1.5 mag above the locus of other objects of the same color despite having a Gaia DR3 RUWE value of 1.114. This could alternatively be interpreted as this object's being ∼0.5 mag redder than the bulk of objects of similar absolute magnitude. In colors not involving Gaia magnitudes, no discrepancy is seen; this object falls at an M dwarf spectral type where many of these other colors ($J - K_s$, J − W2, W1−W2) are degenerate with spectral type over a large range, so such a discrepancy may not be noticeable. Malo et al. (2014a), and Ujjwal et al. (2020) identify this as a possible member of the Argus Association, so these discrepancies may be related to a young, active chromosphere.
[d] Also identified as a member of the 500 Myr old Oceanus Group (Gagné et al. 2023).
[e] The possible β Pic Moving Group association for α Cir A is listed for both components, as the "high" likelihood Greater Scorpius–Centaurus association for α Cir B is highly suspect.

(This table is available in machine-readable form.)

and the Octans-Near Association (∼55 Myr).[82] These are listed in Table 13.

Because a mass of $0.4M_{\odot}$ corresponds to a spectral type of M2.5–M3 (Table 7 of Mann et al. 2019), we can use the spectral type to identify which of the young 20 pc objects are the ones whose mass estimations may need special handling. The only objects in Table 13 with spectral types earlier than this are BD−21 1074 ABC, V2689 Ori, β Pic, α Cir AB, HD 182488 A, AU Mic, and HD 220140 A. Three of these are early M dwarfs for which the brief jog along the Henyey track before reaching the main sequence covers such a small range in temperature that their mass estimates should not be unduly affected.

This leaves only four individual objects to consider, and two of these have dynamical mass measurements already. For β Pic, Lacour et al. (2021) used astrometry of the exoplanet system to derive the mass of the host star ($1.75 \pm 0.03\ M_{\odot}$) using only a uniform mass prior between 1.4 and 2.0 $M_{\odot}$ on β Pic itself. HD 182488 A has a loosely constrained dynamical mass measurement from Brandt et al. (2019) of $0.94^{+0.17}_{-0.27}M_{\odot}$. This leaves only two young systems with possibly skewed mass estimates, and this represents such a small percentage of 20 pc stars with types earlier than M0 (<1%) that no bias will be imparted on the overall derived mass distribution.

[82] These age estimates are taken directly from the table `calc_association_properties` in the Montreal Open Clusters and Associations database.

Table 14
20 pc Objects with Low-metallicity and/or Halo Kinematics

Name	Coords (J2000)	Sp. Type[a]	Radial Vel. (km s^{-1})	RV References	Kinem. Group
(1)	(2)	(3)	(4)	(5)	(6)
85 Peg	0002+2704	G5 V Fe-1	−35.57 ± 0.35	1	thin disk
6 Cet	0011−1528	F8 V Fe-0.8 CH-0.5	14.95 ± 0.13	3	thin disk
HD 4391	0045−4733	G5 V Fe-0.8	−10.92 ± 0.12	3	thin disk
μ Cas	0108+5455	K1 V Fe-2	−97.09 ± 0.25	3	thick disk
LP 410-38	0230+1648	sdM6e	49.56 ± 6.65	3	thin disk
LP 651-7	0246−0459	M6 V	33.28 ± 2.32	3	halo
BD+33 529	0252+3423	(sd)K5 V ([Fe/H] = −0.63)	−49.89 ± 0.15	3	thick disk
G 174-25	0258+5014	sdM3	−30.24 ± 0.45	3	thin disk
LP 994-33	0302−3950	sdM5	…	…	thick disk?
Ross 578	0338−1129	d/sdM2	−84.88 ± 0.56	3	halo
HD 25329	0403+3516	K3 Vp Fe-1.7	−25.57 ± 0.13	3	halo
ζ Dor	0505−5728	F9 V Fe-0.5	−1.45 ± 0.12	3	thin disk
Kapteyn's Star	0511−4501	sdM1p	245.05 ± 0.13	3	halo
EGGR 290	0556+0521	DAP8.7	−414.02 ± 10.41	3	(RV in error)[h]
2MASS J06453153−6646120	0645−6646	sdL8	…	…	thick disk?
YY Gem	0734+3152	M0.5 Ve Fe-2	32.66	2	thin disk
212 Pup	0752−3442	F5 V Fe-0.5	28.03 ± 0.16	3	thin disk
HD 65583	0800+2912	K0 V Fe-1.3	14.79 ± 0.12	3	thick disk
UPM J0812−3529	0812−3529	DC	−373.74 ± 8.18	3	(RV in error)[h]
α Cha	0818−7655	F5 V Fe-0.8	−12.60 ± 0.12	3	thin disk
WISE J083337.83+005214.2	0833+0052	(sd)T9	…	…	thick disk?
ψ Vel	0930−4028	F3 V Fe-0.7	8.80 ± 1.80	4	thin disk
L 750-42	0943−1747	sdM3	97.36 ± 0.58	3	thick disk
HD 88230	1011+4927	K6e V Fe-1	−26.48 ± 0.12	3	thin disk
CWISE J105512.11+544328.3[c]	1055+5443	[sdT8]	…	…	thick disk?
HD 103095	1152+3743	K1 V Fe-1.5	−98.05 ± 0.12	3	halo
10 CVn	1244+3916	F9 V Fe-0.3	80.49 ± 0.12	3	thick disk
HD 114837	1314−5906	F6 V Fe-0.4	−63.57 ± 0.12	3	thin disk
SDSS J141624.08+134826.7[b]	1416+1348	sdL7	−87 ± 33	7	thin disk
ULAS J141623.94+134836.3[b]	1416+1348	(sd)T7.5	−87 ± 33[g]	7	thin disk
HD 125276	1419−2548	F9 V Fe-1.5 CH-0.7	−22.28 ± 0.13	3	thin disk
WISE J142320.84+011638.0[d]	1423+0116	sdT8	−19.21 ± 0.14[g]	3	thin disk
σ Boo	1434+2944	F4 V kF2 mF1 (metal weak)	0.75 ± 0.12	3	thin disk
SSSPM J1444−2019	1444−2019	sdL0	…	…	halo
WISEA J153429.75−104303.3[f]	1534−1043	[esdT/Y?]	…	…	halo
χ Her	1552+4227	G0 V Fe-0.8...	−55.99 ± 0.12	3	thin disk
HD 144579	1604+3909	K0 V Fe-1.2	−59.44 ± 0.12	3	thin disk
HD 145417	1613−5734	K3 V Fe-1.7	8.68 ± 0.13	3	thick disk
b Her	1807+3033	F9 V metal-weak	−0.38 ± 0.13	3	thin disk
CWISE J181005.77−101001.2	1810−1010	sdT0:	…	…	thick disk?
χ Dra	1821+7243	F7 V (metal-weak)	31.90 ± 0.14	5	thin disk
HD 190067	2002+1535	K0 V Fe-0.9	20.37 ± 0.12	3	thin disk
WISE J200520.38+542433.9[e]	2005+5424	sdT8	−107.6[g]	8	thick disk
Ross 769	2104−1657	M1 V	−10.89 ± 0.27	3	halo
γ Pav	2126−6521	F9 V Fe-1.4 CH-0.7	−29.78 ± 0.12	3	thin disk
G 188-49 B	2214+2751	…	−351.15 ± 8.18	3	(RV in error)[h]
53 Aqr	2226−1644	G1 V + G5 V Fe-0.8 CH-1	2.28 ± 0.15	6	thin disk

Notes. The references for radial velocity are: (1) Gaia Collaboration et al. (2018), (2) Fouqué et al. (2018), (3) Gaia Collaboration et al. (2023a), (4) Holmberg et al. (2007), (5) Pourbaix et al. (2004), (6) Maldonado et al. (2010), (7) Abazajian et al. (2009), (8) Gizis (1997).

[a] References for spectral type are listed in Table 4 along with information on whether the types are based on optical or near-infrared data. Spectral types sometimes encode information about metallicity. For the coldest objects, this is generally done via a prefix such as sd (subdwarf), esd (extreme subdwarf), or usd (ultra subdwarf), with variations such as d/sd (indicating a spectral morphology intermediate between a normal, solar metallicity dwarf and a subdwarf) also possible (Figure 11 of Kirkpatrick 2005). For hotter stars, the metallicity is included in one of two ways. A suffix type such as "mF1" for an F4 V star would indicate that the metal lines better match that of an F1 standard, despite the fact that the hydrogen line morphology matches the F4 standard. An alternative way of expressing this is to subtract the metal-line best-match subtype from the H-line best-match subtype and to convert that to a metal index; for example, if the iron lines best matched an F1 dwarf although the hydrogen lines best matched an F9 dwarf ($\Delta = +8$ subtypes), the metallicity index for iron would be expressed as Fe $= -0.13\Delta - 0.26$, or more compactly as Fe−1.3. See chapter 6 of Gray & Corbally (2009) for more details.

[b] These two objects form a common-proper-motion pair.

[c] This object does not yet have spectroscopic observations, so its status as a subdwarf is assumed based on its location on color–magnitude diagrams.

[d] This is the companion to HD 126053, which is typed as a G1.5 V.

[e] This is the wide companion in the ξ Ursae Majoris quintuple system, the primary of which is generally typed as M1 V.

[f] Also known as The Accident, this object does not yet have spectroscopic observations because it is too faint for ground-based spectroscopy. Its status as a subdwarf is assumed based on its highly unusual location on color–magnitude and color–color diagrams. See Kirkpatrick et al. (2021b) for details.

[g] The space motion of the primary in this system is used in lieu of an independent measurement for this object.

[h] These objects are flagged by our analysis as belonging to the halo population, but their Gaia DR3 radial velocities are believed to be erroneous. For EGGR 290, the radial velocity measurement is likely incorrect due to the fact that this is a magnetic white dwarf and the fact that the Gaia DR3 radial velocity pipeline lacks white dwarf templates (Bailer-Jones 2022). For UPM J0812−3529, its status as a DC white dwarf (O'Brien et al. 2023) means that there should not be any lines in the optical spectrum with which Gaia could measure a radial velocity, but this suspicious radial velocity measurement has nonetheless created much discussion regarding the object's possible close (future) fly-by of the Sun (Bailer-Jones 2022; Bobylev & Bajkova 2022; de la Fuente Marcos & de la Fuente Marcos 2022). For G 188-48 B, the Gaia DR3 radial velocity is assumed to be spurious because the A component has a much more reasonable—and better measured—value of 20.06 ± 0.14 km s^{-1}.

(This table is available in machine-readable form.)

We acknowledge that our understanding of young moving groups near the Sun is still evolving. Our Sun is currently moving through three groups—the β Pic Moving Group, the AB Dor Moving Group, and the recently identified (but older) Oceanus Group (Gagné et al. 2023)—but it remains unlikely that many new early-M and hotter dwarfs within 20 pc will be associated with any newly recognized groups. Such young objects would have already revealed themselves through, for example, high chromospheric activity.

Young *brown dwarfs*, on the other hand, require their own special handling. For brown dwarfs, we deduce the form of the mass function via the empirical temperature distribution. It has been well established, however, that young brown dwarfs follow a different spectral type (or color) to $T_{\rm eff}$ relation than their older counterparts (Faherty et al. 2016). Corrections to the temperature estimates for these objects were already established for the brown dwarf portion of the 20 pc census in Kirkpatrick et al. (2021a), and none of the new brown dwarfs discussed in Table 12 are known to be youthful themselves. Therefore, no additional work is required here.

6.2.2. Nonsolar Metallicity

Objects with nonsolar metallicity raise two concerns. The first is that metal-poor objects may belong to the Galactic halo population and could skew our calculation of the nearby mass function, which concentrates on the Galactic disk. The second is that these objects, even if they are true disk members, may be sufficiently metal-poor that standard solar-metallicity relations will not adequately predict their masses. Are either of these concerns justified?

A number of objects in Table 4 have spectroscopic classifications indicating subsolar metallicity. For objects earlier than early-M, these classifications can generally be identified via the iron index, "Fe#," which attempts to encode the abundance of metals relative to hydrogen in the spectrum if the spectrum does not match the standards of solar-metallicity (Gray & Corbally 2009). Underabundances are encoded as negative numbers. For objects of spectral type late-K and later, metal-poor spectral types (Gizis 1997; Lépine et al. 2003, 2007; Kirkpatrick 2005; Burgasser et al. 2007a; Zhang et al. 2017) are usually denoted with prefixes of sd (subdwarf), esd (extreme subdwarf), or usd (ultra subdwarf). Table 14 lists all objects in the 20 pc census that have one of these low-metallicity classifications.

To answer the first concern, we use the sky positions, parallaxes, and proper motions in Table 4 along with published radial velocities in Table 14 to calculate the U, V, W space velocities with respect to the local standard of rest. We also calculate the U, V, W values for all objects in Table 4 with Gaia-based radial velocity measurements to see if any objects lacking low-metallicity spectral classifications are found to be halo members merely from their kinematics.[83] Figure 10 shows the Toomre diagram for both sets of objects. Also shown for comparison are stars having radial velocity measurements in Gaia DR2 and lying within 100 pc of the Sun, color coded as thin disk ($V_{\rm tot} \leqslant 85$ km s^{-1}), thick disk ($85 < V_{\rm tot} \leqslant 180$ km s^{-1}), or halo ($V_{\rm tot} > 180$ km s^{-1}) in accordance with the kinematic criteria of Nissen (2004). This comparison demonstrates that only six objects—LP 651-7, Ross 578, HD 25329, Kapteyn's Star, HD 103095, and Ross 769—appear to belong to the kinematic halo population. All others most likely belong to the thin or thick disk populations.

As stated in Section 3.5, Gaia contains radial velocities only for those objects having $G_{\rm RVS} \lesssim 14$ mag, which omits many of the M dwarfs and all of the L, T, and Y dwarfs within 20 pc. For these objects, we leverage spectroscopic indications of low metallicity to build a list of potential halo members; then, we scour the literature for other published radial velocities. These objects are also listed in Table 14. Many of these lack any radial velocity measurements, so assumed values from −200 to +200 km s^{-1}, in increments of 50 km s^{-1}, were used to calculate a range of possible U, V, W velocities. These results, shown in Figure 11, suggest that only two of these colder objects—SSSPM J1444−2019 and WISEA J153429.75−104303.3 (aka "The Accident")—are likely to be true halo members.

Figures 10 and 11 taken together suggest that only eight objects (all of them believed to be single) out of 3589 total in the 20 pc census, or 0.22%, are halo interlopers. Although this is slightly higher than the percentage of 0.15% used in Table A of Bensby et al. (2014) based on F and G stars alone, it nevertheless confirms that contamination by halo objects in the 20 pc census is extremely small. Although these objects will still be included in our mass function, any systematic offset imprinted upon their mass estimates can be ignored in subsequent analyses.

The second concern is difficult to address, as very few low-metallicity objects have had their masses measured via direct methods. The coldest subdwarfs, for instance, have a multiplicity fraction of only ∼1% (González-Payo et al. 2021); therefore, few such objects exist for dynamical analyses (e.g., Rebassa-Mansergas et al. 2019). Single subdwarfs are obvious targets for lensing-based mass measurements, as their high velocities increase the likelihood of "encounters" with background objects, but accurate whole-sky astrometry is just now advancing to the stage at which such measurements can be predicted and planned for (e.g., Sahu et al. 2020). So, to address this concern, we instead note that only forty-two low-metallicity systems are known within the 20 pc census[84] (Table 14), which represents only 1.5% of the total. Thus, if small biases are present in converting a subdwarf's spectral type, colors, or absolute magnitudes to masses, the bias in the overall 20 pc mass distribution will be negligible.

The above logic on the scarcity of objects also holds for systems with a *higher* metallicity than the Sun. This set of objects has a much smaller range in metallicity than the metal-poor objects above, and there are just a handful of examples. Only the higher-mass stars ι Hor AB (Fe+0.3), ν Phe (Fe +0.4), HD 176051 AB (slightly metal strong), and HD 207129 (Fe+0.4) have spectroscopic classifications that fall into this class. Another object, 14 Her, has a supersolar metallicity ([Fe/H] ≈ 0.4; Rosenthal et al. 2021) although its listed spectral type in Table 4 gives no indication of this. Curiously, even though members of the Hyades Cluster have metallicities that are slightly supersolar

[83] Two such objects were found—LP 651-7 and Ross 769—and for ease of reference, these have also been added to Table 14.

[84] It is worth noting that other low-luminosity, low-metallicity objects are likely to be found within this volume given the fact that parallaxes for both WISEA J153429.75−104303.3 ($d_{\rm true} = 16.3^{+1.4}_{-1.2}$ pc, versus $d_{\rm est} = 38.0^{+5.6}_{-4.9}$ pc; Meisner et al. 2020a; Kirkpatrick et al. 2021b) and CWISE J181005.77−101001.2 ($d_{\rm true} = 8.9^{+0.7}_{-0.6}$ pc, versus $d_{\rm est}$ = 14–64 pc; Schneider et al. 2020; Lodieu et al. 2022) placed them far closer to the Sun than original estimates predicted.

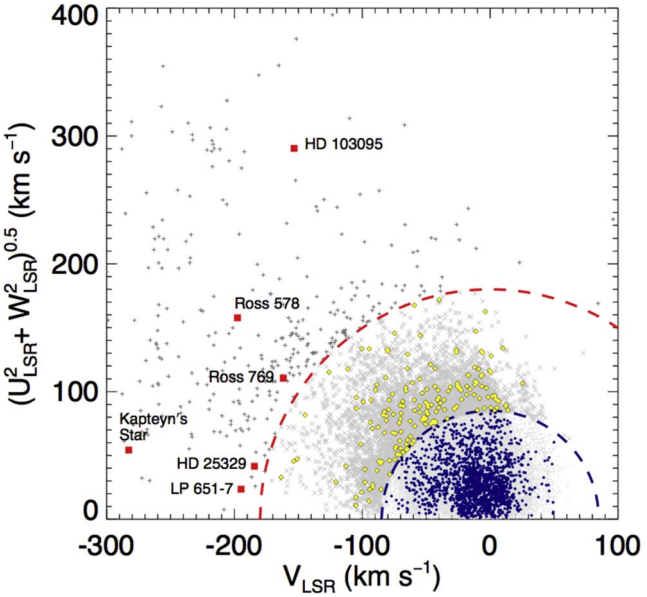

Figure 10. Toomre diagram of *UVW* space motions corrected to the local standard of rest (LSR) for 74,066 Gaia DR2 stars within 100 pc of the Sun and having parallax errors <10% (Kirkpatrick et al. 2021b). Thin disk (light gray dots), thick disk (medium gray crosses), and halo (dark gray pluses) objects are marked, with halo stars falling outside the outer dashed circle (red) and thin disk objects falling inside the inner dashed circle (navy). Objects with measured radial velocities in Table 4 or Table 14 are shown in navy if lying in the thin disk velocity zone, yellow for the thick disk zone, and red for the halo zone. The six halo members are highlighted with black labels.

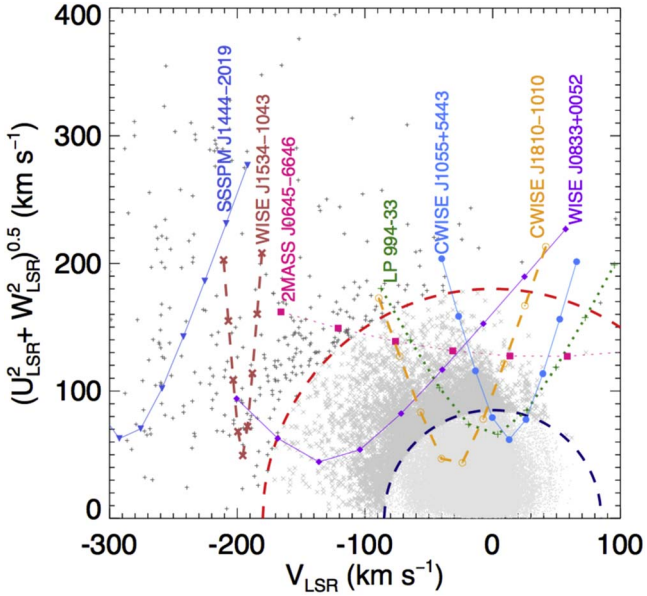

Figure 11. Toomre diagram of the 100 pc sample from Figure 10, now overplotted with the seven objects (various colors and symbols) from Table 14 that lack radial velocity measurements. For these, results are shown for nine assumed radial velocities ranging from −200 to +200 km s^{-1}, in steps of 50 km s^{-1}. As in Figure 10, the demarcation of the thin disk, thick disk, and halo populations are shown by the dashed circles in red and navy.

([Fe/H] $= 0.14 \pm 0.05$; Perryman et al. 1998) and lie, on average, only 47.0 ± 0.2 pc from the Sun (Lodieu et al. 2019), there are no confirmed Hyads within the 20 pc volume (Gaia Collaboration et al. 2021a; Schneider et al. 2022).

6.2.3. Formation Process

Because we are interested in objects formed via the star formation process, we need a criterion to distinguish objects that may have formed via alternative formation mechanisms at the lowest masses. When brown dwarfs were first theorized (Hayashi & Nakano 1963; Kumar 1963), they were regarded as direct products of the star formation process—ones that had insufficient mass to sustain prolonged thermonuclear fusion in their cores—and as such represented the lower-mass extension of hydrogen-burning stars themselves. These could be contrasted with another low-mass formation product, planets, which were believed to be formed via a secondary process—from a protoplanetary disk created around a newly formed protostar or brown dwarf. In the early 1960s, there were no known examples of brown dwarfs, and our own solar system provided the only known examples of planets.

As brown dwarf and exoplanet discoveries began in earnest (see reviews by Kirkpatrick 2005; Winn & Fabrycky 2015), it became clear that nature produces some low-mass products that are difficult to classify as either brown dwarf or exoplanet (e.g., 2MASSWJ 1207334−393254b, Chauvin et al. 2004). The earlier definition based on formation was cumbersome to use in practice; unless an object was still in its infancy, its exact formation process would be difficult, if not impossible, to ascertain from observations. As an alternative, Burrows et al. (1997) proposed another theoretically based definition. This alternative uses mass to distinguish between a brown dwarf and an (exo)planet, the dividing line being the somewhat arbitrarily chosen deuterium burning limit, which is $\sim 13 M_{\rm Jup}$ for solar metallicity. Somewhat surprisingly, this definition was thereafter widely (though not universally) adopted, in no small part because lower-mass discoveries that earlier would have been called *brown dwarfs* could now be referred to by a more attention-grabbing label of *exoplanet*.

This alternative definition, however, came three and a half decades after the original brown dwarf definition, and the concept of planets having being born from a protoplanetary disk (the "nebular hypothesis") had been in the astronomical lexicon for over two centuries (Kant 1755; Laplace 1796). Thus, labeling an object below 13 $M_{\rm Jup}$ as a planet often leads to confusion, as some readers—and even researchers—unwittingly apply both definitions in tandem. That is, they assume that a so-named *planet* (by the new, mass-based definition) must have formed via a protoplanetary disk (by the former, formation-based definition). It is difficult to divorce the term *planet* from its formation scenario.

In this paper, one of our goals is to define, or place limits on, the low-mass terminus of star formation. If we were to use the newer definition to include/exclude objects for the mass function analysis, our results would return a terminus of $13 M_{\rm Jup}$, which merely reflects the dividing line chosen by the arbitrary definition. We must, therefore, more carefully consider whether the lowest-mass objects in the 20 pc census should be counted as star formation products or planetary-formation products.

As stated earlier, this definition also lacks easy observational verification. Nonetheless, some methods have been proposed to distinguish formation mechanisms. Öberg et al. (2011) postulated that the carbon to oxygen ratio could be used as one tracer. Planets that formed close to a star would have a solar-like C/O value, like brown dwarfs formed via gravitational collapse, whereas planets formed via accretion of ices beyond the water snowline would have a supersolar C/O value. Those authors acknowledged, however, that measuring an

accurate value of C/O is fraught with difficulties (even within our own solar system), and Calamari et al. (2022) made a similar conclusion based on their analysis of the spectrum of the brown dwarf Gliese 229B. Mollière et al. (2022) show that this simplified picture of the C/O ratio is somewhat more complicated when disk chemical evolution and pebble accretion are taken into account, as well.

Similarly, Morley et al. (2019) showed that the deuterium to hydrogen ratio could be used to distinguish between planets with solar D/H values like Jupiter and Saturn, which formed directly from accretion of gas in the protostellar nebula, and planets with enhanced D/H values like Neptune and Uranus, which presumably formed from accretion of ices. Both C/O and D/H thus have limitations: some objects formed via a protoplanetary disk have values indistinguishable from those of objects born via star formation.

Another promising avenue is the overall metallicity. The giant planets of our solar system have metal enhancements well above solar values (Wong et al. 2004; Fletcher et al. 2009), and exoplanets are preferentially found around metal-rich host stars (Fischer & Valenti 2005; Wang & Fischer 2015). These facts led Fortney et al. (2008) to propose metallicity-based diagnostics that could distinguish between formation scenarios. Specifically, for objects with $T_{\rm eff} < 1400$ K, a strong 4.5 μm CO absorption band along with enhanced *H*- and *K*-band fluxes (from a relative lack of collision-induced absorption by H_2) is proposed as fingerprints of planet-like formation. However, these diagnostics are likely only useful when comparing populations of objects and not when establishing the formation pathway of individual objects. Metal enrichment is not unique to planet formation, as a collapsing metal-rich cloud can also produce low-mass objects.

Bowler et al. (2023) note that the orientation between the spin axis of the star and the orbital plane of the companion shows promise as another marker of formation, as star-like formation shows a wide range of orientations, whereas planet-like formation prefers values near 90°. This is, however, another marker that can distinguish between populations but cannot be used on an individual object basis.

Schlaufman (2018) demonstrates that companions above $\sim 10 M_{\rm Jup}$ lack the tendency to fall primarily around metal-rich hosts that companions below $\sim 4 M_{\rm Jup}$ exhibit, which is taken as evidence of core accretion in the lower-mass set. Hoch et al. (2023) likewise find a tentative difference in the trend of C/O values at $\sim 4 M_{\rm Jup}$, which is taken as further evidence that those objects are primarily formed via core accretion, although, as stated above, C/O ratios can be difficult to interpret. Similarly, Ribas & Miralda-Escudé (2007) find differing radial velocity distributions above and below $M \sin(i)$ values of $\sim 4 M_{\rm Jup}$. Schlaufman (2018) states that planet-like formation appears to cease above $\sim 4 M_{\rm Jup}$, but not necessarily that star-like formation ceases below $\sim 10 M_{\rm Jup}$. There might still be a range in mass, below $\sim 4 M_{\rm Jup}$, where both processes contribute.

The methods addressed above require data that are so far lacking for most exoplanets or can be used only in comparing populations. Instead, for this paper, we propose a simple scheme whose purpose is merely to exclude objects with a high likelihood of having been formed via a protoplanetary disk while including all others as *possible* products of star formation. For our scheme, we require at least three bodies in a system because the only parameters available for two-body systems—mass ratio, separation, etc.—can lead to ambiguities when trying to distinguish between formation scenarios.

As an example, Bowler et al. (2020) have used 27 long-period companions labeled as giant planets and brown dwarfs to search for differences in parameters. They find that the population of brown dwarfs has an eccentricity distribution peaking in the range $0.6 < e < 0.9$, whereas binaries with mass ratios significantly different from 1 have an eccentricity distribution peaking closer to $e \approx 0$. These results indicate that the star formation process tends to create binaries with large eccentricity, and the protoplanetary process tends to form binaries with near-zero eccentricity. To reiterate a point from above, while such trends may be indicative of a *population* of objects, eccentricity alone cannot be used on an object-by-object basis to distinguish between formation scenarios. The same is true for mass ratio, as doing so can bias our list of potential companions to only the higher-mass ones, which could impact our ability to determine star formation's low-mass cutoff. (Similarly, *not* selecting on mass ratio can bias our results in the opposite direction, a point we address further in the next section.)

In triple (and higher-order) systems, however, we have other parameters available. Specifically, we note that the hierarchy of empirically observed triple *star* systems is such that the period of the outer component must be at least 5 times that of the inner pair (Tokovinin 2004). This is in good agreement with dynamical stability expectations for objects in circular orbits, and the period of the outer component must be even larger than 5 times the inner one when elliptical orbits are considered (Mardling & Aarseth 2001). Planets that have formed from a protoplanetary disk, on the other hand, can often arrange themselves in stable orbital configurations (e.g., in resonances with one another) that violate the above law. A multistar system that formed via a collapsing cloud could, presumably, arrange itself in a similar manner if conditions were ideal, but such examples must be exceedingly rare. Therefore, we will use the ratios of orbital periods to identify *exoplanet* systems in the 20 pc census that most likely formed via a protoplanetary disk, and we retain all others for consideration as possible products of star formation.

To this end, Table 15 lists all of the host objects from Table 4 that were labeled as having one or more confirmed exoplanets in the NASA Exoplanet Archive as of 2022 September 1.[85] For systems in which any pair of *exoplanets* violate the $P_{\rm outer} < 5 P_{\rm inner}$, we indicate the innermost pair that violates the rule and exclude all of the planets, thus including only the host star in the later analysis. For all others, we have used the NASA Exoplanet Archive to compile their mass measurements. For objects identified only through radial velocity monitoring, we list the $M \sin(i)$ values, since the inclination of the system is not known. For other objects—transiting systems, radial velocity systems with astrometric imaging, etc.—we list the actual measured masses. Incorporating these objects into the stellar mass function analysis will be discussed further in Section 7.

[85] One additional complication, as stated in Section 3.6.4, is that the NASA Exoplanet Archive uses a $30 M_{\rm Jup}$ dividing line, not $13 M_{\rm Jup}$, to distinguish between brown dwarfs and exoplanets. Hence, some of the brown dwarfs already listed in Table 4 will be double counted; that is, they will have their own separate row in the table while also being listed under the "#Planets" column. Such objects are flagged in Table 15.

Table 15
20 pc Objects Hosting *Planets*

Name	Coords (J2000)	No. of Planets	Note[a]	$M \sin(i)$ ($M_{\rm Jup}$)	M ($M_{\rm Jup}$)	Mass References
(1)	(2)	(3)	(4)	(5)	(6)	(7)
Sun	⋯	8	$P_{\rm Venus} < 5P_{\rm Mercury}$	⋯	⋯	⋯
HD 1237 A	0016−7951	1	consider	3.37 ± 0.09	⋯	(1)
GX And	0018+4401	2[b]	consider	$0.11^{+0.08}_{-0.06}$	⋯	(2)
54 Psc AB	0039+2115	1	consider	0.228 ± 0.011	⋯	(3)
HD 3765	0040+4011	1	consider	$0.173^{+0.014}_{-0.013}$	⋯	(4)
G 268-38	0044−1516	2	consider	⋯	0.0201 ± 0.0014	(5)
⋯	⋯	⋯	consider	⋯	$0.00554^{+0.00053}_{-0.00050}$	(5)
BD+61 195	0102+6220	1	consider	0.0177 ± 0.0021	⋯	(6)
YZ Cet	0112−1659	3	$P_c < 5P_b$	⋯	⋯	⋯
CD−54 269	0114−5356	1	consider	0.026 ± 0.005	⋯	(7)
HD 7924	0121+7642	3	$P_c < 5P_b$	⋯	⋯	⋯
υ And A	0136+4124	3	consider	0.6876 ± 0.0044	⋯	(8)
⋯	⋯	⋯	consider	1.981 ± 0.019	⋯	(8)
⋯	⋯	⋯	consider	4.132 ± 0.029	⋯	(8)
q01 Eri	0142−5344	1	consider	0.94 ± 0.08	⋯	(9)
τ Cet	0144−1556	4	$P_h < 5P_g$	⋯	⋯	⋯
TZ Ari	0200+1303	2[c]	consider	0.21 ± 0.02	⋯	(10)
HD 13445 A	0210−5049	1	consider	4.42 ± 0.20	⋯	(11)
BD+47 612	0222+4752	1	consider	$0.0619^{+0.0076}_{-0.0072}$	⋯	(12)
ι Hor AB	0242−5048	1[d]	already included	2.27 ± 0.25	⋯	(11)
Teegarden's Star	0253+1652	2	$P_c < 5P_b$	⋯	⋯	⋯
G 245-61	0257+7633	1	consider	⋯	0.00733 ± 0.00063	(13)
BD−17 588 A	0301−1635	2	$P_b < 5P_c$	⋯	⋯	⋯
CD Cet	0313+0446	1	consider	$0.0124^{+0.0013}_{-0.0014}$	⋯	(14)
e Eri	0319−4304	4	$P_c < 5P_b$	⋯	⋯	⋯
HD 21749	0326−6329	2	$P_b < 5P_c$	⋯	⋯	⋯
ϵ Eri	0332−0927	1	consider	⋯	$0.66^{+0.12}_{-0.09}$	(15)
HD 22496	0335−4825	1	consider	$0.0175^{+0.0023}_{-0.0021}$	⋯	(16)
L 372-58	0335−4430	3	$P_c < 5P_b$	⋯	⋯	⋯
L 229-91	0409−5322	3	$P_c < 5P_b$	⋯	⋯	⋯
o^2 Eri A	0415−0739	1	consider	0.0266 ± 0.0015	⋯	(17)
ϵ Ret A	0416−5918	1	consider	1.56 ± 0.14	⋯	(18)
L 375-2 AB	0432−3947	2	$P_c < 5P_b$	⋯	⋯	⋯
HD 285968	0442+1857	1	consider	0.0285 ± 0.0043	⋯	(4)
Wolf 1539	0452+0628	1	consider	0.82 ± 0.07	⋯	(19)
L 736-30	0453−1746	3	$P_c < 5P_b$	⋯	⋯	⋯
LP 656-38	0501−0656	2	consider	$0.00636^{+0.00082}_{-0.00079}$	⋯	(20)
⋯	⋯	⋯	consider	$0.0073^{+0.0016}_{-0.0015}$	⋯	(20)
UCAC4 211-005570	0505−4756	1[e]	consider	⋯	⋯	⋯
Kapteyn's Star	0511−4501	1	consider	$0.022^{+0.004}_{-0.003}$	⋯	(21)
π Men	0537−8028	3	consider	$0.0113^{+0.0015}_{-0.0014}$	⋯	(22)
⋯	⋯	⋯	consider	0.0421 ± 0.0043	⋯	(23)
⋯	⋯	⋯	consider	⋯	12.2 ± 1.3	(22)
β Pic	0547−5103	2	exclude[f]	⋯	⋯	⋯
HD 40307	0554−6001	5	$P_c < 5P_b$	⋯	⋯	⋯
Gl 229 A	0610−2151	2	$P_b < 5P_c$	⋯	⋯	⋯
HD 260655	0637+1733	2	$P_c < 5P_b$	⋯	⋯	⋯
HD 265866	0654+3316	1	consider	0.0126 ± 0.0013	⋯	(24)
BD+05 1668	0727+0513	2	$P_b < 5P_c$	⋯	⋯	⋯
β Gem	0745+2801	1	consider	2.30 ± 0.45	⋯	(25)
L 34-26	0749−7642	1[g]	already included	⋯	⋯	⋯
CD−24 6144	0754−2518	2	consider	0.025 ± 0.005	⋯	(26)
⋯	⋯	⋯	consider	0.152 ± 0.023	⋯	(26)
L 97-3 A	0806−6618	1[h]	already included	⋯	⋯	⋯
L 98-59	0818−6818	4	$P_c < 5P_b$	⋯	⋯	⋯
HD 69830	0818−1237	3	$P_c < 5P_b$	⋯	⋯	⋯
L 675-81	0840−2327	2	consider	1.753 ± 0.058	⋯	(26)
⋯	⋯	⋯	consider	1.644 ± 0.060	⋯	(26)
G 234-45	0841+5929	2	consider	$0.46^{+0.02}_{-0.01}$	⋯	(27)
⋯	⋯	⋯	consider	0.20 ± 0.01	⋯	(27)
ρ^1 Cnc A	0852+2819	5	$P_c < 5P_b$	⋯	⋯	⋯
HD 79211	0914+5241	1	consider	0.0334 ± 0.0038	⋯	(28)
L 678-39	0936−2139	3	$P_c < 5P_b$	⋯	⋯	⋯
CD−45 5378	0944−4546	1	consider	⋯	0.00172 ± 0.00025	(29)
HD 85512	0951−4330	1	consider	0.011 ± 0.002	⋯	(30)
BD+63 869	0956+6247	1	consider	0.0721 ± 0.0088	⋯	(26)
BD+48 1829	1002+4805	1	consider	$0.0410^{+0.0064}_{-0.0063}$	⋯	(31)
HD 87883	1008+3414	1	consider	⋯	$5.37^{+0.51}_{-0.59}$	(22)
L 320-124	1014−4709	2	consider	⋯	0.00522 ± 0.00072	(32)
⋯	⋯	⋯	consider	0.0083 ± 0.0014	⋯	(32)
BD+01 2447	1028+0050	1	consider	0.00538 ± 0.00076	⋯	(33)
47 UMa	1059+4025	3	$P_c < 5P_b$	⋯	⋯	⋯

Table 15
(Continued)

Name	Coords (J2000)	No. of Planets	Note[a]	$M \sin(i)$ ($M_{\rm Jup}$)	M ($M_{\rm Jup}$)	Mass References
(1)	(2)	(3)	(4)	(5)	(6)	(7)
Lalande 21185	1103+3558	2	consider	$0.00846^{+0.00060}_{-0.00057}$	…	(34)
…	…	…	consider	$0.0428^{+0.0076}_{-0.0072}$	…	(34)
BD−18 3106	1107−1917	2	$P_c < 5P_b$	…	…	…
HD 97101 A	1111+3026	2	consider	$0.0239^{+0.0077}_{-0.0069}$	…	(35)
…	…	…	consider	$0.169^{+0.029}_{-0.027}$	…	(35)
HD 304043	1116−5732	1	consider	0.0348 ± 0.0035	…	(7)
83 Leo B	1126+0300	1	consider	0.070 ± 0.050	…	(11)
CD−31 9113	1135−3232	3	$P_d < 5P_b$	…	…	…
Ross 1003	1141+4245	2	consider	$0.3043^{+0.0044}_{-0.0032}$	…	(36)
…	…	…	consider	$0.214^{+0.015}_{-0.007}$	…	(36)
Ross 905	1142+2642	1	consider	…	0.070 ± 0.007	(37)
HD 102365 A	1146−4030	1	consider	0.050 ± 0.008	…	(38)
Ross 128	1147+0048	1	consider	0.00440 ± 0.00066	…	(39)
HD 238090	1212+5429	1	consider	$0.0217^{+0.0029}_{-0.0030}$	…	(24)
Wolf 433	1238+1141	1	consider	0.0415 ± 0.0053	…	(26)
Wolf 437	1247+0945	1	consider	…	$0.00887^{+0.00035}_{-0.00038}$	(40)
BD+13 2618 AB	1300+1222	1[i]	already included	…	…	…
HD 113538	1304−5226	2	$P_c < 5P_b$	…	…	…
e Vir	1316+0925	1[j]	already included	…	…	…
61 Vir	1318−1818	3	$P_d < 5P_c$	…	…	…
Ross 1020	1322+2428	1	consider	0.025 ± 0.002	…	(41)
70 Vir	1328+1346	1	consider	7.416 ± 0.057	…	(42)
BD+11 2576	1329+1022	1	consider	0.016 ± 0.003	…	(43)
τ Boo A	1347+1727	1	consider	4.32 ± 0.04	…	(44)
HD 122303	1401−0239	1	consider	$0.0169^{+0.0022}_{-0.0020}$	…	(45)
Proxima Centauri	1429−6240	1	consider	0.00337 ± 0.00019	…	(46)
HD 128311	1436+0944	2	$P_c < 5P_b$	…	…	…
BD−07 4003	1519−0743	3	$P_b < 5P_e$	…	…	…
ν^2 Lup	1521−4819	3	$P_c < 5P_b$	…	…	…
Ross 508	1523+1727	1	consider	0.0126 ± 0.0017	…	(47)
λ Ser	1546+0721	1	consider	0.0429 ± 0.0046	…	(4)
G 180-18	1558+3524	2	consider	…	0.0055 ± 0.0014	(48)
…	…	…	consider	0.0180 ± 0.0030	…	(48)
ρ CrB	1601+3318	2[k]	$P_c < 5P_b$	…	…	…
GJ 3942	1609+5256	1	consider	0.0225 ± 0.0019	…	(49)
14 Her	1610+4349	2	consider	…	$8.1^{+1.6}_{1.0}$	(22)
…	…	…	consider	…	$5.0^{+0.9}_{-1.0}$	(22)
LP 804-27	1612−1852	1	consider	2.1	…	(50)
HD 147379	1616+6714	1	consider	$0.0898^{+0.0047}_{-0.0046}$	…	(12)
HD 147513	1624−3911	1	consider	1.21	…	(51)
G 202-48	1625+5418	1	consider	0.0089 ± 0.0016	…	(52)
BD−12 4523	1630−1239	3	$P_c < 5P_b$	…	…	…
BD+25 3173	1658+2544	1	consider	0.328 ± 0.032	…	(53)
HD 154345	1702+4704	1	consider	0.82 ± 0.07	…	(11)
HD 154088	1704−2834	1	consider	0.021 ± 0.003	…	(54)
G 139-21	1715+0457	1	consider	…	0.0257 ± 0.0014	(55)
BD+11 3149	1716+1103	2	consider	0.00777 ± 0.00085	…	(56)
…	…	…	consider	$0.0197^{+0.0025}_{-0.0024}$	…	(56)
HD 156384 C	1718−3459	5	$P_c < 5P_b$	…	…	…
CD−46 11540	1728−4653	1	consider	0.035	…	(57)
CD−51 10924	1730−5138	4	consider	0.0120 ± 0.0010	…	(22)
…	…	…	consider	$0.0211^{+0.0022}_{-0.0020}$	…	(22)
…	…	…	consider	…	$5.78^{+0.48}_{-0.46}$	(22)
…	…	…	already included[l]	…	13.43 ± 1.1	(22)
G 226-66	1735+6140	1	consider	$0.0283^{+0.0053}_{-0.0057}$	…	(58)
BD+68 946	1736+6820	2	consider	0.0541 ± 0.0031	…	(26)
…	…	…	consider	0.050 ± 0.013	…	(26)
CD−44 11909	1737−4419	2	$P_c < 5P_b$	…	…	…
BD+18 3421	1737+1835	1	consider	0.0208 ± 0.0014	…	(59)
μ Ara	1744−5150	4	$P_b < 5P_e$	…	…	…
BD+45 2743 A	1835+4544	1	consider	0.0429 ± 0.0025	…	(60)
HD 176029	1858+0554	1	consider	$0.0093^{+0.0016}_{-0.0015}$	…	(61)
HD 177565	1906−3748	1	consider	$0.048^{+0.020}_{-0.019}$	…	(62)
HD 180617	1916+0510	1	consider	0.0384 ± 0.0033	…	(59)
HD 189733	2000+2242	1	consider	…	1.13 ± 0.08	(11)
HD 190007	2002+0319	1	consider	0.0518 ± 0.0052	…	(59)
HD 190360	2003+2953	2	consider	0.0600 ± 0.0076	…	(63)
…	…	…	consider	…	1.8 ± 0.2	(64)
HD 189567	2005−6719	2	$P_c < 5P_b$	…	…	…
HD 192263	2013−0052	1	consider	0.56 ± 0.05	…	(11)
HD 192310	2015−2701	2	consider	0.0532 ± 0.0028	…	(30)

Table 15
(Continued)

Name	Coords (J2000)	No. of Planets	Note[a]	$M \sin(i)$ ($M_{\rm Jup}$)	M ($M_{\rm Jup}$)	Mass References
(1)	(2)	(3)	(4)	(5)	(6)	(7)
…	…	…	consider	0.076 ± 0.016	…	(30)
AU Mic	2045−3120	2	$P_c < 5P_b$	…	…	…
LSPM J2116+0234	2116+0234	1	consider	$0.0418^{+0.0031}_{-0.0035}$	…	(65)
LSPM J2122+2255	2122+2255	1	consider	0.33 ± 0.02	…	(10)
HD 204961	2133−4900	2[m]	consider	0.68 ± 0.09	…	(66)
HN Peg AB	2144+1446	1[n]	already included	…	…	…
G 264-12	2146+6648	2	$P_c < 5P_b$	…	…	…
ϵ Ind A	2203−5647	1	consider	…	$3.25^{+0.39}_{-0.65}$	(67)
BD−05 5715	2209−0438	2	$P_c < 5P_b$	…	…	…
L 788-37	2213−1741	1	consider	0.023 ± 0.002	…	(41)
HD 211970	2222−5433	1	consider	0.0409 ± 0.0079	…	(68)
L 119-213	2241−6910	1	consider[o]	…	…	…
HD 216520	2247+8341	2	$P_c < 5P_b$	…	…	…
BD−15 6290 AB	2253−1415	4	$P_b < 5P_c$	…	…	…
51 Peg	2257+2046	1	consider	0.472 ± 0.039	…	(18)
HD 217987	2305−3551	2	$P_c < 5P_b$	…	…	…
TRAPPIST-1	2306−0502	7	$P_c < 5P_b$	…	…	…
HD 219134	2313+5710	6	$P_c < 5P_b$	…	…	…
γ Cep AB	2339+7737	1	consider	1.85 ± 0.16	…	(69)

Notes.
[a] Indicates whether the *exoplanets* in this system should be considered in our stellar mass function analysis. Notes regarding period violations indicate objects that are excluded, as these are likely objects formed via a protoplanetary disk. In these cases, we list at least one example of component pairs ("b" vs. "c," "c" vs. "d," etc.) that violate the rule.
[b] The "b" planet is currently considered controversial by the NASA Exoplanet Archive, so only the "c" planet is considered for inclusion in our mass function analysis.
[c] This object was reported to have two exoplanets at the time of our original query to the NASA Exoplanet Archive, but it is now believed that the "b" component was a false positive.
[d] This exoplanet, aka HR 810b, has a period from radial velocity variations of 302.8 ± 2.3 days (Stassun et al. 2017) and is presumably the same object listed in Table 4 as ι Hor B, the companion giving rise to the 331.7 days orbital period in the Gaia DR3 non-single-star table.
[e] This transiting exoplanet, aka TOI-540 b, has no mass measurement.
[f] The inner and outer planets do not violate the $P_{\rm outer} < 5P_{\rm inner}$ rule, but the imaging of this youthful system nonetheless shows the debris disk remaining from protoplanetary formation.
[g] This *exoplanet* is the T dwarf WISEPA J075108.79−763449.6, already included as its own row in Table 4.
[h] This *exoplanet* is the Y dwarf L 97-3 B (sometimes referred to as WD 0806−661 B), already included as its own row in Table 4.
[i] This *exoplanet* is the T dwarf ULAS J130041.74+122114.7, already included as its own row in Table 4.
[j] This *exoplanet* is the late-T/early-Y dwarf e Vir Ab, already included as its own row in Table 4.
[k] This assumes that the exoplanet candidate ρ CrB b is real.
[l] In Table 4, we label the object causing the Gaia DR3 acceleration (from the non-single-star list) as CD−51 10924 B. For purposes of accounting, we will equate that object with this one, GJ 676 A c.
[m] The "c" planet is currently considered controversial by the NASA Exoplanet Archive, so only the "b" planet is considered for inclusion in our mass function analysis.
[n] This *exoplanet* is the T dwarf HN Peg B, already included as its own row in Table 4.
[o] This object has no mass determination.
References. References for the mass measurements: (1) = Naef et al. (2001), (2) = Pinamonti et al. (2018), (3) = Wittenmyer et al. (2019), (4) = Rosenthal et al. (2021), (5) = Lillo-Box et al. (2020), (6) = Perger et al. (2019), (7) = Feng et al. (2020a), (8) = Curiel et al. (2011), (9) = Marmier et al. (2013), (10) = Quirrenbach et al. (2022), (11) = Stassun et al. (2017), (12) = Hobson et al. (2018), (13) = Soto et al. (2021), (14) = Bauer et al. (2020), (15) = Llop-Sayson et al. (2021), (16) = Lillo-Box et al. (2021), (17) = Ma et al. (2018), (18) = Butler et al. (2006), (19) = Howard et al. (2010), (20) = Astudillo-Defru et al. (2017), (21) = Anglada-Escude et al. (2014), (22) = Feng et al. (2022), (23) = Hatzes et al. (2022), (24) = Stock et al. (2020), (25) = Hatzes et al. (2006), (26) = Feng et al. (2020b), (27) = Lopez-Santiago et al. (2020), (28) = DiTomasso et al. (2023), (29) = Lam et al. (2021), (30) = Pepe et al. (2011), (31) = Hobson et al. (2019), (32) = Bonfils et al. (2018a), (33) = Amado et al. (2021), (34) = Hurt et al. (2022), (35) = Dedrick et al. (2021), (36) = Trifonov et al. (2018), (37) = Maciejewski et al. (2014), (38) = Tinney et al. (2011), (39) = Bonfils et al. (2018b), (40) = Trifonov et al. (2021), (41) = Luque et al. (2018), (42) = Luhn et al. (2019), (43) = Damasso et al. (2022), (44) = Borsa et al. (2015), (45) = Suárez Mascareño et al. (2017a), (46) = Faria et al. (2022), (47) = Harakawa et al. (2022), (48) = Beard et al. (2022), (49) = Perger et al. (2017), (50) = Apps et al. (2010), (51) = Mayor et al. (2004), (52) = Suárez Mascareño et al. (2017b), (53) = Johnson et al. (2010), (54) = Unger et al. (2021), (55) = Cloutier et al. (2021), (56) = Affer et al. (2016), (57) = Bonfils et al. (2007), (58) = Pinamonti et al. (2019), (59) = Burt et al. (2021), (60) = González-Álvarez et al. (2021), (61) = Toledo-Padrón et al. (2021), (62) = Feng et al. (2017), (63) = Wright et al. (2009), (64) = Feng et al. (2021), (65) = Lalitha et al. (2019), (66) = Wittenmyer et al. (2014), (67) = Feng et al. (2019a), (68) = Feng et al. (2019b), (69) = Endl et al. (2011).

(This table is available in machine-readable form.)

6.3. Objects on the Main Sequence

Main-sequence objects with directly measured masses can be used to calibrate relations of mass versus absolute magnitude or mass versus spectral type. Studies have shown that the relation with the smallest intrinsic scatter for K and M dwarfs is the one using absolute K-band magnitude (Delfosse et al. 2000). The fact that the K-band relation shows the least scatter across the optical to near-infrared range is also predicted by model atmospheres, as this is the wavelength regime where competing physical effects modulated by metallicity variations largely cancel one another (Delfosse et al. 2000; Mann et al. 2019). More (and improved) dynamical mass measurements of binary stars[86] along with improved Gaia parallaxes have enabled Mann et al. (2019) to construct a mass-versus-M_{Ks} relation that results in estimated masses with only 2%–3% uncertainty. Specifically, K_s is used because 2MASS provides all-sky coverage at this band. We use the Mann et al. (2019) mass–M_{Ks} relation (their Equation (2)) over the range $5.0 \leqslant M_{Ks} \leqslant 11.0$, roughly corresponding to spectral types from early-M to late-M.[87] These estimates and their propagated uncertainties are listed in columns "EstMassMKs" and "EstMassMKsErr" of Table 4.

For other main-sequence stars, we can use the methodology employed by Stassun et al. (2019). Using ∼20,000 (non-reddened) stars within 100 pc of the Sun with spectroscopically determined effective temperatures, they established a relation between $T_{\rm eff}$ and $G_{BP} - G_{RP}$ color. This is then mated with the results of Torres et al. (2010) that relate $T_{\rm eff}$ to mass for stars with dynamically measured masses (Stassun et al. 2018b). This gives mass estimates with uncertainties of ∼6.4% (Stassun et al. 2019). We take mass estimates and their uncertainties directly from the revised TIC (Stassun et al. 2019) for stars in our Table 4. These values are listed in columns "EstMassTIC" and "EstMassTICErr." We note, however, that the Stassun et al. (2019) prescription for stars with $T_{\rm eff} \lesssim 4000$ K (see their Appendix A.1 along with Muirhead et al. 2018) followed a different methodology. For these objects, masses were estimated using K_s magnitudes, Gaia DR2 parallaxes, and the Mann et al. (2019) mass-versus-M_{Ks} relation.

Some main-sequence stars lack both K_s magnitudes and an entry in the TIC. For these, we resort to two other estimation methods. The first is the mass-versus-M_G relation. Chontos et al. (2021) took a list of well-studied late-K and M dwarfs (Tables 5–7 from Mann et al. 2015) and refined their mass estimates using more precise Gaia DR3 parallaxes and the Mann et al. (2019) mass-versus-M_{Ks} relation from above. They derived a relation between this estimated mass and the absolute G-band magnitude. However, the coefficients in Chontos et al. (2021) are published with insufficient accuracy to re-create the relation shown in their Figure 7, so we have rederived them here. Our methodology is identical to theirs except that we exclude the sdM3 object L 750-42 (Gizis 1997) and do not incorporate a dependence on metallicity because the metallicity has not been measured for most of the M dwarfs within 20 pc. Using a functional form of

$$\text{Mass} = \sum_{i=0}^{4} c_i (M_G - 10.5)^i, \tag{18}$$

where M_G is the G-band absolute magnitude in magnitudes, and "Mass" is in units of $M_\odot$, we find best-fit coefficients of $c_0 = 0.30548$, $c_1 = -0.10588$, $c_2 = 0.011471$, $c_3 = 0.0021352$, and $c_4 = -0.00041023$. Our fit is illustrated in Figure 12. The relation is valid from $7.5 \leqslant M_G \leqslant 15.0$ (spectral types from ∼K7 to ∼M8). For uncertainty propagation, we adopt the Chontos et al. (2021) practice of a 2.2% uncertainty added in quadrature to the ∼3% uncertainty inherent to the Mann et al. (2019) relation. This mass–M_G relation is particularly useful for estimating masses of individual components of close double systems that are currently resolved only by Gaia. In Table 4, we provide columns labeled "EstMassMG" and "EstMassMGErr" listing the mass estimates for all objects for which these M_G-based estimates can be computed.

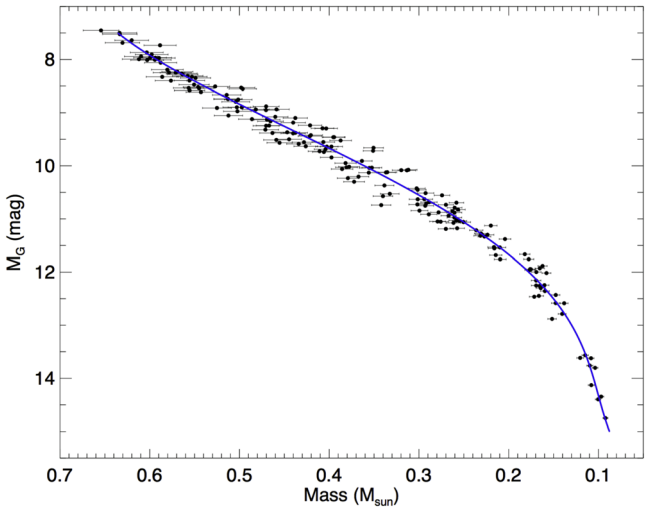

Figure 12. Absolute G-band magnitude plotted against estimated mass for 180 well-studied late-K and M dwarfs from Mann et al. (2015). The solid blue line shows our fitted relation from Equation (18). See text for details.

The second alternative estimation method is StarHorse (Anders et al. 2022), which uses Gaia EDR3 data cross-matched to photometry from Pan-STARRS1, SkyMapper, 2MASS, and AllWISE to estimate stellar parameters from stellar isochrones (from PARSEC 1.2S; Marigo et al. 2017) providing the closest match. When the Anders et al. (2022) mass estimates are available, these are listed in columns "EstMassSH" and "EstMassSHErr" of Table 4. These published mass uncertainties can be anomalously low compared to the other estimates discussed in this section because they pertain only to the internal model errors and do not include the systematic component coming from a model-to-truth comparison.

Figure 13 shows the four estimation techniques compared to each other. The top three panels show the intercomparisons between the TIC estimates, the M_{Ks} estimates, and the M_G estimates. As these are all based on the same underlying mass-versus-M_{Ks} relation of Mann et al. (2019), the

[86] In reality, the total mass of the binary system was used, rather than the masses of the individual components, the latter of which are not generally known. The resulting relation is nonetheless applicable to individual objects, as Sections 7.3 and 7.4 of Mann et al. (2019) discuss in detail. See in particular their Figure 15, which shows a direct comparison between directly measured individual masses and the resulting mass–M_{Ks} relation.

[87] Their relation covers the range from $M_{Ks} \approx 4.0$ mag down to a spectral type of ∼L1. However, the bright end of the relation is poorly constrained, so for these objects, we defer to the TIC mass estimates (see the next paragraph). At the faint end, we use the effective temperature analysis for objects cooler than M9.5, as further described in Section 7.1.

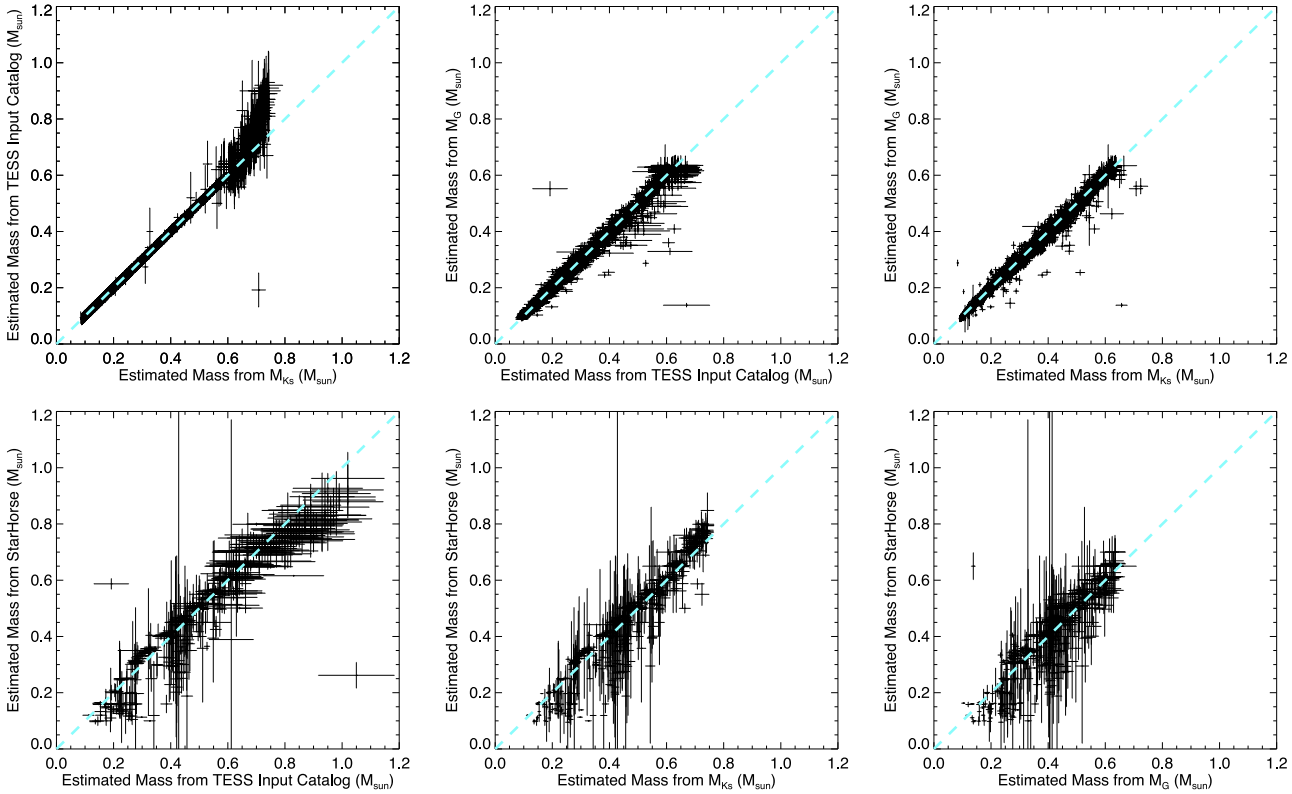

Figure 13. Intercomparisons of results from our four mass estimation techniques. The line of one-to-one correspondence is shown by the blue dashes. See text for details.

correspondence is generally excellent. (In fact, the correspondence between the TIC estimates and estimates from our M_{Ks} technique are nearly perfect, differing only in the Gaia data release from which the parallax values were obtained.) The only deviation is for masses greater than $\sim 0.65 M_{\odot}$ in the comparison between the TIC values and those derived from M_{Ks}, where the difference can be as large as 13%.

The bottom three panels of Figure 13 show small systematics between the three estimation techniques above and StarHorse. As stated above, masses from StarHorse are based on theoretical models, so such systematics might be expected between theory and observation. At masses of $\sim 0.3 M_{\odot}$, StarHorse tends to overpredict (by $\sim$10%) the mass relative to the other techniques, and at smaller masses may significantly underpredict (by $\sim$35%). At masses near $0.8 M_{\odot}$, a small underprediction (by $<$5%) relative to the TIC becomes an overprediction (by $\sim$5%) relative to masses from the M_{Ks} relation. At masses closer to $1.0 M_{\odot}$, StarHorse leads to underpredictions (by $\sim$10%) relative to estimates from the TIC.

Given that systematic offsets of up to 15% are seen even between the sets with empirical underpinnings, we are reluctant to apply corrections to offsets smaller than this value. The only exception to this is the $\sim$35% offset seen for StarHorse estimates below StarHorse values of $\sim 0.275 M_{\odot}$. In this case, rather than applying an offset, we will simply not use any StarHorse estimates below $0.275 M_{\odot}$.

7. Further Analysis

For each individual object ("#CompsOnThisRow" = 1) in Table 4, we have adopted a mass and its uncertainty. These are listed in columns "AdoptedInitialMass" and "AdoptedInitialMassErr" along with an additional column, "AdoptedInitialMassNote," indicating the origin of the data from elsewhere in the table. These are labeled with the term *initial* as a reminder that, for white dwarfs, we need their initial masses on the main sequence; for all other objects, their current masses are assumed identical to their initial masses. The codes for "AdoptedInitialMassNote" are as follows, listed in their order of selection:

1. *wd IFMR, wd low, wd ultra-low*, *or wd conjecture*. The initial mass and its uncertainty have been computed via the initial-to-final mass relation or other means (see Table 10), if this object is a white dwarf.
2. *measured*. Directly measured mass values from "Mass" and "MassErr" are used. The methodology used and its reference are listed in columns "MassMethod" and "MassRef." (For L, T, and Y dwarfs, directly measured masses are not retained because these are estimated in bulk through statistical means; see the Teff point, below.)
3. *M_Ks*. The mass and its uncertainty from the Mann et al. (2019) M_{Ks} relation ("EstMassMKs" and "EstMassMKsErr") are used.
4. *TIC*. The mass and its uncertainty from the TIC (Stassun et al. 2019; "EstMassTIC" and "EstMassTICErr") are used.
5. *M_G*. The mass and its uncertainty from the M_G relation of Equation (18) ("EstMassMG" and "EstMassMGErr") are used.
6. *SH*. The mass and its uncertainty from StarHorse (Anders et al. 2022; "EstMassSH" and "EstMassSHErr") are used, unless that estimate falls below $0.275 M_{\odot}$ (see Section 6.3).

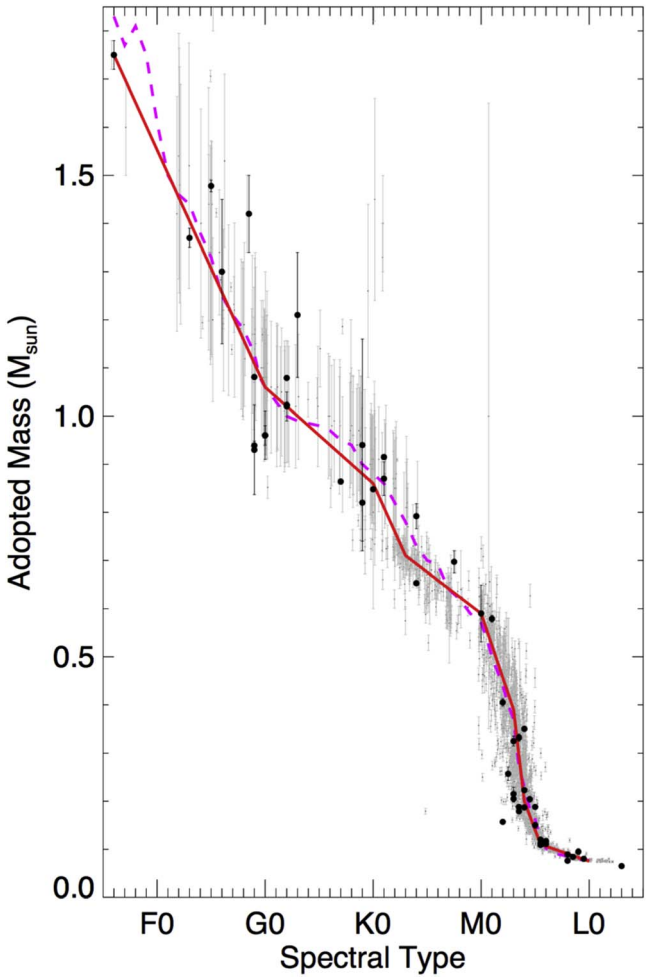

Figure 14. Mass as a function of spectral type for 20 pc objects with measured (black points) or estimated (gray points) masses and optical spectral types in Table 4. The adopted initial mass (see text) is used for each object. For objects with estimated (not measured) masses, a random value between −0.25 and +0.25 has been added to the spectral type to better visualize otherwise overlapping data points. Our piecewise fit to the relation for dwarf stars is shown by the solid red line and is quantified in Table 16. For comparison, we show the average mass per spectral type as tabulated in the 2022.04.16 version of https://www.pas.rochester.edu/~emamajek/EEM_dwarf_UBVIJHK_colors_Teff.txt (Pecaut & Mamajek 2013; magenta dashed line).

7. *literature*. The mass and its uncertainty are taken from columns "EstMassLit" and "EstMassLitErr," the mass estimation method and reference for which are listed in "EstMassLitMethod" and "EstMassLitRef." (Literature values can supersede other values above if the object is listed as a giant or subgiant in Table 11.)
8. *see GeneralNotes*. For objects with this code, the mass and its uncertainty were computed by us, as detailed in the "GeneralNotes" column of the table.
9. *Teff*. For objects of type L, T, or Y, individual masses are not computed. These are handled statistically via the distribution of $T_{\rm eff}$ values and their uncertainties ("Teff" and "Teff_unc"), as described in detail below.

For cases in which literature values did not list a mass uncertainty, a value of 10% is arbitrarily assumed. The quoted StarHorse uncertainty is also replaced with a 10% uncertainty, based on the underpredictions and overpredictions noted when comparing StarHorse values to other estimates (see discussion at end of Section 6.3), unless the quoted StarHorse internal uncertainty is already larger, in which case we retain the published value.

For cases where only a miscellaneous magnitude or delta magnitude of a companion were available, it is instructive to estimate a spectral type for the object in order to estimate its mass. Figure 14 shows a comparison between masses and measured spectral types for those Table 4 objects having mass estimates (or direct measures) from one of the other methods. The piecewise fit (Table 16) shown in the figure is the one we use to translate a dwarf spectral type estimate into a mass estimate. Other per-object details can be found in the GeneralNotes column of Table 4.

7.1. Analysis of Brown Dwarfs

We use the methodology adopted by Kirkpatrick et al. (2019a, 2021a) and Raghu et al. (2024) to determine the mass function for L, T, and Y dwarfs, most of which are brown dwarfs lacking any color (or spectral type or absolute magnitude) to mass correlation. Specifically, the mass function for these objects is determined by comparing the distribution of present-day temperatures to predicted temperature distributions. Predictions are drawn from a grid of models with varying mass functions, birthrates, and low-mass cutoffs. For each point in the grid, we build a predicted mass/age distribution that is then passed through a set of evolutionary models to predict the current-day $T_{\rm eff}$ distribution. Using this grid of predictions allows us to find the combination of mass function, birthrate, and cutoff mass that best fits the observed temperature distribution.

For the empirical distribution, we estimate the $T_{\rm eff}$ value for each L, T, or Y dwarf (see Table 12 in this paper; and Table 11 of Kirkpatrick et al. 2021a) and then calculate space densities as a function of $T_{\rm eff}$. To compute space densities, we need to determine the distances at which our brown dwarf subsamples are truly complete, as the coldest Y dwarfs are so intrinsically dim that we are unable to push their completeness to the 20 pc limit targeted in this paper. As described in Kirkpatrick et al. (2021a), we determine completeness via the $V/V_{\rm max}$ test (Schmidt 1968) using 150 K bins and computing $\langle V/V_{\rm max}\rangle$ at half-parsec steps within each bin. The computation starts with the first half-parsec step falling just larger than the distance of the bin's nearest object and advances in distance out to $d = 20$ pc. These results are shown in Figure 15.

A comparison of this figure to Figure 23 of Kirkpatrick et al. (2021a) shows that, despite the many new discoveries (and many fewer retractions) noted in Table 12, each 150 K bin has the same completeness limit as before. As one example, consider the bin with the largest change, 600–750 K. In both Kirkpatrick et al. (2021a) and here, this bin is complete out to 20 pc, but the number of objects has nonetheless increased from 83 in Kirkpatrick et al. (2021a) to 98 in this paper; see also Table 17. (The $V/V_{\rm max}$ test is only as robust as the Poisson statistics allow, which is why both sets of numbers were deemed to be complete.) As another example, the number of objects interior to the completeness limit of 15.0 pc in the 450–600 K bin has increased from 53 to 56.

As noted in Kirkpatrick et al. (2021a), the $V/V_{\rm max}$ test does not check for inhomogeneities in the surface area, the most likely cause of which would be confusion along the Galactic

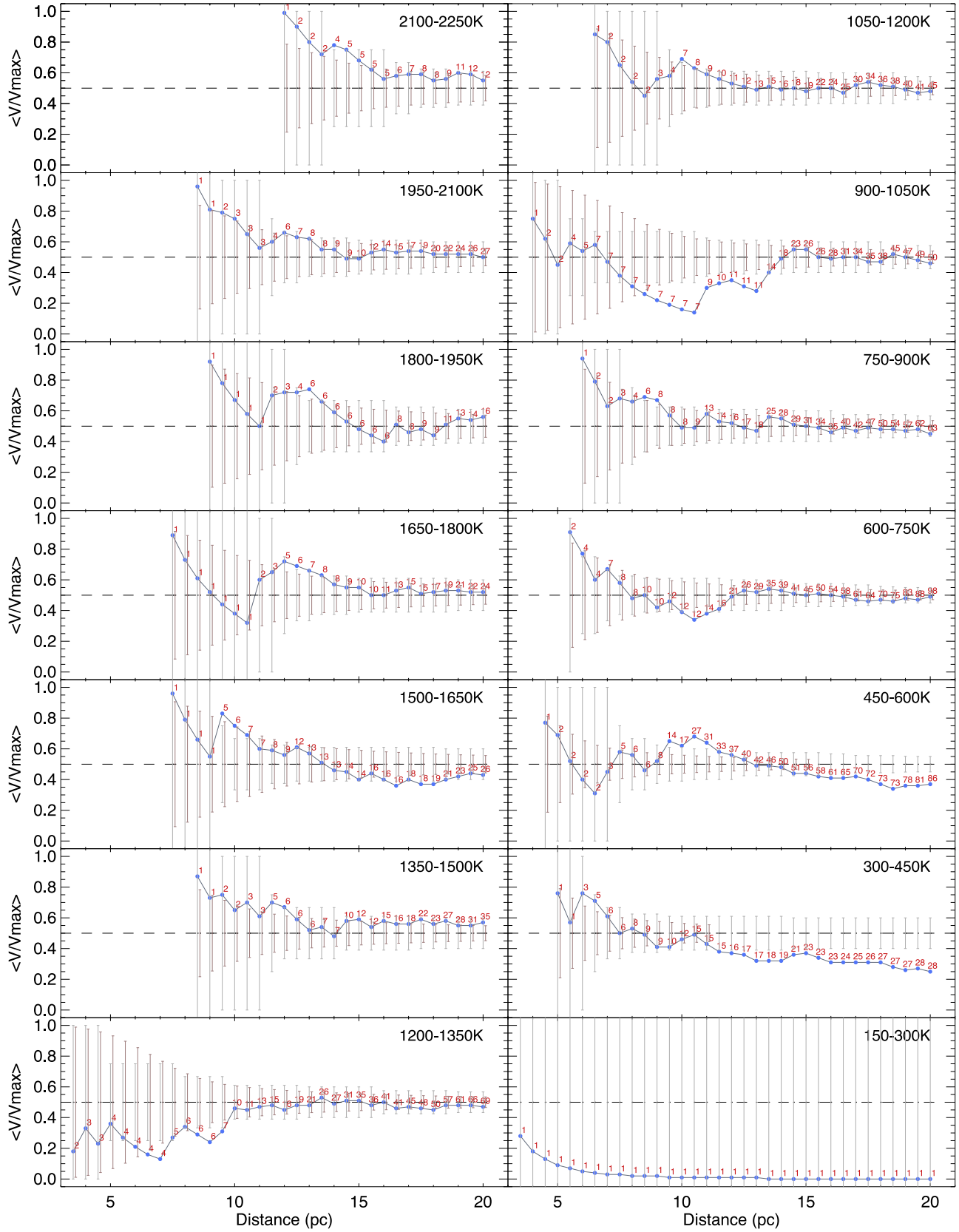

Figure 15. The average $V/V_{\rm max}$ value in 0.5 pc intervals across fourteen 150 K bins encompassing L, T, and Y dwarfs. Blue dots show the empirical sample, and red labels denote the number of objects at each 0.5 pc computation. The black dashed line shows the $\langle V/V_{\rm max}\rangle = 0.5$ level indicative of a complete sample. The gray error bars show the approximate 1σ range that a sample of the size shown in red would exhibit, given random statistics. The brown error bars, offset by +0.05 pc from the gray error bars for clarity, show the 1σ variation obtained by simulations using 10,000 Monte Carlo realizations having the number of objects and completeness limit listed in Table 17. See Section 8.2 of Kirkpatrick et al. (2021a) for more details.

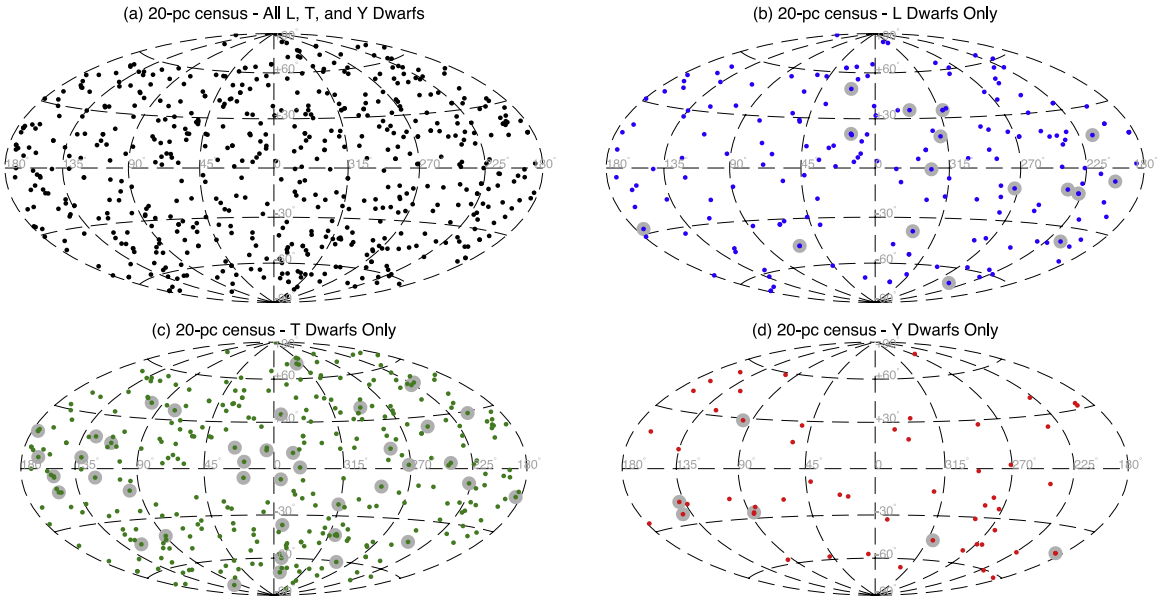

Figure 16. Plots of the 20 pc L, T, and Y dwarf census in Galactic coordinates. The four panels display (a) the sample in its entirety (black), (b) only the L dwarfs (blue), (c) only the T dwarfs (green), and (d) only the Y dwarfs (red). New additions to the sample since Kirkpatrick et al. (2021a) are plotted with gray haloes in panels (b) through (d).

plane that hinders our ability to find nearby brown dwarfs. Do the increased densities now reported in this paper indicate that these corrections can be reduced or dropped altogether?

Figure 16 shows the positions in Galactic coordinates of all 583 L, T, and Y dwarfs in the 20 pc census. As was done in Kirkpatrick et al. (2021a), we divide the sky into two zones: a zone along the Galactic plane ($|\mathrm{glat}| < 14\overset{\circ}{.}48$) and another ($|\mathrm{glat}| \geqslant 14\overset{\circ}{.}48$) well outside of the plane. This value of |glat| was chosen so that the nonplane zone contains exactly 3 times the area of the plane zone. If there is no incompleteness along the Galactic plane, then the ratio of nonplane to plane objects should be 3. For volume-complete portions of our 20 pc census, we find that this ratio is $138/44 = 3.1$ for L dwarfs, $257/65 = 4.0$ for T dwarfs, and $31/4 = 7.8$ for Y dwarfs, suggesting that the Galactic plane does not introduce any significant incompleteness (<1%) for L dwarfs but does still impede the discovery of fainter T and Y dwarfs. In contrast, Kirkpatrick et al. (2021a) derived ratios of $137/34 = 4.0$, $234/34 = 6.9$, and $24/4 = 6.0$ for the L, T, and Y dwarf samples, respectively.

Incompleteness along the Galactic plane has improved in the current 20 pc census for the L and T dwarfs. For Y dwarfs, the view is complicated by smaller number statistics. Taking the nonplane numbers of Y dwarfs as truth, then the number of plane Y dwarfs in the current sample should be $31/3 \pm (\sqrt{31})/3 = 10.3 \pm 1.9$, which is 3.3σ different from the value of 4 actually found. The same computation for the Kirkpatrick et al. (2021a) numbers gives a number of plane Y dwarfs that was only 2.5σ different. Hence, the underdensity of Y dwarfs in the plane is now significantly worse, due to the fact that all new discoveries of Y dwarfs within the volume have been found outside of the plane zone.

L dwarfs no longer show an underdensity in the plane, so no correction is needed for our derived L dwarf space densities. The T dwarf space densities should, however, be multiplied by 1.06 to account for the observed incompleteness. The Y dwarf incompleteness is harder to assess given the small number of Y dwarfs in the plane, but the raw numbers suggest a conservative correction factor of 1.15, slightly larger than the 1.13 factor adopted by Kirkpatrick et al. (2021a). These factors are listed in Table 17.

The final step in measuring the space densities of L, T, and Y dwarfs is assessing their measurement uncertainties. For this, we adopt the same methodology used in Kirkpatrick et al. (2021a). To summarize, our confidence in assigning an object to a $T_{\rm eff}$ bin is directly related to the measurement uncertainty on $T_{\rm eff}$, which is often comparable to the bin size itself. To estimate our confidence in the numbers of objects in each bin, we have run simulations with 10,000 Monte Carlo realizations wherein we take the uncertainty in $T_{\rm eff}$ and multiply it by a random value generated from a normal distribution having a mean of 0 and a standard deviation of 1. For each simulation, this uncertainty is added onto the measured value and the object (re)assigned to the appropriate $T_{\rm eff}$ bin. The computed means and standard deviations across all 10,000 realizations are given in column 5 of Table 17. We use only these computed standard deviations in our adopted space densities, but not the adjusted means. As further explained in Kirkpatrick et al. (2021a), the reason for this is that the number of objects is not preserved across the Monte Carlo simulations because some objects scatter into the hotter, incomplete bin at 2100–2250 K and are lost, while objects at the other temperature extreme may be lost because they fall outside the completeness limit of the colder bin. This last loss is one-sided, however, as any colder objects scattering into the warmer bin would be necessarily retained. Hence, we compute our adopted space densities using the raw number counts, but including the uncertainties derived from our simulations, as shown in the footnote of Table 17. These densities are graphically illustrated in Figure 17.

The measured space densities can now be compared to the simulated $T_{\rm eff}$ distributions (Raghu et al. 2024) to infer the form of the mass function at this low-mass end. Following on the results of Kirkpatrick et al. (2021a), which showed the best match to be a power law, $dN/dM \propto M^{-\alpha}$, with $\alpha \approx 0.6$,

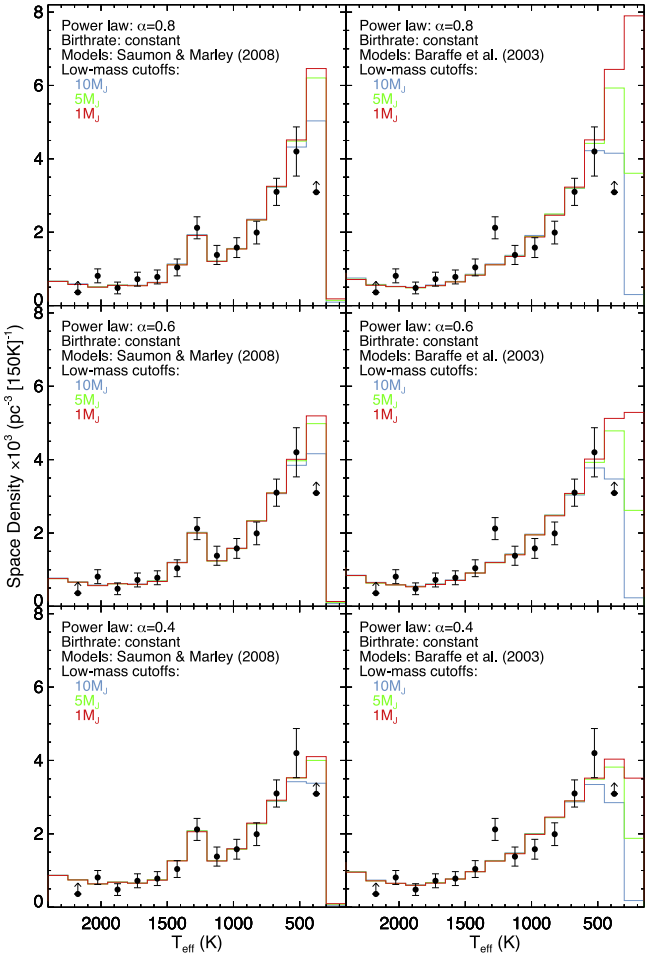

Figure 17. Our measured L, T, and Y dwarf space densities from Table 17 (black dots) as a function of effective temperature overplotted on different simulations from Raghu et al. (2024). In all panels, simulations assuming a constant birthrate are shown, along with the results for three different low-mass cutoffs: 10 $M_{\rm Jup}$ (light blue), 5 $M_{\rm Jup}$ (green), and 1 $M_{\rm Jup}$ (red). Panels in the left column use the Saumon & Marley (2008) evolutionary models, and panels in right column use Baraffe et al. (2003). The top row shows simulations with a power law of $\alpha = 0.8$, the middle row shows $\alpha = 0.6$, and the bottom row shows $\alpha = 0.4$. The best overall fits are those shown in the left panel in the middle row, using $\alpha = 0.6$ and the Saumon & Marley (2008) models.

Raghu et al. (2024) assume power-law functional forms with α values between 0.3 and 0.8 and, like Kirkpatrick et al. (2021a), choose low-mass cutoffs of ∼1, 5, and 10 $M_{\rm Jup}$. Unlike Kirkpatrick et al. (2021a), however, they vary the birthrate to not only include a constant birthrate over the lifetime of the Milky Way but also consider two other birthrates—called inside-out and late-burst—from Johnson et al. (2021) that are constrained by new results from Gaia. The inside-out birthrate represents a declining birthrate over the 10 Gyr lifetime of the Galactic disk, and the late-burst birthrate is identical to the inside-out form, except with an abrupt increase (by a factor of ∼3) in star formation ∼3–5 Gyr ago.

Evolutionary models are used to infer the current $T_{\rm eff}$ value of each simulated object (using its mass and age). Raghu et al. (2024) expand the model set used in Kirkpatrick et al. (2021a) by including the newer Marley et al. (2021) and Phillips et al. (2020) predictions and show (again) that the only evolutionary models able to fit the bump in the L/T transition in the $T_{\rm eff}$ distribution are those of Saumon & Marley (2008).

It has been shown in Kirkpatrick et al. (2021a) and Raghu et al. (2024) that the low-mass cutoff has little effect on the shape of the mass function at $T_{\rm eff}$ values above 450 K, where our fitting is taking place. Therefore, we consider each α + birthrate pair and compute the median of the least squared values for the simulations across all three cutoff masses. The minimum is achieved for $\alpha = 0.6$ and a constant birthrate, identical to the findings in Kirkpatrick et al. (2021a). The second best fit is achieved for $\alpha = 0.5$ and a constant birthrate. The third best fit is a tie among the $\alpha = 0.7$ + constant, the $\alpha = 0.4$ + late-burst, and $\alpha = 0.5$ + late-burst models. Use of either the late-burst or inside-out birthrates results in a slightly reduced α because those birthrates create a small over-abundance, relative to constant birthrate models, of older brown dwarfs that have already cooled to cooler temperatures.

In Figure 17, we show the fits for three values of α (0.4, 0.6, and 0.8) all paired with a constant birthrate. The panels in the left column of the figure show that the $\alpha = 0.6$ model with a constant birthrate and using the Saumon & Marley (2008) evolutionary models is an excellent representation of the empirical data. Can any new conclusions be gleaned regarding the low-mass cutoff? As Figure 4 of Raghu et al. (2024) illustrates, the Saumon & Marley (2008) models are incomplete below masses of $\sim 0.015 M_{\odot}$ ($\sim 16 M_{\rm Jup}$), so they are a poor choice for determining what the low-mass cutoff might be. Instead, we revert back to the Baraffe et al. (2003) models, which are complete down to $\sim 5 M_{\rm Jup}$. As the rightmost panels in Figure 17 illustrate, our ability to distinguish between low-mass cutoffs depends on measuring accurate space densities below 450 K. Using the 20 pc census to say confidently that star formation's terminus is below $10 M_{\rm Jup}$ or even $5 M_{\rm Jup}$ depends on surveying the sky more deeply at the wavelengths of these objects' peak emission *and* obtaining the necessary astrometry to measure accurate distances. As the simulations using the Baraffe et al. (2003) models show, measuring an accurate space density for the 300–450 K bin will allow us to distinguish between the cutoff masses, and even a few more objects discovered in the 150–300 K bin, which currently has only the 250 K Y dwarf WISE J085510.83−071442.5 in it, will provide even tighter constraints.

Have some of these ultra-low-mass products of star formation already been identified, and are they masquerading in the literature as exoplanet discoveries to higher-mass objects? We use our analysis in Table 15 to see first if the omission of these objects has biased our derivation of the brown dwarf mass function above. With the exception of the two objects (the companions to UCAC4 211-005570 and L 119-213) lacking mass estimates, we take all objects labeled as "consider" in column 4 of Table 15 and estimated their contribution to the overall mass function. For objects with $M \sin(i)$ measurements only, we pull a random number from a distribution of values uniformly distributed between 0 and 1 and multiply that number by 90° to assign each an inclination, which we then use to assign an actual mass value. For all masses, whether or not they are true masses or adjusted $M \sin(i)$ measurements, we then pull a random number from a normal distribution with a mean of 0 and standard deviation of 1 and multiply that number by the uncertainty, which we then add back to the mass value. We perform this methodology over 10,000 Monte Carlo iterations and find the mean and standard deviation of the resulting space density, binned over 0.001 $M_{\odot}$ mass intervals, as illustrated in Figure 18.

This figure shows that our derived space density of brown dwarfs (which we find to be $\xi(M) = dN/dM = 0.0469 \times M^{-0.6}$ in units of number $pc^{-3}[1M_{\odot}]^{-1}$, with M in units of $M_{\odot}$; see Section 8), overwhelms the space density above $5M_{\rm Jup}$ where our fitting took place. So, the omission of these objects has no impact on our derivation. However, the second question is whether any of these objects could be products of star formation itself rather than the secondary by-products of a protoplanetary disk. That question cannot be answered from this diagram, but it is a statistical certainty that at least a few of objects on the high-mass tail of this distribution are star formation products. One striking result from Figure 18, however, is the high space density of objects in the lowest-mass bin, given that the census of such low-mass objects, whether resulting from star formation or protoplanetary disks, is still woefully incomplete. There is clearly no shortage of ultra-low-mass objects in the Milky Way.

7.2. Combined Stellar and Brown Dwarf Space Densities

With the brown dwarf portion of the mass function now fitted, we can combine the stellar and brown dwarf portions to determine the shape of the overall mass function.

First, we take the number counts across the stellar regime and perform a similar Monte Carlo analysis as was done on the brown dwarfs. Specifically, for each object, we pull a random number from a normal distribution with a mean of 0 and a standard deviation of 1. We then multiply the mass measurement uncertainty by the random number and add that back to the mass value to get a true mass. We do this for each of the stars in our sample, and repeat the process 10,000 times to simulate 10,000 possible histograms. We then compute the mean value in each histogram bin along with its standard deviation. Because the 20 pc volume around the Sun is just one of many such volumes that can be taken as a sample of the Milky Way, we add the Poisson uncertainty and the standard deviation from above in quadrature to provide the final uncertainty per bin. (This parallels the brown dwarf space density analysis of Table 17.)

We can now append the substellar contribution onto this stellar distribution. To do this, we look at the predictions from the best-fit Raghu et al. (2024) model to the brown dwarf $T_{\rm eff}$ distribution from above, which is the $\alpha = 0.6$ power law with a constant birthrate function and passed through the Saumon & Marley (2008) evolutionary models. We also choose a $0.005M_{\odot}$ ($\sim 5M_{\rm Jup}$) cutoff to parallel the more detailed cutoff analysis from Kirkpatrick et al. (2021a). This simulation gives the predicted mass distributions shown in Figure 19. Each histogram is scaled so that the total number of objects in each histogram matches the raw numbers of objects per bin listed in Table 17. As one example, the 27 objects in the 1950–2100 K bin are predicted to fall almost exclusively in the 0.075–0.080 $M_{\odot}$ bin, and these predictions suggest that our 27 objects be apportioned as 20.5 objects in the 0.075–0.080 $M_{\odot}$ bin, 2.0 objects in the 0.070–0.075 $M_{\odot}$ bin, 1.0 object in the 0.065–0.070 $M_{\odot}$ bin, and fractional numbers of objects in bins of lower mass. As another example, the 63 objects in the 750–900 K bin are spread over a wide range of masses from 0.005 to $0.060M_{\odot}$ and are apportioned as 2.6 objects in the 0.055–$0.060M_{\odot}$ bin, 10.8 objects in the 0.050–$0.055M_{\odot}$ bin, 12.3 objects in the 0.045–$0.050M_{\odot}$ bin, 10.7 objects in the 0.040–$0.045M_{\odot}$ bin, 8.3 objects in the 0.035–$0.040M_{\odot}$ bin, etc.

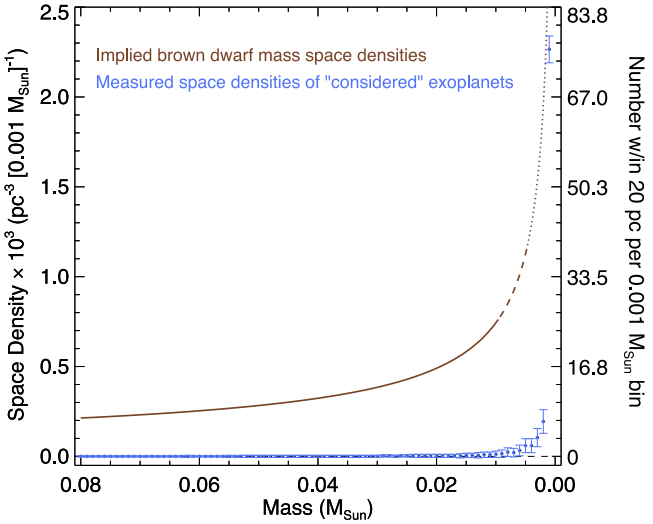

Figure 18. Plots of the implied space densities of brown dwarfs (brown) in $0.001M_{\odot}$ bins compared to the measured space densities of other possible low-mass star formation products from Table 15 (blue). The brown dwarf space densities are divided into three mass zones—$M > 10M_{\rm Jup}$ (solid brown), $5M_{\rm Jup} < M < 10M_{\rm Jup}$ (dashed brown), and $1M_{\rm Jup} < M < 5M_{\rm Jup}$ (dotted brown). Note that the densities of the possible pseudo-exoplanets do not affect our measurement of the brown dwarf space densities, as their numbers only become appreciable at masses well below $5M_{\rm Jup}$.

We take the apportionment across all 13 temperature bins and tally the results in each of the $0.005M_{\odot}$ wide mass bins, after also applying the factor (*corr* in Table 17) to correct for losses of objects along the Galactic plane and extrapolating the numbers to the full 20 pc volume if that temperature bin was not complete to 20 pc. For example, the raw number counts in the 450–600 K bin shown in both Table 17 and Figure 19 were multiplied by the 1.06 correction factor then multiplied by $(20/15)^3$ to extrapolate to the full volume. In Table 17, we find that our lowest temperature bin with a space density measurement, 300–450 K, is considered to be incomplete, and the mass distribution for that bin in Figure 19 suggests that that bin's objects fall exclusively below $0.025M_{\odot}$. Therefore, we consider any space density measurements below this mass value to be lower limits only.

We now add these brown dwarf masses to the results of our Monte Carlo analysis of stellar masses above to produce a mass function across the entire mass range. This initial mass function is illustrated in Figure 20. Panel (a) shows the mass function across the full mass range from 0 to 8 $M_{\odot}$, binned in 0.1 $M_{\odot}$ increments. The mass function rises with decreasing mass, and it continues to rise beyond our 0.025 $M_{\odot}$ (~ 26 $M_{\rm Jup}$) completeness limit. The subsequent panels show details. Panel (b) shows the high-mass end of the initial mass function from 1.5 to 8.0 $M_{\odot}$, again with 0.1 $M_{\odot}$ binning. The statistics above 3 $M_{\odot}$ are poor but nonetheless show a steady increase from there down to 1.5 $M_{\odot}$. Panel (c) shows the mid-mass range ($0.4 < M < 1.5$ $M_{\odot}$), now binned into smaller 0.02 $M_{\odot}$ increments because the statistics here are richer. Panel (d) zooms in on the smallest mass portion, below 0.4 $M_{\odot}$, and chooses yet a smaller mass binning of 0.005 $M_{\odot}$. With the exception of a few small features (discussed below), the mass function is seen to rise monotonically from 1.5 to 0.025 $M_{\odot}$. Mostly within the measurement errors (see more discussion

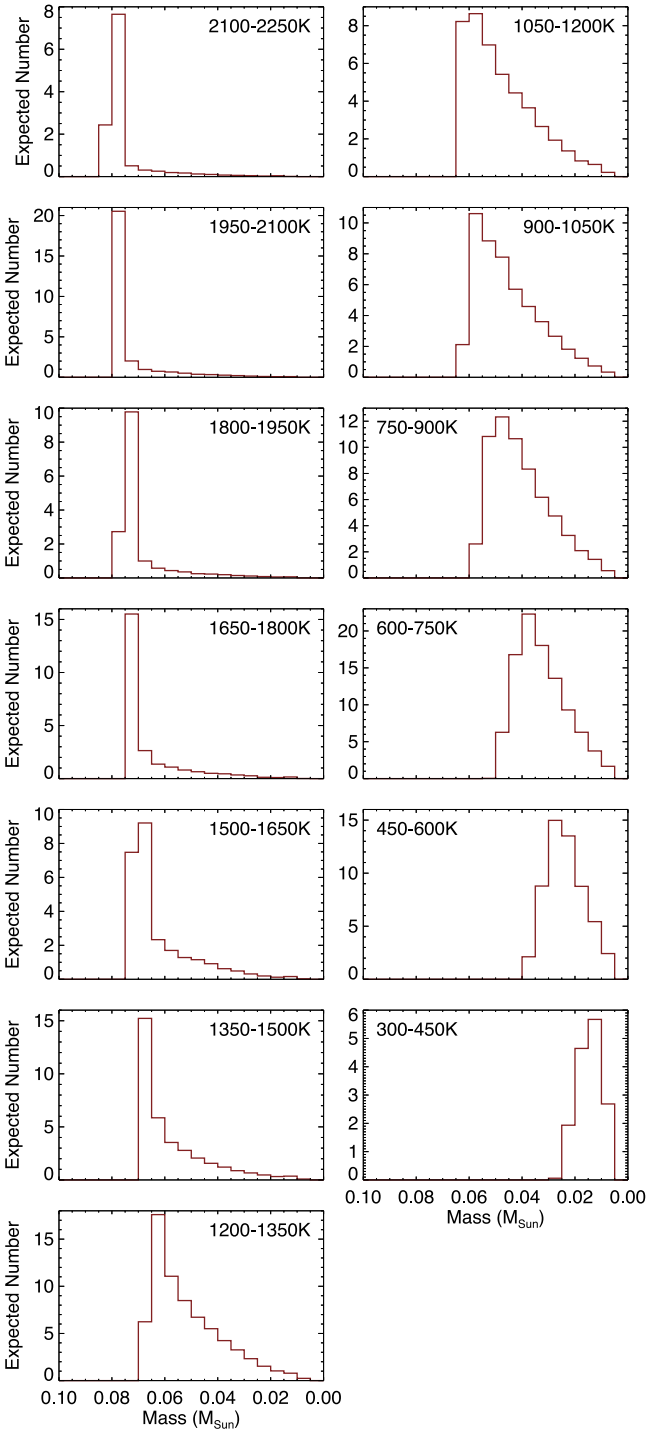

Figure 19. The predicted distributions of brown dwarf masses in each of our 150 K effective temperature bins based on the best-fit Raghu et al. (2024) simulation to our measured L, T, and Y dwarf space densities (see text for details). Each histogram is scaled to match the total number of objects listed for that $T_{\rm eff}$ bin in Table 17.

below), the initial mass function is seen to continue rising well below our 0.025 $M_{\odot}$ completeness limit and at least down to $0.015M_{\odot}$.

The numbers on which Figure 20 is based are given in Table 18. For ease of reference, both the number of stars and the space density are given for each mass bin. Three mass binnings are tabulated, roughly paralleling what is shown in Figure 20: $0.1M_{\odot}$ binning across the entire 0.0–$8.0M_{\odot}$ range (80 bins), $0.02M_{\odot}$ binning across the range 0.0–$1.6M_{\odot}$ (80 bins), and $0.005M_{\odot}$ binning across the range 0.0–$0.4M_{\odot}$ (80 bins). Mass bins with incomplete statistics are labeled as lower limits in the final column of the table.

There are a few features in Figures 20(c) and (d) that warrant special attention. The first is the bump in the object counts near $0.55M_{\odot}$ in panel (c). This falls near the point at which our mass estimation switches from that of the TIC relations of Stassun et al. (2019) at higher masses to that of the M_{Ks} relation of Mann et al. (2019) at lower masses. Currently, we switch between these two relations at $M_{Ks} = 5.0$ mag, corresponding to a mass of $\sim 0.6M_{\odot}$. As a test, if we change the switchover point to be at $M_{Ks} = 4.0$ mag ($M \approx 0.7M_{\odot}$) instead, we find that this bump in the space densities moves to higher masses, with a deficit around $0.8M_{\odot}$, as shown in Figure 21. We also note that the uncertainties in the masses resulting from the Mann et al. (2019) relation are 3 to 4 times smaller than those derived from the Stassun et al. (2019) relation. As another test, we can artificially inflate the mass uncertainties on the Mann et al. (2019)-derived masses while keeping the current switchover point at $M_{Ks} = 5.0$ mag. That result is also shown in Figure 21. In this case, the bump is greatly diminished in the number counts, but an inflection point is still seen near $0.6M_{\odot}$. Given that this feature in the number counts moves in response to the mass estimation used, we believe it is an artificial effect. Furthermore, given that the Stassun et al. (2019) mass estimation relies on dynamically measured *individual* masses whereas the Mann et al. (2019) relation uses Bayesian statistics to ferret out individual masses from binaries in which only the *total* system mass is measured, this likely indicates a small systematic offset that slightly deflates the Mann et al. (2019)-derived masses relative to the truth. In fact, an effect in this direction and representing a systematic offset of $\sim$2% is seen when comparing results of the M_{Ks} relation to individually derived masses (Figure 15 of Mann et al. 2019). Obtaining more directly measured individual masses in this regime, corresponding to late-K and early-M dwarfs, would help to put this issue to rest.

Other features are seen in Figure 20(d). There is a small drop in the number counts near $0.13M_{\odot}$ followed by a sudden rise near $0.11M_{\odot}$. This feature is likely artificial, as the bump at $0.11M_{\odot}$ is due primarily to components in multiple systems about which little information is known, and these were arbitrarily assigned masses of $0.11M_{\odot}$ based on an anticipated spectral type of M5.5. This type lies at a very sharp inflection point (see Table 16) in our mass-versus-spectral type relation (Figure 14).

The other feature is the rapidly changing number count between masses of 0.06 and 0.08 $M_{\odot}$, a mass range that straddles the stellar/substellar break. Some of the early-L to mid-L dwarfs that we have included in our brown dwarf mass function analysis are likely very low-mass stars and not brown dwarfs themselves. As a consequence, these are assigned masses that are a bit too high (the extraneous high point in the $0.075–0.080M_{\odot}$ bin), which likely leads to concomitant deficits in the next higher-mass bins. In fact, Table 4 lists three early-L dwarfs in the 20 pc census that have dynamical mass measurements, and one of these (LP 388-55 B; Dupuy & Liu 2017) has a mass just above the $0.075–0.080M_{\odot}$ mass bin (0.083 ± 0.03 $M_{\odot}$).

8. Discussion

How do our 20 pc results compare to other attempts in the literature to measure the initial mass function? Pioneering work by Salpeter (1955) found that a power-law form

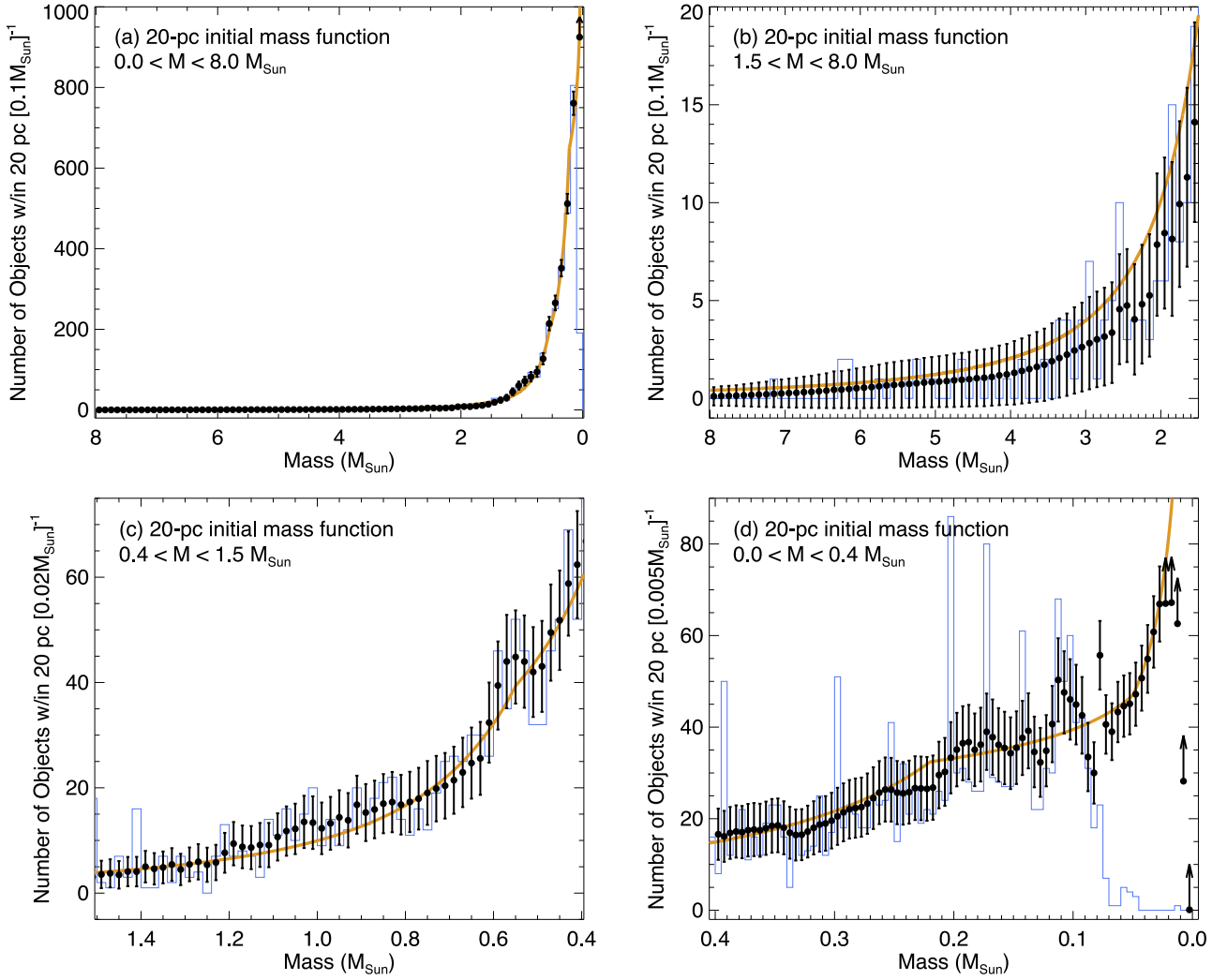

Figure 20. The 20 pc initial mass function across all stellar and substellar masses. Our measured values and their uncertainties are shown in black. The raw number counts for stars of type M9.5 and earlier are shown by the blue histogram. (a) The full mass range, 0.0–8.0$M_{\odot}$, with 0.1$M_{\odot}$ binning. (b) A zoom-in of the high-mass end, from 1.5 to 8.0 $M_{\odot}$, with the same binning. (c) A zoom-in of the mid-range, from 0.4 to 1.5 $M_{\odot}$, with 0.02$M_{\odot}$ binning. (d) A zoom-in of the low-mass portion, 0.0–0.4$M_{\odot}$, with 0.005$M_{\odot}$ binning. Our fit to the mass function is shown by the orange line.

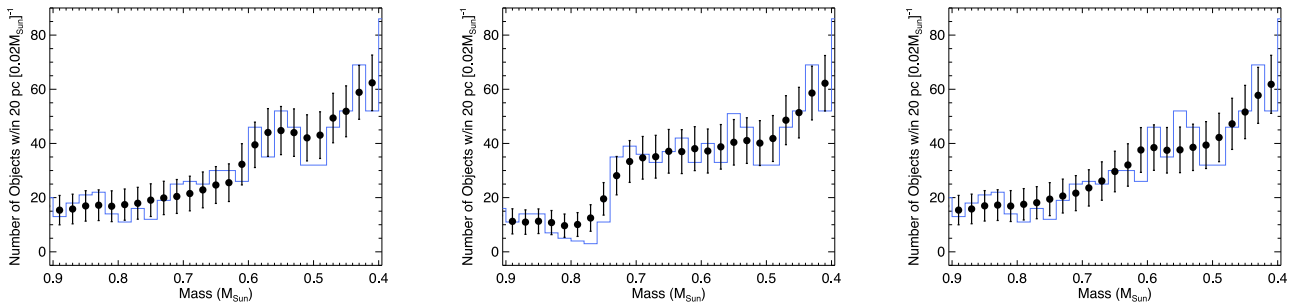

(a) (b) (c)

Figure 21. Tests of the bump in the initial mass function seen near 0.55$M_{\odot}$ in Figure 20. (a) A zoom-in showing the bump in Figure 20(c). (b) The number counts over the same mass range but where we have moved the switchover in the mass estimate from $M_{Ks} = 5.0$ mag, to $M_{Ks} = 4.0$ mag. (c) The number counts over the same mass range but where we have kept the $M_{Ks} = 5.0$ mag switchover point and inflated the uncertainties on the M_{Ks}-derived masses by a factor of 4. For other details, see the caption to Figure 20.

$\xi(M) = dN/dM \propto M^{-\alpha}$ with $\alpha = 2.35$ best fit the initial mass function over the range $0.3 \leqslant M \leqslant 10M_{\odot}$. Subsequent work by Miller & Scalo (1979) found $\alpha = 1.4$ for $0.1 \leqslant M \leqslant 1M_{\odot}$, and $\alpha = 2.5$ for $1 \leqslant M \leqslant 10M_{\odot}$. Scalo (1986) determined $\alpha = 2.7$ for $2 \leqslant M \leqslant 10M_{\odot}$, and Reid et al. (2002) found $\alpha = 1.3$ for $0.1 \leqslant M \leqslant 0.7M_{\odot}$.

As more accurate measurements of the initial mass function became possible, researchers realized the importance of

Table 16
Piecewise Fit to Mass versus Dwarf Spectral Type Relation

Spectral Type	Spectral Index	Mass ($M_\odot$)
(1)	(2)	(3)
A6	6.0	1.75
G0	20.0	1.06
K0	30.0	0.86
K3	33.0	0.71
M0	40.0	0.59
M3	43.0	0.39
M4	44.0	0.20
M5.5	45.5	0.11
L0	50.0	0.075

Note. Each row in this table represents an inflection point in the red, piecewise fit of Figure 14.

distinguishing whether the masses used for the computation were that of the stellar system or of its individual components. For example, in an analysis of data from the Sloan Digital Sky Survey, Bochanski et al. (2010) found $\alpha = 2.38$ for $0.32 < M < 0.80M_\odot$, and $\alpha = 0.35$ for $0.10 < M < 0.32M_\odot$ for the mass function of systems, but $\alpha = 2.66$, and $\alpha = 0.98$ for the mass function of single stars over the same two mass regimes, respectively. Earlier, Kroupa (2001) had found that single-star initial mass functions resulting from the analysis of young star clusters generally gave values of α that were higher by $\sim$0.5 (for $0.1 < M < 1.0M_\odot$) than the field initial mass function, for which systems were not resolved. Reid (2005) cautions that unresolved multiplicity complicates interpretation of the initial mass function; the initial mass function of *systems* is more directly tied to the fragmentation of the original molecular cloud, but the initial mass function of *individual objects* gives the mass distribution of the (sub)stellar bodies formed.

Our work on the 20 pc census has concentrated on analysis of the individual products of star formation, as we are curious to know how frequently this process produces, for example, very low-mass brown dwarfs compared to higher-mass objects. We will therefore restrict subsequent analysis here to the single-object initial mass function and leave analysis of the 20 pc census regarding multiplicity and the system mass function to those investigating how the formation of systems relates back to cloud fragmentation.

8.1. Comparison of Initial Mass Functions

Here, we compare two very well established forms of the initial mass function and compare their predictions to our results based on the 20 pc census.

Chabrier (2001, 2003a, 2003b) developed several functional forms for the initial mass function. The latest one relating to single objects is given by Chabrier (2003b) and is comprised of a power law at high masses and a log-normal form at lower masses:

$$\begin{aligned}\xi(M) &= \frac{C_1}{\ln 10} M^{-\alpha}, \text{ for } M > 1.0M_\odot \\ &= \frac{C_2}{M \ln 10} e^{\frac{-(\log M - \log M_c)^2}{2\sigma^2}}, \text{ for } M \leqslant 1.0M_\odot \end{aligned} \quad (19)$$

where $C_1 = 0.0443$, $\alpha = 2.3$, $C_2 = 0.158$, $M_c = 0.079M_\odot$, and $\sigma = 0.69M_\odot$. The value of $\xi(M)$ is in units of number of objects per pc^3 per $M_\odot$. See Equation (2) and Table 1 of Chabrier (2003b) for the derivation shown above. We note that the values of C_1 and C_2 are set by Chabrier (2003b) to match an empirical space density measurement (at $1M_\odot$ from Scalo 1986) of the initial mass function in the Milky Way's disk population.

Likewise, Kroupa et al. (2013) found that a tripartite power-law form best describes the single-object initial mass function:

$$\begin{aligned}\xi(M) &= C\left(\frac{0.5}{0.07}\right)^{-\alpha_2}\left(\frac{M}{0.5}\right)^{-\alpha_1}, \text{ for } 0.5 < M < 150M_\odot \\ &= C\left(\frac{M}{0.07}\right)^{-\alpha_2}, \text{ for } 0.07 < M < 0.5M_\odot \\ &= \frac{C}{3}\left(\frac{M}{0.07}\right)^{-\alpha_3}, \text{ for } 0.01 < M < 0.15M_\odot \end{aligned} \quad (20)$$

where $\alpha_1 = 2.3$, $\alpha_2 = 1.3$, and $\alpha_3 = 0.3$. As above, the value of $\xi(M)$ is in units of number of objects per pc^3 per $M_\odot$. Note that there are two components of this mass function that contribute to the mass range $0.15 < M < 0.07M_\odot$. The value of C is not specified by Kroupa et al. (2013). However, Figures 4–24 of Kroupa et al. (2013) provide a comparison of this initial mass function with the Chabrier (2003b) version in Equation (19), showing that they are identical at $\sim 0.85M_\odot$, resulting in a value of $C \approx 1.15$.

As shown in Figure 22, neither of these parameterizations adequately describes the 20 pc initial mass function derived here. The main reason for this is that the prior determinations were done pre-WISE, pre-Spitzer, and pre-Gaia before the L, T, and Y dwarf complement of the mass function was fully characterized and before exquisite parallax determinations became available for almost all objects in the 20 pc volume. As such, these prior works relied on poorer statistics with fits done in logarithmic scaling on both the *dN* and *dM* axes. Our careful accounting of objects within the 20 pc volume now allows for a more precise determination of the single-object initial mass function.

We thus provide a new multipart power-law parameterization that is bounded by the following caveats: (1) We assume $\alpha = 2.3$ at the high-mass end, as has been determined from earlier studies, and we do this because our 20 pc census has few stars with $M > 2M_\odot$ to better constrain this. (2) We assume $\alpha = 1.3$ at intermediate masses, as this has also been established by earlier studies. (3) We take $\alpha = 0.6$ in the brown dwarf regime, as was determined in Section 7.1. We do not constrain the stitch points in mass between the power-law pieces nor do we limit the number of power-law pieces to only three. We perform these fits by eye, keeping in mind the caveats from Section 7.2 concerning the nonphysical bumps and troughs in the number counts as a function of mass. Given the constraints above, we find that a three-piece power law does not adequately describe the number counts in the mid- to late-M dwarf regime ($0.08 \lesssim M \lesssim 0.20M_\odot$), but that a four-piece power law can. This best fit is given below and illustrated by the orange line in Figure 20:

$$\begin{aligned}\xi(M) &= C_1(M)^{-\alpha_1}, \text{ for } 0.55 < M < 8.0M_\odot \\ &= C_2(M)^{-\alpha_2}, \text{ for } 0.22 < M < 0.55M_\odot \\ &= C_3(M)^{-\alpha_3}, \text{ for } 0.05 < M < 0.22M_\odot \\ &= C_4(M)^{-\alpha_4}, \text{ for } 0.01 < M < 0.05M_\odot \end{aligned} \quad (21)$$

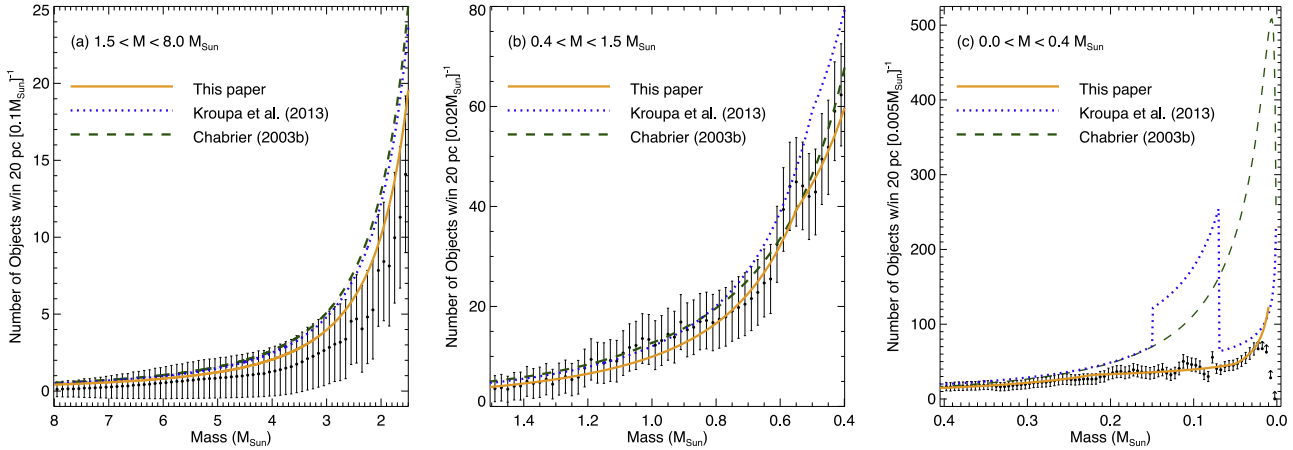

Figure 22. A comparison of our 20 pc number counts (black points with error bars) and our fit of the initial mass function (solid orange line) to the functional forms of Kroupa et al. (2013; dotted blue line) and Chabrier (2003b; dashed green line). Each panel shows a zoom-in of a different mass segment: (a) $1.5 < M < 8.0 M_{\odot}$, (b) $0.4 < M < 1.5 M_{\odot}$, (c) $0.0 < M < 0.4 M_{\odot}$.

Table 17
Space Densities for Early-L through Early-Y Dwarfs

$T_{\rm eff}$ Bin (K)	Completeness Limit ($d_{\rm max}$) (pc)	Raw No. of Objects (raw)	Corr. Factor (corr)[a]	Adjusted No. of Objects (adj)	Adopted Space Density (dens)[b] ($\times 10^{-3}$ pc^{-3})
(1)	(2)	(3)	(4)	(5)	(6)
2100–2250	20.0[c]	12	1.00	13.3 ± 2.8	>0.36
1950–2100	20.0	27	1.00	21.2 ± 3.4	0.81 ± 0.19
1800–1950	20.0	16	1.00	21.1 ± 3.6	0.48 ± 0.16
1650–1800	20.0	24	1.00	23.0 ± 3.8	0.72 ± 0.19
1500–1650	20.0	26	1.00	25.1 ± 3.9	0.78 ± 0.19
1350–1500	20.0	35	1.00	34.2 ± 4.7	1.04 ± 0.23
1200–1350	20.0	69	1.03	54.6 ± 5.4	2.12 ± 0.30
1050–1200	20.0	45	1.03	44.3 ± 5.3	1.38 ± 0.26
900–1050	20.0	50	1.06	43.5 ± 5.0	1.58 ± 0.27
750–900	20.0	63	1.06	54.9 ± 5.6	1.99 ± 0.31
600–750	20.0	98	1.06	77.6 ± 6.3	3.10 ± 0.37
450–600	15.0	56	1.06	44.8 ± 4.9	4.20 ± 0.67
300–450	11.0	15	1.15	17.2 ± 3.0	>3.09[d]
150–300	…	1	…	…	…

Notes.
[a] As the $T_{\rm eff}$ bins from 1050 to 1350 K encompass both L and T dwarfs (see Figure 22(b) of Kirkpatrick et al. 2021a), we average the correction factor for L dwarfs (1.00) and T dwarfs (1.06).
[b] This value is computed via the equations dens = (raw)(corr)$\Big/\left(\frac{4}{3}\pi {d_{\rm max}}^3\right)$, and $\sigma_{\rm dens} = \sqrt{({\sigma_{\rm raw}}^2 + {\sigma_{\rm adj}}^2)}$(corr)$\Big/\left(\frac{4}{3}\pi {d_{\rm max}}^3\right)$, where $\sigma_{\rm raw} = \sqrt{\rm raw}$.
[c] This bin is complete only for its L dwarf complement. Since late-M dwarfs are also expected to populate this bin, the derived space density is considered to be a lower limit.
[d] This temperature bin is not fully populated, as WISE sensitivity limits cannot probe to the quoted completeness distance for Y dwarfs below $T_{\rm eff} \approx 400$ K.

where $C_1 = 0.0150$, $\alpha_1 = 2.3$, $C_2 = 0.0273$, $\alpha_2 = 1.3$, $C_3 = 0.134$, $\alpha_3 = 0.25$, $C_4 = 0.0469$, $\alpha_4 = 0.6$. As above, the value of $\xi(M)$ is in units of numbers of objects per pc^3 per $M_{\odot}$.

If we integrate under our best fit from 0.075 to 8.0 $M_{\odot}$, we find 3002 stars, which can be compared to the 3000 individual objects in the 20 pc census that have (measured or implied) types of M9.5 or earlier. The integration under our fit for 0.020 to 0.075 $M_{\odot}$ gives 789 brown dwarfs, compared to the 582 individual L, T, and Y dwarfs in Table 4. Most of the missing ~200 brown dwarfs are ones with $T_{\rm eff}$ values 450–600 K and distances of 15–20 pc or ones with 300–450 K temperatures and 11–20 pc distances, where our current accounting is known to be incomplete (see Table 17). These results show that the number of stars relative to brown dwarfs is 3002/789, or ~4. However, we believe that the brown dwarf mass function extends to at least 0.010 $M_{\odot}$, which would give a ratio of 3002/986 (~3) if the $\alpha = 0.6$ functional form continues to that mass. In the limiting case in which it continues to zero mass, we find a star-to-brown-dwarf ratio of 3002/1602, or ~2. We note that, as recently as a decade ago, this ratio in the solar neighborhood was believed to be as high as 6:1 (Kirkpatrick et al. 2012).

This decrease in the ratio of stars to brown dwarfs is not in tension with microlensing results, as an analysis of Optical Gravitational Lensing Experiment data found that an even steeper power law in the brown dwarf regime ($\alpha = 0.8$ for $0.01 < M < 0.08 M_{\odot}$; Mróz et al. 2017) best fits the observed distribution of short-timescale (low-mass) events. Furthermore, the possibility that the mass function extends into a regime significantly below 0.010 $M_{\odot}$ is bolstered by recent JWST

Table 18
Number of Objects and Space Densities per Mass Bin for the 20 pc Census

Mass Bin ($M_\odot$) (1)	Total No. (2)	Space Density[a] (pc^{-3} $[M\ bin]^{-1}$) (3)	Lower Limit? (4)
0.00-0.10	924.9 ± 30.4	0.0276005 ± 0.0009072	yes
0.10-0.20	761.0 ± 28.9	0.0227094 ± 0.0008624	
0.20-0.30	511.6 ± 24.2	0.0152669 ± 0.0007222	
0.30-0.40	351.7 ± 20.5	0.0104953 ± 0.0006118	
0.40-0.50	265.6 ± 18.2	0.0079259 ± 0.0005431	
0.50-0.60	214.3 ± 16.8	0.0063950 ± 0.0005013	
0.60-0.70	127.0 ± 14.1	0.0037899 ± 0.0004208	
0.70-0.80	94.5 ± 12.6	0.0028200 ± 0.0003760	

Note.
[a] The $[M\ bin]^{-1}$ portion of the units should be replaced with the bin size for that row. For example, for the first row of the table, the units will be pc^{-3} $[0.10\ M_\odot]^{-1}$ because that bin is 0.10 $M_\odot$ wide.

(This table is available in its entirety in machine-readable form.)

observations of the Orion Nebula Complex that show a significant population of objects, down to at least $0.001M_\odot$, that are apparently direct products of star formation (McCaughrean & Pearson 2023; Pearson & McCaughrean 2023).

Finally, we note that our accounting of the mass of hydrogen-burning stars in the 20 pc census along with our best fit to the mass function of brown dwarfs allows us to calculate the average mass of an object in this sample. Integrating our mass function down to a mass of 0.020 $M_\odot$, we find that value to be 0.41 $M_\odot$. There are likely many undiscovered brown dwarfs in the solar neighborhood too faint to be currently detected, so this average value could be pushed lower. Assuming there is no low-mass cutoff of star formation and the brown dwarf mass function continues to zero mass with a power-law slope of $\alpha = 0.6$, we find that the average mass of objects in the 20 pc census would drop to 0.34 $M_\odot$. This can be considered as the limiting case unless the functional form at the lowest masses has an α value considerably greater than 0.6.

9. Conclusions

In this paper our aim was to study the initial mass distribution of star formation's by-products, from the highest-mass progenitors of present-day white dwarfs to the lowest-mass brown dwarfs. For this, we have produced a volume-complete sample of stellar and substellar objects within 20 pc of the Sun. We have split multiple systems into their separate components and characterized each individual object to provide an accurate mass assignment.

Our main conclusions can be summarized as follows:

(1) The initial mass function steadily increases as a function of descending mass. Its peak in (linear) mass space is not yet defined but is located below $0.020M_\odot$ ($\sim 20M_{Jup}$; Figure 20). We find that a quadripartite power-law ($\xi(M) = dN/dM \propto M^{-\alpha}$) fits the observed space densities well (Equation (21)). Going from high mass to low mass, we find exponents of α = 2.3, 1.3, 0.25, and 0.6, with stitch points between segments of 0.55, 0.22, and 0.05 $M_\odot$, respectively. Although the rate of ascent of the mass function is slowly retarded as a function of descending mass through the stellar and high-mass brown dwarf regimes, its ascent increases again for the lower-mass brown dwarfs.

(2) This initial mass function agrees well with previous determinations in the high-mass regime (by design) but differs markedly from other established formalisms in the M, L, T, and Y dwarf regimes (Section 8). The functional forms proposed by Chabrier (2003b), Kroupa et al. (2013) overpredict the number of these lower-mass dwarfs relative to their more massive counterparts.

(3) The 20 pc census currently consists of ∼3000 stars and ∼600 brown dwarfs (Table 4). At face value, this implies a stellar-to-substellar ratio of ∼5, but corrections for incompleteness for brown dwarfs with temperatures from 300 to 600 K show that the ratio is currently measured at ∼4. The incompletenesses at lower temperatures may yet bring this ratio as low as ∼3 (Section 8). The average mass of objects in the 20 pc census is currently measured as 0.41 $M_\odot$ but could drop as low as 0.34 $M_\odot$ if many colder brown dwarfs, yet to be discovered, actually exist (Section 8).

(4) The 20 pc census of objects colder than 600 K, corresponding to spectral type ∼T8.5, is still incomplete beyond 15 pc, and the completeness volume shrinks to 11 pc at 450 K, corresponding to spectral type ∼Y0 (Table 17). Moreover, additional sources of incompleteness for objects as warm as 1350 K are high backgrounds and confusion along the Galactic plane (Section 7.1).

(5) There are direct indications that many unrecognized companions still exist to already identified members of the 20 pc census. Acceleration (aka proper-motion anomaly) has been used to flag many such systems (Section 5.1.1), and large Gaia RUWE/LUWE values significantly higher than 1.0 flag many others (Section 5.2). Additional follow-up of these systems would help to better flesh out the 20 pc census itself while also providing much firmer statistics on multiplicity and the prevalence of hierarchical systems.

(6) Our *complete* (see caveats (4) and (5), above) 20 pc census produced for this paper is available for additional uses (Table 4). As one example, this nearby sample is particularly useful as the hunting grounds for the closest habitable worlds to our own solar system and is thus also available via the NASA Exoplanet Archive.[88]

(7) Except for white dwarfs (Section 6.1.1) and brown dwarfs (Section 6.1.3), masses are used directly when they have been measured (Section 4). Most objects, though, lack actual mass determinations. For these, we use a variety of mass estimation methods and select the ones that provide the most reliable results, when comparison to truth is available (Section 6.3). Nonetheless, our resulting space density computations binned by mass show some spurious features that appear to be caused by shortcomings in the estimation method. These are most obvious in the early-M dwarf region and in the regime from late-M to early-L dwarfs (Section 7.2). Dedicated programs, such as those by Vrijmoet et al. (2022) and Dupuy et al. (2022) directly determining masses of objects in these zones are clearly needed.

(8) Dueling definitions in the literature of *brown dwarf* and *exoplanet* could bias our results if objects tagged as

[88] https://exoplanetarchive.ipac.caltech.edu/docs/20pcCensus.html

exoplanets are omitted from the initial mass function. We account for this and find that most of objects labeled exoplanets (via the $13M_{\rm Jup}$-based definition) fall in a small-mass regime separate from objects that have been more traditionally labeled as brown dwarfs (via the formation-based definition) and do not affect our conclusions regarding the mass function (Section 6.2.3). This having been stated, future studies of the initial mass function might wisely consider no such division, as planet formation can be thought of merely as a (delayed) secondary process resulting from star formation itself. Including planetary formation products as another branch of the initial mass function will, however, not be feasible until a statistically robust, volume-complete set of exoplanets can be reliably measured.

(9) Gaia DR3 detections comprise only ∼75% of the volume-complete 20 pc census. Objects within 20 pc of the Sun can be missed by Gaia because they are too bright for Gaia observations, too faint for Gaia to detect, or are companions to Gaia-detected host stars that are (presently) inadequately characterized astrometrically (Section 2.1).

(10) Citizen science continues to produce new discoveries within 20 pc (Section 2.1.2), even including a possible new Y dwarf with a *bonus* Spitzer parallax (Appendix A.3). Such discoveries are coming largely from WISE data sets, but these sets are being pushed to their sensitivity limits. Completing the 20 pc census in the 300–600 K temperature range will require a deeper survey at ∼5 um, the best prospect for which is the NASA mission NEO Surveyor (Kirkpatrick et al. 2019b; Mainzer et al. 2023). Results from that mission, along with searches for cooler companions to known 20 pc hosts with JWST, represent our best short-term prospects for determining the occurrence rate of objects such as WISE J085510.83−071442.5 that reside below 300 K.

(11) The 20 pc census enables us to identify the nearest star or brown dwarf in each constellation (Table B1). Interestingly, six of the eighty-eight constellations have a Y dwarf as their nearest member despite the fact that Y dwarfs have not yet been fully mapped within this 20 pc volume.

Note added in proof. The nearby brown dwarf candidate CWISE J165909.91−351108.5 from Table 2 has been confirmed as a late-L dwarf by Robbins et al. (2023a), but it likely falls outside the 20 pc census. Additionally, Robbins et al. (2023b) find that CWISE J105512.11+544328.3, from Table 14, is not a T subdwarf but rather an anomalously blue Y dwarf.

Acknowledgments

D.K., F.M., and C.G. acknowledge support from grant No. 80NSSC20K0452 awarded for proposal 18-2ADAP18-0175 under the NASA Astrophysics Data Analysis Program. Data presented here are based on observations obtained at the Hale Telescope, Palomar Observatory as part of a continuing collaboration between the California Institute of Technology, NASA/JPL, Yale University, and the National Astronomical Observatories of China. Some of the data presented herein were obtained at the W. M. Keck Observatory, which is operated as a scientific partnership among the California Institute of Technology, the University of California, and the National Aeronautics and Space Administration. The Observatory was made possible by the generous financial support of the W. M. Keck Foundation. The authors wish to recognize and acknowledge the very significant cultural role and reverence that the summit of Maunakea has always had within the indigenous Hawaiian community. We are most fortunate to have the opportunity to conduct observations from this mountain. This research has made use of the Keck Observatory Archive (KOA), which is operated by the W. M. Keck Observatory and the NASA Exoplanet Science Institute (NExScI), under contract with the National Aeronautics and Space Administration. The first author would like to thank Patrick Shopbell at Caltech for resurrecting an Exabyte drive that successfully read raw CTIO data from 1997. Part of this research was carried out at the Jet Propulsion Laboratory, California Institute of Technology, under a contract with the National Aeronautics and Space Administration (80NM0018D0004). He would also like to thank Mike Cushing for discussion of evolved star loci in the 20 pc color–magnitude diagrams.

One observation reported in this paper was obtained with the Southern African Large Telescope (SALT) under program 2021-2-SCI-027 (PI: Faherty). R.R. acknowledges support from grant RYC2021-030837-I funded by MCIN/AEI/ 10.13039/ 501100011033 and by "European Union NextGenerationEU/ PRTR," and partial support by the AGAUR/Generalitat de Catalunya grant SGR-386/2021 and by the Spanish MINECO grant PID2020-117252GB-I00. E.G. acknowledges support from the Heising-Simons Foundation through a 51 Pegasi b Fellowship. This publication makes use of VOSA, developed under the Spanish Virtual Observatory (https://svo.cab.inta-csic.es) project funded by MCIN/AEI/10.13039/501100011033/ through grant PID2020-112949GB-I00. This research made use of the Montreal Open Clusters and Associations (MOCA) database, operated at the Montréal Planétarium (J. Gagné et al. 2024, in preparation). Backyard Worlds research was supported by NASA grant 2017-ADAP17-0067 and by the NSF under grants AST- 2007068, AST-2009177, and AST-2009136. J.V. acknowledges support from a Royal Society—Science Foundation Ireland University Research Fellowship (URF\1\221932). The authors would like to thank the Near-Earth Object Surveyor mission for covering the page charges for this paper through contract No. 80MSFC20C0043.

Facilities: WISE, Gaia, Spitzer (IRAC), Hale (WIRC, DBSP, TSpec), Keck:I (MOSFIRE, NIRES), IRTF (SpeX), Gemini:South (FLAMINGOS-2), Blanco (RCSPec, ARCoIRIS), NTT (SOFI), Magellan:Baade (FIRE), Shane (Kast), SALT (RSS), SOAR (OSIRIS), ARC (TSpec)

Software: WiseView (Caselden et al. 2018), `Spextool` (Vacca et al. 2003; Cushing et al. 2004), `MOPEX/APEX` (Makovoz & Khan 2005; Makovoz & Marleau 2005), `IRAF` (Tody 1986, 1993), `kastredux` (A. J. Burgasser et al. 2024, in preparation), `FIREHOSE/MASE` (Bochanski et al. 2009), `crowdsource` (Schlafly et al. 2018).

Appendix A
Photometric, Spectroscopic, and Astrometric Follow-up

A.1. Photometry

For possible M, L, T, and Y dwarf additions to the 20 pc census, we have searched for published near- and mid-infrared photometry using online surveys such as 2MASS (Skrutskie et al. 2006), the VISTA Hemisphere Survey (VHS; McMahon et al. 2013), the UKIRT Hemisphere Survey (UHS; Dye et al.

Table A1
Ancillary Spitzer Data

Object Name	AOR	Bands[a]	Obs. Date (UT)	Program + Phase[b]	PI Name
(1)	(2)	(3)	(4)	(5)	(6)
CWISE J001322.53−114300.7	60981248	1,2	2017-10-13	13116PC	Kelley
	60981504	1,2	2017-10-16	13116PC	Kelley
CWISE J025711.65−390626.9	45160192	1,2	2012-03-20	80109PC	Kirkpatrick
CWISE J041822.64+272958.8	11233792	1,2	2005-02-20	3584C	Padgett
	11237632	1,2	2005-02-21	3584C	Padgett
	19030272	1,2	2007-03-30	30816C	Padgett
	47116288	1,2	2013-11-07	90071PC	Kraus
CWISE J042325.55+264045.0	5074688	1,2	2004-10-05	139C	Evans
	5075200	1,2	2004-10-07	139C	Evans
	11233280	1,2	2005-02-21	3584C	Padgett
	11237120	1,2	2005-02-21	3584C	Padgett
	14604544	1,2	2005-09-16	20386C	Myers
	14604800	1,2	2005-09-17	20386C	Myers
	42296064	1	2011-11-04	80053PC	Paladini
	47105280	1,2	2013-11-15	90071PC	Kraus
CWISE J043227.67+260616.7	11231744	1,2	2005-02-24	3584C	Padgett
	11235584	1,2	2005-02-24	3584C	Padgett
	47096320	1	2013-11-10	90071PC	Kraus
	47096832	2	2013-11-10	90071PC	Kraus
CWISE J044947.80−681745.6	14351616	1,2	2005-07-18	20203C	Meixner
	14364160	1,2	2005-10-25	20203C	Meixner
CWISE J054921.19+264755.0	38861568	1,2	2010-04-22	61070PC	Whitney
	38873600	2	2010-04-23	61070PC	Whitney
CWISE J070314.97−062929.8	38991360	2	2010-05-08	61071PC	Whitney
	38996992	1	2010-05-07	61071PC	Whitney
	39024896	1,2	2010-05-10	61071PC	Whitney
	42089728	1	2011-05-30	61071PC	Whitney
	42133760	1	2011-06-07	61073PC	Whitney
CWISE J072900.97−742943.1	41550592	1,2	2011-04-14	70062PC	Kirkpatrick
CWISE J073748.86−252613.0	39051520	1,2	2010-05-20	61071PC	Whitney
CWISE J075744.48−300504.3	39030528	1,2	2010-05-31	61071PC	Whitney
	39032320	2	2010-05-31	61071PC	Whitney
CWISE J080940.43−372003.7	6580224	1,2	2003-12-07	104C	Soifer
	39328768	1,2	2010-06-13	61072PC	Whitney
	39337984	1	2010-06-13	61072PC	Whitney
CWISE J091942.64−495243.7	23707392[d]	1,2	2008-03-04	40791C	Majewski
CWISE J093035.01−743148.6	44563200	1,2	2012-04-04	80109PC	Kirkpatrick
CWISE J110238.85−775039.7	19986432	1,2	2007-05-16	30574C	Allen
	20006400	1,2	2007-05-16	30574C	Allen
	43320064	1	2011-07-23	80053PC	Paladini
	47091712	1,2	2013-08-24	90071PC	Kraus
CWISE J112106.36−623221.5	23699712[d]	1,2	2008-07-20	40791C	Majewski
	42735360	1,2	2012-03-21	80074PC	Whitney
CWISE J112440.19+663051.1	70016512	1,2	2019-07-13	14299PC	Faherty
CWISE J123455.88−641923.7	42703104	1,2	2012-04-05	80074PC	Whitney
CWISE J133427.46−625736.6	9233664	2	2004-03-10	190C	Churchwell
	9234176	1	2004-03-10	190C	Churchwell
	11761920	2	2004-07-21	189C	Churchwell
	11768832	1	2004-07-21	189C	Churchwell
	45388800	1	2012-04-10	80074PC	Whitney
CWISE J135338.04+441017.6	43424512	2	2011-08-25	80095PC	Werner
	45116416	1,2	2012-04-04	80109PC	Kirkpatrick
VVV J165507.19−421755.5	11955712[c]	1,2	2004-09-06	192C	Churchwell
CWISE J181125.34+665806.4	49728000	1,2	2014-05-09	10147PC	Bock
	49728256	1,2	2014-05-09	10147PC	Bock
	49728512	1,2	2014-05-09	10147PC	Bock
	49739520	2	2014-07-24	10147PC	Bock
	49739776	2	2014-07-24	10147PC	Bock
	49740032	1,2	2014-07-25	10147PC	Bock
	49752576	1,2	2014-09-14	10147PC	Bock
	49752832	1,2	2014-09-14	10147PC	Bock
	49753088	2	2014-09-14	10147PC	Bock

Table A1
(Continued)

Object Name	AOR	Bands[a]	Obs. Date (UT)	Program + Phase[b]	PI Name
(1)	(2)	(3)	(4)	(5)	(6)
	62371328	1	2017-02-19	13153PC	Capak
	62377728	2	2017-02-14	13153PC	Capak
	62846464	1	2017-07-05	13153PC	Capak
	62921984	1,2	2018-01-04	13153PC	Capak
	62937344	2	2017-07-17	13153PC	Capak
	62949120	2	2017-11-20	13153PC	Capak
	65073152	2	2018-01-19	13153PC	Capak
	65094400	1,2	2018-01-12	13153PC	Capak
	65114624	1	2018-06-09	13153PC	Capak
	65124608	1,2	2018-06-04	13153PC	Capak
	65133312	2	2018-06-03	13153PC	Capak
	65190656	1	2018-02-27	13153PC	Capak
	65196288	1,2	2018-02-26	13153PC	Capak
	65692160	1	2019-01-05	13153PC	Capak
	65718016	2	2018-06-22	13153PC	Capak
	65765632	1,2	2018-08-05	13153PC	Capak
	65810176	1,2	2019-01-15	13153PC	Capak
	65817088	1	2018-06-26	13153PC	Capak
	68615680	1,2	2019-02-27	13153PC	Capak
	68631296	2	2019-02-13	13153PC	Capak
	68632576	1	2019-02-09	13153PC	Capak
CWISE J181429.08−202534.4	21272832	1	2007-05-16	30570C	Benjamin
	21339392	2	2007-05-16	30570C	Benjamin
CWISE J185316.77−540658.0	45091584	1,2	2012-05-25	80109PC	Kirkpatrick
CWISE J190405.09−372616.9	27041280	1,2	2008-05-10	30574C	Allen
	47020032	1,2	2012-12-02	90071PC	Kraus
CWISE J191118.88+085456.3	11966976	1,2	2004-10-09	187C	Churchwell
CWISE J191839.52+441835.6	50112512[e]	1,2	2014-01-03	10067PC	Werner
CWISE J192738.93−851335.6	46936064	1,2	2012-12-03	80077PC	Leggett
CWISE J204055.20+465148.0	39489280[c]	1,2	2010-07-15	61072PC	Whitney
CWISE J205338.54−353922.5	45070336	1,2	2012-06-23	80109PC	Kirkpatrick
CWISE J213322.07−174151.5	53349888	1	2016-09-05	11097PC	Rozitis

Notes.
[a] The bands refer to 1 = ch1 = 3.6 μm, and 2 = ch2 = 4.5 μm.
[b] The letter code after the program number refers to C = cryogenic data, or PC = postcryogenic data.
[c] Source identification is uncertain or blended in both bands.
[d] Source is undetected in both bands, as these data are very shallow.
[e] Source is badly blended and not extracted in ch1.

2018), and WISE (Wright et al. 2010). These photometric measurements are listed in Table 2. In other cases, we have obtained our own ground-based follow-up or have searched the Spitzer Heritage Archive[89] for images with which to measure photometry. These results are also presented in Table 2 but discussed further in the subsections below.

A.1.1. Palomar/WIRC

Eighteen objects were observed with the Wide-field Infrared Camera (WIRC; Wilson et al. 2003a) at the Hale 5 m telescope on Palomar Mountain during the nights 2014 July 3, 2014 September 14, 2016 February 26, 2018 September 1, 2019 July 14, 2020 February 5, 2020 June 3, 2020 July 3, 2020 September 3, 2020 October 9, 2021 July 1, and 2021 August 10 UT. Data were acquired in the Maunakea Observatory filter system's J and H bands. Our standard observing technique, calibration strategy, and reduction methodology have been discussed in Section 3.1.5 of Kirkpatrick et al. (2011) with updates as discussed in Section 9.2 of Meisner et al. (2020a).

A.1.2. Keck/MOSFIRE

Thirteen objects were observed with the Multi-Object Spectrometer For Infra-Red Exploration (MOSFIRE; McLean et al. 2012) at the 10 m W. M. Keck I telescope on Maunakea, Hawai'i, on the nights of 2021 August 27 and 2022 January 21 UT. Photometric acquisition and reductions followed the procedures described in Section 3.1.1 of Schneider et al. (2021).

A.1.3. Gemini-South/FLAMINGOS-2

Nine objects were observed with the FLoridA Multi-object Imaging Near-infrared Grism Observational Spectrometer 2 (FLAMINGOS-2; Elston et al. 2003; Jannuzi & Bechtold 2004; Eikenberry et al. 2006) at the 8.1 m Gemini-South Observatory on Cerro Pachón, Chile, on the nights of 2014 December 1, 2015 June 30, 2019 April 14, 2019 April 29, 2021 February 22,

[89] https://sha.ipac.caltech.edu/applications/Spitzer/SHA/

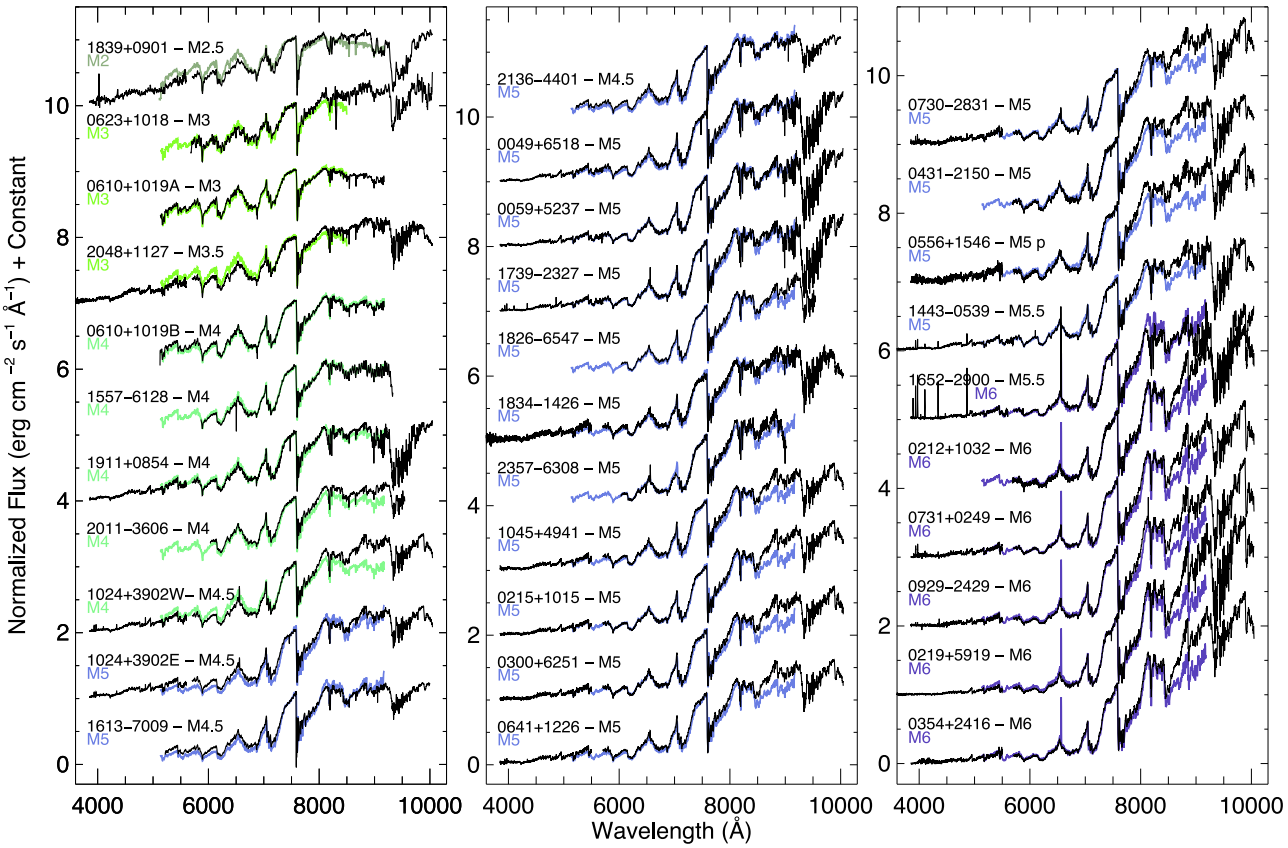

Figure A1. Optical spectroscopic follow-up for objects classified as early-M through mid-M. Each target object (black) is normalized to one at 7500 Å and overplotted (in other colors) with the spectral standard nearest the same spectral type. Integral offsets have been added to separate the spectra vertically. Target objects are labeled with brief R.A./decl. (hhmm ± ddmm) identifiers. The two target objects at upper left—1839+0901 and 0623+1018—have been smoothed to improve the signal-to-noise in each wavelength bin. Most spectra have not been corrected for Earth's atmospheric absorption, so the contaminating *B* and *A* bands of O_2 at ∼6850–6900 and ∼7600–7700 Å and telluric bands of H_2O at ∼7150–7300, 8150–8350, and 9000–9600 Å remain.

2021 July 17, 2021 July 21, and 2021 October 18 UT. Photometric acquisition and reductions followed the procedures described in Section 9.1 of Meisner et al. (2020a).

A.1.4. SOAR/OSIRIS

One object was observed with the Ohio State Infra-Red Imager/Spectrometer (OSIRIS) at the 4.1 m SOuthern Astrophysics Research (SOAR) Telescope on Cerro Pachón, Chile, on the night of 2012 March 12 UT. Photometric acquisition and reduction of this lone *H*-band data point followed the methodology outlined in Section 2.2.5 of Kirkpatrick et al. (2012).

A.1.5. Spitzer/IRAC

The Spitzer Heritage Archive was queried for directed or serendipitous observations of objects in our 20 pc candidate list (Table 2). The locations of 31 of these candidates were found to have Spitzer/IRAC observations in ch1 and/or ch2. The full list is shown in Table A1. Although some of the Spitzer data were too shallow to detect our objects or were obtained at an epoch when our candidate was blended with a background source, most objects had measurable photometry. We used the MOPEX/APEX software (Makovoz & Khan 2005; Makovoz & Marleau 2005) on each Astronomical Observation Request (AOR) to create mosaics, perform source detection, and then measure the photometry using the stack of individual frames. The output of the APEX code is the flux, in μJy, for each detection using both aperture and point response function (PRF)-fit techniques. The Spitzer photometry reported in Table 2 is the PRF-fit photometry after converting to magnitudes using the correction factors listed in Table C.1 of the IRAC Handbook[90] along with the flux zero-points in each band, as given in Table 4.1 of the Handbook. For objects having multiple AORs for a band, the reported photometry in that band is a weighted mean of the individual measurements in each AOR.

A.2. Spectroscopy

To aid in the characterization of objects, spectroscopy was acquired of 20 pc members discovered by Gaia, 20 pc suspects discovered by the Backyard Worlds: Planet 9 citizen science group, or 20 pc members lacking published spectral types. These reduced spectra are illustrated in Figures A1–A5. Ten different instruments were used for this follow-up, as detailed below and summarized in Table A2.

A.2.1. CTIO/RCSpec

Optical follow-up of five objects was obtained on the UT dates of 1995 August 13–14, 1997 July 14, and 1997 July 16 at the Cerro Tololo Interamerican Observatory (CTIO) 4 m telescope and on 1996 May 20 at the CTIO 1.5 m telescope using the R-C Spectrograph with Folded Schmidt Camera

[90] https://irsa.ipac.caltech.edu/data/SPITZER/docs/irac/iracinstrumenthandbook/home/

Table A2
Spectroscopic Follow-up

Object	Coords (hhmm ± ddmm)	Instrument	Obs. Date (UT)	Observer Code	Opt. Spec. Type	Near-infrared Spec. Type[a]
(1)	(2)	(3)	(4)	(5)	(6)	(7)
2MASS J00251602+5422547	0025+5422	Palomar/DBSP	2022 Aug 27	S	M7	⋯
CWISER J003350.99+434010.6	0033+4340	Palomar/DBSP	2022 Jan 2	E,L,S,T	L2	⋯
2MASS J00492565+6518038	0049+6518	Palomar/DBSP	2022 Aug 27	S	M5	⋯
WISE J005936.73+523719.0	0059+5237	Palomar/DBSP	2022 Aug 27	S	M5	⋯
1RXS J010228.1+633256	0102+6332	Palomar/DBSP	2022 Jan 2	E,L,S,T	M6 pec	⋯
CWISE J013343.58+803153.1	0133+8031	APO/TSpec	2019 Oct 8	A,Q	⋯	T4
CWISE J014407.64+380255.6	0144+3802	IRTF/SpeX	2022 Jan 9	C,F	⋯	L5.5 blue
WISEA J015815.65+180713.7	0158+1807	Palomar/DBSP	2022 Feb 3	S	M6.5	⋯
2MASS J02124635+1032546	0212+1032	Palomar/DBSP	2022 Feb 3	S	M6	⋯
LP 941-19	0213−3345	Palomar/DBSP	2021 Dec 6	S	DA4.5	⋯
LP 469-205	0215+1015	Palomar/DBSP	2022 Feb 3	S	M5	⋯
2MASS J02195603+5919273	0219+5919	Palomar/DBSP	2021 Dec 6	S	M6	⋯
2MASS J02224767−2732349	0222−2732	Palomar/DBSP	2021 Dec 6	S	M8	⋯
2MASS J03000272+6251582	0300+6251	Palomar/DBSP	2022 Feb 3	S	M5	⋯
CWISE J034547.29+513716.0	0345+5137	IRTF/SpeX	2021 Nov 25	C,F,R	⋯	L5.5 sl. red
LP 357-56	0354+2416	Palomar/DBSP	2022 Feb 3	S	M6	⋯
2MASS J04134574+3709087	0413+3709	Palomar/TSpec	2018 Oct 17	U,V,W	⋯	L3
Gaia EDR3 180116295441149824	0430+4118	Palomar/DBSP	2021 Dec 6	S	L0	⋯
LP 834-48	0431−2150	Palomar/DBSP	2022 Feb 7	S	M5	⋯
2MASS J04490464+5138412	0449+5138	Palomar/DBSP	2022 Feb 3	S	M6.5	⋯
UCAC4 767-032810	0449+6317	Palomar/DBSP	2022 Jan 2	E,L,S,T	early G	⋯
CWISE J045334.34+203350.2	0453+2033	IRTF/SpeX	2018 Oct 1	K,Y,Z	⋯	early sdL to mid-sdL
2MASS J05053461+4648017	0505+4647	Palomar/DBSP	2021 Dec 6	S	M8	⋯
NLTT 14748	0516+5640	Palomar/DBSP	2022 Feb 3	S	M6.5	⋯
CWISE J053046.20+440849.2	0530+4408	IRTF/SpeX	2020 Nov 25	C,F,R	⋯	T5
LSPM J0540+6417	0540+6417	Palomar/DBSP	2021 Dec 6	S	M8.5	⋯
CWISE J054034.89+414401.7	0540+4144	IRTF/SpeX	2022 Jan 9	C,F	⋯	T3
Gaia DR2 2652013842813204 48	0551+5511	Palomar/DBSP	2022 Feb 3	S	M6.5	⋯
WISEA J055600.48+154559.3	0556+1546	Palomar/DBSP	2022 Feb 3	S	M5 pec[b]	⋯
CWISE J055816.67−450233.4	0558−4502	Magellan/FIRE	2020 Feb 18	D	⋯	T8.5
CWISE J055829.92−233053.4	0558−2330	IRTF/SpeX	2019 Mar 16	F	⋯	L7 blue
CWISE J055942.94−012002.4	0559−0120	IRTF/SpeX	2022 Jan 9	F	⋯	L5.5 red
TYC 3382-603-1	0606+4851	Palomar/DBSP	2022 Jan 2	E,L,S,T	mid-F	⋯
CWISE J060822.15−421244.7	0608−4212	Magellan/FIRE	2016 Jan 23	M	⋯	L5.5 sl. blue
CWISE J060938.91+062513.2	0609+0625	IRTF/SpeX	2020 Oct 30	C,F,R,X	⋯	L7
BD+10 1032A	0610+1019A	Palomar/DBSP	1995 Dec 2	5	M3	⋯
BD+10 1032B	0610+1019B	Palomar/DBSP	1995 Dec 2	5	M4	⋯
CWISE J061741.79+194512.8 A	0617+1945A	Palomar/DBSP	2021 Dec 6	S	L2	⋯
Gaia EDR3 3330473222213987072	0623+1018	Palomar/DBSP	2021 Dec 6	S	M3	⋯
CWISE J063513.64−143029.4	0635−1430	IRTF/SpeX	2022 Jan 9	F	⋯	L9 sl. blue
UPM J0641+1226	0641+1226	Palomar/DBSP	2022 Feb 3	S	M5	⋯
WISEA J064313.95+163143.6	0643+1631	Palomar/DBSP	2021 Dec 6	S	M7	⋯
CWISE J064341.04+195039.3	0643+1950	Magellan/FIRE	2019 Dec 11	G,K	⋯	T2 sl. red
Gaia EDR3 2936126887218756736	0705−1535	Palomar/DBSP	2021 Dec 6	S	bkg	⋯
CWISE J072418.16+430717.3	0724+4307	Keck/NIRES	2019 Feb 14	B,2	⋯	T6
UCAC4 414-032626	0727−0718	Palomar/DBSP	2021 Dec 6	S	A[c]	⋯
UPM J0730−2831	0730−2831	Palomar/DBSP	2022 Feb 3	S	M5	⋯
2MASS J07312949+0249084	0731+0249	Palomar/DBSP	2022 Feb 3	S	M6	⋯
CWISE J073748.86−252613.0	0737−2526	IRTF/SpeX	2019 Jan 23	F,H	⋯	L3 sl. red
CWISE J074346.98+314603.4	0743+3146	Keck/NIRES	2021 Feb 24	B,J,2	⋯	T8
CWISE J075227.38+053802.6	0752+0538	IRTF/SpeX	2022 Jan 9	F	⋯	L9 pec (composite)
CWISE J075628.41−063709.5	0756−0637	CTIO/ARCoIRIS	2018 Apr 3	F	⋯	L6: blue

Table A2
(Continued)

Object	Coords (hhmm ± ddmm)	Instrument	Obs. Date (UT)	Observer Code	Opt. Spec. Type	Near-infrared Spec. Type[a]
(1)	(2)	(3)	(4)	(5)	(6)	(7)
CWISE J075744.48-300504.3	0757−3005	IRTF/SpeX	2022 Feb 12	F,N,O,R	⋯	T4.5
CWISE J075853.12−232645.8	0758−2326	IRTF/SpeX	2022 Feb 21	F,O	⋯	T2.5 pec (composite?)
CWISE J080940.43−372003.7	0809−3720	IRTF/SpeX	2019 Mar 17	F	⋯	L5 sl. blue
CWISER J090720.27−430856.7	0907−4308	CTIO/ARCoIRIS	2018 Apr 2	F	⋯	L5
LP 846-7	0929−2429	Palomar/DBSP	2022 Feb 3	S	M6	⋯
CWISE J093035.01−743148.6	0930−7431	CTIO/ARCoIRIS	2018 Apr 3	F	⋯	T7
LSPM J1024+3902W	1024+3902W	Palomar/DBSP	2022 Feb 3	S	M4.5	⋯
LSPM J1024+3902E	1024+3902E	Palomar/DBSP	2022 Feb 3	S	M4.5	⋯
LP 848-50	1042−2416	Palomar/DBSP	2021 Dec 6	S	M6.5	⋯
NLTT 25223	1045+4941	Palomar/DBSP	2022 Feb 3	S	M5	⋯
CWISE J113646.36+205733.9	1136+2057	IRTF/SpeX	2019 Jan 23	F,H	⋯	M9:
CWISE J120258.26+305233.3	1202+3052	IRTF/SpeX	2022 Mar 7	C,O	⋯	T6
UCAC4 641-049451	1318+3810	Palomar/DBSP	2022 Jan 2	E,L,S,T	early G	⋯
CWISE J132403.81−052631.4	1324−0526	IRTF/SpeX	2022 Jan 19	C,F	⋯	sdT4
CWISE J135338.04+441017.6	1353+4410	IRTF/SpeX	2022 Mar 11	C,N,O	⋯	T7.5
2MASS J14194617+3137094	1419+3137	Palomar/DBSP	2022 Feb 3	S	M6.5	⋯
NLTT 37185	1423+5146	Lick/Kast	2022 Jul 2	B,1,2	M7[d]	⋯
LP 440-17	1423+1426	IRTF/SpeX	2021 Jun 30	3	⋯	M7
CWISE J142830.96−064435.5	1428−0644	IRTF/SpeX	2019 Mar 16	F	⋯	L5 sl. blue
UCAC3 169-135909	1443−0539	Palomar/DBSP	2022 Feb 3	S	M5.5	⋯
(ditto)	(ditto)	Palomar/DBSP	2022 May 24	S	M5.5	⋯
Gaia EDR3 6305165514134625024	1459−1832	Palomar/DBSP	2022 May 24	S	bkg	⋯
Gaia EDR3 6013647666939138688	1529−3552	Palomar/DBSP	2022 May 24	S	bkg	⋯
L 153-43	1557−6128	CTIO 1.5 m/RCSpec	1996 May 20	5	M4	⋯
L 74-208	1613−7009	CTIO 4 m/RCSpec	1997 Jul 16	5	M4.5	⋯
SCR J1630−3633	1630−3633	Palomar/TSpec	2018 Apr 28	U,V	⋯	M5.5
2MASS J16523515−2900186	1652−2900	Palomar/DBSP	2022 Aug 27	S	M5.5	⋯
SCR J1656−2046	1656−2046	Palomar/DBSP	2022 Aug 27	S	M6	⋯
DENIS J171204.4−032328	1712−0323	Palomar/TSpec	2018 Apr 28	U,V	⋯	M7.5
CWISER J171509.58−151534.6	1715−1515	IRTF/SpeX	2019 Mar 16	F	⋯	M8 pec
Gaia DR2 4053559111471124608	1736−3425	Palomar/DBSP	2022 Aug 27	S	M6.5	⋯
2MASS J17392440−2327071	1739−2327	Palomar/DBSP	2022 Aug 27	S	M5	⋯
NLTT 45285	1741+0940	Lick/Kast	2020 Mar 6	B,J,2	M7.5	⋯
SCR J1746−3214	1746−3214	Palomar/TSpec	2018 Apr 29	U,V	⋯	M5.5
CWISE J181429.08−202534.4	1814−2025	IRTF/SpeX	2021 May 31	3	⋯	M8
WISEA J182423.61−053653.6	1824−0536	Palomar/TSpec	2018 Apr 28	U,V	⋯	M6.5
WT 562	1826−6547	CTIO 4 m/RCSpec	1995 Aug 14	5	M5	⋯
Gaia DR2 4159791176135290752	1831−0732	Palomar/DBSP	2022 May 30	P	M9.5	⋯
UCAC4 378-124295	1834−1426	Palomar/DBSP	2022 May 30	P	M5	⋯

Table A2
(Continued)

Object	Coords (hhmm ± ddmm)	Instrument	Obs. Date (UT)	Observer Code	Opt. Spec. Type	Near-infrared Spec. Type[a]
(1)	(2)	(3)	(4)	(5)	(6)	(7)
Gaia EDR3 4479498508613790464	1839+0901	Palomar/DBSP	2022 Aug 27	S	M2.5	⋯
CWISE J185608.94−082257.6	1856−0822	Lick/Kast	2019 Sep 20	J,1	L0	⋯
WISEP J190648.47+401106.8	1906+4011	Palomar/DBSP	2022 Aug 27	S	L1	⋯
NLTT 47423	1907+0443	Palomar/DBSP	2022 May 30	P	M6	⋯
CWISE J191118.88+085456.3	1911+0854	Palomar/DBSP	2022 Aug 27	S	M4	⋯
2MASS J19212977−2915507	1921−2915	Lick/Kast	2020 Aug 16	B	M7	⋯
CWISE J192351.88+234611.8	1923+2346	IRTF/SpeX	2021 Sep 11	C,F,R	⋯	M9
CWISE J194929.61+171301.3	1949+1713	APO/TSpec	2018 Sep 23	A	⋯	L2.5
Gaia DR2 2034222547248988032	1955+3215	Palomar/TSpec	2019 Sep 18	U,V	⋯	L1 pec
UCAC4 563-099325	1955+2224	Palomar/DBSP	2022 May 30	P	mid-F?	⋯
HD 191408 B	2011−3606	CTIO 4 m/RCSpec	1995 Aug 13	5	M4	⋯
EC 20173−3036	2020−3027	Palomar/DBSP	2022 Jun 7	S	DC	⋯
LSPM J2044+1517	2044+1517	Palomar/DBSP	2022 Aug 27	S	M7.5	⋯
G 25-4	2048+1127	Palomar/DBSP	2022 May 30	P	M3.5	⋯
2MASS J20492745+3336512	2049+3336	Palomar/DBSP	2022 May 30	P	M7	⋯
MFL2000 J210104.18+030705.1	2101+0307	Palomar/DBSP	2022 Aug 27	S	M6.5	⋯
2MASS J21272531+5553150	2127+5553	Lick/Kast	2020 Aug 15	B,J,1	M7.5	⋯
UCAC4 230-189452	2136−4401	CTIO 4 m/RCSpec	1997 Jul 14	5	M4.5	⋯
2MASS J21381698+5257188	2138+5257	Lick/Kast	2020 Dec 14	B,I,J,1,2	M6	⋯
CWISE J221113.55+054006.6	2211+0540	IRTF/SpeX	2021 Oct 23	C,F	⋯	T6
CWISE J221859.41+114642.7	2218+1146	Keck/NIRES	2020 Jul 7	B,I,J	⋯	T7 pec
Gaia DR2 2206265777300448768	2225+6421	Palomar/TSpec	2019 Sep 18	U,V	⋯	L1 pec
CWISE J231403.13+693935.2	2314+6939	IRTF/SpeX	2018 Jun 16	F	⋯	L7 blue
CWISE J233135.66+644356.5	2331+6443	IRTF/SpeX	2018 Nov 25	F	⋯	M8:
CWISE J233819.49−385421.2	2338−3854	IRTF/SpeX	2021 Sep 11	C,F,R	⋯	T0
WISEA J235713.21−630827.6	2357−6308	SALT/RSS	2021 Dec 26	F	M5	⋯

Notes. Observer code: A = Katelyn Allers, B = Adam Burgasser, C = Emily Calamari, D = Adam Schneider, E = Peter Eisenhardt, F = Jacqueline Faherty, G = Daniella Bardalez Gagliuffi, H = Eileen Gonzales, I = Christopher Theissen, J = Roman Gerasimov, K = Rocio Kiman, L = Guodong Li, M = Jonathan Gagné, N = Dan Caselden, O = Les Hamlet, P = Thomas Connor, Q = Blake Pantoja, R = Austin Rothermich, S = Daniel Stern, T = Chao-Wei Tsai, U = Eric Mamajek, V = Federico Marocco, W = Jon Rees X = Jose I. Adorno, Y = Johanna Vos, Z = Mark Popinchalk, 1 = Christian Aganze, 2 = Chih-Chun Hsu, 3 = Richard Smart, 4 = Ryan Low, 5 = Davy Kirkpatrick.

[a] Near-infrared spectral types of "sl. blue," "blue," "sl. red," and "red" refer to objects that are slightly ("sl.") or considerably bluer or redder in the *H* and *K* bands than the established spectral standard at that subtype, after the standard spectrum and target spectrum are overplotted at *J* band. Those listed as "pec" (peculiar) have spectral morphologies that fail to match the established standards and cannot be characterized as easily. See Section 5.2 of Kirkpatrick et al. (2010) for more discussion.

[b] 0556+1546: spectrum shows slightly stronger CaH bands relative to the M5 standard, although not enough to warrant a d/sdM5 designation.

[c] 0727−0718: See Section 4.7 of Tremblay et al. (2020) for an assessment of the spectral type. The Gaia DR2 parallax, which has a large uncertainty relative to other objects of similar magnitude, must be erroneous. No parallax is given in Gaia DR3. This star must actually fall well outside 20 pc.

[d] 1423+5146: spectrum shows slightly stronger CaH bands relative to the M7 standard, although not enough to warrant a d/sdM7 designation.

(This table is available in machine-readable form.)

(RCSpec). For 1995 and 1996 observations, a 300 line mm^{-1} grating with a GG 495 order-blocking filter was used with the 1024×1024 CCD to cover a wavelength range from 6050 to 9550 Å. For 1997 observations, a 316 line mm^{-1} grating with an OG 515 order-blocking filter was used with the Loral 3K CCD to cover a useable wavelength range from 5200 to 10000 Å. In addition to the targets, standard calibrations—biases, dome flats, arcs, and flux calibration standards—were also obtained. Reductions were accomplished using the Image Reduction and Analysis Facility (IRAF; Tody 1986, 1993), as described in Kirkpatrick et al. (1997).

A.2.2. Lick/Kast

The Kast Double Spectrograph at the Lick 3 m Shane Telescope was used for optical follow-up of six objects on UT dates 2019 September 20, 2020 March 6, 2020 August 15–16, 2020 December 14, and 2022 July 2. The only data used were from the red arm, which employed a 600 line mm^{-1} grating blazed at 7500 Å to cover the wavelength range from ∼6000 to ∼9000 Å. In addition to standard wavelength and flux calibrations, G2V and A0V stars were obtained near in time and on sky to the targets to correct for telluric absorption. The data were reduced using the kastredux[91] package (A. J. Burgasser et al. 2024, in preparation), as further described in Schneider et al. (2021).

A.2.3. Palomar/DBSP

The Double Spectrograph (DBSP; Oke & Gunn 1982) at the Hale 5 m telescope on Palomar Mountain was used for 60 additional follow-up spectra. The UT nights of observation were 1995 December 2, 2021 December 6, 2022 January 2, 2022 February 3, 2022 February 7, 2022 May 24, 2022 May 30, 2022 June 7, and 2022 August 27. For 1995 run, the D68 dichroic was used to split the light at ∼6800 Å between the two arms. Gratings with 300 line mm^{-1} blazed at 3990 Å and with 316 line mm^{-1} blazed at 7150 Å were used in the blue and red arms, respectively, producing continuous wavelength coverage from ∼5100 to 9200 Å. For 2021 and 2022 runs, the D55 dichroic was used instead to split the light near 5500 Å. A 600 line mm^{-1} grating blazed at 3780 Å was used in the blue arm and a 316 line mm^{-1} blazed at 7150 Å was used in the red arm, producing coverage from ∼3300 to 5500 Å on the blue side and from ∼5700 to 10000 Å on the red side. (For the 2022 June run, fringing in the blue arm caused data shortward of 4500 Å to be unusable.) Standard calibrations and IRAF data reductions were employed, as further described in Kirkpatrick et al. (1991).

A.2.4. SALT/RSS

An additional optical spectrum was acquired with the Robert Stobie Spectrograph (RSS; Burgh et al. 2003; Kobulnicky et al. 2003) on the 11.1×9.8 m Southern African Large Telescope (SALT; Buckley et al. 2006) on 2021 December 26 UT. The spectrograph was used in long slit mode using the PG0900 grating at an angle of 20°, which produces coverage over the ranges 6033–7028, 7079–8045, and 8091–9023 Å across the 3×1 minimosaic. Our reductions began with the observatory-provided preprocessed data, for which gain correction, correction for crosstalk, and overscan subtraction had been applied. We then wavelength calibrated using neon arc lines obtained immediately after the target's spectroscopic data and flux calibrated using the Hamuy et al. (1994) standard EG21 acquired with the same spectroscopic setup on 2023 January 24 UT.

A.2.5. APO/TSpec

TripleSpec (Wilson et al. 2004) on the ARC 3.5 m telescope at Apache Point Observatory (APO) was used for near-infrared follow-up of two objects on the nights of 2018 September 23 and 2019 October 8 UT. The spectrograph provides spectral coverage from 0.95 to 2.46 μm across five spectral orders. Data were taken with the conventional near-infrared technique of nodded pairs to perform background/bias subtraction, and standard calibrations were also acquired, including quartz lamps for flat-fielding and A0 stars for telluric correction and flux calibration. Wavelength calibration was accomplished using night sky lines. Data reduction used Tspectool,[92] a modified version of Spextool (Cushing et al. 2004) rewritten specifically for APO/TripleSpec.

A.2.6. CTIO/ARCoIRIS

Three objects were observed on the nights of 2018 April 2–3 UT using the Astronomy Research with the Cornell Infra Red Imaging Spectrograph (ARCoIRIS) at the 4 m Victor Blanco telescope at CTIO. Spectra are acquired across six cross-dispersed orders covering 0.8 to 2.4 μm at a resolving power of ∼3500. Science exposures were taken with AB nod positions along the slit, which has a fixed width of 1.″1. Standard calibrations were acquired as discussed in Greco et al. (2019), and data were reduced using a modified version of the Spextool package (Cushing et al. 2004), which utilizes A0 stars for telluric correction and flux calibration following the methodology of Vacca et al. (2003).

A.2.7. IRTF/SpeX

The SpeX instrument on the NASA Infrared Telescope Facility (IRTF) was used for near-infrared spectroscopy of 27 objects over the nights of 2018 June 16, 2018 November 25, 2019 January 23, 2019 March 16–17, 2020 October 30, 2020 November 25, 2021 May 31, 2021 June 30, 2021 September 11, 2021 October 23, 2022 January 9, 2022 January 19, 2022 February 12, 2022 February 21, 2022 March 7, and 2022 March 11 UT. Two different setups were employed. The first, used mainly for brighter targets, was a cross-dispersed mode that provides spectra over the range 0.9–2.4 μm at a resolving power of $R \equiv \lambda/\Delta\lambda \approx 1200$. The second, used primarily for fainter targets, was the prism mode that provides spectra over the range 0.8–2.5 μm at a resolving power of $R \equiv \lambda/\Delta\lambda \approx 100$–150. As discussed in the subsections above, standard near-infrared calibrations were obtained, and data were reduced using Spextool (Vacca et al. 2003; Cushing et al. 2004).

A.2.8. Keck/NIRES

Three objects were observed over the nights of 2019 February 14, 2020 July 7, and 2021 February 24 UT using the Near-Infrared Echellette Spectrometer (NIRES; e.g.,

[91] https://github.com/aburgasser/kastredux

[92] http://www.apo.nmsu.edu/arc35m/Instruments/TRIPLESPEC/#7

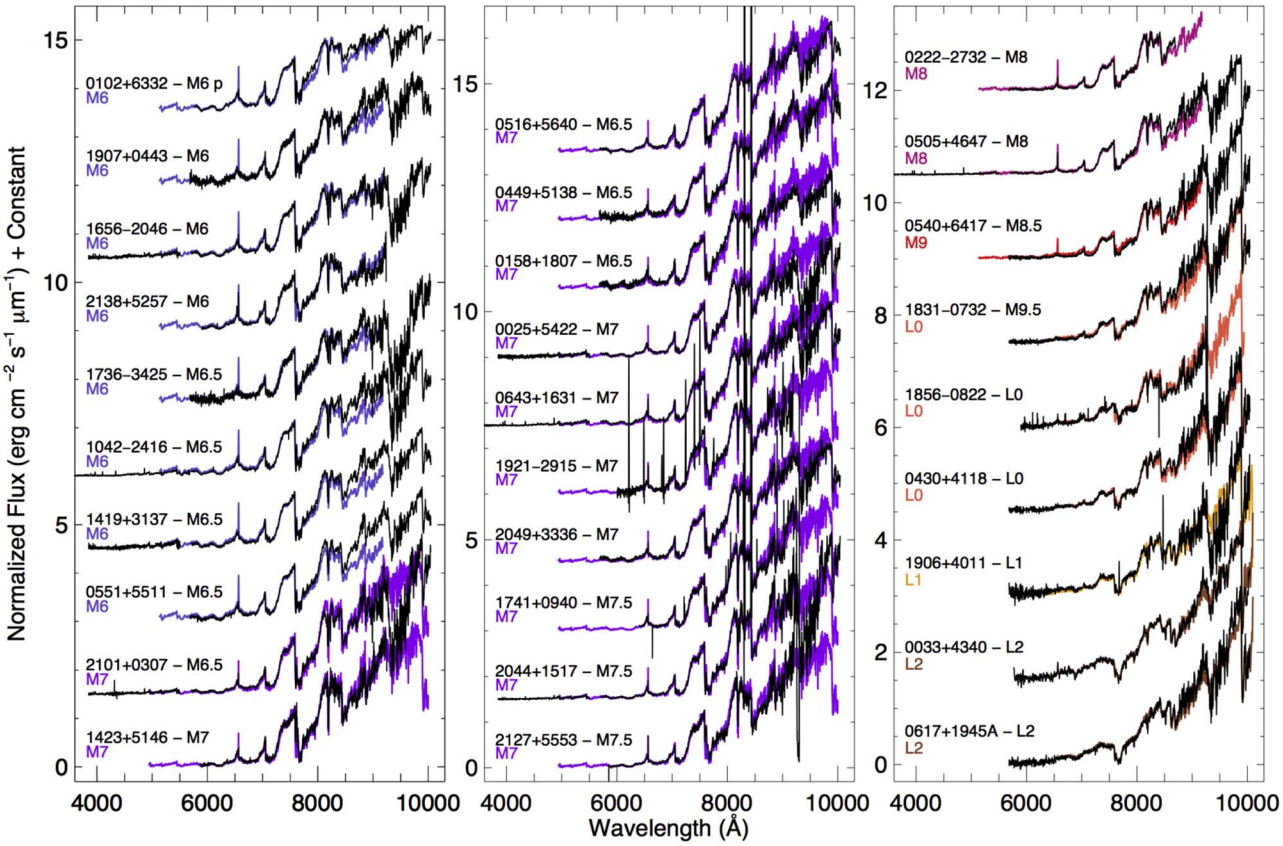

Figure A2. Optical spectroscopic follow-up for objects classified as mid-M through early-L. Each target object (black) in the two left panels is normalized to one at 7500 Å and overplotted (in other colors) with the spectral standard nearest the same spectral type. In the far right panel, this normalization is done instead at 8250 Å. Offsets in steps of 1.5 have been added to separate the spectra vertically. A few target objects—1921−2915 (M7), 1906+4011 (L1), 0033+4340 (L2), and 0617 +1945A (L2)—have been smoothed to improve the signal-to-noise in each wavelength bin. The spectrum of 1921−2915 (M7) also suffers from residual cosmic ray hits. See the caption to Figure A1 for more details.

Wilson et al. 2004) at the 10 m W. M. Keck II telescope. These data provided spectral coverage from 0.94 to 2.45 μm. Setup and calibrations were identical to those described in Meisner et al. (2020b), and reductions used a modified version of `Spextool` (Vacca et al. 2003; Cushing et al. 2004).

A.2.9. Magellan/FIRE

The Folded-port Infrared Echellette spectrograph (FIRE; Simcoe et al. 2013) at the 6.5 m Walter Baade (Magellan I) telescope at Las Campanas Observatory was used to observe three objects over the nights of 2016 January 23, 2019 December 11, and 2020 February 18 UT. Observations were done in prism mode, which covers the range from 0.80 to 2.45 μm. Standard calibrations were acquired, and data were reduced using the `FIREHOSE` pipeline, which is based on the `MASE` (Bochanski et al. 2009) and `Spextool` (Vacca et al. 2003; Cushing et al. 2004) packages.

A.2.10. Palomar/TSpec

Finally, seven near-infrared spectra were acquired with the Triple Spectrograph (TSpec; Herter et al. 2008) at Palomar Mountain's 5 m Hale telescope on the nights of 2018 April 28–29, 2018 October 17, and 2019 September 18 UT. Setup and calibrations were identical to those described in Kirkpatrick et al. (2011). As with many of the other near-infrared spectroscopic data sets discussed above, TSpec data were also reduced with a modified version of `Spextool` (Vacca et al. 2003; Cushing et al. 2004).

A.2.11. Analysis

Spectral classification was accomplished by comparing spectra of the target objects to established on-sky anchors for each integral spectral type. For optical spectra, these anchor points were taken from Kirkpatrick et al. (1991) for objects of type mid-K through late-M and from Kirkpatrick et al. (1999) for L dwarfs (Figures A1–A2). Optical classifications of objects earlier than type K (Figure A3) used spectral anchors taken from Gray & Corbally (2009). Near-infrared classification (Figures A4–A5) for M dwarfs, L dwarfs, and early-T dwarfs used the anchors described in Kirkpatrick et al. (2010), with the rest of the T dwarf anchors coming from Burgasser et al. (2006). For more on the methodology employed for both optical and near-infrared classifications, see Kirkpatrick et al. (2010).

These classification anchors are generally old disk objects with metallicities similar to the Sun. In a few cases, described below, the target object failed to match an anchor spectrum because of anomalous features attributable to extreme youth, lower metallicity, or other reasons including unresolved binarity. These special cases are addressed further below:

CWISE J045334.34+203350.2. At *J* band, this object best matches the L5 standard, but there are clear discrepancies with the L5 standard across all wavelengths (Figure A4). The continuum of

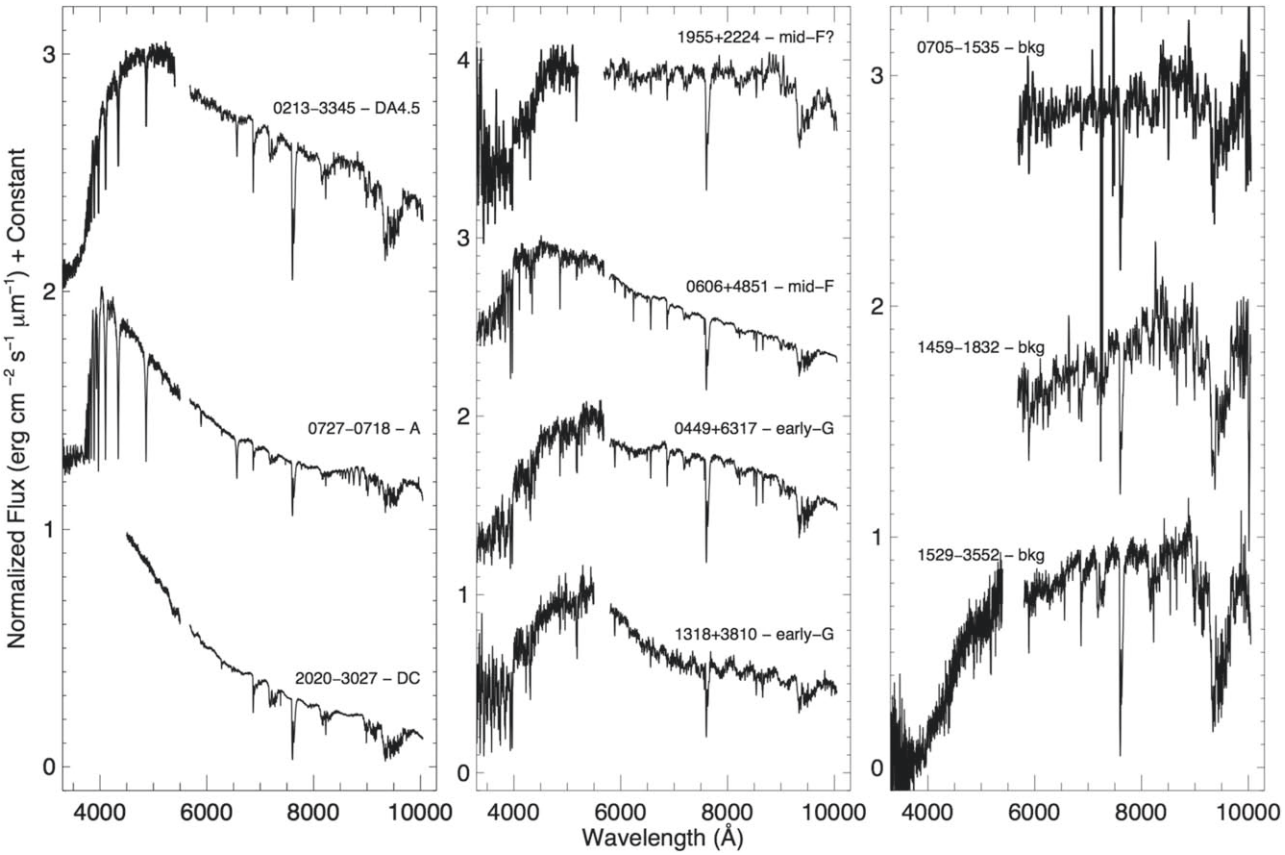

Figure A3. Optical spectroscopic follow-up of objects not classified as M dwarfs or L dwarfs. Each target object is normalized to one at its peak flux. Objects in the far left panel are hot stars, and objects in the two right panels are colder stars or other background objects. Integral offsets have been added to separate the spectra vertically. A few spectra—0213−3345 (wd), 1955+2224 (mid-F?), 1318+3810 (early G), and all of those in the rightmost panel—have been smoothed to improve the signal-to-noise in each wavelength bin. See the caption to Figure A1 for more details.

0453+2033 is much flatter between 1.1 and 1.3 μm, the FeH band at 0.99 μm is much stronger, and the *H*- and *K*-band portions emit less flux relative to *J* band than does the standard. We find that the *J*-band spectrum of 0453+2033 is a better match to 2MASS J17561080+2815238, which is typed in both the optical and the near-infrared as an sdL1 (Kirkpatrick et al. 2010; Zhang et al. 2018), in both the continuum shape and the strength of the FeH band. However, 0453+2033 has more flux at *H* and *K* relative to *J* than does 2MASS J1756+2815, possibly indicating that the former is a slightly later subdwarf. Given that the set of anchors for the L subdwarf spectral sequence is still incomplete (Zhang et al. 2018), we tentatively classify this object as an early sdL to mid-sdL.

CWISE J055942.94−012002.4. Of the spectra in Figures A4–A5 that have a *red* or *slightly red* classification, only 0559−0120 has the triangular-shaped *H*-band peak indicative of low gravity. Such low-gravity objects are necessarily young, as they have not yet contracted to their final radii. Using just the sky position and proper-motion values (Table 2), as its parallax and radial velocity have not yet been measured, BANYAN Σ (Bayesian Analysis for Nearby Young Associations; Gagné et al. 2018) gives the object an 80% chance of belonging to a known, young moving group—either the AB Doradus group or, less likely, the β Pictoris group. If it is an AB Dor member, BANYAN Σ predicts 46 ± 3 pc with a radial velocity of 22 ± 2 km s^{-1}; if it is a β Pic member, the predictions are $d = 21 \pm 3$ pc, and radial velocity $= 19 \pm 2$ km s^{-1}. Using solely an M_{Ks} versus spectral type relation (Dupuy & Liu 2012), as advocated for young L dwarfs in Schneider et al. (2023), we estimate a distance of ∼28.8 pc for this L5.5 dwarf, based on a value of $K_s = 14.34 \pm 0.09$ mag from the 2MASS All-Sky Point Source Catalog.

CWISE J075227.38+053802.6. We classify this object as L9 pec (Figure A5). The peculiarities stem from the two unusual absorption troughs at 1.63 and 1.67 μm within the *H*-band plateau and the unusual inflection near 2.21 μm at *K* band. Such features are indicative of methane absorption, which should not be present shortward of 2.5 μm in an L9 dwarf. As previous papers such as Burgasser (2007), Burgasser et al. (2010a), and Bardalez Gagliuffi et al. (2014) have noted, such spectra may indicate the presence of an unresolved binary comprised of two morphologically distinct spectra—a non-methane M or L dwarf and a methane-rich T dwarf. If 0752+0538 represents such an unresolved binary, modeling (see Section 4.5 of Kirkpatrick et al. 2016) suggests it is likely a late-L plus early-T composite system.

CWISE J075853.12−232645.8. We classify this object as T2.5 pec (Figure A5). Although its *J*-band peak matches both the T2 and T3 standards equally well, the *H*-band flux is suppressed, and the *K*-band flux is elevated relative to the standards. We find that a synthetic spectrum made up of components of types L8–L9 and T5–T6 fits the overall spectral shape slightly better than the single standards, suggesting perhaps that this object is an unresolved binary.

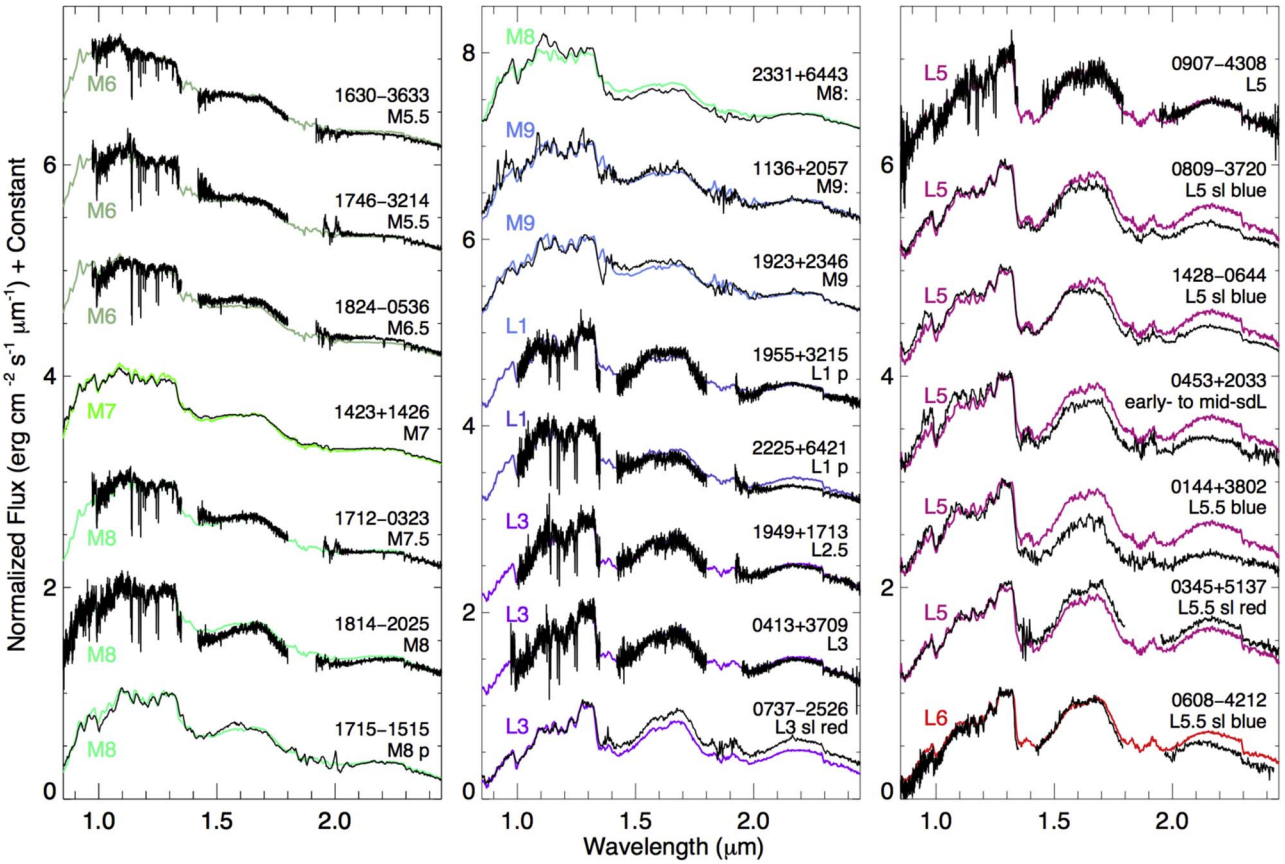

Figure A4. Near-infrared spectroscopic follow-up of objects classified as mid-M through mid-L. Each target object (black) is normalized to one at 1.28 μm and overplotted (in other colors) with the spectral standard nearest the same spectral type. Integral offsets have been added to separate the spectra vertically. Target objects are labeled with brief R.A./decl. (hhmm ± ddmm) identifiers. One spectrum—0907−4308 (L5)—has been smoothed to improve the signal-to-noise in each wavelength bin. Data deep within the telluric water bands near ∼1.4 and ∼1.75 μm are not displayed for some targets because of the poor signal-to-noise in those regions.

CWISE J132403.81−052631.4. The width of the *J*-band peak in this object best matches that of the T4 standard (Figure A5), but the fits at both shorter and longer wavelengths are much poorer. Specifically, the *H*- and *K*-band portions of 1324−0526 emit less flux relative to *J* band than does the standard, and the *K*-band portion is notably flattened, an effect often ascribed to increased collision-induced absorption by H_2. Moreover, the *Y*-band portion emits more flux relative to *J* band than does the standard. The elevated *Y*-band flux and suppressed *K*-band flux are seen in a comparison of the sdT5.5 dwarf HIP 73786B (Figure 1 of Zhang et al. 2019) to standards of type T5 and T6, although the discrepancies are stronger in 1324−0526, and the latter also shows suppressed *H*-band flux. In the case of HIP 73786, the system has a measured subsolar metallicity of [Fe/H] = −0.3 ± 0.1 (Murray et al. 2011) from the K5 V primary, suggesting that the metallicity of 1324−0526 is somewhat lower still. We classify 1324−0526 as sdT4.

CWISE J221859.41+114642.7. The width of this object's *J*-band peak is most similar to the T7 standard, but its *H*- and *K*-band flux peaks are suppressed, with the latter being noticeably flattened. As with 1324−0526 above, such features are typical of subdwarfs, although the suppression of the *Y*-band peak in 2218+1146 runs contrary to the trend seen in T subdwarfs of slightly earlier type. In the sdT8 WISE J200520.38+542433.9, a wide companion in the low-metallicity ([Fe/H] = −0.64 ± 0.17) Wolf 1130 system (Mace et al. 2013b), the *Y*-band peak is shifted notably to the blue—from 1.09 to 1.03 μm—relative to the standards, an effect also seen in the isolated sdT6.5 dwarf ULAS J131610.28+075553.0 (Burningham et al. 2014). Our spectrum is too noisy in this region to determine whether the same effect is present in 2218+1146, so we classify this object as T7 pec pending further confirmation of its subdwarf status.

A.3. Astrometry

Additional parallaxes have been measured as part of an ongoing ground-based program and through serendipitous imaging data found in the Spitzer Heritage Archive. These results are discussed further below.

A.3.1. NPARSEC Results

Nearby objects continue to be targeted as part of the New Technology Telescope (NTT) PARallaxes of Southern Extremely Cool objects (NPARSEC) project, a long-term program (186.C-0756 with R. Smart, PI; 105.C-0781, 108.21XQ.0001, and 108.21XQ.002 with E. Costa, PI) using the infrared spectrograph and imaging camera Son OF ISAAC (SOFI; Moorwood et al. 1998) on the NTT. The observational methodology and reduction procedures are identical to those discussed in Smart et al. (2013). For eleven objects listed in Table A3, the new NPARSEC preliminary values have smaller uncertainties than previously published parallaxes. The table

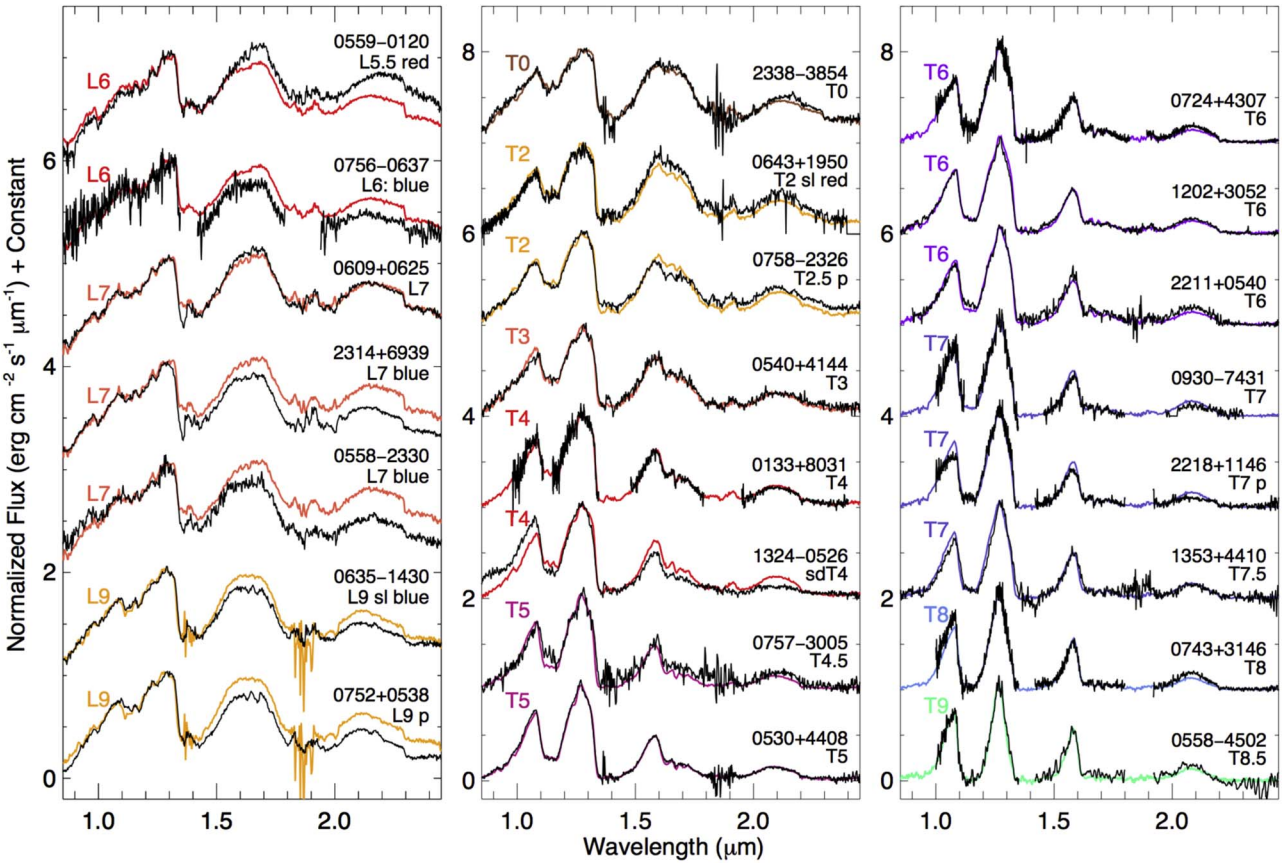

Figure A5. Near-infrared spectroscopic follow-up of objects classified as mid-L through late-T. One spectrum—0133+8031 (T4)—has been smoothed to improve the signal-to-noise in each wavelength bin. Data deep within the telluric water bands near ∼1.15, ∼1.4, and ∼1.75 μm are not displayed for some targets because of the poor signal-to-noise in those regions. See the caption to Figure A4 for other details.

gives the object names, J2000 coordinates, mean epoch of observation, the absolute parallax, the correction applied to the relative parallax to convert to absolute, the proper-motion values in R.A. and decl., the total time baseline of the NTT observations, the number of reference stars used, and the total number of separate observational epochs.

Nine of the targets have absolute parallaxes greater than 50 mas, but for SDSS J163022.92+081822.0 and 2MASS J23312378−4718274, these better determined parallaxes have values below 50 mas, so we now exclude these three from the 20 pc census. We note, however, that these results are still considered preliminary and will be finalized once the NPARSEC program draws to a close.

A.3.2. Spitzer Results

CWISE J181125.34+665806.4 (hereafter 1811+6658; see Figure A6) is located only 1°.2 from the north ecliptic pole (NEP), and the area around the NEP was routinely observed by the Spitzer Space Telescope. As shown in Table A1, the location of 1811+6658 was observed repeatedly in postcryogenic programs 10147 (PI: Bock) and 13153 (PI: Capak) in an attempt to explore the genesis of fluctuations in the extragalactic background light and to provide IRAC/ch1 and IRAC/ch2 data on touchstone fields that will be used by Euclid, Roman, and JWST to study galaxy growth during the epoch of reionization. The data in program 10147 cover the timeframe from 2014 May to 2014 September, and those in program 13153 cover 2017 February to 2019 February.

To extract astrometry from these data sets, we searched for blocks of ch2 coverage that had sufficient depth and redundancy to provide a similar per-epoch astrometric accuracy to that obtained in our own Spitzer parallax programs (Kirkpatrick et al. 2019a, 2021a). (This cold brown dwarf is much brighter at ch2, 15.95 mag, than at ch1, 18.23 mag, so only the longer-wavelength band would provide sufficient S/N for our astrometric needs.) Program 10147 used 30 s exposures per frame, and the position of 1811+6658 was observed at four or fewer epochs. The data from program 13153, on the other hand, used 100 s exposures per frame and had more coverage at each sky position.

We pared this data set down to include only those frames for which the location of 1811+6658 was far enough from the frame edge to provide a reasonable number of Gaia DR3 reference stars surrounding the target's location. Specifically, we retained only those ch2 frames that imaged all six of our preselected Gaia DR3 astrometric reference objects encircling a 60″ zone centered on the location of 1811+6658. For program 10147, this left only two or three frames per epoch; this lack of redundancy combined with the short exposure time means that these data are unsuitable for astrometric analysis. For program 13153, however, we are left with four to six redundant, longer exposure frames per epoch (defined here to be per AOR), which is suitable for our reduction techniques. Of those program 13153 AORs listed in Table A1, only the ch2 data in 62377728, 65133312, 68615680, and 68631296 lacked

Table A3
Preliminary Parallax and Motion Fits for Objects on the NPARSEC Parallax Programs

Object Name	R.A. J2000 (deg)	Decl. J2000 (deg)	Epoch	ϖ_{abs} (mas)	Abs. Corr. (mas)	$\mu_{R.A.}$ (mas yr^{-1})	$\mu_{Decl.}$ (mas yr^{-1})	Baseline (yr)	No. of Reference Stars	No. of Obs.
(1)	(2)	(3)	(4)	(5)	(6)	(7)	(8)	(9)	(10)	(11)
2MASS J04070885+1514565	61.787883	15.248440	2019.80	57.01 ± 2.24	0.73	211.81 ± 0.34	−120.64 ± 0.33	11.1	62	20
2MASS J05103524−4208146	77.647251	−42.135453	2011.12	51.39 ± 2.64	0.66	86.89 ± 0.55	588.34 ± 0.39	11.1	87	24
WISEPA J054231.26−162829.1	85.629759	−16.473971	2019.79	63.26 ± 1.65	0.68	−216.97 ± 0.29	297.02 ± 0.35	12.1	93	29
WISEPA J062720.07−111428.8	96.840776	−11.246393	2015.92	77.02 ± 2.86	0.35	−11.68 ± 0.53	−339.32 ± 0.68	12.1	342	27
2MASS J07290002−3954043	112.247022	−39.893729	2013.23	110.80 ± 1.50	0.36	−564.46 ± 0.33	1694.63 ± 0.31	12.1	394	29
2MASS J09393548−2448279	144.900600	−24.812421	2016.22	189.80 ± 2.68	0.64	569.65 ± 0.60	−1040.60 ± 0.63	12.1	124	27
SDSS J163022.92+081822.0	247.595321	8.305773	2013.33	41.76 ± 2.79	0.46	−60.81 ± 0.84	−104.31 ± 0.98	7.0	107	19
2MASS J18283572−4849046	277.139127	−48.803065	2013.33	86.91 ± 2.34	0.39	230.08 ± 0.72	88.50 ± 0.58	10.9	503	22
2MASS J22282889−4310262	337.120937	−43.175128	2011.86	95.60 ± 2.23	0.62	97.98 ± 0.42	−306.91 ± 0.46	11.0	31	19
2MASS J23312378−4718274	352.849548	−47.307891	2012.58	49.00 ± 4.23	0.44	73.01 ± 0.70	−64.37 ± 0.69	11.0	18	19
2MASSI J2356547−155310	359.226264	−15.888962	2013.55	64.78 ± 2.26	1.12	−432.19 ± 0.39	−605.38 ± 0.63	11.1	13	19

(This table is available in machine-readable form.)

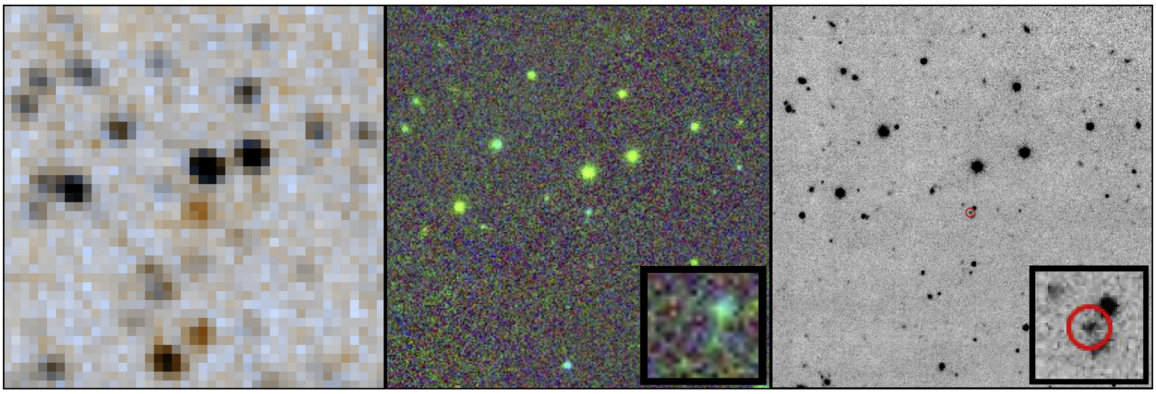

Figure A6. Cutout images, 120″ on a side with north up and east to left, of 1811+6658. Left: WISE data at epoch 2021.6. The separate W1 and W2 bands have been mapped into a color scheme in which objects appearing at roughly equal brightness in each will appear black, and those appearing primarily in W2 will appear orange (Caselden et al. 2018). The brown dwarf 1811+6658 is the orange object at the center of the field. Center: PanSTARRS data. Bands $y/i/g$ have been mapped into red/green/blue. Note the two blue background sources lying near the center of the field, which is shown in the zoomed inset. Right: Keck/MOSFIRE data at epoch 2021.7. The detection of 1811+6658 is marked with a red circle (matched to the size of the aperture used in our photometric reductions) and is sandwiched between the two blue background sources seen in the PanSTARRS view. The inset shows a zoom of the field center.

Table A4
Astrometry on the Gaia DR3 Reference Frame for 1811+6658

R.A. (deg) (1)	Decl. (deg) (2)	$\sigma_{\rm R.A.}$ (arcsec) (3)	$\sigma_{\rm Decl.}$ (arcsec) (4)	Band (5)	MJD (day) (6)	X (km) (7)	Y (km) (8)	Z (km) (9)
272.8555557	66.9680473	0.01926	0.01576	ch2	57951.3599612	−146,795,664.394331	−29,137,217.001001	−15,336,117.968022
272.8554312	66.9680074	0.02229	0.02085	ch2	58077.0419038	105,457,481.330533	−102,108,810.219802	−44,432,690.607376
272.8554058	66.9679956	0.02281	0.01313	ch2	58122.9951224	153,046,661.423622	−8,618,952.216674	−1,585,273.269887
272.8554273	66.9679729	0.02411	0.01427	ch2	58130.1216015	152,890,751.809545	7,809,001.342473	5,815,875.561150
272.8554284	66.9679740	0.01951	0.01134	ch2	58137.7633120	150,349,854.612387	25,297,184.572655	13,659,004.961915
272.8554287	66.9679583	0.01908	0.02450	ch2	58175.0395945	105,086,559.337856	99,767,940.252168	46,540,371.773800

(This table is available in its entirety in machine-readable form.)

Table A5
Parallax and Motion Fit for 1811+6658

Parameter (1)	Value (2)
R.A. at t_0	272.855621° ± 33.5 mas
Decl. at t_0	66.968261° ± 28.7 mas
t_0 (MJD)	57293.81
$\varpi_{\rm abs}$	69.7 ± 6.8 mas
$\mu_{\rm R.A.}$	−91.7 ± 13.9 mas yr^{-1}
$\mu_{\rm decl.}$	−439.8 ± 11.6 mas yr^{-1}
χ^2	65.903
ν	129
χ^2_ν	0.511
$\#_{\rm Spitzer}$	10
$\#_{\rm WISE}$	57
$\#_{\rm Gaia}$	6

Note. The R.A. and decl. values are listed on the ICRS coordinate system. The last three rows represent the number of Spitzer ch2 epochs ($\#_{\rm Spitzer}$) and the number of unWISE W2 epochs ($\#_{\rm WISE}$) used in the fits, along with the number of five-parameter Gaia DR3 stars used for the astrometric reregistration ($\#_{\rm Gaia}$).

sufficient redundancy. The time span covered by the remaining data sets is 2017 July to 2019 January. These data were extracted and astrometrically calibrated to the Gaia DR3 reference frame as described in Kirkpatrick et al. (2021a).

Given that the usable Spitzer data only cover a year and a half, we turned to WISE astrometry to provide the additional baseline needed to disentangle parallax from proper motion. The NEP is within the boresight of the WISE spacecraft on every orbit, but given the 47′ wide field of view, 1811+6658 is not within the continuous viewing zone. However, that location *is* viewed by WISE during a span of 50+ days every 6 months as the scan pattern rotates around the ecliptic pole. As such, there are several weeks of coverage twice per year covering its location.

We ran the `crowdsource` detection software (Schlafly et al. 2018) on time-resolved unWISE coadds (Meisner et al. 2018) for all 10 day epochal mosaics covering the position of 1811+6658. We retained those source lists for which the frame coverage depth at the location of 1811+6658 was 40 or greater. This was done in an effort to assure that the area surrounding the target's location also had sufficient coverage, as this area is needed for the astrometric calibrators. The measured positions of these surrounding astrometric standards were used to place the measured position of 1811+6658 onto the same Gaia DR3 reference frame used for the Spitzer observations.

This astrometry from Spitzer and WISE is listed in Table A4. A fit to the parallax and proper motion was performed on the combined astrometry using the methodology outlined in Kirkpatrick et al. (2021a), resulting in the values shown in Table A5. The results of this fit are shown graphically in Figure A7. We find that the object has a distance of $14.3^{+1.6}_{-1.2}$ pc and a value of $M_{\rm ch2} = 15.16 \pm 0.21$ mag. A comparison to Figure 16(d) of Kirkpatrick et al. (2021a) suggests a spectral type of early-Y for this absolute magnitude. We further note

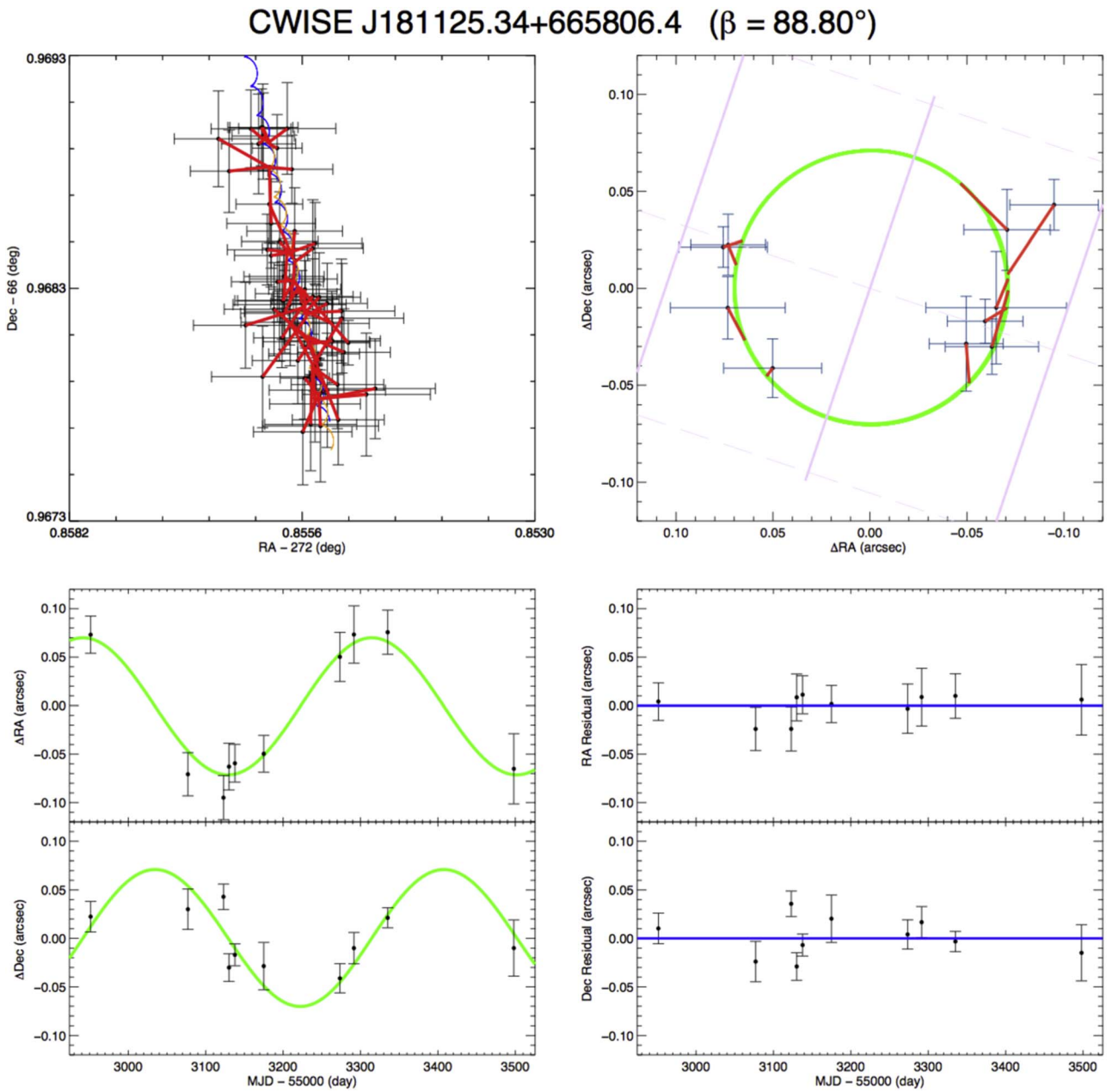

Figure A7. Best fit to the parallax and proper motion of 1811+6658. Upper left: Sky plot showing the track of the object along the sky. Black points with large uncertainties are the 57 individual unWISE time-resolved measurements. The orange curve shows the best fit as seen from the vantage point of WISE, and the blue curve shows this same fit from the vantage point of Spitzer. Red lines connect each observation to its predicted point along the best-fit curve. Upper right: The parallax solution (green) with the proper-motion component subtracted out. For clarity, only the 10 Spitzer data points are shown. Red lines connect the times of the Spitzer observations to their predicted points on the curve. Lower left: the parallactic fit (green) as a function of time in R.A. and decl., along with the measured Spitzer astrometry. Lower right: Residuals around the parallactic fit as function of time in both R.A. and decl. Blue lines mark residuals of zero. For additional info on this plot, see Figure 2 of Kirkpatrick et al. (2021a).

that the measured colors—$J_{\rm MKO} - {\rm ch2} = 5.66 \pm 0.04$ mag, W1−W2 $= 3.04 \pm 0.09$ mag, and ch1−ch2 $= 2.28 \pm 0.02$ mag—suggest a slightly earlier spectral type of around T9–T9.5 based on Figures 16(e), (g), and (h) of Kirkpatrick et al. (2021a). A comparison of our Keck/MOSFIRE $J_{\rm MKO}$, and WISE W1+W2 images with data from PanSTARRS (Figure A6) shows that 1811+6658 is passing near two blue PanSTARRS sources. Given the low spatial resolution of the WISE (and Spitzer) data, we believe that our measurements of W1 (and ch1) are contaminated by these background objects. The higher resolution of the Keck/MOSFIRE data allows us to separate all three components, but our aperture photometry at $J_{\rm MKO}$ is likely still compromised given our aperture radius of 6 pixels (1.″1). Therefore, our measured $J_{\rm MKO}$ − ch2, W1−W2, and ch1−ch2 color are all likely bluer than their true values, supporting our assertion of a Y dwarf spectral type.

Appendix B
The List of Proximal Systems

Despite recent WISE-based discoveries of the L+T dwarf binary system WISE J104915.57−531906.1 AB (Luhman 2013; 1.99 pc distant) and the Y dwarf WISE J085510.83−071442.5 (Luhman 2014; 2.28 pc distant) adding to our

Table B1
The Proximal Systems for Each Constellation

Constellation (1)	Proximal System (2)	Spectral Class (3)	Parallax (mas) (4)
And	Ross 248	M	316.48
Ant	DENIS J104814.6−395606	M	247.21
Aps	L 43-72 AB	M+M	85.71
Aql	Altair (α Aql)	A	194.95
Aqr	EZ Aqr ABC	M+M+M	289.50
Ara	CD−46 11540	M	219.64
Ari	Teegarden's Star	M	260.98
Aur	QY Aur AB	M+M	165.21
Boo	HD 119850	M	183.99
Cae	L 374-6	M	70.06
Cam	G 254-29	M	190.32
Cap	LP 816-60	M	177.93
Car	L 143-23	M	206.96
Cas	Achird (η Cas AB)	F+K	168.83
Cen	α Cen AB + Proxima Cen	G+K+M	768.06
Cep	HD 239960 AB	M+M	249.96
Cet	G 272-61 AB	M+M	373.84
Cha	SCR J1138−7721	M	119.34
Cir	DENIS-P J1454078−660447	L	93.94
CMa	Sirius (α CMa AB)	A+wd	79.21
CMi	Procyon (α CMi AB)	F+wd	284.56
Cnc	G 51-15	M	279.24
Col	AP Col	M	115.39
Com	β Com	F	108.72
CrA	L 489-58	M	80.41
CrB	LSPM J1524+2925	M	76.46
Crt	CD−23 9765	M	92.80
Cru	L 194-11	M	76.35
Crv	Ross 695	M	112.67
CVn	Chara (β CVn)	G	118.02
Cyg	61 Cyg AB	K+K	286.00
Del	WISEPC J205628.90 +145953.3	Y	140.80
Dor	L 230-188	M	140.69
Dra	HD 173739 + HD 173740	M+M	283.84
Equ	HD 200779	K	66.46
Eri	Ran (ϵ Eri)	K	310.57
For	LP 944-20	M	155.59
Gem	HD 265866	M	179.06
Gru	HD 204961	M	201.32
Her	WISEPA J174124.26 +255319.5	T	214.30
Hor	L 372-58	M	272.16
Hya	WISE J085510.83−071442.5	Y	439.00
Hyi	β Hyi	G	133.71
Ind	ϵ Ind ABC	K+T+T	274.84
Lac	EV Lac	M	197.95
Leo	Wolf 359	M	415.17
Lep	Gl 229 AB	M+T	173.69
Lib	Gl 570 ABCD	K+M+M+T	170.01
LMi	G 119-36	M	102.75
Lup	CD−40 9712	M	168.99
Lyn	G 111-47	M	112.99
Lyr	2MASSI J1835379+325954	M	175.79
Men	L 32-8+L 32-9	M+M	113.13
Mic	AX Mic	M	251.91
Mon	Ross 614 AB[a]	M+M	242.96
Mus	LAWD 37	wd	215.67
Nor	WISEA J154045.67−510139.3	M	187.72
Oct	L 49-19	M	116.31
Oph	Barnard's Star	M	546.97
Ori	G 99-49	M	192.01
Pav	SCR J1845−6357 AB	M+T	249.91
Peg	WISE J220905.73+271143.9[b]	Y	161.70
Per	2MASS J04195212+4233304[c]	M	97.44
Phe	LAWD 96	wd	120.01
Pic	Kapteyn's Star	M	254.19
PsA	HD 217987	M	304.13
Psc	Wolf 28	wd	231.78
Pup	2MASS J07290002−3954043[d]	T	126.30
Pyx	CD−32 5613	wd	117.39
Ret	WISE J035000.32−565830.2	Y	176.40
Scl	HD 225213	M	230.09
Sco	CD−44 11909	M	199.69
Sct	WISEA J182423.61−053653.6	M	75.67
Ser	HD 165222	M	129.21
Sex	LP 731-58	M	219.33
Sge	HD 349726 + Ross 730	M+M	113.25
Sgr	Ross 154	M	336.02
Tau	WISEPA J041022.71 +150248.5	Y	151.30
Tel	L 347-14	M	169.23
TrA	WISE J163940.86−684744.6	Y	219.60
Tri	LP 245-10	M	96.73
Tuc	CD−68 47	M	121.44
UMa	Lalande 21185	M	392.75
UMi	WISEPC J150649.97 +702736.0	T	193.94
Vel	WISE J104915.57 −531906.1AB	L+T	501.55
Vir	Ross 128	M	296.30
Vol	LAWD 26	wd	122.41
Vul	WISE J192841.35+235604.9	T	146.40

Notes.
[a] The T dwarf UGPS J072227.51−054031.2 is equidistant with this source within the measurement uncertainties.
[b] The M dwarf pair BD+19 5116AB is equidistant with this source within the measurement uncertainties.
[c] The T dwarf WISE J043052.92+463331.6 is equidistant with this source within the measurement uncertainties.
[d] The M dwarf SCR J0740−4257 is equidistant with this source within the measurement uncertainties.

(This table is available in machine-readable form.)

knowledge of the Sun's immediate neighbors, Proxima Centauri (Innes 1915; 1.30 pc distant) remains the closest. It is often just referred to as Proxima, Latin for "nearest," because it is *the* nearest to the Sun. Yet, its full name translates to "nearest of Centaurus." This has led some curious individuals to wonder what are the nearest stars—i.e., the other proximal objects—of each of the other 87 official constellations.

Table 4 allows us to answer this question, given our current knowledge of the 20 pc census. Proxima Centauri and its primary, α Centauri AB, represent a rare multiobject system for which the parallaxes of the individual components are so accurate that we can determine the far-flung companion to be closer to us than its host binary. For other multiobject systems, discerning the closest component may be far more difficult. Using a short-period binary as an example, determining the

closest object in the system depends upon the orbital period and orientation with respect to the Sun, as one component may be the closer one at some epochs and the more distant one at others. Hence, we will identify only the proximal *systems* in each constellation when a multiobject system arises.

Table B1 lists these proximal systems. As examples, the closest system in Canis Major is the binary Sirius AB, and the closest in Delphinus is the Y dwarf WISEPC J205628.90 +145953.3. For several constellations, the proximal system is still ambiguous, given current uncertainties in the measured trigonometric parallaxes of the closest candidates. Constellations having two objects within 1σ of the same closest value are indicated by footnotes. Note that all constellations have a proximal system within the 20 pc limit of Table 4, the most distant being the K dwarf HD 200779 at 15.05 pc, the closest known object in Equuleus.

It is worth noting the prevalence of brown dwarfs in Table B1. There are four T dwarf companions residing in proximal systems with K or M dwarf primaries, one L+T binary as its own proximal system, and eleven solivagant L, T, or Y dwarfs that are proximal objects in their own right. In this latter group, over half (six) of the these are Y dwarfs, a spectral type that is not yet fully sampled near the Sun.

ORCID iDs

J. Davy Kirkpatrick https://orcid.org/0000-0003-4269-260X
Federico Marocco https://orcid.org/0000-0001-7519-1700
Christopher R. Gelino https://orcid.org/0000-0001-5072-4574
Yadukrishna Raghu https://orcid.org/0000-0001-9778-7054
Jacqueline K. Faherty https://orcid.org/0000-0001-6251-0573
Daniella C. Bardalez Gagliuffi https://orcid.org/0000-0001-8170-7072
Steven D. Schurr https://orcid.org/0000-0003-1785-5550
Adam C. Schneider https://orcid.org/0000-0002-6294-5937
Aaron M. Meisner https://orcid.org/0000-0002-1125-7384
Marc J. Kuchner https://orcid.org/0000-0002-2387-5489
Dan Caselden https://orcid.org/0000-0001-7896-5791
R. L. Smart https://orcid.org/0000-0002-4424-4766
S. L. Casewell https://orcid.org/0000-0003-2478-0120
Roberto Raddi https://orcid.org/0000-0002-9090-9191
Aurora Kesseli https://orcid.org/0000-0002-3239-5989
Nikolaj Stevnbak Andersen https://orcid.org/0000-0003-4714-3829
Thomas P. Bickle https://orcid.org/0000-0003-2235-761X
Martin Bilsing https://orcid.org/0009-0000-5790-7488
Guillaume Colin https://orcid.org/0000-0002-7630-1243
Katharina Doll https://orcid.org/0000-0002-2993-9869
Hugo A. Durantini Luca https://orcid.org/0000-0002-4143-2550
Jean Marc Gantier https://orcid.org/0000-0002-1044-1112
Léopold Gramaize https://orcid.org/0000-0002-8960-4964
Leslie K. Hamlet https://orcid.org/0000-0002-7389-2092
Hiro Higashimura (東村 滉) https://orcid.org/0009-0004-9088-7510
Michiharu Hyogo https://orcid.org/0000-0001-8343-0820
Peter A. Jałowiczor https://orcid.org/0000-0002-4175-295X
Alexander Jonkeren https://orcid.org/0000-0003-3743-3320
Martin Kabatnik https://orcid.org/0000-0003-4905-1370
Frank Kiwy https://orcid.org/0000-0001-8662-1622
Marianne N. Michaels https://orcid.org/0009-0000-8800-3174
Benjamin Pumphrey https://orcid.org/0000-0001-9692-7908
Austin Rothermich https://orcid.org/0000-0003-4083-9962
Arttu Sainio https://orcid.org/0000-0003-4864-5484
Jörg Schümann https://orcid.org/0000-0002-7587-7195
Guoyou Sun (孙国佑) https://orcid.org/0000-0003-3162-3350
Melina Thévenot https://orcid.org/0000-0001-5284-9231
Christian Aganze https://orcid.org/0000-0003-2094-9128
Katelyn N. Allers https://orcid.org/0000-0003-0580-7244
Hunter Brooks https://orcid.org/0000-0002-5253-0383
Adam J. Burgasser https://orcid.org/0000-0002-6523-9536
Emily Calamari https://orcid.org/0000-0002-2682-0790
Thomas Connor https://orcid.org/0000-0002-7898-7664
Edgardo Costa https://orcid.org/0000-0003-4142-1082
Jonathan Gagné https://orcid.org/0000-0002-2592-9612
Roman Gerasimov https://orcid.org/0000-0003-0398-639X
Eileen C. Gonzales https://orcid.org/0000-0003-4636-6676
Chih-Chun Hsu https://orcid.org/0000-0002-5370-7494
Rocio Kiman https://orcid.org/0000-0003-2102-3159
Guodong Li https://orcid.org/0000-0003-4007-5771
Ryan Low https://orcid.org/0000-0002-5024-0075
Eric Mamajek https://orcid.org/0000-0003-2008-1488
Mark Popinchalk https://orcid.org/0000-0001-9482-7794
Jon M. Rees https://orcid.org/0000-0002-5376-3883
Daniel Stern https://orcid.org/0000-0003-2686-9241
Genaro Suárez https://orcid.org/0000-0002-2011-4924
Christopher Theissen https://orcid.org/0000-0002-9807-5435
Chao-Wei Tsai https://orcid.org/0000-0002-9390-9672
Johanna M. Vos https://orcid.org/0000-0003-0489-1528

References

Abazajian, K. N., Adelman-McCarthy, J. K., Agüeros, M. A., et al. 2009, ApJS, 182, 543
Aberasturi, M., Burgasser, A. J., Mora, A., et al. 2014, AJ, 148, 129
Aberasturi, M., Caballero, J. A., Montesinos, B., et al. 2014, AJ, 148, 36
Abt, H. A. 1965, ApJS, 11, 429
Abt, H. A. 1970, ApJS, 19, 387
Abt, H. A. 1981, ApJS, 45, 437
Abt, H. A. 2017, PASP, 129, 044201
Abt, H. A., & Levy, S. G. 1976, ApJS, 30, 273
Abt, H. A., & Willmarth, D. 2006, ApJS, 162, 207
Adams, W. S., Joy, A. H., Humason, M. L., et al. 1935, ApJ, 81, 187
Aerts, C. 2021, RvMP, 93, 015001
Affer, L., Micela, G., Damasso, M., et al. 2016, A&A, 593, A117
Affer, L., Micela, G., Morel, T., et al. 2005, A&A, 433, 647
Agati, J.-L., Bonneau, D., Jorissen, A., et al. 2015, A&A, 574, A6
Akeson, R., Beichman, C., Kervella, P., et al. 2021, AJ, 162, 14
Albert, L., Artigau, É., Delorme, P., et al. 2011, AJ, 141, 203
Alberts, F., Savonije, G. J., van den Heuvel, E. P. J., et al. 1996, Natur, 380, 676
Allen, C., Poveda, A., & Herrera, M. A. 2000, A&A, 356, 529
Allen, P. R., Burgasser, A. J., Faherty, J. K., et al. 2012, AJ, 144, 62
Allen, R. H. 1899, Star-names and Their Meanings (New York: G. E. Stechert)
Allende Prieto, C., & Lambert, D. L. 1999, A&A, 352, 555
Allers, K. N., & Liu, M. C. 2013, ApJ, 772, 79
Alonso-Floriano, F. J., Morales, J. C., Caballero, J. A., et al. 2015, A&A, 577, A128
Amado, P. J., Bauer, F. F., Rodríguez López, C., et al. 2021, A&A, 650, A188
Anders, F., Khalatyan, A., Queiroz, A. B. A., et al. 2022, A&A, 658, A91
Andersen, M., Meyer, M. R., Greissl, J., et al. 2008, ApJL, 683, L183
Andrade, M. 2019, A&A, 630, A96

Andrews, J. J., Agüeros, M. A., Gianninas, A., et al. 2015, ApJ, 815, 63
Andrews, J. J., Breivik, K., & Chatterjee, S. 2019, ApJ, 886, 68
Anglada-Escude, G., Arriagada, P., Tuomi, M., et al. 2014, MNRAS, 443, L89
Apps, K., Clubb, K. I., Fischer, D. A., et al. 2010, PASP, 122, 156
Arenou, F., Halbwachs, J.-L., Mayor, M., et al. 2000, in IAU Symp. 200, Birth and Evolution of Binary Stars, ed. B. Reipurth & H. Zinnecker (San Francisco, CA: ASP), 135
Argelander, F. W. A. (ed.) 1903, Bonner Durchmusterung des Nördlichen Himmels (Bonn: Marcus and Weber's Verlag)
Artigau, É., Radigan, J., Folkes, S., et al. 2010, ApJL, 718, L38
Astudillo-Defru, N., Forveille, T., Bonfils, X., et al. 2017, A&A, 602, A88
Azulay, R., Guirado, J. C., Marcaide, J. M., et al. 2015, A&A, 578, A16
Azulay, R., Guirado, J. C., Marcaide, J. M., et al. 2017, A&A, 607, A10
Bach, K., Lee, J., Demarque, P., et al. 2009, ApJ, 703, 362
Bagnulo, S., & Landstreet, J. D. 2020, A&A, 643, A134
Bailer-Jones, C. A. L. 2022, ApJL, 935, L9
Baines, E. K., & Armstrong, J. T. 2012, ApJ, 744, 138
Baines, E. K., Armstrong, J. T., Schmitt, H. R., et al. 2018, AJ, 155, 30
Balega, I., Balega, Y. Y., Maksimov, A. F., et al. 2004, A&A, 422, 627
Balega, I., Bonneau, D., & Foy, R. 1984, A&AS, 57, 31
Balega, I. I., Balega, Y. Y., Gasanova, L. T., et al. 2013, AstBu, 68, 53
Baraffe, I., Chabrier, G., Barman, T. S., et al. 2003, A&A, 402, 701
Bardalez Gagliuffi, D. C., Burgasser, A. J., Gelino, C. R., et al. 2014, ApJ, 794, 143
Bardalez Gagliuffi, D. C., Burgasser, A. J., Schmidt, S. J., et al. 2019, ApJ, 883, 205
Bardalez Gagliuffi, D. C., Faherty, J. K., Schneider, A. C., et al. 2020, ApJ, 895, 145
Baroch, D., Morales, J. C., Ribas, I., et al. 2018, A&A, 619, A32
Baroch, D., Morales, J. C., Ribas, I., et al. 2021, A&A, 653, A49
Barrientos, M., & Chanamé, J. 2021, ApJ, 923, 181
Barry, R. K., Demory, B.-O., Ségransan, D., et al. 2012, ApJ, 760, 55
Bartlett, J. L., Lurie, J. C., Riedel, A., et al. 2017, AJ, 154, 151
Bastian, N., Covey, K. R., & Meyer, M. R. 2010, ARA&A, 48, 339
Batten, A. H., & Fletcher, J. M. 1992, JRASC, 86, 99
Batten, A. H., Fletcher, J. M., & Mann, P. J. 1978, PDAO, 15, 121
Bauer, F. F., Zechmeister, M., Kaminski, A., et al. 2020, A&A, 640, A50
Bayer, J. (ed.) 1603, Uranometria omnium asterismorum continens schemata, nova methodo delineata aereis laminis expressa (Augsburg: excudit Christophorus Mangus), doi:10.3931/e-rara-309
Bayo, A., Rodrigo, C., & Barrado Y Navascués, D. 2008, A&A, 492, 277
Bazot, M., Creevey, O., Christensen-Dalsgaard, J., et al. 2018, A&A, 619, A172
Bazot, M., Ireland, M. J., Huber, D., et al. 2011, A&A, 526, L4
Beamín, J. C., Minniti, D., Gromadzki, M., et al. 2013, A&A, 557, L8
Beard, C., Robertson, P., Kanodia, S., et al. 2022, ApJ, 936, 55
Beavers, W. I., & Salzer, J. J. 1985, PASP, 97, 355
Bédard, A., Bergeron, P., & Fontaine, G. 2017, ApJ, 848, 11
Beichman, C. A., Lisse, C. M., Tanner, A. M., et al. 2011, ApJ, 743, 85
Belokurov, V., Penoyre, Z., Oh, S., et al. 2020, MNRAS, 496, 1922
Benedict, G. F., Henry, T. J., Franz, O. G., et al. 2016, AJ, 152, 141
Benedict, G. F., McArthur, B. E., Franz, O. G., et al. 2001, AJ, 121, 1607
Benjamin, R. A., Churchwell, E., Babler, B. L., et al. 2003, PASP, 115, 953
Bensby, T., Feltzing, S., & Oey, M. S. 2014, A&A, 562, A71
Berdnikov, L. N., & Pastukhova, E. N. 2008, PZ, 28, 9
Bergeron, P., Dufour, P., Fontaine, G., et al. 2019, ApJ, 876, 67
Bergeron, P., Kilic, M., Blouin, S., et al. 2022, ApJ, 934, 36
Bergeron, P., Leggett, S. K., & Ruiz, M. T. 2001, ApJS, 133, 413
Bergeron, P., Ruiz, M.-T., Leggett, S. K., et al. 1994, ApJ, 423, 456
Bergeron, P., Ruiz, M. T., & Leggett, S. K. 1997, ApJS, 108, 339
Bergeron, P., Saffer, R. A., & Liebert, J. 1992, ApJ, 394, 228
Bergfors, C., Brandner, W., Bonnefoy, M., et al. 2016, MNRAS, 456, 2576
Bergfors, C., Brandner, W., Janson, M., et al. 2010, A&A, 520, A54
Bernat, D., Bouchez, A. H., Ireland, M., et al. 2010, ApJ, 715, 724
Bernkopf, J., Chini, R., Buda, L.-S., et al. 2012, MNRAS, 425, 1308
Berski, F., & Dybczyński, P. A. 2016, A&A, 595, L10
Bessel, F. W. 1844, MNRAS, 6, 136
Best, W. M. J., Liu, M. C., Magnier, E. A., et al. 2013, ApJ, 777, 84
Best, W. M. J., Liu, M. C., Magnier, E. A., et al. 2015, ApJ, 814, 118
Best, W. M. J., Liu, M. C., Magnier, E. A., et al. 2020, AJ, 159, 257
Best, W. M. J., Liu, M. C., Magnier, E. A., et al. 2021, AJ, 161, 42
Beuzit, J.-L., Ségransan, D., Forveille, T., et al. 2004, A&A, 425, 997
Bidelman, W. P. 1980, PASP, 92, 345
Bidelman, W. P. 1985, ApJS, 59, 197
Bihain, G., Scholz, R.-D., Storm, J., et al. 2013, A&A, 557, A43
Biller, B. A., Grandjean, A., Messina, S., et al. 2022, A&A, 658, A145
Blomme, R., Fremat, Y., Sartoretti, P., et al. 2023, A&A, 674, A7
Blouin, S., Dufour, P., Thibeault, C., et al. 2019, ApJ, 878, 63
Bobylev, V., & Bajkova, A. 2022, AstL, 48, 542
Boccaletti, A., Chauvin, G., Lagrange, A.-M., et al. 2003, A&A, 410, 283
Bochanski, J. J., Hawley, S. L., Covey, K. R., et al. 2010, AJ, 139, 2679
Bochanski, J. J., Hawley, S. L., Reid, I. N., et al. 2005, AJ, 130, 1871
Bochanski, J. J., Hennawi, J. F., Simcoe, R. A., et al. 2009, PASP, 121, 1409
Boden, A. F., Koresko, C. D., van Belle, G. T., et al. 1999, ApJ, 515, 356
Boeshaar, P. C. 1976, PhD thesis, Ohio State Univ.
Boeshaar, P. C., & Tyson, J. A. 1985, AJ, 90, 817
Bonavita, M., & Desidera, S. 2020, Galax, 8, 16
Bond, H. E., Gilliland, R. L., Schaefer, G. H., et al. 2018, RNAAS, 2, 147
Bond, H. E., Schaefer, G. H., Gilliland, R. L., et al. 2017, ApJ, 840, 70
Bond, H. E., Schaefer, G. H., Gilliland, R. L., et al. 2020, ApJ, 904, 112
Bonfils, X., Almenara, J.-M., Cloutier, R., et al. 2018a, A&A, 618, A142
Bonfils, X., Astudillo-Defru, N., Díaz, R., et al. 2018b, A&A, 613, A25
Bonfils, X., Delfosse, X., Udry, S., et al. 2005, A&A, 442, 635
Bonfils, X., Delfosse, X., Udry, S., et al. 2013, A&A, 549, A109
Bonfils, X., Mayor, M., Delfosse, X., et al. 2007, A&A, 474, 293
Bonnefoy, M., Chauvin, G., Lagrange, A.-M., et al. 2014, A&A, 562, A127
Bonnefoy, M., Perraut, K., Lagrange, A.-M., et al. 2018, A&A, 618, A63
Borgniet, S., Lagrange, A.-M., Meunier, N., et al. 2019, A&A, 621, A87
Borsa, F., Scandariato, G., Rainer, M., et al. 2015, A&A, 578, A64
Bouy, H., Brandner, W., Martín, E. L., et al. 2003, AJ, 126, 1526
Bouy, H., Duchêne, G., Köhler, R., et al. 2004, A&A, 423, 341
Bouy, H., Martín, E. L., Brandner, W., et al. 2005, AJ, 129, 511
Bowler, B. P., Blunt, S. C., & Nielsen, E. L. 2020, AJ, 159, 63
Bowler, B. P., Hinkley, S., Ziegler, C., et al. 2019, ApJ, 877, 60
Bowler, B. P., Liu, M. C., Shkolnik, E. L., et al. 2015a, ApJS, 216, 7
Bowler, B. P., Shkolnik, E. L., Liu, M. C., et al. 2015b, ApJ, 806, 62
Bowler, B. P., Tran, Q. H., Zhang, Z., et al. 2023, AJ, 165, 164
Boyajian, T. S., McAlister, H. A., van Belle, G., et al. 2012, ApJ, 746, 101
Boyd, M. R., Henry, T. J., Jao, W.-C., et al. 2011, AJ, 142, 92
Brandão, I. M., Doğan, G., Christensen-Dalsgaard, J., et al. 2011, A&A, 527, A37
Brandt, G. M., Dupuy, T. J., Li, Y., et al. 2021, AJ, 162, 301
Brandt, T. D. 2021, ApJS, 254, 42
Brandt, T. D., Dupuy, T. J., & Bowler, B. P. 2019, AJ, 158, 140
Brandt, T. D., Dupuy, T. J., Bowler, B. P., et al. 2020, AJ, 160, 196
Brandt, T. D., McElwain, M. W., Turner, E. L., et al. 2014, ApJ, 794, 159
Breakiron, L. A., & Gatewood, G. 1974, PASP, 86, 448
Bressan, A., Marigo, P., Girardi, L., et al. 2012, MNRAS, 427, 127
Brewer, J. M., Fischer, D. A., Valenti, J. A., et al. 2016, ApJS, 225, 32
Brown, T. M., Gilliland, R. L., Noyes, R. W., et al. 1991, ApJ, 368, 599
Bruntt, H., Bedding, T. R., Quirion, P.-O., et al. 2010, MNRAS, 405, 1907
Buckley, D. A. H., Swart, G. P., & Meiring, J. G. 2006, Proc. SPIE, 6267, 62670Z
Burgasser, A. J. 2007, ApJ, 659, 655
Burgasser, A. J., Cruz, K. L., Cushing, M., et al. 2010a, ApJ, 710, 1142
Burgasser, A. J., Cruz, K. L., & Kirkpatrick, J. D. 2007a, ApJ, 657, 494
Burgasser, A. J., Geballe, T. R., Leggett, S. K., et al. 2006, ApJ, 637, 1067
Burgasser, A. J., Gillon, M., Melis, C., et al. 2015a, AJ, 149, 104
Burgasser, A. J., Kirkpatrick, J. D., Liebert, J., et al. 2003, ApJ, 594, 510
Burgasser, A. J., Liu, M. C., Ireland, M. J., et al. 2008a, ApJ, 681, 579
Burgasser, A. J., Looper, D., & Rayner, J. T. 2010b, AJ, 139, 2448
Burgasser, A. J., Looper, D. L., Kirkpatrick, J. D., et al. 2007b, ApJ, 658, 557
Burgasser, A. J., Looper, D. L., Kirkpatrick, J. D., et al. 2008b, ApJ, 674, 451
Burgasser, A. J., McElwain, M. W., Kirkpatrick, J. D., et al. 2004, AJ, 127, 2856
Burgasser, A. J., Melis, C., Todd, J., et al. 2015b, AJ, 150, 180
Burgasser, A. J., Sheppard, S. S., & Luhman, K. L. 2013, ApJ, 772, 129
Burgasser, A. J., Sitarski, B. N., Gelino, C. R., et al. 2011, ApJ, 739, 49
Burgh, E. B., Nordsieck, K. H., Kobulnicky, H. A., et al. 2003, Proc. SPIE, 4841, 1463
Burningham, B., Cardoso, C. V., Smith, L., et al. 2013, MNRAS, 433, 457
Burningham, B., Lucas, P. W., Leggett, S. K., et al. 2011, MNRAS, 414, L90
Burningham, B., Pinfield, D. J., Lucas, P. W., et al. 2010, MNRAS, 406, 1885
Burningham, B., Smith, L., Cardoso, C. V., et al. 2014, MNRAS, 440, 359
Burrows, A., Marley, M., Hubbard, W. B., et al. 1997, ApJ, 491, 856
Burt, J., Feng, F., Holden, B., et al. 2021, AJ, 161, 10
Butler, R. P., Vogt, S. S., Laughlin, G., et al. 2017, AJ, 153, 208
Butler, R. P., Wright, J. T., Marcy, G. W., et al. 2006, ApJ, 646, 505
Bychkov, V. D., Bychkova, L. V., & Madej, J. 2013, AJ, 146, 74
Calamari, E., Faherty, J. K., Burningham, B., et al. 2022, ApJ, 940, 164
Calissendorff, P., De Furio, M., Meyer, M., et al. 2023, ApJL, 947, L30
Calissendorff, P., Janson, M., & Bonnefoy, M. 2020, A&A, 642, A57

Cannon, A. J. 1925a, AnHar, 100, 1
Cannon, A. J. 1925b, AnHar, 100, 17
Cannon, A. J. 1927, AnHar, 100, 33
Cannon, A. J. 1928, AnHar, 100, 49
Cannon, A. J. 1931, AnHar, 100, 61
Cannon, A. J. 1936, AnHar, 100, 205
Cannon, A. J., & Mayall, M. W. 1949, AnHar, 112, 1
Cannon, A. J., & Pickering, E. C. 1918a, AnHar, 91, 1
Cannon, A. J., & Pickering, E. C. 1918b, AnHar, 92, 1
Cannon, A. J., & Pickering, E. C. 1919a, AnHar, 93, 1
Cannon, A. J., & Pickering, E. C. 1919b, AnHar, 94, 1
Cannon, A. J., & Pickering, E. C. 1920, AnHar, 95, 1
Cannon, A. J., & Pickering, E. C. 1921, AnHar, 96, 1
Cannon, A. J., & Pickering, E. C. 1922, AnHar, 97, 1
Cannon, A. J., & Pickering, E. C. 1923, AnHar, 98, 1
Cannon, A. J., & Pickering, E. C. 1924, AnHar, 99, 1
Cannon, A. J., & Pickering, E. C. 1993, yCat, III/135A
Cardona Guillén, C., Lodieu, N., Béjar, V. J. S., et al. 2021, A&A, 654, A134
Carey, S. J., Noriega-Crespo, A., Mizuno, D. R., et al. 2009, PASP, 121, 76
Carrier, F., Eggenberger, P., & Bouchy, F. 2005, A&A, 434, 1085
Carroll, B. W., & Ostlie, D. A. 1996, in An Introduction to Modern Astrophysics, ed. B. W. Carroll & D. A. Ostlie (New York: Benjamin-Cummings), 1996
Caselden, D., Westin, P., Meisner, A., et al. 2018, WiseView, Astrophysics Source Code Library, ascl:1806.004
Castro, P. J., Gizis, J. E., Harris, H. C., et al. 2013, ApJ, 776, 126
Catalán, S., Isern, J., García-Berro, E., et al. 2008a, A&A, 477, 213
Catalán, S., Ribas, I., Isern, J., et al. 2008b, A&A, 477, 901
Chabrier, G. 2001, ApJ, 554, 1274
Chabrier, G. 2003a, ApJL, 586, L133
Chabrier, G. 2003b, PASP, 115, 763
Chandra, V., Hwang, H.-C., Zakamska, N. L., et al. 2020, ApJ, 899, 146
Chauvin, G., Lagrange, A.-M., Dumas, C., et al. 2004, A&A, 425, L29
Chauvin, G., Lagrange, A.-M., Udry, S., et al. 2007, A&A, 475, 723
Che, X., Monnier, J. D., Zhao, M., et al. 2011, ApJ, 732, 68
Chen, M., Li, Y., Brandt, T. D., et al. 2022, AJ, 163, 288
Chini, R., Fuhrmann, K., Barr, A., et al. 2014, MNRAS, 437, 879
Chiu, K., Fan, X., Leggett, S. K., et al. 2006, AJ, 131, 2722
Chontos, A., Huber, D., Berger, T. A., et al. 2021, ApJ, 922, 229
Christian, D. J., Craig, N., Dupuis, J., et al. 2001, AJ, 122, 378
Christian, D. J., Mathioudakis, M., Jevremović, D., et al. 2003, ApJL, 593, L105
Cifuentes, C., Caballero, J. A., Cortés-Contreras, M., et al. 2020, A&A, 642, A115
Clark, C. A., van Belle, G. T., Horch, E. P., et al. 2022, AJ, 164, 33
Climent, J. B., Berger, J. P., Guirado, J. C., et al. 2019, ApJL, 886, L9
Close, L. M., Thatte, N., Nielsen, E. L., et al. 2007, ApJ, 665, 736
Cloutier, R., Charbonneau, D., Deming, D., et al. 2021, AJ, 162, 174
Compton, D. L., Bedding, T. R., & Stello, D. 2019, MNRAS, 485, 560
Corbally, C. J. 1984, ApJS, 55, 657
Cortés-Contreras, M., Béjar, V. J. S., Caballero, J. A., et al. 2017, A&A, 597, A47
Cowley, A. P. 1976, PASP, 88, 95
Cowley, A. P., Hiltner, W. A., & Witt, A. N. 1967, AJ, 72, 1334
Creevey, O. L., Thévenin, F., Boyajian, T. S., et al. 2012, A&A, 545, A17
Crifo, F., Phan-Bao, N., Delfosse, X., et al. 2005, A&A, 441, 653
Cruz, K. L., Kirkpatrick, J. D., & Burgasser, A. J. 2009, AJ, 137, 3345
Cruz, K. L., & Reid, I. N. 2002, AJ, 123, 2828
Cruz, K. L., Reid, I. N., Kirkpatrick, J. D., et al. 2007, AJ, 133, 439
Cruz, K. L., Reid, I. N., Liebert, J., et al. 2003, AJ, 126, 2421
Cummings, J. D., Kalirai, J. S., Tremblay, P.-E., et al. 2018, ApJ, 866, 21
Cunningham, T., Wheatley, P. J., Tremblay, P.-E., et al. 2022, Natur, 602, 219
Curiel, S., Cantó, J., Georgiev, L., et al. 2011, A&A, 525, A78
Cushing, M. C., Hardegree-Ullman, K. K., Trucks, J. L., et al. 2016, ApJ, 823, 152
Cushing, M. C., Kirkpatrick, J. D., Gelino, C. R., et al. 2011, ApJ, 743, 50
Cushing, M. C., Kirkpatrick, J. D., Gelino, C. R., et al. 2014, AJ, 147, 113
Cushing, M. C., Rayner, J. T., & Vacca, W. D. 2005, ApJ, 623, 1115
Cushing, M. C., Vacca, W. D., & Rayner, J. T. 2004, PASP, 116, 362
Cutri, R. M., Skrutskie, M. F., van Dyk, S., et al. 2003, Explanatory Supplement to the 2MASS All Sky Data Release and Extended Mission Products, NASA/IPAC Infrared Science Archive, https://irsa.ipac.caltech.edu/data/2MASS/docs/releases/allsky/doc/explsup.html
Cutri, R. M., Wright, E. L., Conrow, T., et al. 2012, Explanatory Supplement to the WISE All-Sky Data Release Products, IPAC, https://wise2.ipac.caltech.edu/docs/release/allsky/
Cutri, R. M., Wright, E. L., Conrow, T., et al. 2013, Explanatory Supplement to the AllWISE Data Release Products, IPAC, https://wise2.ipac.caltech.edu/docs/release/allwise/
Cvetkovic, Z., & Ninkovic, S. 2010, SerAJ, 180, 71
Cvetković, Z., Pavlović, R., Damljanović, G., et al. 2011, AJ, 142, 73
Dahn, C. C., Harrington, R. S., Kallarakal, V. V., et al. 1988, AJ, 95, 237
Dahn, C. C., Harris, H. C., Subasavage, J. P., et al. 2017, AJ, 154, 147
Dahn, C. C., Harris, H. C., Vrba, F. J., et al. 2002, AJ, 124, 1170
Dalba, P. A., Kane, S. R., Howell, S. B., et al. 2021, AJ, 161, 123
Damasso, M., Perger, M., Almenara, J. M., et al. 2022, A&A, 666, A187
Damasso, M., Sozzetti, A., Lovis, C., et al. 2020, A&A, 642, A31
David, T. J., & Hillenbrand, L. A. 2015, ApJ, 804, 146
Davison, C. L., White, R. J., Jao, W.-C., et al. 2014, AJ, 147, 26
de la Fuente Marcos, R., & de la Fuente Marcos, C. 2022, A&A, 668, A14
de Lalande, J. 1783, Éphémérides des mouvemens célestes pour le méridien de Paris, tome huitième (Paris: Vve Hérissant), 72
Deacon, N. R., & Hambly, N. C. 2007, A&A, 468, 163
Deacon, N. R., Hambly, N. C., & Cooke, J. A. 2005, A&A, 435, 363
Deacon, N. R., Liu, M. C., Magnier, E. A., et al. 2012a, ApJ, 757, 100
Deacon, N. R., Liu, M. C., Magnier, E. A., et al. 2012b, ApJ, 755, 94
Deacon, N. R., Magnier, E. A., Best, W. M. J., et al. 2017, MNRAS, 468, 3499
Dedrick, C. M., Fulton, B. J., Knutson, H. A., et al. 2021, AJ, 161, 86
Deeg, H. J., Ocaña, B., Kozhevnikov, V. P., et al. 2008, A&A, 480, 563
Delfosse, X., Forveille, T., Beuzit, J.-L., et al. 1999a, A&A, 344, 897
Delfosse, X., Forveille, T., Ségransan, D., et al. 2000, A&A, 364, 217
Delfosse, X., Forveille, T., Udry, S., et al. 1999b, A&A, 350, L39
Delrez, L., Ehrenreich, D., Alibert, Y., et al. 2021, NatAs, 5, 775
Di Folco, E., Thévenin, F., Kervella, P., et al. 2004, A&A, 426, 601
Díaz, R. F., González, J. F., Cincunegui, C., et al. 2007, A&A, 474, 345
Dieterich, S. B., Henry, T. J., Golimowski, D. A., et al. 2012, AJ, 144, 64
Dieterich, S. B., Henry, T. J., Jao, W.-C., et al. 2014, AJ, 147, 94
Dieterich, S. B., Simler, A., Henry, T. J., et al. 2021, AJ, 161, 172
Dieterich, S. B., Weinberger, A. J., Boss, A. P., et al. 2018, ApJ, 865, 28
DiTomasso, V., Nava, C., López-Morales, M., et al. 2023, AJ, 165, 38
Dittmann, J. A., Irwin, J. M., Charbonneau, D., et al. 2014, ApJ, 784, 156
Docobo, J. A., Gomez, J., Campo, P. P., et al. 2019, MNRAS, 482, 4096
Docobo, J. A., Tamazian, V. S., Balega, Y. Y., et al. 2006, AJ, 132, 994
D'Orazi, V., Desidera, S., Gratton, R. G., et al. 2017, A&A, 598, A19
dos Santos, L. A., Meléndez, J., Bedell, M., et al. 2017, MNRAS, 472, 3425
Downes, R. A., Webbink, R. F., Shara, M. M., et al. 2006, yCat, V/123A
Ducati, J. R., Penteado, E. M., & Turcati, R. 2011, A&A, 525, A26
Dupuy, T. J., Forbrich, J., Rizzuto, A., et al. 2016, ApJ, 827, 23
Dupuy, T. J., & Kraus, A. L. 2013, Sci, 341, 1492
Dupuy, T. J., & Liu, M. C. 2012, ApJS, 201, 19
Dupuy, T. J., & Liu, M. C. 2017, ApJS, 231, 15
Dupuy, T. J., Liu, M. C., Best, W. M. J., et al. 2019, AJ, 158, 174
Dupuy, T. J., Liu, M. C., Bowler, B. P., et al. 2010, ApJ, 721, 1725
Dupuy, T. J., Liu, M. C., Brandt, G. M., et al. 2022, in 21st Cambridge Workshop on Cool Stars, Stellar Systems, and the Sun, 61
Duquennoy, A., & Mayor, M. 1988, A&A, 200, 135
Duquennoy, A., & Mayor, M. 1991, A&A, 248, 485
Durkan, S., Janson, M., Ciceri, S., et al. 2018, A&A, 618, A5
Dyck, H. M., Benson, J. A., van Belle, G. T., et al. 1996, AJ, 111, 1705
Dye, S., Lawrence, A., Read, M. A., et al. 2018, MNRAS, 473, 5113
Edwards, T. W. 1976, AJ, 81, 245
Eggen, O. J. 1979, ApJS, 39, 89
Eggen, O. J. 1980, ApJS, 43, 457
Eggen, O. J., & Greenstein, J. L. 1965a, ApJ, 141, 83
Eggen, O. J., & Greenstein, J. L. 1965b, ApJ, 142, 925
Eggen, O. J., & Greenstein, J. L. 1967, ApJ, 150, 927
Eggleton, P. P., & Tokovinin, A. A. 2008, MNRAS, 389, 869
Eikenberry, S., Elston, R., Raines, S. N., et al. 2006, Proc. SPIE, 6269, 626917
Eisenhardt, P. R. M., Marocco, F., Fowler, J. W., et al. 2020, ApJS, 247, 69
El-Badry, K., Rix, H.-W., & Weisz, D. R. 2018, ApJL, 860, L17
Elston, R., Raines, S. N., Hanna, K. T., et al. 2003, Proc. SPIE, 4841, 1611
Endl, M., Cochran, W. D., Hatzes, A. P., et al. 2011, in AIP Conf. Proc., 1331, Planetary Systems Beyond the Main Sequence, ed. S. Schuh et al. (Melville, NY: AIP), 88
Endl, M., Cochran, W. D., Kürster, M., et al. 2006, ApJ, 649, 436
ESA 1997, ESA Special Publication, 1200, The HIPPARCOS and TYCHO Catalogues (Noordwijk: ESA)
Evans, D. S. 1968, QJRAS, 9, 388
Evans, D. S., Laing, J. D., Menzies, A., et al. 1964, RGOB, 85, 207
Evans, D. S., Menzies, A., Stoy, R. H., et al. 1961, RGOB, 48, 389
Evans, D. W., Riello, M., De Angeli, F., et al. 2018, A&A, 616, A4
Fabricius, C., Luri, X., Arenou, F., et al. 2021, A&A, 649, A5

Fabricius, C., & Makarov, V. V. 2000, A&AS, 144, 45
Faherty, J. K., Burgasser, A. J., Walter, F. M., et al. 2012, ApJ, 752, 56
Faherty, J. K., Gagné, J., Burgasser, A. J., et al. 2018, ApJ, 868, 44
Faherty, J. K., Goodman, S., Caselden, D., et al. 2020, ApJ, 889, 176
Faherty, J. K., Riedel, A. R., Cruz, K. L., et al. 2016, ApJS, 225, 10
Faherty, J. K., Tinney, C. G., Skemer, A., et al. 2014, ApJL, 793, L16
Fan, X., Knapp, G. R., Strauss, M. A., et al. 2000, AJ, 119, 928
Faria, J. P., Suárez Mascareño, A., Figueira, P., et al. 2022, A&A, 658, A115
Farihi, J., Hoard, D. W., & Wachter, S. 2006, ApJ, 646, 480
Fekel, F. C., Henry, G. W., & Tomkin, J. 2017, AJ, 154, 120
Feng, F., Anglada-Escudé, G., Tuomi, M., et al. 2019a, MNRAS, 490, 5002
Feng, F., Butler, R. P., Jones, H. R. A., et al. 2021, MNRAS, 507, 2856
Feng, F., Butler, R. P., Shectman, S. A., et al. 2020a, ApJS, 246, 11
Feng, F., Butler, R. P., Vogt, S. S., et al. 2022, ApJS, 262, 21
Feng, F., Crane, J. D., Xuesong Wang, S., et al. 2019b, ApJS, 242, 25
Feng, F., Shectman, S. A., Clement, M. S., et al. 2020b, ApJS, 250, 29
Feng, F., Tuomi, M., & Jones, H. R. A. 2017, MNRAS, 470, 4794
Finch, C. T., Henry, T. J., Subasavage, J. P., et al. 2007, AJ, 133, 2898
Finch, C. T., & Zacharias, N. 2016a, AJ, 151, 160
Finch, C. T., & Zacharias, N. 2016b, yCat, I/333
Finch, C. T., Zacharias, N., Boyd, M. R., et al. 2012, ApJ, 745, 118
Finch, C. T., Zacharias, N., & Henry, T. J. 2010, AJ, 140, 844
Finch, C. T., Zacharias, N., & Jao, W.-C. 2018, AJ, 155, 176
Finch, C. T., Zacharias, N., Subasavage, J. P., et al. 2014, AJ, 148, 119
Finley, D. S., Koester, D., & Basri, G. 1997, ApJ, 488, 375
Fischer, D. A., Marcy, G. W., & Spronck, J. F. P. 2014, ApJS, 210, 5
Fischer, D. A., & Valenti, J. 2005, ApJ, 622, 1102
Fletcher, L. N., Orton, G. S., Teanby, N. A., et al. 2009, Icar, 199, 351
Fontaine, G., Brassard, P., & Bergeron, P. 2001, PASP, 113, 409
Fontaine, G., Brassard, P., Charpinet, S., et al. 2013, EPJWC, 43, 05001
Fortney, J. J., Marley, M. S., Saumon, D., et al. 2008, ApJ, 683, 1104
Forveille, T., Beuzit, J.-L., Delfosse, X., et al. 1999, A&A, 351, 619
Forveille, T., Beuzit, J.-L., Delorme, P., et al. 2005, A&A, 435, L5
Forveille, T., Ségransan, D., Delorme, P., et al. 2004, A&A, 427, L1
Fouqué, P., Moutou, C., Malo, L., et al. 2018, MNRAS, 475, 1960
Freed, M., Close, L. M., & Siegler, N. 2003, ApJ, 584, 453
Fuhrmann, K. 2008, MNRAS, 384, 173
Fuhrmann, K., & Chini, R. 2012, ApJS, 203, 30
Fuhrmann, K., Chini, R., Haas, M., et al. 2012, ApJ, 761, 159
Fuhrmann, K., Chini, R., Hoffmeister, V. H., et al. 2011a, MNRAS, 411, 2311
Fuhrmann, K., Chini, R., Hoffmeister, V. H., et al. 2011b, MNRAS, 416, 391
Fuhrmann, K., Chini, R., Kaderhandt, L., et al. 2016, MNRAS, 459, 1682
Fuhrmann, K., Chini, R., Kaderhandt, L., et al. 2017, ApJ, 836, 139
Gagné, J., & Faherty, J. K. 2018, ApJ, 862, 138
Gagné, J., Faherty, J. K., Cruz, K. L., et al. 2015, ApJS, 219, 33
Gagné, J., Mamajek, E. E., Malo, L., et al. 2018, ApJ, 856, 23
Gagné, J., Moranta, L., Faherty, J. K., et al. 2023, ApJ, 945, 119
Gaia Collaboration, Arenou, F., Babusiaux, C., et al. 2023b, A&A, 674, A34
Gaia Collaboration, Brown, A. G. A., Vallenari, A., et al. 2018, A&A, 616, A1
Gaia Collaboration, Brown, A. G. A., Vallenari, A., et al. 2021b, A&A, 649, A1
Gaia Collaboration, Prusti, T., de Bruijne, J. H. J., et al. 2016, A&A, 595, A1
Gaia Collaboration, Smart, R. L., Sarro, L. M., et al. 2021a, A&A, 649, A6
Gaia Collaboration, Vallenari, A., Brown, A. G. A., et al. 2023a, A&A, 674, A1
Gaidos, E., Mann, A. W., Lépine, S., et al. 2014, MNRAS, 443, 2561
Garcia, E. V., Ammons, S. M., Salama, M., et al. 2017, ApJ, 846, 97
Gardner, T., Monnier, J. D., Fekel, F. C., et al. 2021, ApJ, 921, 41
Gatewood, G., Coban, L., & Han, I. 2003, AJ, 125, 1530
Gaudi, B. S. 2012, ARA&A, 50, 411
Geballe, T. R., Knapp, G. R., Leggett, S. K., et al. 2002, ApJ, 564, 466
Genest-Beaulieu, C., & Bergeron, P. 2019, ApJ, 882, 106
Gentile Fusillo, N. P., Tremblay, P.-E., Cukanovaite, E., et al. 2021, MNRAS, 508, 3877
Gentile Fusillo, N. P., Tremblay, P.-E., Gänsicke, B. T., et al. 2019, MNRAS, 482, 4570
Giammichele, N., Bergeron, P., & Dufour, P. 2012, ApJS, 199, 29
Gianninas, A., Bergeron, P., & Ruiz, M. T. 2011, ApJ, 743, 138
Giclas, H. L., Burnham, R., & Thomas, N. G. 1971, Lowell Proper Motion Survey Northern Hemisphere (Flagstaff, AZ: Lowell Observatory)
Giclas, H. L., Burnham, R., & Thomas, N. G. 1978, LowOB, 8, 89
Gigoyan, K. S., & Mickaelian, A. M. 2012, MNRAS, 419, 3346
Gill, D., & Kapteyn, J. C. 1896, AnCap, 3, 1
Gill, D., & Kapteyn, J. C. 1897, AnCap, 4, 1
Gill, D., & Kapteyn, J. C. 1900, AnCap, 5, 1
Gizis, J. E. 1997, AJ, 113, 806
Gizis, J. E. 2002, ApJ, 575, 484
Gizis, J. E., Burgasser, A. J., & Vrba, F. J. 2015, AJ, 150, 179
Gizis, J. E., Monet, D. G., Reid, I. N., et al. 2000a, AJ, 120, 1085
Gizis, J. E., Monet, D. G., Reid, I. N., et al. 2000b, MNRAS, 311, 385
Gizis, J. E., & Reid, I. N. 1997, PASP, 109, 849
Gizis, J. E., Reid, I. N., & Hawley, S. L. 2002, AJ, 123, 3356
Gizis, J. E., Scholz, R.-D., Irwin, M., et al. 1997, MNRAS, 292, L41
Gizis, J. E., Troup, N. W., & Burgasser, A. J. 2011, ApJL, 736, L34
Gliese, W. 1969, VeARI, 22, 1
Gliese, W., & Jahreiß, H. 1979, A&AS, 38, 423
Gliese, W., & Jahreiß, H. 1991, in The Astronomical Data Center CD-ROM: Selected Astronomical Catalogs, Vol. 1, ed. L. E. Brotzmann & S. E. Gesser (Greenbelt, MD: NASA/Astronomical Data Center, Goddard Space Flight Center)
Goldin, A., & Makarov, V. V. 2006, ApJS, 166, 341
Goldin, A., & Makarov, V. V. 2007, ApJS, 173, 137
Golovin, A., Reffert, S., Just, A., et al. 2023, A&A, 670, A19
Gomes, J. I., Pinfield, D. J., Marocco, F., et al. 2013, MNRAS, 431, 2745
González-Álvarez, E., Petralia, A., Micela, G., et al. 2021, A&A, 649, A157
González-Fernández, C., Hodgkin, S. T., Irwin, M. J., et al. 2018, MNRAS, 474, 5459
González-Payo, J., Cortés-Contreras, M., Lodieu, N., et al. 2021, A&A, 650, A190
Goto, M., Kobayashi, N., Terada, H., et al. 2002, ApJL, 567, L59
Grandjean, A., Lagrange, A.-M., Keppler, M., et al. 2020, A&A, 633, A44
Gray, R. O., & Corbally, C. J. (ed.) 2009, Stellar Spectral Classification (Princeton, NJ: Princeton Univ. Press)
Gray, R. O., Corbally, C. J., Garrison, R. F., et al. 2003, AJ, 126, 2048
Gray, R. O., Corbally, C. J., Garrison, R. F., et al. 2006, AJ, 132, 161
Gray, R. O., Napier, M. G., & Winkler, L. I. 2001, AJ, 121, 2148
Greco, J. J., Schneider, A. C., Cushing, M. C., et al. 2019, AJ, 158, 182
Greenstein, J. L. 1969, ApJ, 158, 281
Greenstein, J. L. 1970, ApJL, 162, L55
Greenstein, J. L. 1974, ApJL, 189, L131
Greenstein, J. L. 1975, ApJL, 196, L117
Greenstein, J. L. 1976, ApJL, 207, L119
Greenstein, J. L. 1979, ApJ, 227, 244
Greenstein, J. L. 1980, ApJ, 242, 738
Greenstein, J. L. 1984, ApJ, 276, 602
Greenstein, J. L., Oke, J. B., Richstone, D., et al. 1977, ApJL, 218, L21
Griffin, R. F. 2004, Obs, 124, 258
Griffin, R. F. 2010, Obs, 130, 75
Guenther, E. W., & Wuchterl, G. 2003, A&A, 401, 677
Guzik, J. A., Houdek, G., Chaplin, W. J., et al. 2016, ApJ, 831, 17
Halbwachs, J. L., Arenou, F., Mayor, M., et al. 2000, A&A, 355, 581
Halbwachs, J.-L., Mayor, M., & Udry, S. 2012, MNRAS, 422, 14
Halbwachs, J.-L., Mayor, M., & Udry, S. 2018, A&A, 619, A81
Halbwachs, J.-L., Pourbaix, D., Arenou, F., et al. 2023, A&A, 674, A9
Hambaryan, V., Staude, A., Schwope, A. D., et al. 2004, A&A, 415, 265
Hambly, N. C., Henry, T. J., Subasavage, J. P., et al. 2004, AJ, 128, 437
Hamuy, M., Suntzeff, N. B., Heathcote, S. R., et al. 1994, PASP, 106, 566
Hansen, B. M. S. 2022, AJ, 163, 44
Hansen, C. J., & Kawaler, S. D. 1994, Stellar Interiors. Physical Principles, Structure, and Evolution (Berlin: Springer), 445
Harakawa, H., Takarada, T., Kasagi, Y., et al. 2022, PASJ, 74, 904
Harrington, R. S., Dahn, C. C., Kallarakal, V. V., et al. 1993, AJ, 105, 1571
Hartkopf, W. I., McAlister, H. A., Mason, B. D., et al. 1994, AJ, 108, 2299
Hartkopf, W. I., Tokovinin, A., & Mason, B. D. 2012, AJ, 143, 42
Hatzes, A. P., Cochran, W. D., Endl, M., et al. 2006, A&A, 457, 335
Hatzes, A. P., Gandolfi, D., Korth, J., et al. 2022, AJ, 163, 223
Hatzes, A. P., Zechmeister, M., Matthews, J., et al. 2012, A&A, 543, A98
Hawley, S. L., Covey, K. R., Knapp, G. R., et al. 2002, AJ, 123, 3409
Hawley, S. L., Gizis, J. E., & Reid, N. I. 1997, AJ, 113, 1458
Hayashi, C., & Nakano, T. 1963, PThPh, 30, 460
Hearnshaw, J. B. (ed.) 2014, The Analysis of Starlight (Cambridge: Cambridge Univ. Press)
Heintz, W. D. 1986, AJ, 92, 446
Heintz, W. D. 1990, AJ, 99, 420
Heintz, W. D. 1993, AJ, 105, 1188
Heintz, W. D. 1994, AJ, 108, 2338
Heiter, U., Jofré, P., Gustafsson, B., et al. 2015, A&A, 582, A49
Hełminiak, K. G., Konacki, M., Kulkarni, S. R., et al. 2009, MNRAS, 400, 406
Hełminiak, K. G., Konacki, M., Muterspaugh, M. W., et al. 2012, MNRAS, 419, 1285
Henry, T. J., Franz, O. G., Wasserman, L. H., et al. 1999, ApJ, 512, 864
Henry, T. J., Jao, W.-C., Subasavage, J. P., et al. 2006, AJ, 132, 2360

Henry, T. J., Jao, W.-C., Winters, J. G., et al. 2018, AJ, 155, 265
Henry, T. J., Kirkpatrick, J. D., & Simons, D. A. 1994, AJ, 108, 1437
Henry, T. J., Subasavage, J. P., Brown, M. A., et al. 2004, AJ, 128, 2460
Henry, T. J., Walkowicz, L. M., Barto, T. C., et al. 2002, AJ, 123, 2002
Herbig, G. H. 1977, IBVS, 1323, 1
Hermes, J. J., Charpinet, S., Barclay, T., et al. 2014, ApJ, 789, 85
Herter, T. L., Henderson, C. P., Wilson, J. C., et al. 2008, Proc. SPIE, 7014, 70140X
Hinkley, S., Monnier, J. D., Oppenheimer, B. R., et al. 2011, ApJ, 726, 104
Hobson, M. J., Delfosse, X., Astudillo-Defru, N., et al. 2019, A&A, 625, A18
Hobson, M. J., Díaz, R. F., Delfosse, X., et al. 2018, A&A, 618, A103
Hoch, K., Konopacky, Q., Theissen, C., et al. 2023, AAS Meeting, 241, 247.07D
Hoffleit, D., & Jaschek, C. (ed.) 1982, The Bright Star Catalogue (4th ed.; New Haven, CT: Yale Univ. Observatory)
Hoffleit, D., & Jaschek, C. (ed.) 1991, The Bright Star Catalogue (5th ed.; New Haven, CT: Yale Univ. Observatory)
Hoffleit, D., Saladyga, M., & Wlasuk, P. (ed.) 1983, A Supplement to the Bright Star Catalogue (New Haven, CT: Yale Univ. Observatory)
Hoffleit, D. (ed.) 1964, The Bright Star Catalogue (3rd ed.; New Haven, CT: Yale Univ. Observatory)
Høg, E., Fabricius, C., Makarov, V. V., et al. 2000, A&A, 355, L27
Holberg, J. B., Oswalt, T. D., & Sion, E. M. 2002, ApJ, 571, 512
Hollands, M. A., Tremblay, P.-E., Gänsicke, B. T., et al. 2018, MNRAS, 480, 3942
Holmberg, J., Nordström, B., & Andersen, J. 2007, A&A, 475, 519
Horch, E. P., Bahi, L. A. P., Gaulin, J. R., et al. 2012, AJ, 143, 10
Horch, E. P., Casetti-Dinescu, D. I., Camarata, M. A., et al. 2017, AJ, 153, 212
Horch, E. P., Gomez, S. C., Sherry, W. H., et al. 2011, AJ, 141, 45
Houk, N., & Smith-Moore, M. (ed.) 1988, Michigan Catalogue of Two-dimensional Spectral Types for the HD Stars, Vol. 4 (Ann Arbor, MI: Univ. Michigan)
Houk, N. (ed.) 1982, Michigan Catalogue of Two-dimensional Spectral Types for the HD Stars, Vol. 3 (Ann Arbor, MI: Univ. Michigan)
Howard, A. W., Johnson, J. A., Marcy, G. W., et al. 2010, ApJ, 721, 1467
Howarth, I. D., Goss, K. J. F., Stevens, I. R., et al. 2014, MNRAS, 440, 1674
Hsu, C.-C., Burgasser, A. J., Theissen, C. A., et al. 2021, ApJS, 257, 45
Huber, D., Bryson, S. T., Haas, M. R., et al. 2016, ApJS, 224, 2
Huber, D., Matthews, J. M., Croll, B., et al. 2009, A&A, 505, 715
Humphreys, A., Meisner, A. M., Burgasser, A. J., et al. 2023, RNAAS, 7, 184
Hurt, S. A., Fulton, B., Isaacson, H., et al. 2022, AJ, 163, 218
Hussein, A. M., Al-Wardat, M. A., Abushattal, A., et al. 2022, AJ, 163, 182
Iben, I. 1967, ARA&A, 5, 571
Innes, R. T. A. 1903, AnCap, 9, 0.1
Innes, R. T. A. 1915, CiUO, 30, 235
Ireland, M. J., Kraus, A., Martinache, F., et al. 2008, ApJ, 678, 463
Jackson, J., & Stoy, R. H. 1955, AnCap, 18, 0
Jahreiß, H., Meusinger, H., Scholz, R.-D., et al. 2008, A&A, 484, 575
Jahreiß, H., Scholz, R., Meusinger, H., et al. 2001, A&A, 370, 967
Jannuzi, B. T., & Bechtold, J. 2004, BAAS, 36, 1671
Janson, M., Bergfors, C., Brandner, W., et al. 2014a, ApJ, 789, 102
Janson, M., Bergfors, C., Brandner, W., et al. 2014b, ApJS, 214, 17
Janson, M., Carson, J., Thalmann, C., et al. 2011, ApJ, 728, 85
Janson, M., Hormuth, F., Bergfors, C., et al. 2012, ApJ, 754, 44
Jao, W.-C., Henry, T. J., Beaulieu, T. D., et al. 2008, AJ, 136, 840
Jao, W.-C., Henry, T. J., Subasavage, J. P., et al. 2003, AJ, 125, 332
Jao, W.-C., Henry, T. J., Subasavage, J. P., et al. 2011, AJ, 141, 117
Jao, W.-C., Henry, T. J., Subasavage, J. P., et al. 2014, AJ, 147, 21
Jeffers, S. V., Dreizler, S., Barnes, J. R., et al. 2020, Sci, 368, 1477
Jeffers, S. V., Schöfer, P., Lamert, A., et al. 2018, A&A, 614, A76
Jeffries, R. D., & Bromage, G. E. 1993, MNRAS, 260, 132
Jódar, E., Pérez-Garrido, A., Díaz-Sánchez, A., et al. 2013, MNRAS, 429, 859
Johnson, H. L., & Morgan, W. W. 1953, ApJ, 117, 313
Johnson, J. A., Howard, A. W., Marcy, G. W., et al. 2010, PASP, 122, 149
Johnson, J. W., Weinberg, D. H., Vincenzo, F., et al. 2021, MNRAS, 508, 4484
Joyce, S. R. G., Barstow, M. A., Holberg, J. B., et al. 2018, MNRAS, 481, 2361
Kallinger, T., Beck, P. G., Hekker, S., et al. 2019, A&A, 624, A35
Kallinger, T., Hekker, S., Garcia, R. A., et al. 2016, SciA, 2, 1500654
Kallinger, T., Weiss, W. W., Barban, C., et al. 2010, A&A, 509, A77
Kant, I. 1755, Allgemeine Naturgeschichte und Theorie des Himmels (Konigsberg: Johann Friederich Petersen)
Karovicova, I., White, T. R., Nordlander, T., et al. 2022, A&A, 658, A47
Kasper, M., Biller, B. A., Burrows, A., et al. 2007, A&A, 471, 655
Katoh, N., Itoh, Y., & Sato, B. 2021, PASJ, 73, 78
Katoh, N., Itoh, Y., Toyota, E., et al. 2013, AJ, 145, 41
Katz, D., Sartoretti, P., & Guerrier, A. 2023, A&A, 674, A5
Kawka, A., Vennes, S., Allard, N. F., et al. 2021, MNRAS, 500, 2732
Keenan, P. C., & McNeil, R. C. 1976, An Atlas of Spectra of the Cooler Stars: Types G, K, M, S, and C (Columbus: Ohio State Univ. Press)
Keenan, P. C., & McNeil, R. C. 1989, ApJS, 71, 245
Keenan, P. C., & Yorka, S. B. 1988, BICDS, 35, 37
Kellogg, K., Metchev, S., Geißler, K., et al. 2015, AJ, 150, 182
Kellogg, K., Metchev, S., Miles-Páez, P. A., et al. 2017, AJ, 154, 112
Kendall, T. R., Delfosse, X., Martín, E. L., et al. 2004, A&A, 416, L17
Kendall, T. R., Jones, H. R. A., Pinfield, D. J., et al. 2007, MNRAS, 374, 445
Kennedy, G. M., Wyatt, M. C., Sibthorpe, B., et al. 2012, MNRAS, 421, 2264
Kerr, R. M. P., Rizzuto, A. C., Kraus, A. L., et al. 2021, ApJ, 917, 23
Kervella, P., Arenou, F., Mignard, F., et al. 2019, A&A, 623, A72
Kervella, P., Arenou, F., & Thévenin, F. 2022, A&A, 657, A7
Kervella, P., Mérand, A., Ledoux, C., et al. 2016a, A&A, 593, A127
Kervella, P., Mignard, F., Mérand, A., et al. 2016b, A&A, 594, A107
Kesseli, A. Y., Kirkpatrick, J. D., Fajardo-Acosta, S. B., et al. 2019, AJ, 157, 63
Khovritchev, M. Y., & Kulikova, A. M. 2015, AstL, 41, 833
Kilic, M., Bergeron, P., Kosakowski, A., et al. 2020, ApJ, 898, 84
Kiman, R., Schmidt, S. J., Angus, R., et al. 2019, AJ, 157, 231
King, R. R., McCaughrean, M. J., Homeier, D., et al. 2010, A&A, 510, A99
Kirkpatrick, J. D. 2005, ARA&A, 43, 195
Kirkpatrick, J. D., Cruz, K. L., Barman, T. S., et al. 2008, ApJ, 689, 1295
Kirkpatrick, J. D., Cushing, M. C., Gelino, C. R., et al. 2011, ApJS, 197, 19
Kirkpatrick, J. D., Cushing, M. C., Gelino, C. R., et al. 2013, ApJ, 776, 128
Kirkpatrick, J. D., Dahn, C. C., Monet, D. G., et al. 2001, AJ, 121, 3235
Kirkpatrick, J. D., Gelino, C. R., Cushing, M. C., et al. 2012, ApJ, 753, 156
Kirkpatrick, J. D., Gelino, C. R., Faherty, J. K., et al. 2021a, ApJS, 253, 7
Kirkpatrick, J. D., Henry, T. J., & Irwin, M. J. 1997, AJ, 113, 1421
Kirkpatrick, J. D., Henry, T. J., & McCarthy, D. W. 1991, ApJS, 77, 417
Kirkpatrick, J. D., Henry, T. J., & Simons, D. A. 1995, AJ, 109, 797
Kirkpatrick, J. D., Kellogg, K., Schneider, A. C., et al. 2016, ApJS, 224, 36
Kirkpatrick, J. D., Looper, D. L., Burgasser, A. J., et al. 2010, ApJS, 190, 100
Kirkpatrick, J. D., Marocco, F., Caselden, D., et al. 2021b, ApJL, 915, L6
Kirkpatrick, J. D., Martin, E. C., Smart, R. L., et al. 2019a, ApJS, 240, 19
Kirkpatrick, J. D., & McCarthy, D. W. 1994, AJ, 107, 333
Kirkpatrick, J. D., Metchev, S. A., Hillenbrand, L. A., et al. 2019b, BAAS, 51, 108
Kirkpatrick, J. D., Reid, I. N., Liebert, J., et al. 1999, ApJ, 519, 802
Kirkpatrick, J. D., Reid, I. N., Liebert, J., et al. 2000, AJ, 120, 447
Kirkpatrick, J. D., Schneider, A., Fajardo-Acosta, S., et al. 2014, ApJ, 783, 122
Kiyaeva, O. V., Kiselev, A. A., Polyakov, E. V., et al. 2001, AstL, 27, 391
Kjeldsen, H., & Bedding, T. R. 1995, A&A, 293, 87
Klüter, J., Bastian, U., Demleitner, M., et al. 2018, A&A, 615, L11
Kniazev, A. Y., Vaisanen, P., Mužić, K., et al. 2013, ApJ, 770, 124
Kobulnicky, H. A., Nordsieck, K. H., Burgh, E. B., et al. 2003, Proc. SPIE, 4841, 1634
Kochukhov, O., & Shulyak, D. 2019, ApJ, 873, 69
Kochukhov, O., Shulyak, D., & Ryabchikova, T. 2009, A&A, 499, 851
Koen, C., Miszalski, B., Väisänen, P., et al. 2017, MNRAS, 465, 4723
Koester, D., Schulz, H., & Weidemann, V. 1979, A&A, 76, 262
Koester, D., Voss, B., Napiwotzki, R., et al. 2009, A&A, 505, 441
Koizumi, Y., Kuzuhara, M., Omiya, M., et al. 2021, PASJ, 73, 154
Konopacky, Q. M., Ghez, A. M., Barman, T. S., et al. 2010, ApJ, 711, 1087
Kota, T., Kirkpatrick, J. D., Caselden, D., et al. 2022, AJ, 163, 116
Kraus, A. L., Tucker, R. A., Thompson, M. I., et al. 2011, ApJ, 728, 48
Kroupa, P. 2001, MNRAS, 322, 231
Kroupa, P., Weidner, C., Pflamm-Altenburg, J., et al. 2013, Planets, Stars and Stellar Systems, Vol. 5 (Dordrecht: Springer), 115
Kuchner, M. J., Faherty, J. K., Schneider, A. C., et al. 2017, ApJL, 841, L19
Kumar, S. S. 1963, ApJ, 137, 1121
Kürster, M., Endl, M., & Reffert, S. 2008, A&A, 483, 869
Kuzuhara, M., Tamura, M., Kudo, T., et al. 2013, ApJ, 774, 11
Lacour, S., Wang, J. J., Rodet, L., et al. 2021, A&A, 654, L2
Lalitha, S., Baroch, D., Morales, J. C., et al. 2019, A&A, 627, A116
Lam, K. W. F., Csizmadia, S., Astudillo-Defru, N., et al. 2021, Sci, 374, 1271
Lamman, C., Baranec, C., Berta-Thompson, Z. K., et al. 2020, AJ, 159, 139
Laplace, P. S. 1796, Exposition du Systéme du Monde (Paris: Imprimerie Cercle-Social)
Lasker, B. M. & STSCI Sky-Survey Team 1998, AAS Meeting, 192, 64.03
Laugier, R., Martinache, F., Ceau, A., et al. 2019, A&A, 623, A164
Law, N. M., Hodgkin, S. T., & Mackay, C. D. 2006, MNRAS, 368, 1917
Lawrence, A., Warren, S. J., Almaini, O., et al. 2007, MNRAS, 379, 1599
Lazorenko, P. F., & Sahlmann, J. 2018, A&A, 618, A111

Lee, S.-G. 1984, AJ, 89, 702
Leggett, S. K., Saumon, D., Marley, M. S., et al. 2012, ApJ, 748, 74
Leinert, C., Allard, F., Richichi, A., et al. 2000, A&A, 353, 691
Lépine, S. 2005b, AJ, 130, 1247
Lépine, S. 2008, AJ, 135, 2177
Lépine, S., & Gaidos, E. 2011, AJ, 142, 138
Lépine, S., Hilton, E. J., Mann, A. W., et al. 2013, AJ, 145, 102
Lépine, S., Rich, R. M., Neill, J. D., et al. 2002, ApJL, 581, L47
Lépine, S., Rich, R. M., & Shara, M. M. 2003, AJ, 125, 1598
Lépine, S., Rich, R. M., & Shara, M. M. 2007, ApJ, 669, 1235
Lépine, S., & Shara, M. M. 2005, AJ, 129, 1483
Lépine, S., Thorstensen, J. R., Shara, M. M., et al. 2009, AJ, 137, 4109
Li, T., Bedding, T. R., Kjeldsen, H., et al. 2019, MNRAS, 483, 780
Li, T. D., Bi, S. L., Liu, K., et al. 2012, A&A, 546, A83
Liebert, J., Fontaine, G., Young, P. A., et al. 2013, ApJ, 769, 7
Liebert, J., & Gizis, J. E. 2006, PASP, 118, 659
Liebert, J., Kirkpatrick, J. D., Cruz, K. L., et al. 2003, AJ, 125, 343
Liebert, J., & Sion, E. M. 1994, in ASP Conf. Ser. 60, The MK Process at 50 Years, ed. C. Corbally et al. (San Francisco: ASP), 64
Lillo-Box, J., Faria, J. P., Suárez Mascareño, A., et al. 2021, A&A, 654, A60
Lillo-Box, J., Figueira, P., Leleu, A., et al. 2020, A&A, 642, A121
Limoges, M.-M., Bergeron, P., & Lépine, S. 2015, ApJS, 219, 19
Lindegren, L., & Dravins, D. 2021, A&A, 652, A45
Lindegren, L., Hernández, J., Bombrun, A., et al. 2018, A&A, 616, A2
Lindegren, L., Klioner, S. A., Hernández, J., et al. 2021, A&A, 649, A2
Lindegren, L., Mignard, F., Söderhjelm, S., et al. 1997, A&A, 323, L53
Liu, M. C., Dupuy, T. J., & Allers, K. N. 2016, ApJ, 833, 96
Liu, M. C., Dupuy, T. J., Bowler, B. P., et al. 2012, ApJ, 758, 57
Liu, M. C., Dupuy, T. J., & Leggett, S. K. 2010, ApJ, 722, 311
Liu, M. C., Fischer, D. A., Graham, J. R., et al. 2002, ApJ, 571, 519
Liu, M. C., & Leggett, S. K. 2005, ApJ, 634, 616
Llop-Sayson, J., Wang, J. J., Ruffio, J.-B., et al. 2021, AJ, 162, 181
Lloyd, C., & Wonnacott, D. 1994, MNRAS, 266, L13
Lodieu, N., Burningham, B., Day-Jones, A., et al. 2012, A&A, 548, A53
Lodieu, N., Pinfield, D. J., Leggett, S. K., et al. 2007, MNRAS, 379, 1423
Lodieu, N., Scholz, R.-D., McCaughrean, M. J., et al. 2005, A&A, 440, 1061
Lodieu, N., Smart, R. L., Pérez-Garrido, A., et al. 2019, A&A, 623, A35
Lodieu, N., Zapatero Osorio, M. R., Martín, E. L., et al. 2022, A&A, 663, A84
Looper, D. L., Kirkpatrick, J. D., & Burgasser, A. J. 2007, AJ, 134, 1162
Looper, D. L., Kirkpatrick, J. D., Cutri, R. M., et al. 2008, ApJ, 686, 528
López-Morales, M. 2007, ApJ, 660, 732
Lopez-Santiago, J., Martino, L., Míguez, J., et al. 2020, AJ, 160, 273
Loth, A. L., & Bidelman, W. P. 1998, PASP, 110, 268
Loutrel, N. P., Luhman, K. L., Lowrance, P. J., et al. 2011, ApJ, 739, 81
Low, R., Burgasser, A. J., Reylé, C., et al. 2021, RNAAS, 5, 26
Lowrance, P. J., Kirkpatrick, J. D., & Beichman, C. A. 2002, ApJL, 572, L79
Lu, J. R., Sinukoff, E., Ofek, E. O., et al. 2016, ApJ, 830, 41
Luck, R. E. 2017, AJ, 153, 21
Luhman, K. L. 2013, ApJL, 767, L1
Luhman, K. L. 2014, ApJ, 781, 4
Luhman, K. L., Loutrel, N. P., McCurdy, N. S., et al. 2012, ApJ, 760, 152
Luhman, K. L., & Sheppard, S. S. 2014, ApJ, 787, 126
Luhn, J. K., Bastien, F. A., Wright, J. T., et al. 2019, AJ, 157, 149
Luque, R., Nowak, G., Pallé, E., et al. 2018, A&A, 620, A171
Lurie, J. C., Henry, T. J., Jao, W.-C., et al. 2014, AJ, 148, 91
Luyten, W. J. 1949, ApJ, 109, 528
Luyten, W. J. 1955, A Catalogue of 1849 Stars with Proper Motions Exceeding 0.5″ Annually (Minneapolis, MN: Lund Press)
Luyten, W. J. 1957, A Catalogue of 9867 Stars in the Southern Hemisphere with Proper Motions Exceeding 0.2″ Annually (Minneapolis, MN: Lund Press)
Luyten, W. J. 1961, A Catalogue of 7127 Stars in the Northern Hemisphere with Proper Motions Exceeding 0.2″ Annually (Minneapolis, MN: Lund Press)
Luyten, W. J. 1962, LTT Catalogues–Supplement (Minneapolis, MN: Univ. of Minnesota)
Luyten, W. J. 1963, Bruce Proper Motion Survey: The General Catalogue, Vol. 1 (Minneapolis, MN: Univ. of Minnesota)
Luyten, W. J. 1970a, PMMin, 24, 1
Luyten, W. J. 1970b, PMMin, 26, 1
Luyten, W. J. 1970c, PMMin, 27, 1
Luyten, W. J. 1972a, PMMin, 30, 1
Luyten, W. J. 1972b, PMMin, 31, 1
Luyten, W. J. 1972c, PMMin, 33, 1
Luyten, W. J. 1973a, PMMin, 34, 1
Luyten, W. J. 1973b, PMMin, 35, 1
Luyten, W. J. 1974a, PMMin, 36, 1
Luyten, W. J. 1974b, PMMin, 37, 1
Luyten, W. J. 1975a, PMMin, 40, 1
Luyten, W. J. 1975b, PMMin, 42, 1
Luyten, W. J. 1976a, PMMin, 47, 1
Luyten, W. J. 1976b, PMMin, 48, 1
Luyten, W. J. 1976c, PMMin, 49, 1
Luyten, W. J. 1979a, LHS Catalogue (2nd ed.; Minneapolis, MN: Univ. Minnesota)
Luyten, W. J. 1979b, New Luyten Catalogue of Stars with Proper Motions Larger than Two Tenths of an Arcsecond (Minneapolis, MN: Univ. Minnesota)
Luyten, W. J. 1980a, PMMin, 53, 1
Luyten, W. J., & Hughes, H. 1987a, PMMin, 69, 1
Luyten, W. J., & Hughes, H. 1987b, PMMin, 70, 1
Luyten, W. J., & Hughes, H. S. 1980, PMMin, 55, 1
Luyten, W. J., & Hughes, H. S. 1982, PMMIn, 62, 1
Luyten, W. J., & Hughes, H. S. 1983, PMMin, 63, 1
Luyten, W. J., & Hughes, H. S. 1985, PMMin, 67, 1
Luyten, W. J., & Kowal, C. T. 1975, PMMin, 43, 1
Luyten, W. J., & La Bonte, A. E. 1971, PMMin, 28, 1
Luyten, W. J., & La Bonte, A. E. 1972, PMMin, 32, 1
Luyten, W. J., Morris, S., & Hill, G. 1981, PMMin, 60, 1
Luyten, W. J., Morris, S., Hill, G., et al. 1985a, PMMin, 65, 1
Luyten, W. J., Morris, S., & Hill, G. 1985b, PMMin, 66, 1
Luyten, W. J. (ed.) 1980b, NLTT Catalogue, Vol. 3 (Mineapolis, MN: Univ. Minnesota), 283
Luyten, W. J. (ed.) 1980c, NLTT Catalogue, Vol. 4 (Minneapolis, MN: Univ. Minnesota), 151
Ma, B., Ge, J., Muterspaugh, M., et al. 2018, MNRAS, 480, 2411
Mace, G. N., Kirkpatrick, J. D., Cushing, M. C., et al. 2013a, ApJS, 205, 6
Mace, G. N., Kirkpatrick, J. D., Cushing, M. C., et al. 2013b, ApJ, 777, 36
Mace, G. N., Mann, A. W., Skiff, B. A., et al. 2018, ApJ, 854, 145
Maciejewski, G., Niedzielski, A., Nowak, G., et al. 2014, AcA, 64, 323
Mainzer, A. K., Masiero, J. R., & Abell, P. A. 2023, PSJ, 4, 224
Makarov, V. V., Zacharias, N., Hennessy, G. S., et al. 2007, ApJL, 668, L155
Makovoz, D., & Khan, I. 2005, in ASP Conf Ser. 347, Astronomical Data Analysis Software and Systems XIV, ed. P. Shopbell et al. (San Francisco, CA), 81
Makovoz, D., & Marleau, F. R. 2005, PASP, 117, 1113
Maldonado, J., Martínez-Arnáiz, R. M., Eiroa, C., et al. 2010, A&A, 521, A12
Malkov, O. Y., Oblak, E., Snegireva, E. A., et al. 2006, A&A, 446, 785
Malkov, O. Y., Tamazian, V. S., Docobo, J. A., et al. 2012, A&A, 546, A69
Malo, L., Artigau, É., Doyon, R., et al. 2014a, ApJ, 788, 81
Malo, L., Doyon, R., Feiden, G. A., et al. 2014b, ApJ, 792, 37
Malogolovets, E. V., Balega, Y. Y., & Rastegaev, D. A. 2007, AstBu, 62, 111
Mamajek, E. E. 2012, ApJL, 754, L20
Mamajek, E. E., Marocco, F., Rees, J. M., et al. 2018, RNAAS, 2, 205
Manjavacas, E., Goldman, B., Reffert, S., et al. 2013, A&A, 560, A52
Mann, A. W., Dupuy, T., Kraus, A. L., et al. 2019, ApJ, 871, 63
Mann, A. W., Feiden, G. A., Gaidos, E., et al. 2015, ApJ, 804, 64
Mardling, R. A., & Aarseth, S. J. 2001, MNRAS, 321, 398
Marigo, P., Girardi, L., Bressan, A., et al. 2017, ApJ, 835, 77
Mariotti, J.-M., Perrier, C., Duquennoy, A., et al. 1990, A&A, 230, 77
Marley, M. S., Saumon, D., Visscher, C., et al. 2021, ApJ, 920, 85
Marmier, M., Ségransan, D., Udry, S., et al. 2013, A&A, 551, A90
Marocco, F., Andrei, A. H., Smart, R. L., et al. 2013, AJ, 146, 161
Marocco, F., Eisenhardt, P. R. M., Fowler, J. W., et al. 2021, ApJS, 253, 8
Marocco, F., Smart, R. L., Jones, H. R. A., et al. 2010, A&A, 524, A38
Marsh, T. R., Dhillon, V. S., & Duck, S. R. 1995, MNRAS, 275, 828
Martin, C., & Mignard, F. 1998, A&A, 330, 585
Martin, C., Mignard, F., Hartkopf, W. I., et al. 1998, A&AS, 133, 149
Martin, E. C., Kirkpatrick, J. D., Beichman, C. A., et al. 2018, ApJ, 867, 109
Martin, E. L., & Brandner, W. 1995, A&A, 294, 744
Martinache, F., Lloyd, J. P., Ireland, M. J., et al. 2007, ApJ, 661, 496
Martinache, F., Rojas-Ayala, B., Ireland, M. J., et al. 2009, ApJ, 695, 1183
Mason, B. D., Hartkopf, W. I., Gies, D. R., et al. 2009, AJ, 137, 3358
Mason, B. D., Hartkopf, W. I., & Miles, K. N. 2017, AJ, 154, 200
Mason, B. D., Hartkopf, W. I., Miles, K. N., et al. 2018, AJ, 155, 215
Maxted, P. F. L., Marsh, T. R., & Moran, C. K. J. 2002, MNRAS, 332, 745
Mayor, M., Udry, S., Naef, D., et al. 2004, A&A, 415, 391
McCaughrean, M. J., & Pearson, S. G. 2023, arXiv:2310.03552
McCleery, J., Tremblay, P.-E., Gentile Fusillo, N. P., et al. 2020, MNRAS, 499, 1890
McCook, G. P., & Sion, E. M. 1999, ApJS, 121, 1
McCook, G. P., & Sion, E. M. 2016, yCat, B/wd
McElwain, M. W., & Burgasser, A. J. 2006, AJ, 132, 2074

McLean, I. S., Steidel, C. C., Epps, H. W., et al. 2012, Proc. SPIE, 8446, 84460J
McMahon, R. G., Banerji, M., Gonzalez, E., et al. 2013, Msngr, 154, 35
Meisner, A. M., Caselden, D., Kirkpatrick, J. D., et al. 2020a, ApJ, 889, 74
Meisner, A. M., Caselden, D., Schlafly, E. F., et al. 2023a, AJ, 165, 36
Meisner, A. M., Faherty, J. K., Kirkpatrick, J. D., et al. 2020b, ApJ, 899, 123
Meisner, A. M., Lang, D., & Schlegel, D. J. 2018, AJ, 156, 69
Meisner, A. M., Leggett, S. K., Logsdon, S. E., et al. 2023b, AJ, 166, 57
Mendez, R. A., Clavería, R. M., & Costa, E. 2021, AJ, 161, 155
Merc, J., Gális, R., Wolf, M., et al. 2021, MNRAS, 506, 4151
Mermilliod, J. C. 1987, BICDS, 32, 37
Metcalfe, T. S., van Saders, J. L., Basu, S., et al. 2021, ApJ, 921, 122
Miller, G. E., & Scalo, J. M. 1979, ApJS, 41, 513
Minkowski, R. L., & Abell, G. O. 1963, Basic Astronomical Data: Stars and Stellar Systems (Chicago, IL: Univ. Chicago Press), 481
Minniti, D., Lucas, P. W., Emerson, J. P., et al. 2010, NewA, 15, 433
Mitrofanova, A., Dyachenko, V., Beskakotov, A., et al. 2020, AJ, 159, 266
Mitrofanova, A., Dyachenko, V., Beskakotov, A., et al. 2021, AJ, 162, 156
Mollière, P., Molyarova, T., Bitsch, B., et al. 2022, ApJ, 934, 74
Monnier, J. D., Che, X., Zhao, M., et al. 2012, ApJL, 761, L3
Monnier, J. D., Zhao, M., Pedretti, E., et al. 2007, Sci, 317, 342
Montagnier, G., Ségransan, D., Beuzit, J.-L., et al. 2006, A&A, 460, L19
Montes, D., Crespo-Chacón, I., Gálvez, M. C., et al. 2007, in IAU Symp. 240, Binary Stars as Critical Tools & Tests in Contemporary Astrophysics, ed. W. I. Hartkopf et al. (Cambridge: Cambridge Univ. Press), 690
Montes, D., Gálvez, M. C., Fernández-Figueroa, M. J., et al. 2006, Ap&SS, 304, 367
Moorwood, A., Cuby, J.-G., & Lidman, C. 1998, Msngr, 91, 9
Morales, J. C., Ribas, I., Jordi, C., et al. 2009, ApJ, 691, 1400
Morbey, C. L., & Griffin, R. F. 1987, ApJ, 317, 343
Morgan, W. W., Abt, H. A., & Tapscott, J. W. 1978, Revised MK Spectral Atlas for Stars Earlier than the Sun (Williams Bay, WI/Tucson, AZ: Yerkes Observatory/Kitt Peak National Observatory)
Morgan, W. W., & Keenan, P. C. 1973, ARA&A, 11, 29
Morgan, W. W., Keenan, P. C., & Kellman, E. 1943, An Atlas of Stellar Spectra, with an Outline of Spectral Classification (Chicago, IL: Univ. Chicago Press)
Morley, C. V., Skemer, A. J., Miles, B. E., et al. 2019, ApJL, 882, L29
Mosser, B., Deheuvels, S., Michel, E., et al. 2008, A&A, 488, 635
Mowlavi, N., Eggenberger, P., Meynet, G., et al. 2012, A&A, 541, A41
Mowlavi, N., Meynet, G., Maeder, A., et al. 1998, A&A, 335, 573
Mróz, P., Udalski, A., Skowron, J., et al. 2017, Natur, 548, 183
Mugrauer, M., Schlagenhauf, S., Buder, S., et al. 2022, AN, 343, e24014
Muirhead, P. S., Dressing, C. D., Mann, A. W., et al. 2018, AJ, 155, 180
Murray, C. A., Argyle, R. W., & Corben, P. M. 1986, MNRAS, 223, 629
Murray, D. N., Burningham, B., Jones, H. R. A., et al. 2011, MNRAS, 414, 575
Mužić, K., Radigan, J., Jayawardhana, R., et al. 2012, AJ, 144, 180
Naef, D., Mayor, M., Pepe, F., et al. 2001, A&A, 375, 205
Ness, M., Hogg, D. W., Rix, H.-W., et al. 2016, ApJ, 823, 114
Neuhäuser, R., Mugrauer, M., Fukagawa, M., et al. 2007, A&A, 462, 777
Newton, E. R., Charbonneau, D., Irwin, J., et al. 2014, AJ, 147, 20
Nidever, D. L., Marcy, G. W., Butler, R. P., et al. 2002, ApJS, 141, 503
Nielsen, E. L., De Rosa, R. J., Macintosh, B., et al. 2019, AJ, 158, 13
Nilsson, R., Veicht, A., Giorla Godfrey, P. A., et al. 2017, ApJ, 838, 64
Nissen, P. E. 2004, Carnegie Observatories Centennial Symposium 4, Origin and Evolution of the Elements (Cambridge: Cambridge Univ. Press), 154
Nordström, B., Mayor, M., Andersen, J., et al. 2004, A&A, 418, 989
Öberg, K. I., Murray-Clay, R., & Bergin, E. A. 2011, ApJL, 743, L16
O'Brien, M. W., Tremblay, P.-E., Gentile Fusillo, N. P., et al. 2023, MNRAS, 518, 3055
Oke, J. B., & Gunn, J. E. 1982, PASP, 94, 586
Bakos, G. Á., Pál, A., Latham, D. W., et al. 2006, ApJL, 641, L57
Pan, X. P., Shao, M., Colavita, M. M., et al. 1990, ApJ, 356, 641
Pearson, S. G., & McCaughrean, M. J. 2023, arXiv:2310.01231
Pecaut, M. J., & Mamajek, E. E. 2013, ApJS, 208, 9
Penoyre, Z., Belokurov, V., & Evans, N. W. 2022a, MNRAS, 513, 2437
Penoyre, Z., Belokurov, V., & Evans, N. W. 2022b, MNRAS, 513, 5270
Penoyre, Z., Belokurov, V., Wyn Evans, N., et al. 2020, MNRAS, 495, 321
Pepe, F., Lovis, C., Ségransan, D., et al. 2011, A&A, 534, A58
Peretti, S., Ségransan, D., Lavie, B., et al. 2019, A&A, 631, A107
Perger, M., Ribas, I., Damasso, M., et al. 2017, A&A, 608, A63
Perger, M., Scandariato, G., Ribas, I., et al. 2019, A&A, 624, A123
Perrine, C. D. 1932, RNAO, 21, 1
Perryman, M. A. C., Brown, A. G. A., Lebreton, Y., et al. 1998, A&A, 331, 81
Pettersen, B. R. 2006, Obs, 126, 397
Phan-Bao, N., & Bessell, M. S. 2006, A&A, 446, 515
Phan-Bao, N., Bessell, M. S., Martín, E. L., et al. 2008, MNRAS, 383, 831
Phan-Bao, N., Bessell, M. S., Nguyen-Thanh, D., et al. 2017, A&A, 600, A19
Phillips, M. W., Tremblin, P., Baraffe, I., et al. 2020, A&A, 637, A38
Piccotti, L., Docobo, J. Á, Carini, R., et al. 2020, MNRAS, 492, 2709
Pinamonti, M., Damasso, M., Marzari, F., et al. 2018, A&A, 617, A104
Pinamonti, M., Sozzetti, A., Giacobbe, P., et al. 2019, A&A, 625, A126
Pinamonti, M., Sozzetti, A., Maldonado, J., et al. 2022, A&A, 664, A65
Pineda, J. S., Hallinan, G., Kirkpatrick, J. D., et al. 2016, ApJ, 826, 73
Pinfield, D. J., Burningham, B., Lodieu, N., et al. 2012, MNRAS, 422, 1922
Pinfield, D. J., Burningham, B., Tamura, M., et al. 2008, MNRAS, 390, 304
Pinfield, D. J., Gomes, J., Day-Jones, A. C., et al. 2014a, MNRAS, 437, 1009
Pinfield, D. J., Gromadzki, M., Leggett, S. K., et al. 2014b, MNRAS, 444, 1931
Planck Collaboration, Aghanim, N., & Akrami, Y. 2020, A&A, 641, A6
Pokorny, R. S., Jones, H. R. A., & Hambly, N. C. 2003, A&A, 397, 575
Pokorny, R. S., Jones, H. R. A., Hambly, N. C., et al. 2004, A&A, 421, 763
Pourbaix, D. 2000, A&AS, 145, 215
Pourbaix, D., Tokovinin, A. A., Batten, A. H., et al. 2004, A&A, 424, 727
Pourbaix, D., Tokovinin, A. A., Batten, A. H., et al. 2009, yCat, B/sb9
Poveda, A., Allen, C., Costero, R., et al. 2009, ApJ, 706, 343
Pravdo, S. H., Shaklan, S. B., Wiktorowicz, S. J., et al. 2006, ApJ, 649, 389
Queiroz, A. B. A., Anders, F., Santiago, B. X., et al. 2018, MNRAS, 476, 2556
Quirrenbach, A., Passegger, V. M., Trifonov, T., et al. 2022, A&A, 663, A48
Raghavan, D., McAlister, H. A., Henry, T. J., et al. 2010, ApJS, 190, 1
Raghu, Y., Kirkpatrick, J. D., Marocco, F., et al. 2024, ApJ, submitted.
Rajpurohit, A. S., Kumar, V., Srivastava, M. K., et al. 2020, MNRAS, 492, 5844
Rajpurohit, A. S., Reylé, C., Allard, F., et al. 2013, A&A, 556, A15
Ramírez, I., & Allende Prieto, C. 2011, ApJ, 743, 135
Ramm, D. J., Hearnshaw, J. B., & Skuljan, J. 2005, Obs, 125, 30
Ramm, D. J., Nelson, B. E., Endl, M., et al. 2016, MNRAS, 460, 3706
Ramm, D. J., Robertson, P., Reffert, S., et al. 2021, MNRAS, 502, 2793
Rebassa-Mansergas, A., Parsons, S. G., Dhillon, V. S., et al. 2019, NatAs, 3, 553
Rebassa-Mansergas, A., Parsons, S. G., García-Berro, E., et al. 2017, MNRAS, 466, 1575
Reffert, S., & Quirrenbach, A. 2011, A&A, 527, A140
Reid, I. N. 2005, The Initial Mass Function 50 Years Later (Dordrecht: Springer), 53
Reid, I. N., Brewer, C., Brucato, R. J., et al. 1991, PASP, 103, 661
Reid, I. N., Cruz, K. L., Allen, P., et al. 2003, AJ, 126, 3007
Reid, I. N., Cruz, K. L., Allen, P., et al. 2004, AJ, 128, 463
Reid, I. N., Cruz, K. L., & Allen, P. R. 2007, AJ, 133, 2825
Reid, I. N., Cruz, K. L., Burgasser, A. J., et al. 2008a, AJ, 135, 580
Reid, I. N., Cruz, K. L., Kirkpatrick, J. D., et al. 2008b, AJ, 136, 1290
Reid, I. N., & Gizis, J. E. 2005, PASP, 117, 676
Reid, I. N., Gizis, J. E., & Hawley, S. L. 2002, AJ, 124, 2721
Reid, I. N., Gizis, J. E., Kirkpatrick, J. D., et al. 2001, AJ, 121, 489
Reid, I. N., Hawley, S. L., & Gizis, J. E. 1995, AJ, 110, 1838
Reid, I. N., Kirkpatrick, J. D., Gizis, J. E., et al. 2000, AJ, 119, 369
Reid, I. N., Lewitus, E., Allen, P. R., et al. 2006, AJ, 132, 891
Reid, N., & Mould, J. 1990, ApJ, 360, 490
Reiners, A., Joshi, N., & Goldman, B. 2012, AJ, 143, 93
Ren, S., & Fu, Y. 2013, AJ, 145, 81
Reuyl, D. 1943, ApJ, 97, 186
Reylé, C. 2018, A&A, 619, L8
Reylé, C., Jardine, K., Fouqué, P., et al. 2021, A&A, 650, A201
Reylé, C., Robin, A. C., Scholz, R.-D., et al. 2002, A&A, 390, 491
Reylé, C., Scholz, R.-D., Schultheis, M., et al. 2006, MNRAS, 373, 705
Riaz, B., Gizis, J. E., & Harvin, J. 2006, AJ, 132, 866
Ribas, I. 2003, A&A, 398, 239
Ribas, I., & Miralda-Escudé, J. 2007, A&A, 464, 779
Rice, J. B., & Strassmeier, K. G. 1998, A&A, 336, 972
Richichi, A., Fabbroni, L., Ragland, S., et al. 1999, A&A, 344, 511
Ricker, G. R., Winn, J. N., Vanderspek, R., et al. 2015, JATIS, 1, 014003
Riedel, A. R., Alam, M. K., Rice, E. L., et al. 2017, ApJ, 840, 87
Riedel, A. R., Finch, C. T., Henry, T. J., et al. 2014, AJ, 147, 85
Riedel, A. R., Silverstein, M. L., Henry, T. J., et al. 2018, AJ, 156, 49
Riedel, A. R., Subasavage, J. P., Finch, C. T., et al. 2010, AJ, 140, 897
Riello, M., De Angeli, F., Evans, D. W., et al. 2021, A&A, 649, A3
Robbins, G., Meisner, A. M., Schneider, A. C., et al. 2023a, RNAAS, 7, 144
Robbins, G., Meisner, A. M., Schneider, A. C., et al. 2023b, ApJ, 958, 94
Robert, J., Gagné, J., Artigau, É., et al. 2016, ApJ, 830, 144
Roberts, L. C., Turner, N. H., ten Brummelaar, T. A., et al. 2011, AJ, 142, 175
Rodet, L., Bonnefoy, M., Durkan, S., et al. 2018, A&A, 618, A23
Rodigas, T. J., Males, J. R., Hinz, P. M., et al. 2011, ApJ, 732, 10

Rodler, F., Lopez-Morales, M., & Ribas, I. 2012, ApJL, 753, L25
Rodriguez, D. R., Duchêne, G., Tom, H., et al. 2015, MNRAS, 449, 3160
Roman, N. G. 1987, PASP, 99, 695
Romero, A. D., Córsico, A. H., Althaus, L. G., et al. 2012, MNRAS, 420, 1462
Romero, A. D., Kepler, S. O., Córsico, A. H., et al. 2013, ApJ, 779, 58
Rosenthal, L. J., Fulton, B. J., Hirsch, L. A., et al. 2021, ApJS, 255, 8
Ross, F. E. 1925, AJ, 36, 96
Ross, F. E. 1926a, AJ, 36, 124
Ross, F. E. 1926b, AJ, 36, 172
Ross, F. E. 1926c, AJ, 37, 53
Ross, F. E. 1927, AJ, 37, 193
Ross, F. E. 1928, AJ, 38, 117
Ross, F. E. 1929, AJ, 39, 140
Ross, F. E. 1930, AJ, 40, 38
Ross, F. E. 1931, AJ, 41, 88
Ross, F. E. 1937, AJ, 46, 157
Ross, F. E. 1939a, AJ, 48, 10
Ross, F. E. 1939b, AJ, 48, 163
Rothermich, A., Faherty, J. K., Bardalez-Gagliuffi, D., et al. 2024, ApJ, submitted.
Sahlmann, J., Dupuy, T. J., Burgasser, A. J., et al. 2021, MNRAS, 500, 5453
Sahlmann, J., Lazorenko, P. F., Ségransan, D., et al. 2015, A&A, 577, A15
Sahu, K. C., Anderson, J., Bellini, A., et al. 2020, HST Proposal, 16251
Sahu, K. C., Anderson, J., Casertano, S., et al. 2017, Sci, 356, 1046
Salama, M., Ou, J., Baranec, C., et al. 2021, AJ, 162, 102
Salama, M., Ziegler, C., Baranec, C., et al. 2022, AJ, 163, 200
Salim, S., Lépine, S., Rich, R. M., et al. 2003, ApJL, 586, L149
Salpeter, E. E. 1955, ApJ, 121, 161
Samus, N. N., & Durlevich, O. V. 2004, yCat, II/250
Samus', N. N., Goranskii, V. P., Durlevich, O. V., et al. 2003, AstL, 29, 468
Samus', N. N., Kazarovets, E. V., Durlevich, O. V., et al. 2017, ARep, 61, 80
Sandford, E., & Kipping, D. 2017, AJ, 154, 228
Santos, N. C., Udry, S., Mayor, M., et al. 2003, A&A, 406, 373
Sarna, M. J., Antipova, J., & Ergma, E. 1999, in ASP Conf. Ser. 169, 11th European Workshop on White Dwarfs, ed. S. E. Solheim & E. G. Meistas (San Francisco, CA: ASP), 400
Saumon, D., & Marley, M. S. 2008, ApJ, 689, 1327
Scalo, J. M. 1986, FCPh, 11, 1
Schapera, N., Caselden, D., Meisner, A. M., et al. 2022, RNAAS, 6, 189
Schlafly, E. F., Green, G. M., Lang, D., et al. 2018, ApJS, 234, 39
Schlaufman, K. C. 2018, ApJ, 853, 37
Schlesinger, F. 1930, Catalogue of Bright Stars (New Haven, CT: The Tuttle, Morehouse & Taylor Company)
Schlesinger, F., & Jenkins, L. F. 1940, Catalogue of Bright Stars (New Haven, CT: The New Haven Printing Company)
Schlieder, J. E., Bonnefoy, M., Herbst, T. M., et al. 2014, ApJ, 783, 27
Schlieder, J. E., Lépine, S., & Simon, M. 2010, AJ, 140, 119
Schlieder, J. E., Lépine, S., & Simon, M. 2012, AJ, 143, 80
Schmidt, M. 1968, ApJ, 151, 393
Schmidt, S. J., Cruz, K. L., Bongiorno, B. J., et al. 2007, AJ, 133, 2258
Schmidt, S. J., West, A. A., Hawley, S. L., et al. 2010, AJ, 139, 1808
Schneider, A. C., Burgasser, A. J., Bruursema, J., et al. 2023, ApJL, 943, L16
Schneider, A. C., Burgasser, A. J., Gerasimov, R., et al. 2020, ApJ, 898, 77
Schneider, A. C., Cushing, M. C., Kirkpatrick, J. D., et al. 2014, AJ, 147, 34
Schneider, A. C., Cushing, M. C., Kirkpatrick, J. D., et al. 2015, ApJ, 804, 92
Schneider, A. C., Greco, J., Cushing, M. C., et al. 2016, ApJ, 817, 112
Schneider, A. C., Meisner, A. M., Gagné, J., et al. 2021, ApJ, 921, 140
Schneider, A. C., Shkolnik, E. L., Allers, K. N., et al. 2019, AJ, 157, 234
Schneider, A. C., Vrba, F. J., Munn, J. A., et al. 2022, AJ, 163, 242
Schneider, A. C., Windsor, J., Cushing, M. C., et al. 2017, AJ, 153, 196
Scholz, R.-D., Bihain, G., & Storm, J. 2014, A&A, 567, A43
Scholz, R.-D., Ibata, R., Irwin, M., et al. 2002, MNRAS, 329, 109
Scholz, R.-D., Irwin, M., Ibata, R., et al. 2000, A&A, 353, 958
Scholz, R.-D., Irwin, M., Schweitzer, A., et al. 1999, A&A, 345, L55
Scholz, R.-D., Lehmann, I., Matute, I., et al. 2004, A&A, 425, 519
Scholz, R.-D., McCaughrean, M. J., Lodieu, N., et al. 2003, A&A, 398, L29
Scholz, R.-D., & Meusinger, H. 2002, MNRAS, 336, L49
Scholz, R.-D., Meusinger, H., & Jahreiß, H. 2005, A&A, 442, 211
Schönfeld, E. (ed.) 1886, Bonner Durchmusterung des Sudlichen Himmels (Bonn: Marcus and Weber's Verlag)
Schuster, W. J. 1979, RMxAA, 4, 233
Schweitzer, A., Passegger, V. M., Cifuentes, C., et al. 2019, A&A, 625, A68
Schweitzer, A., Scholz, R.-D., Stauffer, J., et al. 1999, A&A, 350, L62
Seager, S., & Mallén-Ornelas, G. 2003, ApJ, 585, 1038
Ségransan, D., Delfosse, X., Forveille, T., et al. 2000, A&A, 364, 665
Seifahrt, A., Röll, T., Neuhäuser, R., et al. 2008, A&A, 484, 429
Serenelli, A. M., Althaus, L. G., Rohrmann, R. D., et al. 2001, MNRAS, 325, 607
Shan, Y., Yee, J. C., Bowler, B. P., et al. 2017, ApJ, 846, 93
Shibahashi, H. 2007, in AIP Conf. Proc. 948, Unsolved Problems in Stellar Physics: A Conf. in Honor of Douglas Gough, ed. R. J. Stancliffe et al. (Melville, NY: AIP), 35
Shkolnik, E., Liu, M. C., & Reid, I. N. 2009, ApJ, 699, 649
Shkolnik, E. L., Anglada-Escudé, G., Liu, M. C., et al. 2012, ApJ, 758, 56
Shkolnik, E. L., Hebb, L., Liu, M. C., et al. 2010, ApJ, 716, 1522
Silverstein, M. L., Schlieder, J. E., Barclay, T., et al. 2022, AJ, 163, 151
Silvestri, N. M., Oswalt, T. D., Wood, M. A., et al. 2001, AJ, 121, 503
Simcoe, R. A., Burgasser, A. J., Schechter, P. L., et al. 2013, PASP, 125, 270
Sion, E. M., Holberg, J. B., Oswalt, T. D., et al. 2014, AJ, 147, 129
Skemer, A. J., Morley, C. V., Zimmerman, N. T., et al. 2016, ApJ, 817, 166
Skiff, B. A. 2013, yCat, 1, 2023
Skrutskie, M. F., Cutri, R. M., Stiening, R., et al. 2006, AJ, 131, 1163
Skrzypek, N., Warren, S. J., & Faherty, J. K. 2016, A&A, 589, A49
Skuljan, J., Ramm, D. J., & Hearnshaw, J. B. 2004, MNRAS, 352, 975
Smart, R. L., Bucciarelli, B., Jones, H. R. A., et al. 2018, MNRAS, 481, 3548
Smart, R. L., Tinney, C. G., Bucciarelli, B., et al. 2013, MNRAS, 433, 2054
Smith, L., Lucas, P. W., Bunce, R., et al. 2014, MNRAS, 443, 2327
Söderhjelm, S. 1999, A&A, 341, 121
Soriano, M., & Vauclair, S. 2010, A&A, 513, A49
Soto, M. G., Anglada-Escudé, G., Dreizler, S., et al. 2021, A&A, 649, A144
Soto, M. G., & Jenkins, J. S. 2018, A&A, 615, A76
Sousa, S. G., Santos, N. C., Mayor, M., et al. 2008, A&A, 487, 373
Sperauskas, J., Deveikis, V., & Tokovinin, A. 2019, A&A, 626, A31
Stahler, S. W., & Palla, F. (ed.) 2004, The Formation of Stars (New York: Wiley-VCH), 865
Stassun, K. G., Collins, K. A., & Gaudi, B. S. 2017, AJ, 153, 136
Stassun, K. G., Corsaro, E., Pepper, J. A., et al. 2018a, AJ, 155, 22
Stassun, K. G., Oelkers, R. J., Paegert, M., et al. 2019, AJ, 158, 138
Stassun, K. G., Oelkers, R. J., Pepper, J., et al. 2018b, AJ, 156, 102
Stassun, K. G., & Torres, G. 2016, AJ, 152, 180
Stassun, K. G., & Torres, G. 2021, ApJL, 907, L33
Stauffer, J., Tanner, A. M., Bryden, G., et al. 2010, PASP, 122, 885
Stelzer, B., & Burwitz, V. 2003, A&A, 402, 719
Stepanov, R., Bondar', N. I., Katsova, M. M., et al. 2020, MNRAS, 495, 3788
Stephenson, C. B., & Sanduleak, N. 1975, AJ, 80, 972
Stephneson, C. B., & Terrill, C. L. 1967, ApJ, 147, 148
Stevens, D. J., Gaudi, B. S., & Stassun, K. G. 2018, ApJ, 862, 53
Stock, S., Nagel, E., Kemmer, J., et al. 2020, A&A, 643, A112
Strassmeier, K. G., & Fekel, F. C. 1990, A&A, 230, 389
Strassmeier, K. G., Ilyin, I., & Weber, M. 2018, A&A, 612, A45
Struve, O., & Franklin, K. L. 1955, ApJ, 121, 337
Struve, O., & Ratcliffe, E. 1954, PASP, 66, 31
Suárez Mascareño, A., González Hernández, J. I., Rebolo, R., et al. 2017a, A&A, 597, A108
Suárez Mascareño, A., González Hernández, J. I., Rebolo, R., et al. 2017b, A&A, 605, A92
Subasavage, J. P., Henry, T. J., Hambly, N. C., et al. 2005a, AJ, 129, 413
Subasavage, J. P., Henry, T. J., Hambly, N. C., et al. 2005b, AJ, 130, 1658
Subasavage, J. P., Jao, W.-C., Henry, T. J., et al. 2017, AJ, 154, 32
Sun, M., & Arras, P. 2018, ApJ, 858, 14
Takeda, G., Ford, E. B., Sills, A., et al. 2007, ApJS, 168, 297
Tamazian, V. S., Docobo, J. A., Melikian, N. D., et al. 2006, PASP, 118, 814
Teixeira, T. C., Kjeldsen, H., Bedding, T. R., et al. 2009, A&A, 494, 237
Terrien, R. C., Mahadevan, S., Deshpande, R., et al. 2015, ApJS, 220, 16
Theissen, C. A. 2018, ApJ, 862, 173
Thévenin, F., Kervella, P., Pichon, B., et al. 2005, A&A, 436, 253
Thome, J. M. 1890, AJ, 10, 105
Thome, J. M. 1892, RNAO, 16, 1
Thome, J. M. 1894, RNAO, 17, 1
Thome, J. M. 1900, Cordoba Durchmusterung (Buenos Aires: Coni)
Thome, J. M. 1914, RNAO, 21, 1
Thompson, M. A., Kirkpatrick, J. D., Mace, G. N., et al. 2013, PASP, 125, 809
Thorstensen, J. R., & Kirkpatrick, J. D. 2003, PASP, 115, 1207
Tinney, C. G., Burgasser, A. J., & Kirkpatrick, J. D. 2003, AJ, 126, 975
Tinney, C. G., Butler, R. P., Jones, H. R. A., et al. 2011, ApJ, 727, 103
Tinney, C. G., Faherty, J. K., Kirkpatrick, J. D., et al. 2014, ApJ, 796, 39
Tinney, C. G., Kirkpatrick, J. D., Faherty, J. K., et al. 2018, ApJS, 236, 28
Tody, D. 1986, Proc. SPIE, 627, 733
Tody, D. 1993, in ASP Conf. Ser. 52, Astronomical Data Analysis Software and Systems II, ed. R. J. Hanisch et al. (San Francisco, CA: ASP), 173
Tokovinin, A. 2004, RMxAC, 21, 7
Tokovinin, A. 2008, MNRAS, 389, 925

Tokovinin, A. 2014, AJ, 147, 87
Tokovinin, A. 2017, AJ, 154, 110
Tokovinin, A. 2021b, AJ, 161, 144
Tokovinin, A., Everett, M. E., Horch, E. P., et al. 2019, AJ, 158, 167
Tokovinin, A., Hartung, M., Hayward, T. L., et al. 2012, AJ, 144, 7
Tokovinin, A., & Horch, E. P. 2016, AJ, 152, 116
Tokovinin, A., Kiyaeva, O., Sterzik, M., et al. 2005, A&A, 441, 695
Tokovinin, A., Mason, B. D., & Hartkopf, W. I. 2014, AJ, 147, 123
Tokovinin, A., Mason, B. D., Mendez, R. A., et al. 2020, AJ, 160, 7
Tokovinin, A., Mason, B. D., Mendez, R. A., et al. 2021, AJ, 162, 41
Tokovinin, A., Thomas, S., Sterzik, M., et al. 2006, A&A, 450, 681
Tokovinin, A. A. 1997, A&AS, 124, 75
Tokunaga, A. T., Simons, D. A., & Vacca, W. D. 2002, PASP, 114, 180
Toledo-Padrón, B., Suárez Mascareño, A., González Hernández, J. I., et al. 2021, A&A, 648, A20
Toonen, S., Hollands, M., Gänsicke, B. T., et al. 2017, A&A, 602, A16
Torres, C. A. O., Quast, G. R., da Silva, L., et al. 2006, A&A, 460, 695
Torres, G. 2022, MNRAS, 514, 5183
Torres, G., Andersen, J., & Giménez, A. 2010, A&ARv, 18, 67
Torres, G., Claret, A., Pavlovski, K., et al. 2015, ApJ, 807, 26
Torres, G., & Ribas, I. 2002, ApJ, 567, 1140
Tremblay, P.-E., Bergeron, P., & Gianninas, A. 2011, ApJ, 730, 128
Tremblay, P.-E., Cukanovaite, E., Gentile Fusillo, N. P., et al. 2019, MNRAS, 482, 5222
Tremblay, P.-E., Hollands, M. A., Gentile Fusillo, N. P., et al. 2020, MNRAS, 497, 130
Trifonov, T., Caballero, J. A., Morales, J. C., et al. 2021, Sci, 371, 1038
Trifonov, T., Kürster, M., Zechmeister, M., et al. 2018, A&A, 609, A117
Trifonov, T., Tal-Or, L., Zechmeister, M., et al. 2020, A&A, 636, A74
Tsantaki, M., Sousa, S. G., Adibekyan, V. Z., et al. 2013, A&A, 555, A150
Turon, C., Creze, M., Egret, D., et al. 1993, BICDS, 43, 5
Ujjwal, K., Kartha, S. S., Mathew, B., et al. 2020, AJ, 159, 166
Unger, N., Ségransan, D., Queloz, D., et al. 2021, A&A, 654, A104
Upgren, A. R., Grossenbacher, R., Penhallow, W. S., et al. 1972, AJ, 77, 486
Vacca, W. D., Cushing, M. C., & Rayner, J. T. 2003, PASP, 115, 389
Valenti, J. A., & Fischer, D. A. 2005, ApJS, 159, 141
van Altena, W. F., Lee, J. T., & Hoffleit, E. D. 1995, The General Catalogue of Trigonometric [Stellar] Parallaxes (4th ed.; New Haven, CT: Yale Univ. Observatory)
van Belle, G. T., Ciardi, D. R., & Boden, A. F. 2007, ApJ, 657, 1058
van Belle, G. T., & von Braun, K. 2009, ApJ, 694, 1085
van Biesbroeck, G. 1974, ApJS, 28, 413
van de Kamp, P., & Worth, M. D. 1971, AJ, 76, 1129
van Leeuwen, F. 2007, A&A, 474, 653
Volk, K., Blum, R., Walker, G., et al. 2003, IAUC, 8188, 2
von Braun, K., Boyajian, T. S., ten Brummelaar, T. A., et al. 2011, ApJ, 740, 49
Vrba, F. J., Henden, A. A., Luginbuhl, C. B., et al. 2004, AJ, 127, 2948
Vrijmoet, E. H., Henry, T. J., Jao, W.-C., et al. 2020, AJ, 160, 215
Vrijmoet, E. H., Tokovinin, A., Henry, T. J., et al. 2022, AJ, 163, 178
Walker, M. A. 1995, ApJ, 453, 37
Wang, J., & Fischer, D. A. 2015, AJ, 149, 14
Ward-Duong, K., Patience, J., De Rosa, R. J., et al. 2015, MNRAS, 449, 2618
Weidemann, V. 2000, A&A, 363, 647
Wenger, M., Ochsenbein, F., Egret, D., et al. 2000, A&AS, 143, 9
West, A. A., Hawley, S. L., Bochanski, J. J., et al. 2008, AJ, 135, 785
West, A. A., Morgan, D. P., Bochanski, J. J., et al. 2011, AJ, 141, 97
West, A. A., Weisenburger, K. L., Irwin, J., et al. 2015, ApJ, 812, 3
Willmarth, D. W., Fekel, F. C., Abt, H. A., et al. 2016, AJ, 152, 46
Wilson, J. C., Eikenberry, S. S., Henderson, C. P., et al. 2003a, Proc. SPIE, 4841, 451
Wilson, J. C., Henderson, C. P., Herter, T. L., et al. 2004, Proc. SPIE, 5492, 1295
Wilson, J. C., Miller, N. A., Gizis, J. E., et al. 2003b, in IAU Symp. 211, Brown Dwarfs, ed. E. Martín (San Francisco, CA: ASP), 197
Wilson, R. E., & Joy, A. H. 1950, ApJ, 111, 221
Wilson, R. E., Pilachowski, C. A., & Terrell, D. 2017, ApJ, 835, 251
Winn, J. N., & Fabrycky, D. C. 2015, ARA&A, 53, 409
Winters, J. G., Charbonneau, D., Henry, T. J., et al. 2021, AJ, 161, 63
Winters, J. G., Henry, T. J., Jao, W.-C., et al. 2011, AJ, 141, 21
Winters, J. G., Henry, T. J., Jao, W.-C., et al. 2019a, AJ, 157, 216
Winters, J. G., Henry, T. J., Lurie, J. C., et al. 2015, AJ, 149, 5
Winters, J. G., Irwin, J., Newton, E. R., et al. 2018, AJ, 155, 125
Winters, J. G., Irwin, J. M., Charbonneau, D., et al. 2020, AJ, 159, 290
Winters, J. G., Medina, A. A., Irwin, J. M., et al. 2019b, AJ, 158, 152
Winters, J. G., Sevrinsky, R. A., Jao, W.-C., et al. 2017, AJ, 153, 14
Wittenmyer, R. A., Clark, J. T., Zhao, J., et al. 2019, MNRAS, 484, 5859
Wittenmyer, R. A., Endl, M., Cochran, W. D., et al. 2006, AJ, 132, 177
Wittenmyer, R. A., Tinney, C. G., Butler, R. P., et al. 2011, ApJ, 738, 81
Wittenmyer, R. A., Tuomi, M., Butler, R. P., et al. 2014, ApJ, 791, 114
Wittrock, J. M., Kane, S. R., Horch, E. P., et al. 2017, AJ, 154, 184
Wizinowich, P., Acton, D. S., Shelton, C., et al. 2000, PASP, 112, 315
Woitas, J., Leinert, C., & Jahreiß, H. 2000, A&A, 353, 253
Wolf, M. 1919a, VeHei, 10, 195
Wolf, M. 1919b, AN, 209, 11
Wolf, M. 1919c, AN, 209, 91
Wolf, M. 1919d, AN, 209, 159
Wolf, M. 1919e, AN, 209, 62
Wolf, M. 1920a, AN, 210, 293
Wolf, M. 1920b, AN, 210, 327
Wolf, M. 1920c, AN, 210, 387
Wolf, M. 1920d, AN, 211, 223
Wolf, M. 1920e, AN, 212, 167
Wolf, M. 1920f, AN, 212, 303
Wolf, M. 1921a, AN, 212, 381
Wolf, M. 1921b, AN, 212, 381
Wolf, M. 1921c, AN, 213, 31
Wolf, M. 1921d, AN, 213, 15
Wolf, M. 1921e, AN, 214, 135
Wolf, M. 1921f, AN, 214, 261
Wolf, M. 1922, AN, 215, 357
Wolf, M. 1923a, AN, 218, 81
Wolf, M. 1923b, AN, 219, 185
Wolf, M. 1923c, AN, 220, 95
Wolf, M. 1924a, AN, 221, 15
Wolf, M. 1924b, AN, 221, 157
Wolf, M. 1924c, AN, 221, 221
Wolf, M. 1924d, AN, 222, 15
Wolf, M. 1924e, AN, 222, 47
Wolf, M. 1924f, AN, 222, 253
Wolf, M. 1925a, AN, 224, 383
Wolf, M. 1925b, AN, 225, 215
Wolf, M. 1925c, AN, 225, 215
Wolf, M. 1925d, AN, 225, 351
Wolf, M. 1925e, AN, 225, 259
Wolf, M. 1926a, AN, 228, 55
Wolf, M. 1926b, AN, 226, 357
Wolf, M. 1926c, AN, 228, 399
Wolf, M. 1927a, AN, 229, 441
Wolf, M. 1927b, AN, 230, 383
Wolf, M. 1929, AN, 236, 293
Wolf, M. 1931, AN, 243, 407
Wolf, M., & Reinmuth, K. 1925, AN, 223, 231
Wong, M. H., Mahaffy, P. R., Atreya, S. K., et al. 2004, Icar, 171, 153
Woolley, R., Epps, E. A., Penston, M. J., et al. 1970, ROAn, 5
Woosley, S. E., Heger, A., & Weaver, T. A. 2002, RvMP, 74, 1015
Wright, E. L., Eisenhardt, P. R. M., Mainzer, A. K., et al. 2010, AJ, 140, 1868
Wright, E. L., Skrutskie, M. F., Kirkpatrick, J. D., et al. 2013, AJ, 145, 84
Wright, J. T., Upadhyay, S., Marcy, G. W., et al. 2009, ApJ, 693, 1084
Wright, N. J., Newton, E. R., Williams, P. K. G., et al. 2018, MNRAS, 479, 2351
Wroblewski, H., & Costa, E. 1999, A&AS, 139, 25
Wroblewski, H., & Costa, E. 2001, A&A, 367, 725
Wroblewski, H., & Torres, C. 1989, A&AS, 78, 231
Wroblewski, H., & Torres, C. 1991, A&AS, 91, 129
Wroblewski, H., & Torres, C. 1994, A&AS, 105, 179
Wroblewski, H., & Torres, C. 1996, A&AS, 115, 481
Wroblewski, H., & Torres, C. 1997, A&AS, 122, 447
Wyatt, M. C., Smith, R., Su, K. Y. L., et al. 2007, ApJ, 663, 365
Xia, F., Fu, Y., & Wang, X. 2019, ApJ, 882, 147
Zacharias, N., Finch, C. T., Girard, T. M., et al. 2013, AJ, 145, 44
Zasche, P., Wolf, M., Hartkopf, W. I., et al. 2009, AJ, 138, 664
Zeng, Y., Brandt, T. D., Li, G., et al. 2022, AJ, 164, 188
Zhang, Q., Hallinan, G., Brisken, W., et al. 2020, ApJ, 897, 11
Zhang, Z. H., Burgasser, A. J., Gálvez-Ortiz, M. C., et al. 2019, MNRAS, 486, 1260
Zhang, Z. H., Galvez-Ortiz, M. C., Pinfield, D. J., et al. 2018, MNRAS, 480, 5447
Zhang, Z. H., Pinfield, D. J., Gálvez-Ortiz, M. C., et al. 2017, MNRAS, 464, 3040
Zhao, J. K., Oswalt, T. D., Willson, L. A., et al. 2012, ApJ, 746, 144
Zhuchkov, R. Y., Malogolovets, E. V., Kiyaeva, O. V., et al. 2012, ARep, 56, 512
Zuckerman, B., & Becklin, E. E. 1987, Natur, 330, 138
Zurlo, A., Gratton, R., Mesa, D., et al. 2018, MNRAS, 480, 236